Small Molecules Based on Novel Electron-deficient Acceptor Units for Organic Electronic Applications

Submitted by

Joseph Cameron

A thesis submitted in fulfilment of the requirements for the degree of Doctor of Philosophy in Department of Pure and Applied Chemistry, University of Strathclyde

2016

This thesis is the result of the author's original research. It has been composed by the author and has not been previously submitted for examination which has led to the award of a degree.

Signed:

Date:

.

Abstract

Demand for photovoltaic cells is ever-increasing due to the diminishing supply of oil-based fuels and the associated harmful environmental effects. Organic photovoltaic devices offer a light and flexible alternative to Si-based PVs. In addition to this, they can be processed using fabrication methods such as spin-coating and inkjet printing hence, such devices have potential to be produced cheaply on a large scale. Although they have been applied as donor materials with success, polymers often show end-group variation and are polydisperse so there can be batch-to-batch variation with respect to OPV performance. A solution to these problems is the use of small donor molecules which are monodisperse and have well-defined structures. However, the shorter conjugation of small molecules with respect to polymers requires measures to shorten the HOMO-LUMO gap. A common approach is the incorporation of electron-deficient acceptor units into the donor molecule, lowering the LUMO level and therefore the HOMO-LUMO gap.

Chapter 1 reviews band theory, the development of organic semiconductors, including a summary of oligothiophene based materials and common electron-deficient acceptor units used, the principles behind OPV and OFET devices and how organic semiconductors can be optimised in order to produce the best working devices.

The synthesis, physical properties and OPV performance of materials based on naphthyridine-2,6-dione acceptor unit are presented in chapter 2, focussing on the difference between compounds with Donor-Acceptor-Donor and Acceptor-Donor-Acceptor structures.

Chapter 3 shows the novel naphthyridin-2-one moiety and the synthesis of materials containing the unit and how they have been used for different applications including ambipolar OFETs and both donor and acceptor materials for bulk heterojunction OPV devices.

A study in improving the mobility of OFET devices is presented in chapter 4. Different inorganic nanoparticles were added to organic semiconductor solutions for and the effect of this simple process on the performance of the OFET devices is discussed.

Chapter 5 introduces the thieno[3,2-b]thiophene-2,5-dione and novel furo[3,2-b]furan-2,5-dione acceptor units. The synthesis, optical and electrochemical properties, and OFET and OPV device optimisation of materials based on these moieties are presented and discussed.

A summary of the work discussed is presented in chapter 6 whilst chapter 7 presents the experimental methods for electrochemistry, device work, and synthetic procedures for each compound presented in Chapters 2, 3, 4 and 5

Acknowledgements

I thank Prof. Peter Skabara for the opportunity to work in his research group and for providing continuous advice and support throughout my PhD studies. I am also thankful to Merck Chemicals and EPSRC for funding my PhD and am particularly grateful to Dr. Nicolas Blouin, Dr. Lana Nanson and Dr. Steve Tierney from Merck for advice during the project.

I would also like to extend thanks to postdoctoral researchers Dr. Neil Findlay, Dr. Anto Inigo, Dr. Alex Kanibolotsky and Dr. Rupert Taylor who have always been happy to provide assistance and willing to sacrifice their own time to help during my studies.

I would also like to acknowledge all of the members of the Skabara group, past and present, for each contributing to an enjoyable working environment. I am grateful to the technical staff in the department for all of their assistance: Pat Keating, Alexander Clunie, Denise Gilmour, Craig Irving and Lindsay McCulloch.

I am thankful to Prof. Paul O'Brien (University of Manchester) and his research group for providing nanoparticle samples for the studies carried out in chapter 4.

I would like give thanks to all of my friends and family who have given me support and encouragement during my studies. I would particularly like to mention Gerard,

who is all right for a brother, and my mum and dad who have given me endless support throughout my life.

Lastly, I would like to thank my wife Caroline and my son Luke who have been patient, understanding and supportive through the highs and lows of my PhD and make everything worthwhile.

Abbreviations and symbols

°C	Degrees Celsius
AFM	Atomic force microscopy
AO	Atomic orbital
BHJ	Bulk heterojunction
BT	Benzothiadiazole
D-A	Donor-acceptor
DFT	Density Functional Theory
DIO	1,8-Diiodooctane
DMF	Dimethylformamide
DPP	Diketopyrrolopyrrole
EDG	Electron donating group
eV	Electron volts
EWG	Electron withdrawing group
FET	Field-effect transistor
Fc	Ferrocene
Fc^+	Ferrocenium
FF	Fill factor
HOMO	Highest occupied molecular orbital
I_{SC}	Short circuit current
I_{SD}	Source-drain current
IUPAC	International Union of Pure and Applied Chemists
J_{SC}	Short circuit current density
LUMO	Lowest unoccupied molecular orbital
MALDI	Matrix assisted laser desorption/ionisation
MO	Molecular orbital
n-Bu	N-butyl
NAO	Natural atomic orbital
NBO	Natural bond order

NBS	N-Bromosuccinimide
ND	Naphthyridine-2,6-dione
NDI	Naphthalene diimide
NMR	Nuclear magnetic resonance
OFET	Organic field-effect transistor
OLED	Organic light emitting diode
OPV	Organic photovoltaic
OSC	Organic semiconductor
OTFT	Organic thin film transistor
OTS	Octadecyltrichlorosilane
P3HT	Poly(3-hexylthiophene)
$PC_{61}BM$	[6,6]-phenyl-C_{61}-butyric acid methyl ester
$PC_{71}BM$	[6,6]-phenyl-C_{71}-butyric acid methyl ester
PCE	Power conversion efficiency
PDI	Perylene diimide
PEDOT:PSS	Poly(3,4-ethylenedioxythiophene) poly(styrenesulfonate)
PFBT	Pentafluorobenzenethiol
PV	Photovoltaic
ppm	Parts per million
RI-J	Resolution of the identity approximation
rpm	Revolutions per minute
RT	Room temperature
SAM	Self-assembled monolayer
THF	Tetrahydrofuran
TMEDA	Tetramethylethylenediamine
UPS	Ultraviolet Photoelectron Spectroscopy
UV/Vis	Ultra-violet/visible
V	Volt
V_G	Gate voltage
V_{OC}	Open circuit voltage
V_{SD}	Source-drain voltage
V_T	Threshold voltage

Greek

δ	Chemical shift
ε	Dielectric constant/molar absorptivity
η	Power conversion efficiency
λ	Wavelength
λ_{max}	Wavelength at maximum absorption
$\lambda_{emission}$	Wavelength at maximum emission
μ	Charge carrier mobility
π	Pi-bonding orbital
π^*	Pi-antibonding orbital
σ	Sigma-bonding orbital
σ^*	Sigma-antibonding orbital

Symbols

C	Capacitance
e	Elementary charge
E	Electric field
$E^{\delta r}$	Bond length alteration energy
E_g	Band gap/HOMO-LUMO gap
E^{θ}	Energy due to average deviation from planarity
E^{int}	Intermolecular interaction energy
E_{ox}	Electrochemical oxidation potential
E_{red}	Electrochemical reduction potential
E^{res}	Aromatic resonance energy
E^{sub}	Energy contributed from substituent effects
h	Planck's constant
I_{max}	Current at maximum power output
L	Channel length
n	Charge carrier density
P_{in}	Power input

P_{out}	Power output
V_{max}	Voltage at maximum power output
W	Channel width

Contents

Chapter 1 - Introduction

1.1 Band Theory

Electrical conductivity is a property that varies with different solids, such that they can be categorised into four different types:

(i) Metals

(ii) Semiconductors

(iii) Insulators

(iv) Superconductors

The conductivity of these solids is well described by band theory. The combination of atomic orbitals (AOs) gives a molecular orbital (MO). In systems with a large number of atoms, there is a subsequent large amount of MOs which are each separated by small energy gaps, appearing as a band. The occupied MOs are contained within the valence band and the conduction band contains the unoccupied MOs.

In metals, the MOs are delocalised throughout the lattice, in an assumption known as the tight-binding approximation.[1] As a result of the large amount of atoms in metallic systems, the MOs are packed together with small energy gaps, meaning that the valence band and conduction band overlap. This is demonstrated for alkali metals in the diagram below:

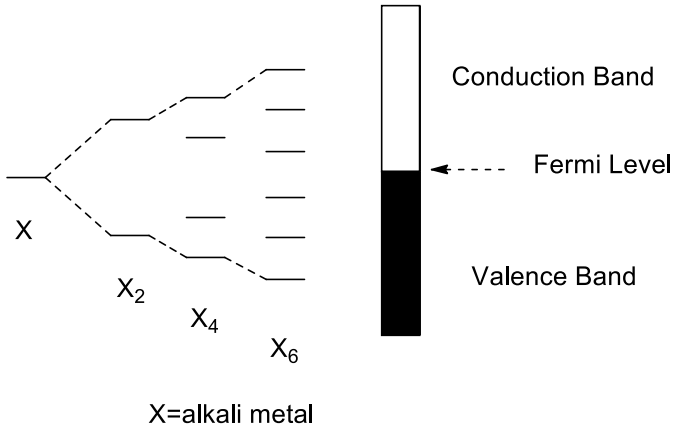

Figure 1.1. Formation of bands in alkali metal.

Metals are considered to be conductors as there is free movement of the electrons due to the overlap between the conduction and valence bands. Conductivity in metals decreases with an increase in temperature, as even though there is an increase in electrons in the conduction band, there are more collisions between electrons, leading to inefficient transfer of charge.

In semiconductors the valence band and conduction band are separated by an energy known as the band gap (**E_g**). Conductivity can occur when there is an increase in temperature, as electrons gain enough energy to be promoted to the unoccupied MOs giving free electrons. The excitation of an electron from the valence band to the conduction band leaves a positive hole in the valence band, which can be filled by another electron, leaving another positive hole as a consequence. If the band gap is too large for electrons to be promoted from the valence band to the conduction band, then the material is termed an insulator.

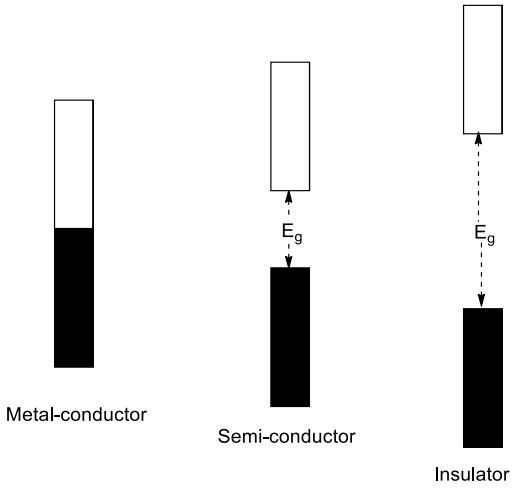

Figure 1.2. Band structure of metals, semi-conductors and insulators

A semiconductor which contains the same number of free electrons as positive holes is known as an intrinsic semiconductor. Semiconductors can also be doped to create a surplus of electrons or holes in the material. This is known as an extrinsic semiconductor. If the dopant has fewer valence electrons than the pure material, there is the formation of a narrow band which electrons can be promoted to from the valence band, giving hole mobility in the band. This material is known as a p-type semiconductor. If the material is doped with a substance with a larger number of valence electrons then a band is formed from which electrons can be promoted to the conduction band. This material is an n-type semiconductor.

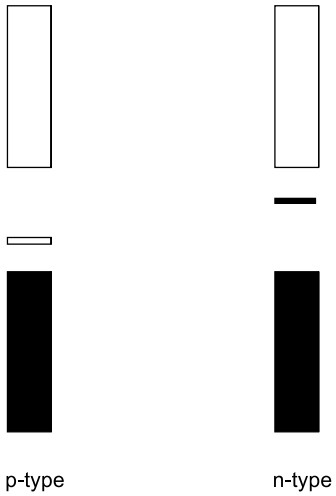

Figure 1.3.P-type and n-type semiconductor band structure

The fourth type of conductivity is superconductivity. A superconductor has a critical temperature, below which the material conducts electricity without resistance. The first superconductors discovered had a very low critical temperature, but development of these materials has led to superconductors with a higher critical temperature,[1] which can simply be reached using liquid nitrogen. Further development of these materials, to an extent where a critical temperature at room temperature is required, could lead to uses such as electrical components which would minimise the loss of energy in electrical devices.

There is a large dependence on the type of material for conductivity, with different compounds having varying abilities of conductivity. This has to be considered as well as other physical properties which are important to the application of the material.

1.2 Organic Semiconductors

Organic semiconductors are a cheap, light and flexible alternative to traditional inorganic semiconductors and have been used in devices such as organic photovoltaics (OPVs),[2-4] organic LEDs (OLEDs)[5-7] and organic field effect transistors (OFETs).[8-10] The processing of organic semiconductors is considerably less expensive than inorganic semiconductors with cheap methods such as ink-jet printing and spin coating. Organic compounds that behave as semiconductors are π-conjugated polymers, oligomers or small molecules in which there is extensive delocalisation of electrons. Examples of such compounds that have been successfully applied to different types of devices include those based on thiophenes,[11-13] fluorenes[14-16]and acenes.[17-19]

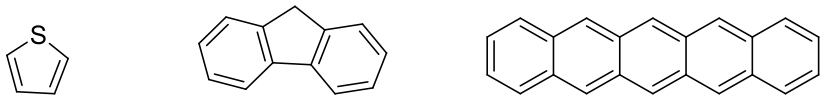

Figure 1.4. Thiophene (left), fluorene (centre), pentacene (right)

The use of different organic compounds for different devices shows that a range of different physical properties can be exhibited by different organic compounds. Even small changes in the molecular structure are enough to change the physical properties of the compound; this tunability of organic semiconductors is advantageous over inorganic semiconductors. For example, in polymers the band gap is dependent on the energy related to bond length alteration in conjugated chain ($E^{\delta r}$), average deviation from planarity for polymer chains (E^{θ}), aromatic cycle resonance energy (E^{Res}), substituent effects from electron withdrawing groups (EWGs) or electron donating

groups (EDGs) (E^{sub}) and the energy from favourable intermolecular interactions (E^{int}).[20] Equation 1[20] below shows these contributions to the band gap. Changing these properties can be applied to lowering the HOMO-LUMO gap of oligomers and small molecules also.

$$E_g = E^{\delta r} + E^{\theta} + E^{Res} + E^{Sub} + E^{Int} \quad (1)$$

In order to ensure that a molecule or a polymer chain is as planar as possible, which leads to a lowering the HOMO-LUMO or band gap, certain intramolecular interactions can be utilised. For example, the dye indigo, is highly planar on account of intramolecular hydrogen bonding.[21]

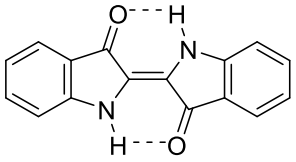

Figure 1.5. Intramolecular hydrogen bonding in Indigo dye

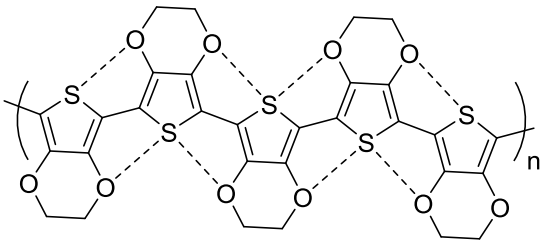

Figure 1.6. Structure of poly(ethylenedioxythiophene) (PEDOT) shows potential S—O interactions

There is much debate as to the extent of certain non-covalent interactions. Whilst the planarisation of PEDOT with respect to P3HT has been attributed to favourable S--O

interactions,[22] Ratner *et al*[23] describe these interactions to have "weak, non-influential binding tendencies", with "non-traditional hydrogen bonding" being a stronger interaction, influencing the planarity of the structure.

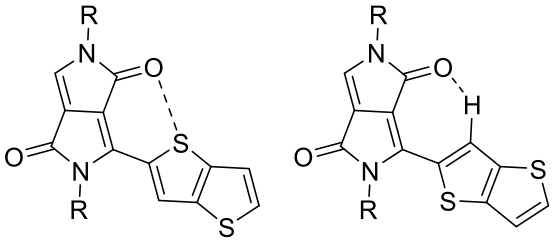

Figure 1.7. Example of possible non-bonding interactions studied by Ratner *et al*.[23] The hydrogen bond shown on the right is determined to be energetically more favourable.

The position of solubilising alkyl chains in the conjugated backbone also has a large influence on planarity. A study by Heeney *et al*[24] on poly(2,5-bis(thiophen-2-yl)thieno[3,2-b]thiophene) showed that placing the alkyl chain adjacent to the vinyl linker reduced the dihedral angle compared to when the alkyl group was situated on or adjacent to the thieno[3,2-b]thiophene unit.

The planarisation of units within an OSC not only leads to a reduced band gap through improved conjugation, but also can contribute to improved π-π stacking of the material. π-π stacking is probably the most important intermolecular interaction in OSC materials.

Besides π-π stacking, hydrogen bonding is another influential intermolecular interaction which has been applied to organic semiconductors. π-π stacking exists in some degree in most organic semiconductors due to their conjugated nature, but careful molecular design is required to encourage effective hydrogen-bonding between

OSC molecules, with the inclusion of hydrogen bond donor and acceptors such as hydroxyl and carbonyl groups respectively. Perepichka *et al*[25] present an interesting example of using NDI compounds which hydrogen-bond with donor molecules in order to form p and n-type heterojunctions which can be applied to ambipolar OTFT and single-crystal OFETs. It should be noted however, that improved π-π stacking as a result of hydrogen-bonding will also contribute to a lowering of the band (or HOMO-LUMO) gap.

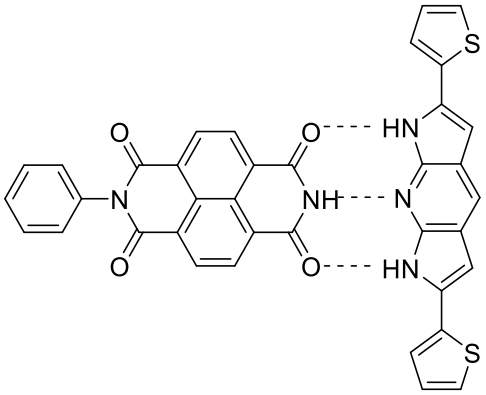

Figure 1.8. Example of hydrogen bonding demonstrated by Perepichka *et al*[25]

The ability to tune the band (or HOMO-LUMO) gap using substituent effects from EDGs or EWGs has given rise to considerable research into donor and acceptor units. In general, the HOMO energy is influenced by donor units and the LUMO can be controlled by acceptor units. This will be discussed further in section 1.5.3.

In addition to the band gap, it is also important to determine the individual HOMO and LUMO energy levels to facilitate charge injection when these materials are applied to devices. Cyclic voltammetry is one of the most commonly used techniques in order to determine these energy levels and will be discussed in the analytical techniques section.

Organic synthesis is key to the fine-tuning of the HOMO-LUMO gap as it can be used to increase the conjugation length or include different electron rich/deficient units, for example. One of the most common methods of extending conjugation and/or introducing electron rich or deficient moieties into a conjugated backbone is by C-C bond formation using Pd-catalysed cross coupling reactions. The general reaction and examples of different Pd-catalysed cross coupling reactions are shown below in Scheme 1.1.

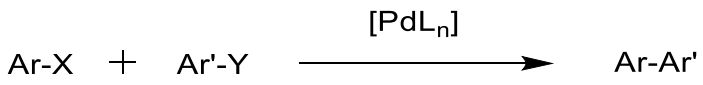

Named Reaction	X	Y
Stille[26]	organohalide	-SnR_3
Suzuki[27]	organohalide	-$B(OH)_2$
Negishi[28]	organohalide	-ZnX
Kumada[29]	aryl/vinyl halide	-MgX
Buchwald-Hartwig[30, 31]	aryl halide	amine
Heck[32]	aryl halide	alkene
Sonogashira[33]	aryl halide	alkyne

Scheme 1.1. General reaction scheme showing different Pd-catalysed cross-coupling reactions

The mechanism for Stille coupling reaction is shown below in scheme 1.2. The mechanism for other cross-coupling reactions is similar, following the oxidative addition and reductive elimination, although there are some variations. For example,

boronic acids are required to be activated using a base. Sonogahsira coupling reactions typically require an amine base and a copper co-catalyst and these reagents are involved in the transmetalltion stage.[33]

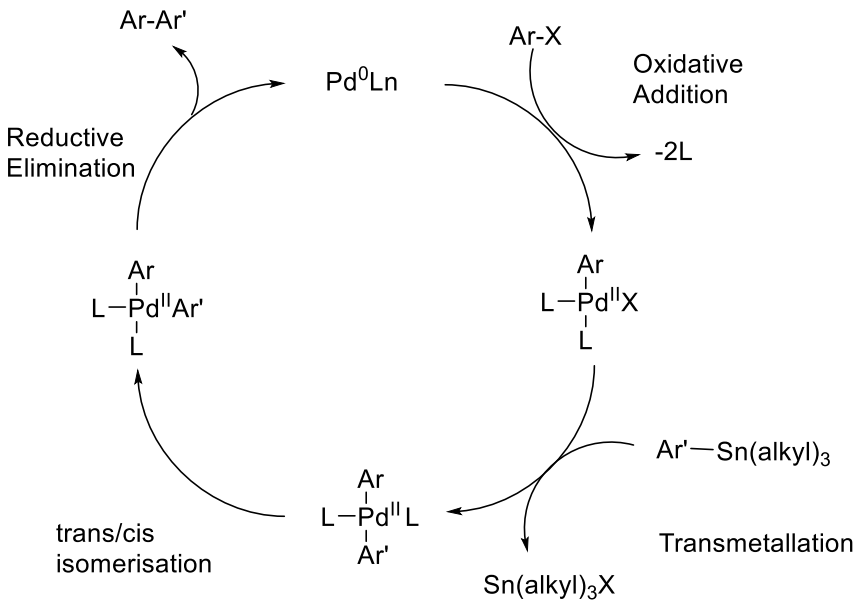

Scheme 1.2. Stille coupling reaction mechanism

As a consequence of the research into Pd-catalysed cross-coupling reactions, there has been the development C-H activation,[34] where the reaction takes place between a C-H and a halide group in the presence of a catalyst. This method would generally reduce the number of steps required to reach a desired target compound when compared with Pd-catalysed cross-coupling reactions such a Stille reactions.

The cross-coupling reactions described above can be used in the synthesis of both polymers and small molecules. Conjugated polymers are frequently used in organic semiconductor devices and often show good performance.[3, 35, 36] An interesting recent study by de Mello *et al*[37] also showed how the physical properties of random regioregular copolymers could be controlled according to the concentration of

monomers in a microfluidic reactor, and this study shows the potential for a simple synthesis of polymers with a high degree of control.

However, there are disadvantages to the use of polymers. Polymers often have batch-to-batch variation of properties, are polydisperse and display end-group variation. These problems can be overcome by using small molecules, which have well-defined monodisperse structures.

In the following section, organic compounds used in OFET and OPV devices will be discussed, showing which molecular characteristics are suitable for optimum device performance.

1.3 Analytical Techniques

UV/Vis absorption, fluorescence and cyclic voltammetry are three of the most commonly used techniques for the characterisation of organic semiconductors. In this section these techniques are discussed and their relevance to OSCs is explained.

1.3.1 UV/Vis Absorption and Emission

UV/Vis absorption and emission measurements are used in order to determine the optical properties of an organic semiconductor, which are especially important for OPV and OLED devices. The absorption and fluorescence can be used to evaluate the effect of certain donor or acceptor groups in the molecule. Using an absorption spectrum, it is possible to determine which parts of the solar spectrum the compound absorbs and the optical HOMO-LUMO gap. The absorption and emission processes are shown in figure 1.9.

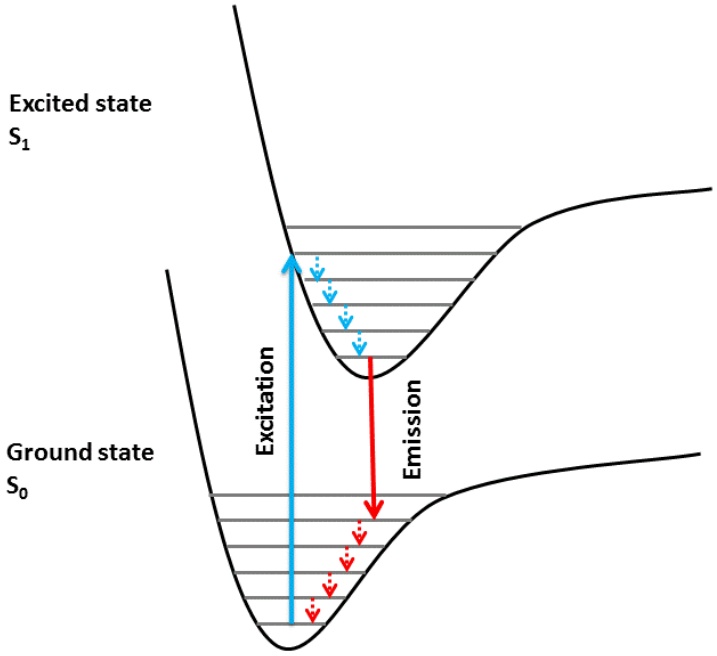

Figure 1.9. Diagram showing absorption and fluorescence

In organic semiconductors most transitions are π-π* transitions. Although n-π* are possible, these are weak as they are symmetry forbidden.

The absorption spectrum is mostly used for organic semiconductors in order to determine the optical HOMO-LUMO gap from the onset of absorption. The energy is calculated from the following equation:

$$E = hc/\lambda \qquad (2)$$

1.3.2 Cyclic Voltammetry

The determination of electrochemical properties of organic semiconductors, such as ionisation potential and electron affinity, are important in the application of these materials to electronic devices. One of the most widely used techniques applied for the electrochemistry of OSCs is cyclic voltammetry.

In cyclic voltammetry, the applied potential sweeps forwards and backwards inducing a current response. In the forward wave oxidation takes place whilst the analyte is reduced in the reverse wave. Upon oxidation (reduction) the current becomes more positive (negative) until a maximum point in the peak is reached. At this point the current then becomes more negative (positive) as the oxidised (reduced) material diffuses away from the electrode. As a material is oxidised/reduced, the potential required for further oxidation/reduction increases as there is more energy required for these processes.

A cyclic voltammetry cell contains a working electrode, reference electrode and counter electrode. Typically the working electrode may be gold, silver, platinum or glassy carbon and this electrode is where the analyte is reduced or oxidised.

In 1983 Gritzner and Kuta[38] reported to IUPAC recommending the use of the ferrocene/ferrocenium ion redox couple to calibrate electrochemical potentials in non-aqueous solvents as it satisfies conditions required for an appropriate reference redox system determined in work by Stkehlow.[39] These conditions are as follows:[38]

(i) The ions or molecules that are present in the reference redox couple should be spherical and have a large radius.

(ii) The ions should carry a low charge.

(iii) At the electrode, there should be a fast and reversible equilibirium.

(iv) The oxidised and reduced species of the redox couple should both be soluble.

(v) There should be no changes in the geometry of ligands present in the organometallic complex.

(vi) The redox potential should be accessible for a range of different solvents.

(vii) The oxidised and reduced species should be suitable stable to allow potentiometric measurements.

In the characterisation of organic semiconductors, cyclic voltammetry is mainly used to determine the HOMO and LUMO energies and therefore the associated HOMO-LUMO gap. If the voltammogram is referenced to Fc/Fc^+, then the HOMO and LUMO energies are determined by subtracting the onset of oxidation or reduction from the HOMO of ferrocene. However, there are many values quoted in literature for the HOMO energy of ferrocene below vacuum level, and this must be considered if comparing the separate HOMO and LUMO energies of different materials.

Bazan *et al*[40] have highlighted the different ferrocene HOMO energies which have been used as a reference for calculation of HOMO/LUMO values from cyclic voltammetry. Thompson *et al*[41] used ultraviolet photoelectron spectroscopy (UPS) to determine the HOMO of bis(biphenyl)ferrocene at -4.76 eV and this should not differ from that of ferrocene, for which it is difficult to measure due to its volatility.

If the HOMO of ferrocene is taken as -4.8 eV, then the HOMO and LUMO are calculated from the onset of oxidation and reduction respectively shown in equation 3:

$$E_{HOMO(LUMO)} = -4.8\ eV - E_{Ox(Red)}^{onset} \quad (3)$$

The HOMO-LUMO gaps determined by UV/Vis spectroscopy and cyclic voltammetry

often differ and this can be explained by the fact that the electron-hole pair is bound in the excitation of an electron due to light absorption but because the HOMO is determined from the ionisation potential in cyclic voltammetry, the electron-hole binding energy is included in the electrochemical HOMO-LUMO gap.[42]

1.4 Organic Field Effect Transistors (OFETs)

Interest in OFETs has increased in recent years and development in the field has resulted in the production of OFETs that can compete in performance with inorganic FETs. The OFET offers a cheap alternative to inorganic FETs as the organic semiconductor can be incorporated into the device via many different methods such as inkjet printing, spin coating and drop casting. OFETs are fundamental components for cheap, flexible electronics and have already been incorporated into display technologies.[43]

The FET was discovered and patented by Lilienfeld in 1930.[44] Field effect transistors consist of a source electrode and drain electrode, linked by a conducting channel. The density of charge carriers can be altered by altering the potential of a third electrode, the gate electrode. In a similar manner to photovoltaic devices, organic semiconductors have been applied for use in OFETs. There are general structures for an OFET. These are top-contact OFETs, where the source and drain electrodes are deposited on top of the OSC layer, and bottom-contact OFETs where the OSC layer is deposited on top of the electrodes. These OFET architectures are shown below in figure 1.10:

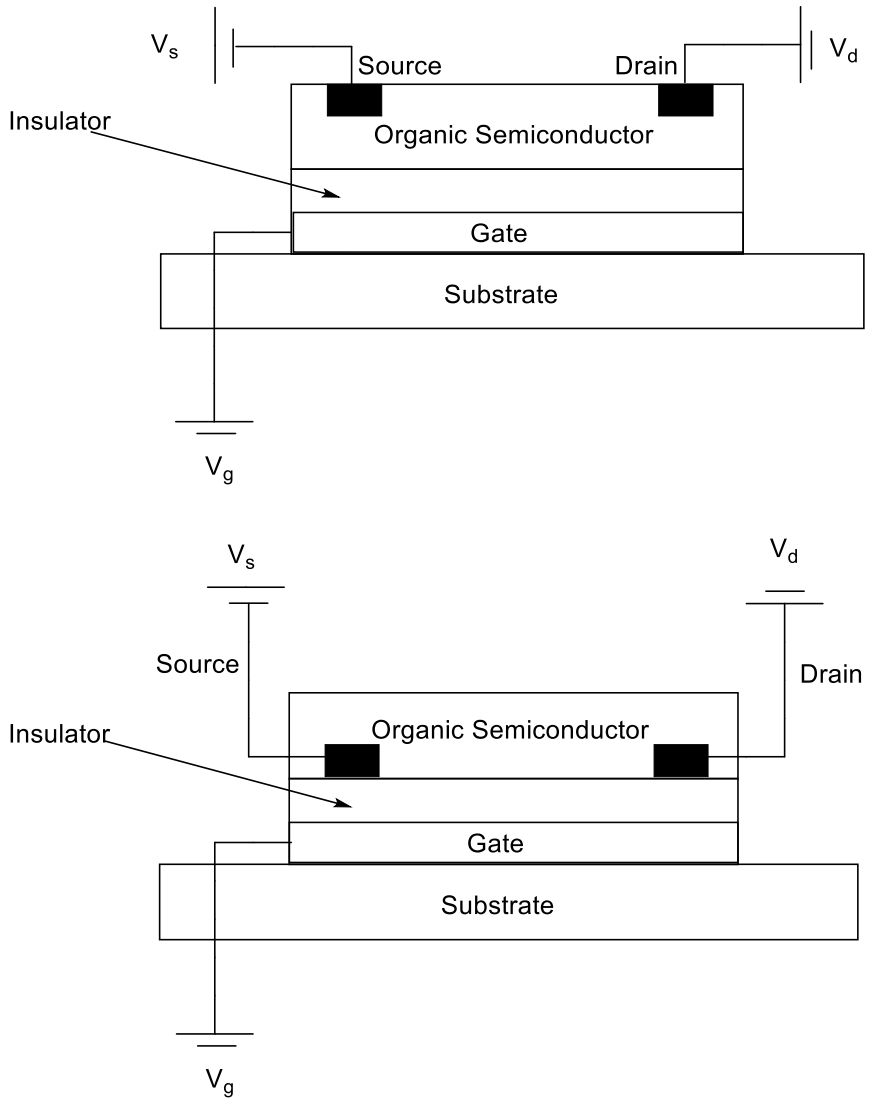

Figure 1.10. Top-contact (upper) and bottom contact (lower) OFETs

When a voltage is applied to the gate, an electric field is formed at the interface between the OSC and dielectric. If a potential between the source and drain is applied, then current can flow, forming a conducting channel between the source and drain. If a positive voltage is applied, then positive charges are formed at the gate, with negative charges subsequently forming at the OSC/dielectric interface, meaning that electrons are the charge carriers contributing to the current. This is an n-channel OFET. Likewise, if a negative voltage is applied, positive holes are formed at the

OSC/dielectric interface giving a p-channel OFET. Most organic semiconductors, show both p-type and n-type conductivity but often perform better as one particular type of OFET. An ambipolar OFET is one which exhibits good hole and electron mobility, and this can be achieved using a combination of two different organic semiconductors[45] or a single donor-acceptor OSC.[46] The type of conductivity is determined by the HOMO and LUMO levels of the semiconductor. For p-channel conduction, it is important that the HOMO of OSC is similar to the work function of the source and drain electrodes[47, 48] (e.g. Au=-4.9eV) and it has been shown that a LUMO of -4.0eV to -4.1eV is optimum for n-type charge transfer in ambient conditions.[49] For ambipolar OFETs, a combination of these properties is ideal.[48] An interesting study by Heeney *et al*[50] showed that a small change in the chemical structure of polymers (changing from difluoro to dicyano derivative in a benzothiadiazole analogue) can lead to a switch from unipolar p-type to unipolar n-type behaviour in OFETs.

An OFET is generally characterised by plotting two graphs: output and transfer characteristics examples of these are shown in figure 1.11.

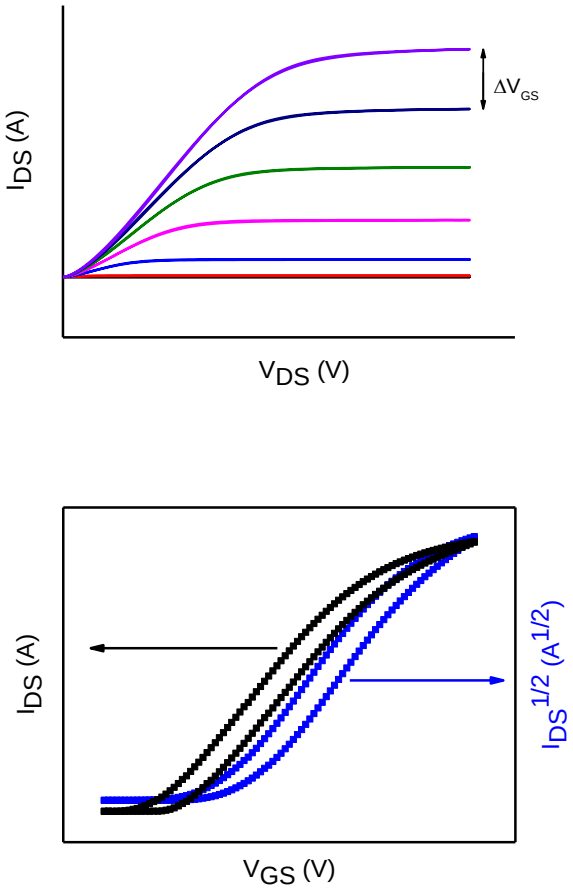

Figure 1.11. Examples of output (top) and transfer (bottom) characteristics

The output graph shows the source-drain current (I_{SD}) plotted against the source-drain voltage (V_{SD}) with a number of sweeps according to the gate-source voltage (V_{GS}). There are two main regions that can be described in these plots. The first is the linear regime where: V_{GS} - V_{SD} > V_T. Initially V_G must be greater than the threshold voltage (V_T) for the generation of charge carriers in the conduction channel. Once the charge carriers are formed, the current for the linear regime increases with the increase in V_{DS}. The current can be determined by the following equation:[51]

$$I_{SD} = \frac{W\mu C}{L}((V_{GS} - V_T)V_{SD} - \frac{V_{SD}^2}{2}) \quad (4)$$

Where I_{SD} is the source-drain current, W is the channel width, μ is the charge carrier mobility, C is the capacitance of the dielectric per unit area, L is the channel length, V_{GS} is the gate voltage, V_T is the threshold voltage and V_{SD} is the source-drain voltage.

When V_{SD} increases to a point where V_{GS}-V_{SD}<V_T, the current decreases, and this point in the plot is known as the saturation regime. To determine the current at the saturation point, V_{SD}=V_{GS}-V_T is substituted into equation 5 above to give the equation below:[51]

$$I_{SD} = \frac{W\mu C}{2L}(V_{GS} - V_T)^2 \quad (5)$$

The transfer characteristics graph often shows two plots displaying both I_{SD} (black in figure 1.11) and $(I_{SD})^{1/2}$ (blue in figure 1.11) against V_{GS} at a specific V_{SD}. The plot of I_{SD} can be used to determine the threshold voltage by extrapolating the linear region of the plot to where it intersects the x-axis. This is shown in figure 1.11. In addition to this, the square root can be used to determine the charge carrier mobility which is calculated from the following equation:

$$\mu_{sat} = \frac{2L}{W\mathrm{C}_i} \times \left(\frac{\partial\sqrt{I_{SD}}}{\partial V_g}\right)^2 \quad (6)$$

From both equations 4 and 5, the charge carrier mobility can be determined. This is an important property of an OSC and an indicator of the performance of an OFET.

Materials that are well ordered and closely packed, give rise to higher charge transport within the material and therefore higher charge mobilities. Techniques such as thermal annealing[52] or simply changing the solvent used[53] can change the morphology of the

OSC layer, and therefore the charge mobility. An interesting example of the effect of thermal annealing on the charge carrier mobility in an OFET device is described by Arumugum et al[54] in which annealing in a stepwise process instead of at the maximum temperature straight after the film is cast results in an order of magnitude increase in the p-type mobility. When the OFET is annealed only at 120°C large crystalline domains are formed with many visible gaps but stepwise annealing leads to a more uniform film and therefore better charge transport.[54]

Another property used to characterise an OFET is the ON/OFF ratio, which is the ratio of the maximum drain current with applied gate voltage with the current when no gate voltage is applied. This can be affected by many parameters such as the voltages used, material used for dielectric layer and the geometry of the OFET, but gives a good indication to the device performance, and can be compared with other devices if the fabrication methods used are identical.[8]

1.5 Organic Photovoltaic Devices

Today there is an ever-increasing requirement for clean, sustainable energy sources due to the limited supply of fossil fuels and harmful environmental effects of carbon based fuels. This has led to the development of different types of sustainable fuels. In addition to this, in 2005 the European Council for Renewable energy (EREC) set a target of 20% of energy consumed in Europe to come from renewable energy by 2020 which EU leaders agreed to in 2007.[55] In order for this to be realised, a combination of solar, wind and tidal energy should be utilised.

Solar energy, like wind and hydro energy, is largely abundant, which is a reason for it becoming a popular means of producing energy. Solar or Photovoltaic (PV) cells are based on the photovoltaic effect, which is when a current is created in a material exposed to light. This was first discovered by Alexandre-Edmond Becquerel in 1839[56] when he observed the formation of electric current when light was irradiated on silver chloride covered platinum electrodes, with electrolyte.[57] This principle has been taken and applied as a means of "green energy", in the search for alternate fuel sources.

OPV devices convert energy from sunlight into electricity. In order to fabricate the most efficient devices, it is important to utilise as much energy from the sun as possible. Shown below in figure 1.12 is a graph showing the AM1.5 standard for solar spectral irradiance.

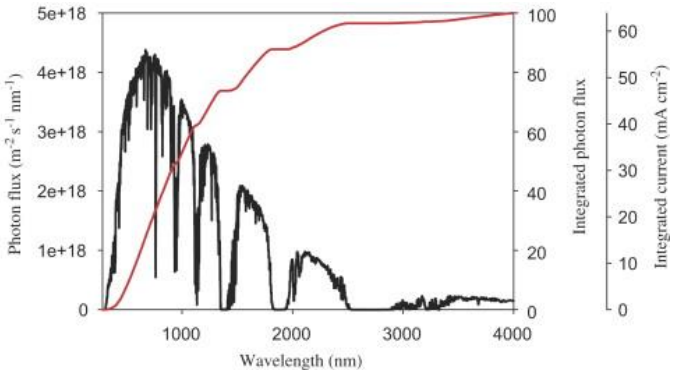

Figure 1.12. Photon flux and integrated photon flux as a function of wavelength. The photon flux is also shown as a current density. Reproduced from F. C. Krebs, *Sol. Energy Mater. Sol. Cells*, 2007, **91**, 953-953.[58]

The graph shows that the lower the band gap, the larger amount of the solar spectrum is absorbed. However, when photons with low energy (at a higher wavelength) are absorbed, the charge carriers are lower in energy and subsequently, a smaller voltage

difference is produced.[58] Thus, it is impossible to convert 100% of energy from the sun into energy using OPVs but the challenge is absorbing as much sunlight whilst having efficient device architecture. This challenge will be discussed as we investigate the structure of OPV devices.

A generic OPV device structure is shown below:

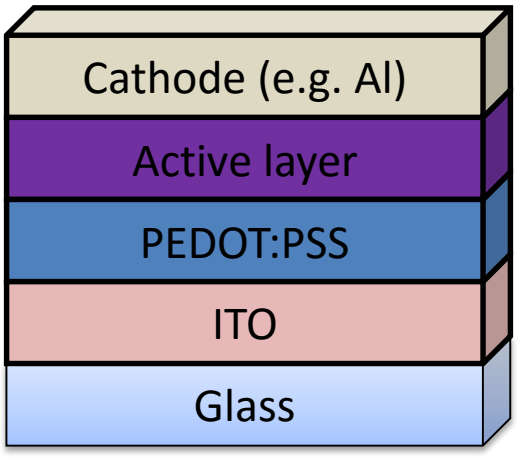

Figure 1.13. OPV device

In between the cathode and anode there is the active layer and a hole acceptor material, often PEDOT: PSS. The active layer contains an electron donor molecule/polymer and an acceptor molecule, often a fullerene derivative. This is based on the first donor: acceptor OPV cell discovered by Tang in 1979[59] and published in 1986,[60] which produced a landmark efficiency of 1% for OPVs at the time.

In an active layer containing an electron donor and electron acceptor, light excites an electron from the HOMO to the LUMO of the donor material. The electron then transfers to the LUMO of the acceptor, leaving an electron hole in the HOMO of the donor material. Brabec *et al*[61] showed that a gap of 0.3 eV is sufficient for effective charge transfer from the LUMO of the donor to the LUMO of the acceptor. Charge

transport of the electron to the cathode and the hole to the hole transport material and subsequently the anode then occurs, which results in the formation of a current.

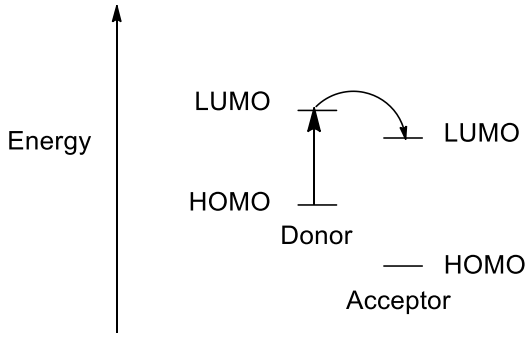

Figure 1.14. Intermolecular charge transfer from donor to acceptor

One of the most popular forms of active layer is the bulk heterojunction, which was first presented in 1995 by Yu et al.[62] In a bulk heterojunction, the donor and acceptor compounds exist in a random mixture, giving a larger interface for charge transfer between the donor and acceptor species compared to donor and acceptor layers deposited in succession, which is a flat heterojunction structure.

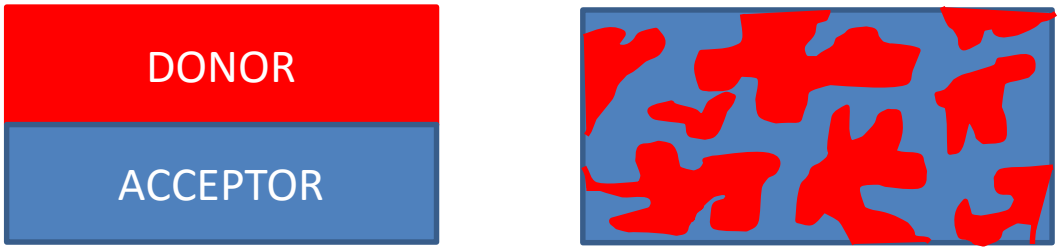

Figure 1.15. Representation of planar heterojunction (left) and bulk heterojunction (right) active layers

There are a number of properties required for a donor compound to be effective for use in the active layer of an OPV device. As mentioned before (figure 1.12), a low band gap for the donor species is favourable for the absorption of a large fraction of

solar energy. However, from figure 1.14, it can also be seen that it is important that the LUMO of the donor must be higher than the LUMO of the acceptor for effective exciton dissociation. As well as having a low band-gap, a broad absorption band in the donor is a favourable property which results in absorption of a larger range of solar energy. It is possible to relate these properties to the performance of the OPV device by specific measurements which characterise the device.

The performance of an OPV cell is primarily determined by the power conversion efficiency of the device which is calculated using the formula shown below:

$$\eta = \frac{P_{out}}{P_{in}} \tag{7}$$

$$\eta = \frac{I_{max} \cdot V_{max}}{P_{in}} \tag{8}$$

Where η is the power conversion efficiency, P_{out} is the power output, P_{in} is the power of incident light, I_{max} is the current at maximum power output of the cell and V_{max} is the voltage at maximum power output.

In practice, to determine how well the OPV device performs, I_{max} and V_{max} are measured along with the open circuit voltage (V_{OC}) and short circuit current (I_{SC}). The V_{OC} is the maximum voltage measured in the cell, and has been shown to have a linear dependence on the HOMO energy of the donor substance[63] and LUMO energy of the acceptor unit.[63, 64] Scharber *et al*[63] explained that by assuming certain levels for fill factor and short-circuit current, the LUMO energy of the donor material can be controlled in order to maximise the PCE. This concept was used by Blouin *et al*,[65] who

correlated theoretical HOMO and LUMO levels with experiment in order to design OPV materials according to the ideal LUMO level stated by Scharber.[63]

The I_{SC} is the maximum current measured in the device and can be described by the following formula:

$$I_{sc} = ne\mu E \quad (9)$$

Where n is the density of charge carriers, e is the elementary charge, μ is the charge mobility and E is the electric field arising from charge transfer at the donor acceptor interface and electrodes with different work functions.

An increase in I_{SC} can be achieved by improving the efficiency of charge transport of the electron and hole to the electrodes[66] and morphology of the active layer can influence this. A well-defined, crystalline active layer results in an improvement in charge transport efficiency and therefore $I_{SC.}$[67] The I_{SC} can also be improved by ensuring the maximum amount of photons are absorbed by the active layer by matching the band gap of the donor material with the solar spectrum,[66] as mentioned previously, and making sure that the absorption of photons in other layers in the OPV is minimum. The I_{SC} is commonly reported as the short circuit current density (J_{SC}, units A/cm^2), which takes the area of the device into consideration.

Using both the I_{SC} and V_{OC} it is possible to calculate the fill factor (FF) and this is shown below:

$$FF=\frac{I_{max}.V_{max}}{I_{SC}.V_{OC}} \quad (10)$$

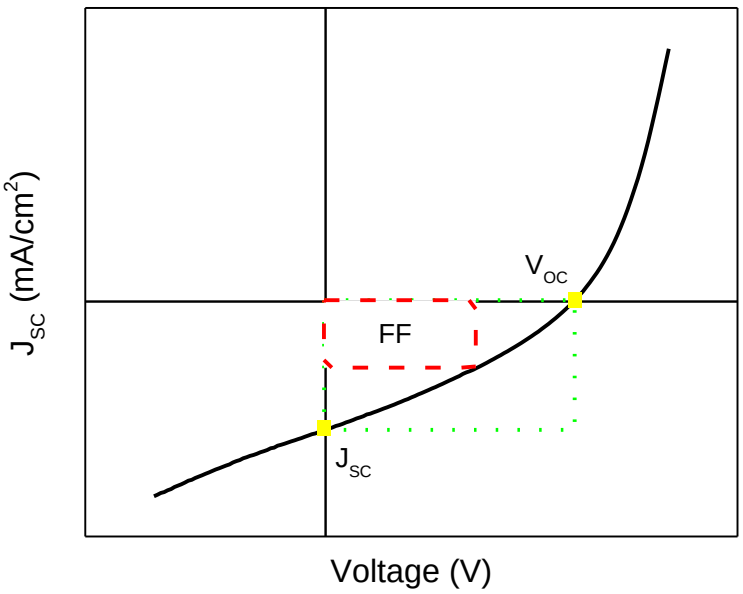

Figure 1.17. Graph showing parameters required for calculation of PCE

The fill factor shows the performance of the device as a whole and specifically, the amount of charge carriers generated from photo-excitation that reach the electrodes. This therefore gives an indication to the competition between charge carrier separation and recombination.

1.5.2 Morphology

The morphology of the active layer is possibly the most crucial factor in high-performing OPV devices. It is a parameter that greatly influences both J_{SC} and FF of the device. Effectively, optimising the morphology can lead to a high surface area for donor: acceptor interface for charge separation and good charge transport to the electrodes.

The donor: PCBM ratio is one of the most important parameters to optimise to ensure good morphology as the optimum ratio can lead to the best possible charge separation and transport. This factor must be studied for every novel donor compound tested as even small changes in chemical structure can result in a different optimum donor: PCBM ratio. The difficulty in prediction of optimum donor: PCBM ratio has resulted in much research into understanding the relationship between donor and acceptor compounds in the bulk-heterojunction and how the morphology can be controlled. Brédas *et al*[68] discuss this using molecular dynamics using a pentacene and C_{60} model.

In addition to the choice of solvent used, the use of solvent additives such as diiodooctane (DIO) can also give improved PCEs, owing to improved morphology. The exact nature of mechanism by which diiodooctane improves the morphology is not yet fully understood but it had been suggested that DIO is a favourable solvent for dissolving fullerene rather than polymer/oligomer and so there is increased aggregation of the polymer without crystallisation of the fullerene.[69] When investigating this further, Samuel *et al* proposed that DIO is involved in formation of large PCBM-rich and polymer-rich fibres which enhances the charge extraction.[70]

There have also been examples of chloronaphthalene[71, 72] and even polystyrene[73] used in a similar manner. The high boiling point of 1-choronaphthalene and improved solubility of PCBM in the additive are explained for the improved performance.[71] The addition of a small amount (2.5 wt%) of high molecular weight polystyrene results in a more viscous solution, contributing to a more even film.[73] It is also suggested that the favourable interaction of the solvent with the insulating polymer results in increased solvent retention time, favouring crystallisation and formation of donor phases.[73]

There is still much research required, however, to understand the true effect of these additives and how important the chemical structure of the additive is to the overall effect.

These factors have been shown to be critical to the morphology and therefore performance of the OPV device, however, chemical structure also has a huge influence on morphology. The use of $PC_{61}BM$ and $PC_{71}BM$ as acceptors in the majority of OPV devices means that most of the focus in optimising morphology through varying chemical structures is through variation of the donor structure.

A common approach to improving the morphology is through modification of the solubilising alkyl chain. Generally, the variation of alkyl chain does not change the electronic properties of the compound and so such a comparison is a fair reflection on the effect of improved morphology. There have been numerous examples shown where the use of branched alkyl chains in place of straight-chain alkyl groups results in better performance,[74, 75] although the reverse can be true for other compounds.[76] Studies have also shown that spacing the branching away from the nearest carbon can also improve morphology, with Kim *et al*[77] showing a decrease in π-π stacking distance as a result of spacing the branching of the side-chain. An example of each of these alkyl chains can be shown below in Figure 1.18.

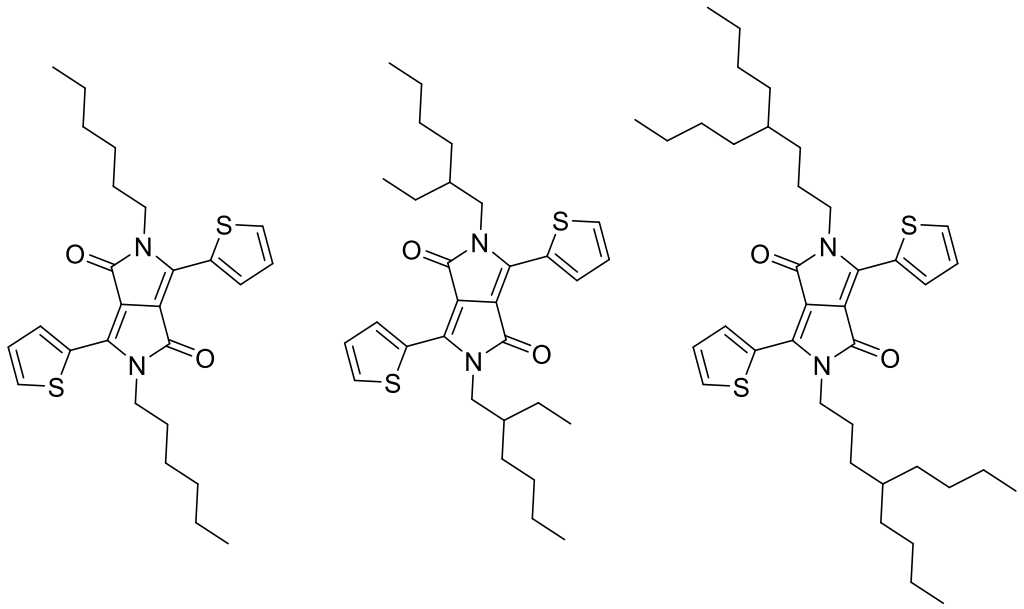

Figure 1.18. Straight-chain (left), branched (centre) and spaced-branched (right) alkyl chains

Further research into the effect of the positioning of alkyl chains will be beneficial in the design of donor compounds for BHJ-OPV devices. A study carried out by McGehee et al[78] shows that swapping the different alkyl chains on conjugated units in a donor-acceptor copolymer results in very different PCEs, emphasising how small changes in structure can impact greatly on device performance.

Device architecture is important in the performance of an OPV device. However due to the fact that the donor material is excited for charge transfer to take place, a process which can change significantly with small molecular structure changes, there has been extensive research into synthesising effective donor molecules. There has been rapid progress in the performance of OPVs, with bulk heterojunction OPV devices giving PCEs of 9-10%[79] for polymer/fullerene blends, although Heliatek have recently reported an efficiency of 12% for a tandem OPV device.[80]

In 2012, Heeger et al[81] reported that the small molecule DTS($PTTh_2$)$_2$ (shown in figure 1.19) had been applied as a donor material in a bulk heterojunction OPV, resulting in a then record PCE of 6.7%. This compound was compared to analogous compounds with the pyridyl N-atom in a different position or benzo[2,1,3]thiadiazole (BT) instead of the [1,2,5]thiadiazolo[3,4-c]pyridine unit and it was demonstrated that the symmetrical, [1,2,5]thiadiazolo[3,4-c]pyridine containing molecules showed better self-assembly and therefore higher OPV performance.[82] It was also shown, through DFT calculations that there was less variation in the net dipole moment of DTS($PTTh_2$)$_2$ conformers with respect to its BT-containing analogues and that this explained improved aggregation of the pyridine containing compound.[82]

The concentration of DIO has a large influence in the performance of OPVs based on DTS($PTTh_2$)$_2$ with 0.25% v/v concentration being used in the optimum device.[81] The OPV fabricated without DIO containing solutions shows a PCE of 4.5% whilst the use of 0.6% and 1% v/v DIO solutions results in efficiencies of 3.2% and 0.4% respectively.[81] In a further study, it was shown that whilst the charge carrier mobility of neat DTS($PTTh_2$)$_2$ films formed using different DIO concentrations showed little variation, the photoconductivity of bulk-heterojunction films was highly sensitive to DIO concentration due to its influence in the bulk-heterojunction morphology.[83]

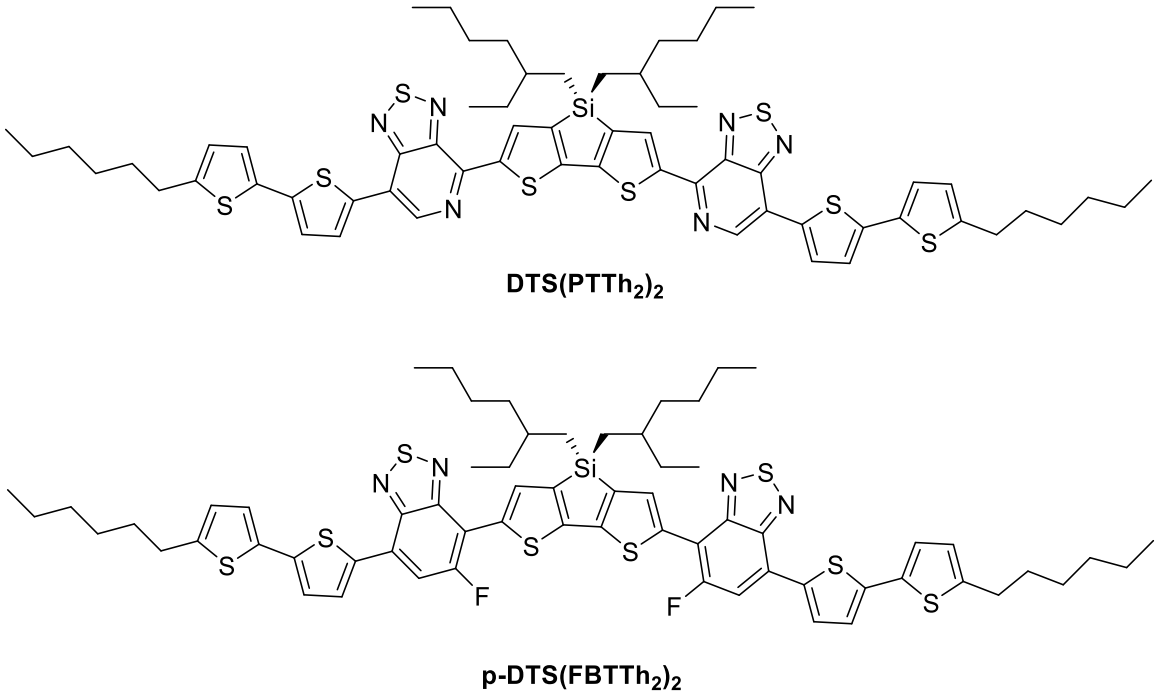

Figure 1.19. Donor molecules used for subsequent record PCE of small molecule based, solution-processed BHJ OPV by Heeger *et* al[81](top) and Bazan *et al*[84](bottom)

Following on from $DTS(PTTh_2)_2$, an analogous compound, $p\text{-}DTS(FBTTh_2)_2$ (figure 1.19) was synthesised by Bazan *et al*[84] and was applied to OPV devices resulting in a PCE 7.0%, overtaking the record small molecule BHJ-OPV PCE at the time. The substitution of the pyridyl N for a CF group results in some important changes to the properties of the compound, although it maintains the same symmetry as $DTS(PTTh_2)_2$, which, as discussed previously, is important to the overall device performance.[82] The red shift going from solution to solid-state is higher for $p\text{-}DTS(FBTTh_2)_2$ than $DTS(PTTh_2)_2$, suggesting more effective aggregation, which could contribute to the higher PCE.[84] Interestingly, it is also demonstrated that the change in chemical structure improved the compounds acid stability.[84] The fluorine

does not contain lone pairs that could take place in acid/base reactions, unlike the nitrogen atoms in DTS(PTTh$_2$)$_2$.

The sensitivity of device performance with respect to DIO concentration is a feature of p-DTS(FBTTh$_2$)$_2$ based devices which is similar to those using the analogous donor compound as it was demonstrated that 0.4% (v/v) DIO was optimum in allowing effective phase separation for good charge transport (poorer without the use of DIO) whilst maintaining a suitably large donor acceptor interfacial layer for charge transfer (reduced in samples with higher DIO concentrations).[85]

On account of p-DTS(FBTTh$_2$)$_2$ being an excellent donor material, efforts have been made to increase the PCE from the 7.0% which was originally reported.[84] Heeger *et al*[86] reported the example of using low sheet-resistance ITO in order to boost the J_{SC} and FF of the OPV device by reducing the series resistance, resulting in a PCE of 8.2%. Furthermore, it was shown that by using barium as a cathode in place of calcium, the FF could be increased, resulting in a PCE of 8.6%.[87] However, the highest reported efficiency for OPVs based on p-DTS(FBTTh$_2$)$_2$, or any other small donor molecule, was achieved using a ZnO optical spacer.[88] This results in improved performance by increasing light absorption, leading to a higher J_{SC} and improving electron collection and hole-blocking at the cathode, reducing charge recombination.[88].

1.5.3 Donor Acceptor Compounds

Although donor polymers tend to have lower band gaps than donor molecules, as an increase in conjugation leads to a lowering of the band gap,[20] it is possible to alter the structure of molecules in order to decrease the band gap. For example, adding an electron-deficient acceptor moiety to an electron-rich donor molecule leads to a "push-

pull effect" where electrons are "pushed" from the electron rich donor and "pulled" to the electron deficient acceptor unit. This contributes to lowering the band gap of a molecule[20]. The molecule pictured above, synthesised by Heeger et al[81] is an example of donor-acceptor molecule which undergoes a "push-pull effect". Common examples of acceptor moieties used in other donor-acceptor small molecules in recent literature include, BT,[82, 89, 90] diketopyrrolo[3,2-b]pyrrole (DPP),[91-93] and squaraine based acceptor units.[94-96]

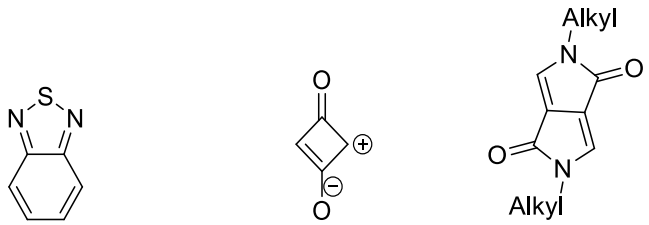

Figure 1.20. Acceptor units BT (left), squaraine (centre) and DPP (right)

The use of intermolecular interactions to improve morphology has already been discussed, and this strategy can also be used in design of donor-acceptor compounds. It has already been shown in section 1.2 that significant distortion from planarity in organic semiconductors can lead to a larger HOMO-LUMO gap due to a lesser degree of conjugation. There is also the possibility that a structure containing twisted units can disrupt π-π stacking and therefore lead to a poorer morphology. These problems can be overcome by careful design of the donor-acceptor molecules, using units which may induce stabilising intramolecular interactions leading to planar structures.

The good performance of such donor-acceptor small molecules has shown that there is a potential to reach high-efficiency solar cells using organic small molecules. In the discussion of OPV devices and characterisation of their performance in this section, it

has been shown that a variety of different chemical structure can give different physical properties, resulting in different device performance. However it has also been demonstrated that there are a number of parameters that can be followed to ensure sensible design of materials for OPV materials and it is important to follow these whilst investigating an optimum chemical structure for use as a donor molecule in a bulk heterojunction OPV cell.

1.5.4 Acceptor Molecules

The majority of BHJ-OPV devices fabricated include either [6,6]-phenyl-C_{61}-butyric acid methyl ester ($PC_{61}BM$) or [6,6]-phenyl-C_{71}-butyric acid methyl ester ($PC_{71}BM$) as the acceptor compound. These fullerene based compounds tend to have high electron affinities and show stable, reversible electrochemical reductions.[97] These properties along with the good electron mobility and the ability to form favourable morphologies from blends with donor materials explain why these acceptor materials have been widely used and highly successful.[97]

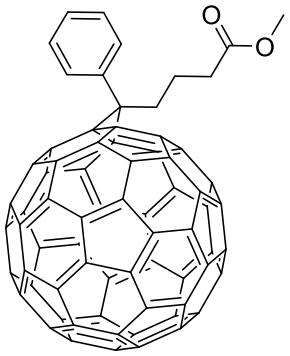

Figure 1.21. Chemical structure of $PC_{61}BM$

However there are some disadvantages in using fullerene based compounds as acceptor compounds. The synthesis and purification of these materials is difficult and

PCBM absorbs poorly in the visible region. For this reason, there has been research into developing novel acceptor compounds for BHJ-OPV devices with simple synthesis and broad absorption. Non-fullerene acceptor compounds could also be used in OPV devices with compounds that have a LUMO that is too low for effective charge transfer with PCBM, therefore expanding the number of potential donor compounds that can be applied effectively to OPV devices.

A common approach to the design of such materials is to incorporate electron-deficient moieties such as naphthalene diimide (NDI) or perylene diimide (PDI) into the molecular or polymer structure.[98, 99] McCulloch *et al* have shown a particularly interesting example of an acceptor compound containing electron-withdrawing rhodanine units using a simple synthetic route.[100] This compound showed broader UV/Vis absorption, increasing the acceptor's contribution to the photocurrent by donating holes at the donor acceptor interface. When the compound was applied to OPV devices, a PCE of 4.11% was achieved, which is higher than analogous device fabricated with a PCBM acceptor.[100] However, there are also examples of different strategies being applied to create effective acceptor materials as an alternative to fullerenes. For example, Hwang et al[101] present the interesting example of 9,9'-bifluorenyldiene can be used as an acceptor, showing a high V_{OC} or 1.0 V and moderate PCE of 2.28% with P3HT. The reduction of this compound results in the favourable gain of aromaticity, explaining why it is such an effective acceptor compound.

Chapter 2 – Donor-Acceptor-Donor Compounds Based on Naphthyridine-2,6-dione Unit

2.1 Abstract

In this chapter we present the synthesis of small molecules based on the novel electron-deficient acceptor unit naphthyridine-2,6-dione (ND). These compounds are based on two categories: Donor-acceptor-donor (D-A-D) compounds based on a central ND core and acceptor-donor-acceptor compounds (A-D-A) based on two ND units linked with an oligothiophene bridge. The synthesis and functionalisation of the ND acceptor unit is discussed and applied to the synthesis of 3 novel D-A-D compounds (ND01, ND02, ND03) and 3 novel A-D-A compounds (ND04, ND05, ND06).

The physical properties of the novel compounds are characterised using UV/Vis spectroscopy and cyclic voltammetry which were used to determine the absorption properties and determine the HOMO and LUMO levels for each material. The effect of the molecular structure on these properties is discussed with a particular focus on the effect of the acceptor units in the conjugated compounds. Density Functional Theory (DFT) and Time-Dependent Density Functional Theory (TDDFT) calculations were also used in order to explain experimental observations.

Finally, compounds ND02-ND06 were applied to OPV devices with each compound studied with various concentrations of $PC_{61}BM$ in order to optimise the PCE of the devices. ND03 was the best performing compound with a PCE of 0.72% achieved using a 1:4 donor: PCBM ratio.

2.2 Introduction

In Chapter 1 the advantages of the inclusion of electron-deficient acceptor units have already been discussed. In this section we discuss the synthesis of a novel N containing heterocyclic acceptor unit and its use in the synthesis of compounds which have been applied to OPV devices. Examples of some N-based heterocycles used successfully in donor-acceptor compounds for OPV, as discussed in chapter 1, include DPP and NDI[102, 103] and the structures of these units are shown below.

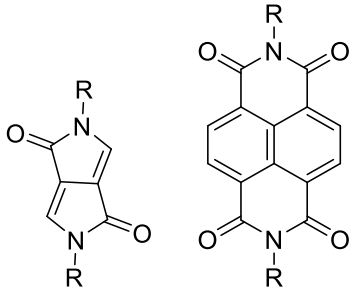

Figure 2.1. Structures of DPP and NDI

In this chapter we show the use of a naphthyridine-2,6-dione core in D-A small molecules for OPV applications. The synthesis of naphthyridine-2,6-dione was first reported in 1963[104] using the synthetic route below in scheme 2.1.

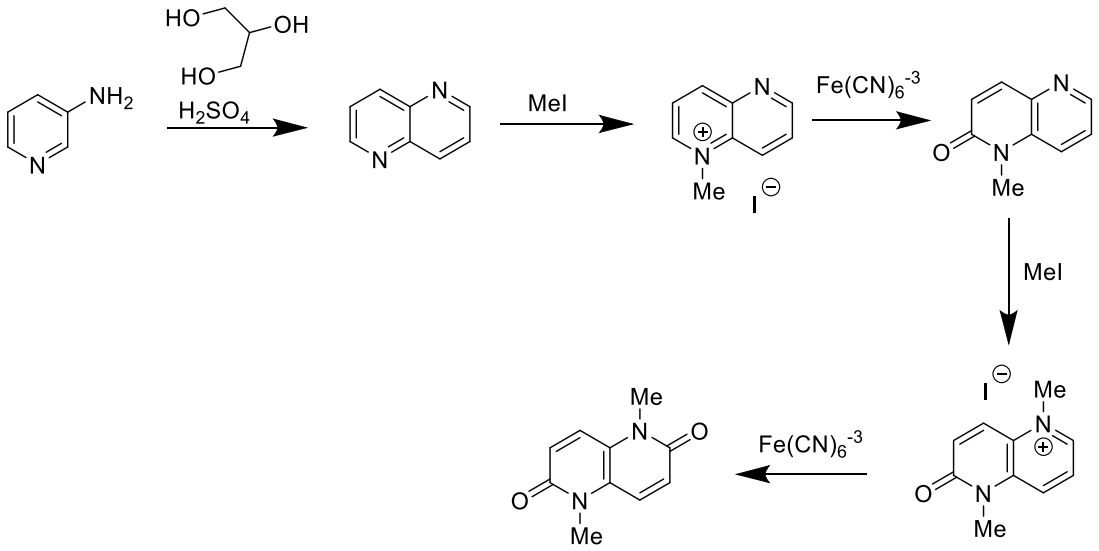

Scheme 2.1. Synthesis of 1,5-dimethylnaphthyridine-2,6-dione reported by Batcho *et al*[104]

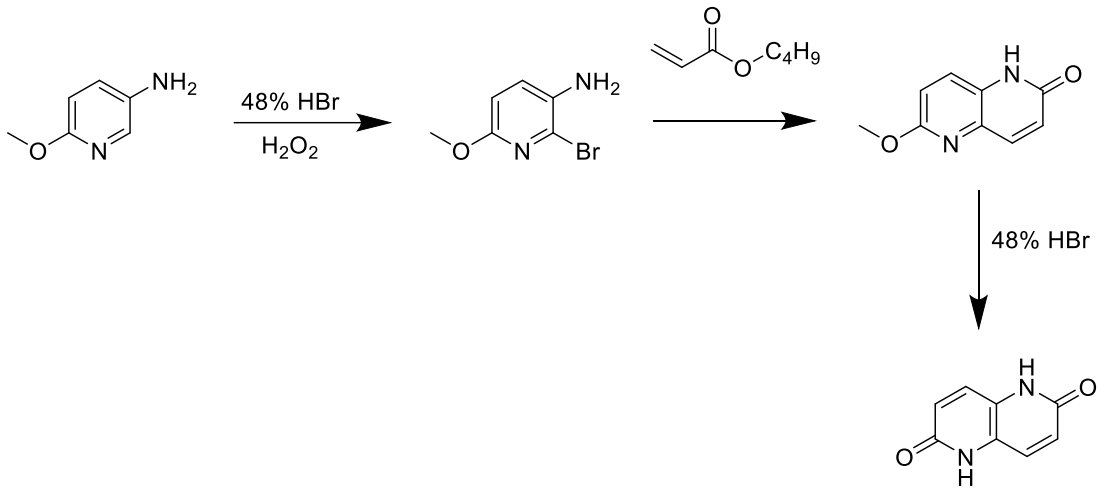

Scheme 2.2. Synthesis of 1,5-naphthyridine-2,6-dione developed by Merck Chemicals[105]

It has been used in polymers with OPV devices using these polymers achieving PCEs over 5%,[105] but there have never been any small molecules applied to organic electronic devices using this acceptor unit. We report the synthesis of six novel naphthyridine-2,6-dione based small molecules and describe how the physical properties of each compound vary with molecular structure. Organic photovoltaic cells were then fabricated using these D-A compounds and the performance of these devices will be discussed.

The location of an acceptor unit in the conjugated backbone can lead to differences in physical properties of analogous compounds. For example Bradley *et al*[16] strategically altered emission of truxene based compounds by altering the position of BT in the quaterfluorene arms.

It is also the case that the inclusion of multiple acceptor units in a donor-acceptor compound can significantly change the properties and OPV performance. Nguyen et al[106] have shown that structures containing three DPP units can exhibit higher p-type mobility and OPV power conversion efficiency than analogous compounds containing fewer chromophores due to a low-lying HOMO and improved film morphology. Interesting examples where the compounds contain different acceptor units include the BODIPY-DPP triads reported by Cortizo- Lacalle *et al*.[107] The inclusion of BODIPY units significantly alters the absorption, with a broader

absorption spectrum and red-shifted DPP absorption band. In these compounds the BODIPY unit influences the LUMO of the compounds.

In this chapter, we present the synthesis of ND-based target molecules containing one acceptor unit as well as compounds which contain two acceptor units in a acceptor-donor-acceptor type structure. The difference in the physical properties of these compounds will be investigated and the performance of OPVs using these compounds will be compared.

2.3 Results and Discussion

2.3.1 Alkylation of ND core

The first step of the synthetic route is the alkylation of the ND core in order to ensure solubility in the target compounds (scheme 2.3). The reaction conditions for the alkylation have been previously optimised at Merck chemicals with a maximum yield of 12% obtained. Despite the low yield, a sufficient amount of the twice N-alkylated core was acquired for the proceeding steps, having carried out the reaction on a large scale.

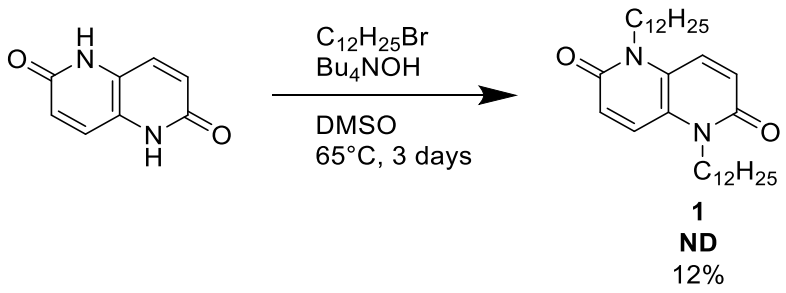

Scheme 2.3. Alkylation of naphthyridine-2,6-dione core.

Further investigation into explaining the origin of the low yield of the desired product showed that two isomers are formed in addition to the ND core. The isomers were isolated by column chromatography (eluent: 20% ethyl acetate: petroleum ether → 100% ethyl acetate) with the

following order of elution: ND20 > NDO > ND. These isomers are compounds in which there is both N-alkylation and O-alkylation giving NDO or O-alkylation on both ketone groups to give ND2O. The structures of the isomers are shown below in figure 2.2.

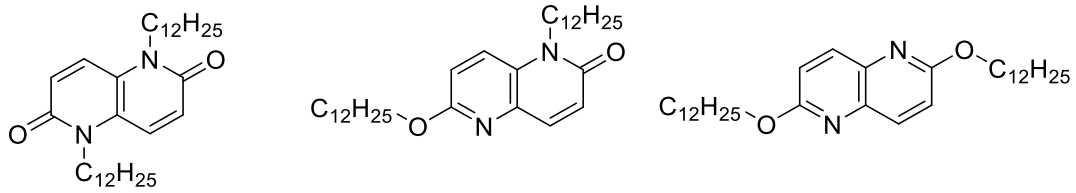

Figure 2.2. Three products obtained from alkylation of ND core

Work from Andersson *et al*[108] describes how O-alkylation is dominant in the functionalisation of the dihydrodithienonaphthyridine-5,10-dione unit whilst the same effect is described by Liu *et al*[109] in the synthesis of a diazaperylene compound. The diazaperylene compound is formed as the most favourable product due to tautomerisation to form a stable aromatic intermediate.[109] This mechanism is demonstrated below in figure 2.4 for the naphthyridine core. The formation of the stable aromatic intermediate explains why there is a low yield for the N-alkylation of the ND core.

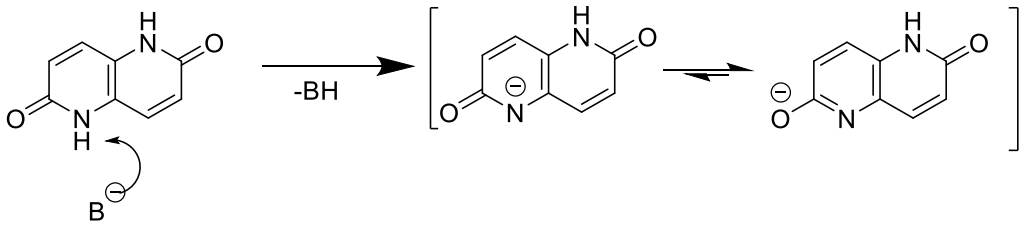

Scheme 2.4. Deprotonation of naphthyridine-2,6-dione and tautomers thereof.

The Presence of two electron withdrawing ketone groups on the doubly N-alklylated isomer suggested that this compound may be most suitable for use as an acceptor unit. It was therefore chosen as the target core for the synthesis of donor-acceptor compounds.

2.3.2 Synthesis

The synthetic pathways for the formation of the novel ND-based compounds are shown below.

The synthesis of the D-A-D compounds is discussed first. Compound 5 was formed using a previously reported procedure[110] before stannylation to form compound 6. This was used in a Stille coupling reaction to form the final product, ND01 (compound 7). These synthetic steps are shown below in scheme 2.5.

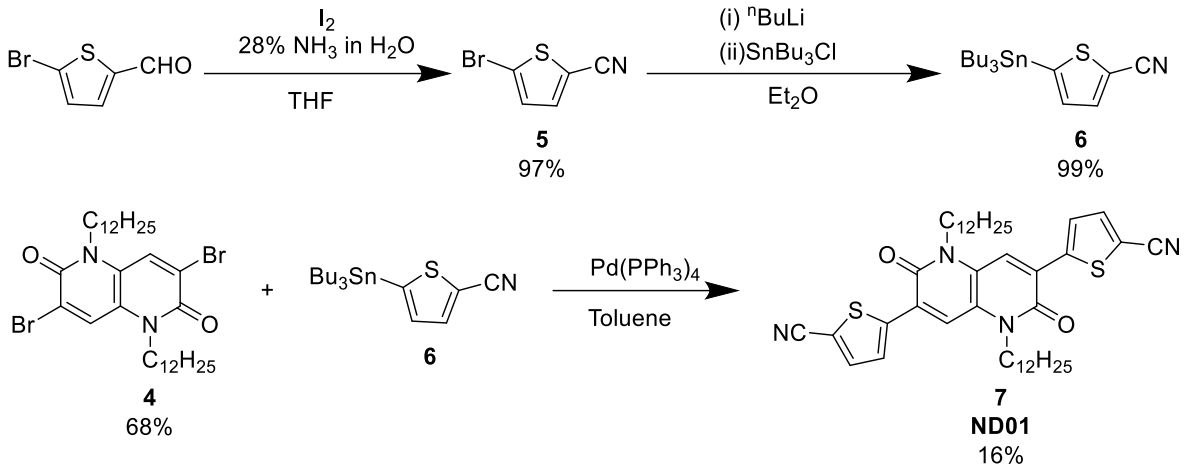

Scheme 2.5. Synthesis of ND01

Scheme 2.6 shows the synthesis of compounds ND02 (compound 11) and ND03 (compound 15) which were formed using analogous synthetic pathways. Benzothiophene and benzofuran were stannylated and used in a Stille coupling reactions with 2-bromothiophene before stannylation of the products and a subsequent Stille coupling reactions to yield the final products ND02 and ND03 respectively.

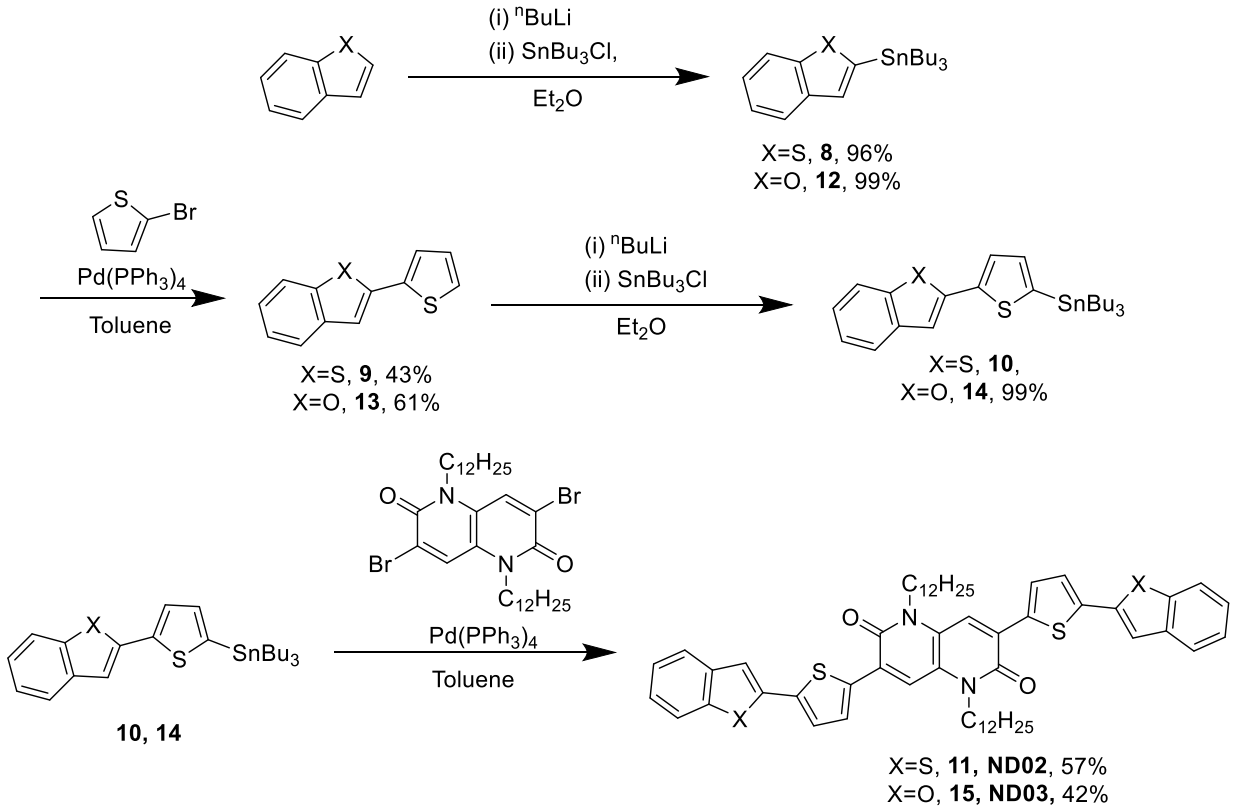

Scheme 2.6. Synthesis of compounds ND02 and ND03

Next the synthesis of the A-D-A ND-based compounds is presented in scheme 2.7. The first of the target compounds was synthesised by carrying out a Stille cross-coupling reaction using 3,7-dibromo-1,5-didodecylnaphthyridine-2,6-dione with 2-tributylstannylthiophene. The product was then brominated using NBS, giving the mono-brominated product in high yield. Finally compound 17 was reacted with 2,5-bis(tributylstannyl)thiophene in a Stille coupling reaction to give the final product ND04.

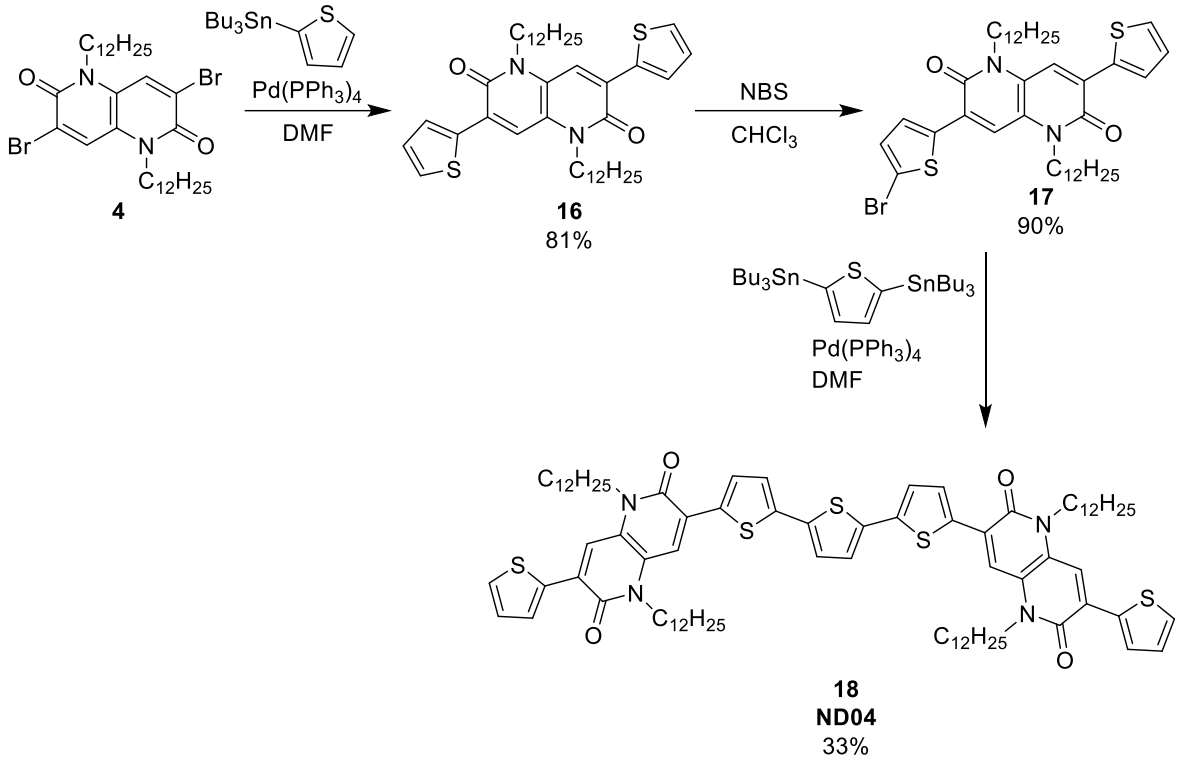

Scheme 2.7. Synthesis of compound ND04

The isomer of compound ND04 was also synthesised in order to examine the effect of the positioning of the naphthyridine units within the compound. The ND units are situated on either end of the central quinquithiophene chain, therefore in order to synthesise this compound, a mono-bromination of 1,5-naphthyridine-2,6-dione using NBS is carried out. This product is then reacted with 5-tributylstannyl-2,2'-bithophene to form compound 21, proceeded by a further bromination at the α-position of the peripheral thiophene. The final step of the synthesis of compound 23 was similar to the equivalent step in the synthesis of its isomer with 2,5-bis(tributylstannyl)thiophene and compound 22 reacting in a Stille cross coupling reaction to form the final product ND05.

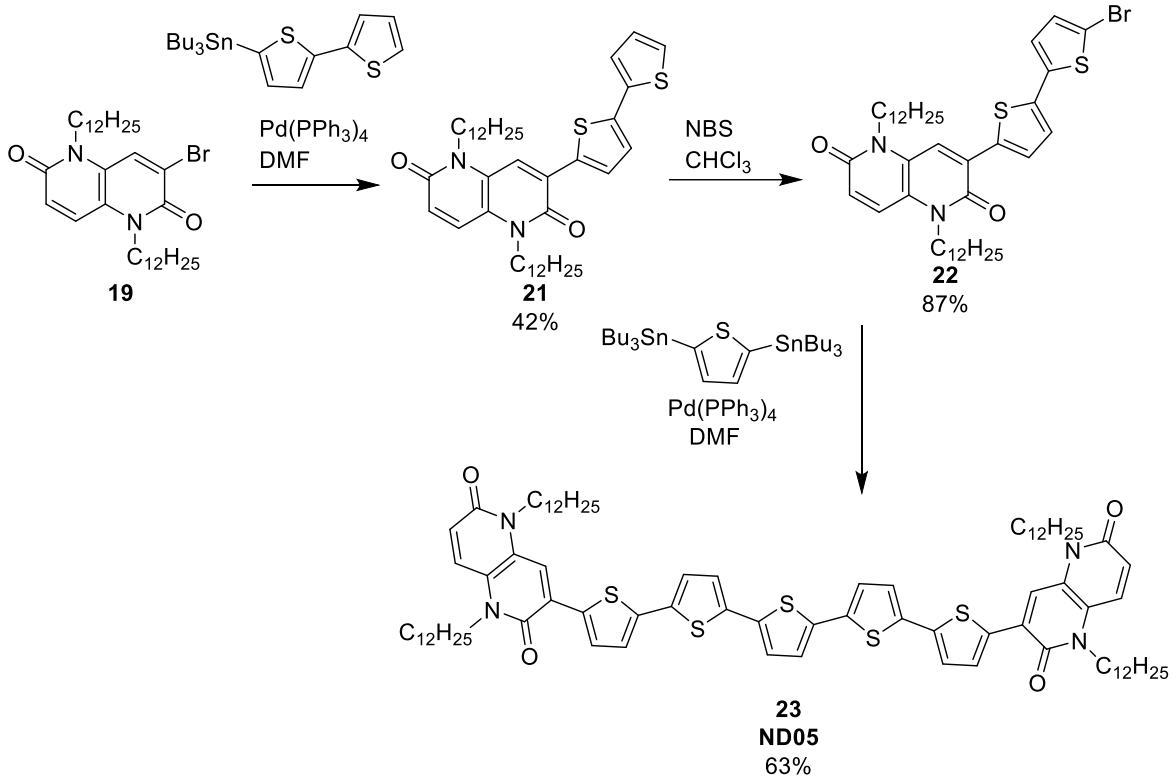

Scheme 2.8. Synthesis of compound ND05

The final target material was synthesised to have a longer conjugation length than the previous two compounds. Having synthesised compound 24 earlier, it was possible to use this compound in a Stille cross-coupling reaction with 2-(tributylstannyl)thiophene in order to form compound 25. A mono-bromination reaction using NBS was then carried out and the product was reacted with 2,5-bis(tributylstannyl)thiophene in order to form final product ND06.

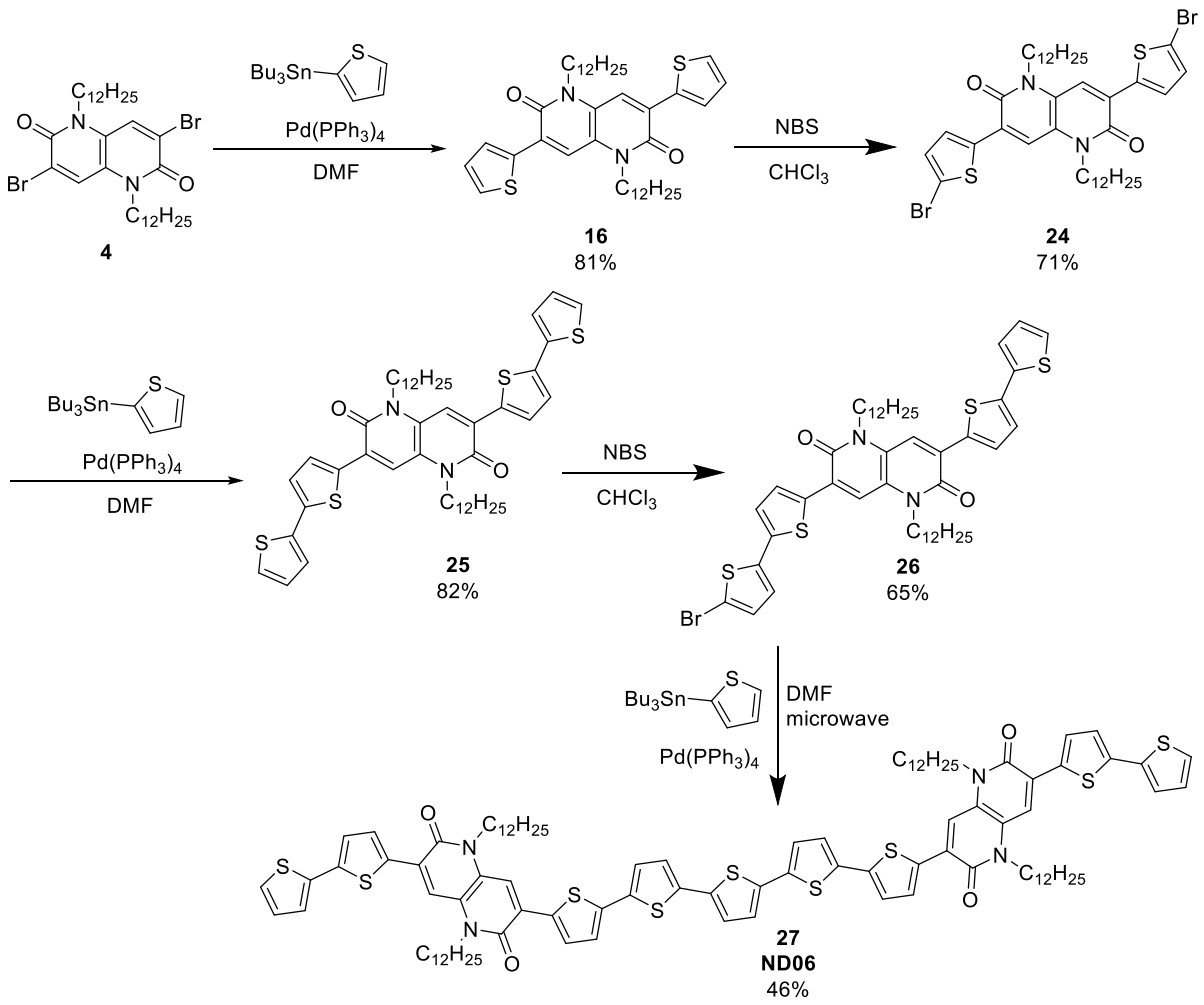

Scheme 2.9. Synthesis of compound ND06

2.3.3 Optical and Electrochemical Properties

The optical and electrochemical properties of each compound synthesised were studied using UV/Vis spectroscopy and cyclic voltammetry. The results of these studies were used in order to understand the effect of the molecular structure of each compound on the physical properties of the compounds. A summary of the optical and electrochemical properties of all compounds studied is shown in Table 2.1.

Firstly, the absorption properties of the D-A-D compounds are presented. All spectra were measured from CH_2Cl_2 solutions. In figure 2.3 the absorption spectra for the ND-core as well as intermediates, compounds 16 and 25 are shown in order to understand the absorption properties of the core and how an increase in conjugation effects these.

The spectrum for the ND-core shows strong vibronic splitting, indicative of planarity. Interestingly, with the addition of thiophene groups there the spectra for compounds 16 and 25 also shows vibronic splitting, suggesting that the addition of these units does not compromise planarity of the molecule. In the absorption spectra for the ND core and compound 16 the peak that absorbs at highest intensity is not the lowest energy peak. However compound 25 shows maximum absorption at the lowest energy peak, which would be more favourable for OPV applications.

The optical HOMO-LUMO gap calculated for the ND core is 2.88 eV. The addition of two thiophene units in compound 16 results in a reduction of the HOMO-LUMO gap to 2.39 eV and a further extension of the conjugation length in compound 25 results in a HOMO-LUMO gap of 2.13 eV.

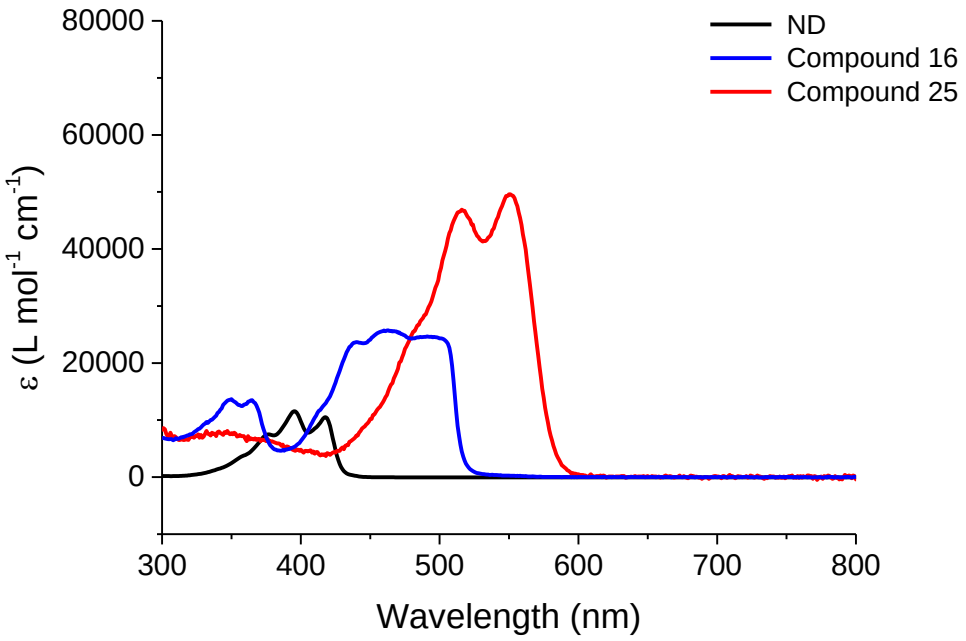

Figure 2.3. UV/Vis absorption spectra of ND-core and intermediates compounds 16 and 25 in CH_2Cl_2.

The spectra of compounds ND01-ND03 show refined vibronic peaks which are of a similar profile to the ND core, suggesting planarity in these compounds, a property which can enhance

π-π stacking between molecules which is beneficial in organic electronic devices. The spectra of ND01-ND03 are similar to that of compound 25 as they each show the lowest energy peak to be the largest. According to all the spectra presented, all compounds with a longer conjugated length that compound 16 show this trend which is preferable for OPV devices.

The only difference in the molecular structures of ND01 and compound 16 is the inclusion of –CN groups in the former and this results in a 0.07 eV reduction in the HOMO-LUMO gap, suggesting that addition of these electron-withdrawing groups has a minimal effect on the HOMO-LUMO gap. The absorption spectra of ND02 and ND03 are similar, suggesting that, as previously reported,[111] the heteroatom makes little difference in the absorption properties of the molecule. As a result of this there is only a small difference in the optical HOMO-LUMO gap of the materials, with that of ND03 being 0.02 eV lower. The HOMO-LUMO gaps of ND02 and ND03 are 0.22 and 0.24 eV lower than ND01 respectively, suggesting these materials may be more suitable for OPV devices.

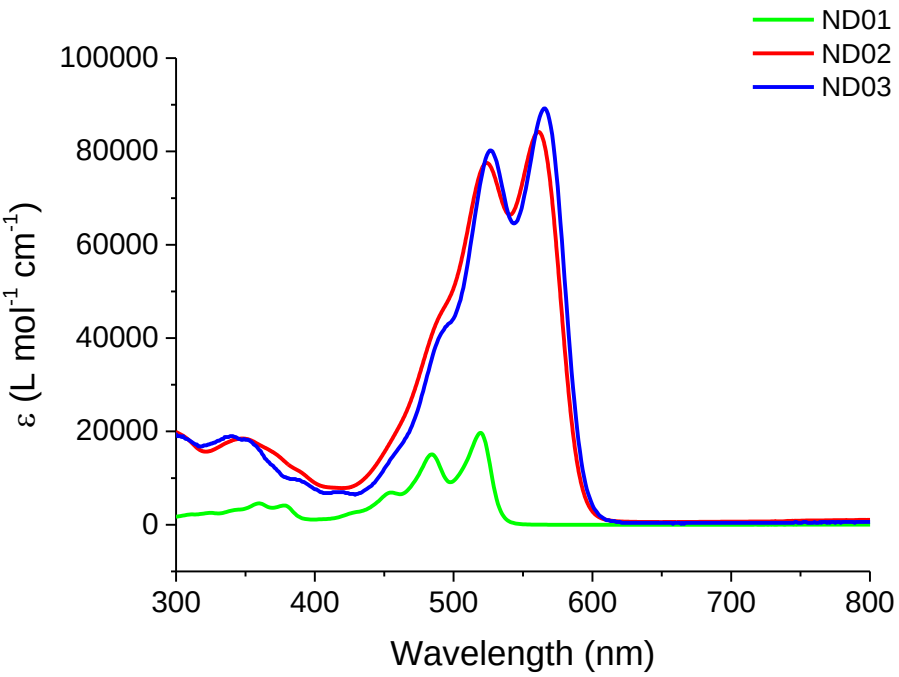

Figure 2.4. UV/Vis absorption spectra of ND-core and ND01-ND03

The absorption spectra of the A-D-A compounds are shown in figure 2.5. Noticeably, each of

the spectra show single broad peaks without the vibronic structure that was prominent in the spectra of the D-A-D compounds. The incorporation of the two ND units in the A-D-A compounds may induce some twists in the conjugated molecule.

A comparison of isomers compounds ND04 and ND05 shows that the two isomers have similarly broad absorption profiles but there is a bathochromic shift of 35 nm, from the λ_{max} of compound ND05 to that of compound ND04. This corresponds to the optical HOMO-LUMO gap for ND04 being 0.11 eV lower. Despite a significant increase in conjugation length for ND06 with respect to the other A-D-A compounds, the red-shift of the λ_{max} for compound ND06 is only 17 nm with respect to compound ND04 and the calculated HOMO-LUMO gap only 0.07 eV lower.

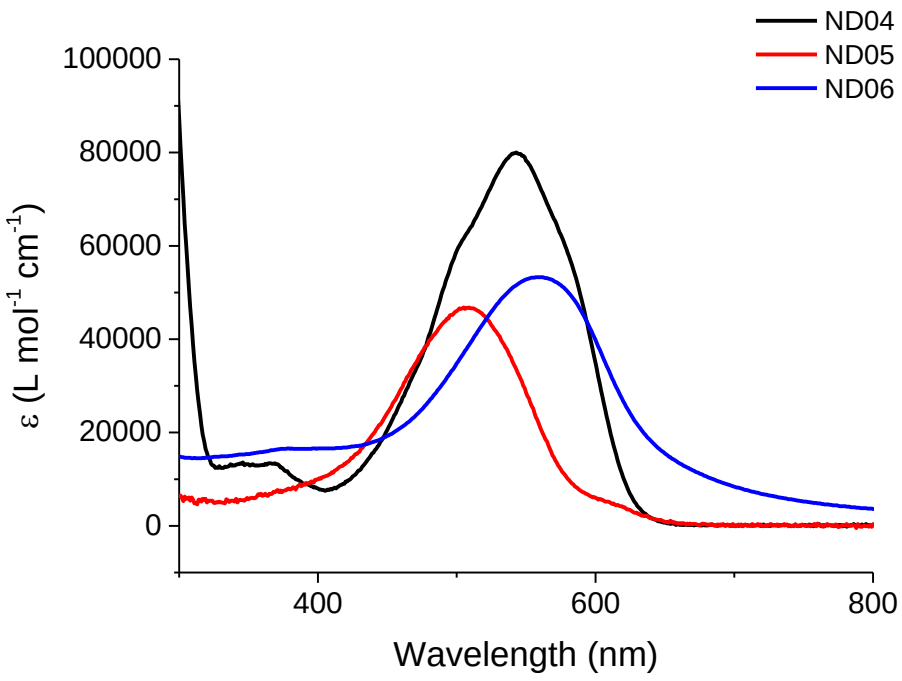

Figure 2.5. UV/Vis absorption spectra of ND04-ND06 in CH_2Cl_2 at 10^{-5} M concentration. Whilst ND04 and ND05 were fully dissolved at this concentration, ND06 remained partly as a suspension due to its poor solubility, explaining why the spectrum does not go to zero at high wavelengths (e.g. 800 nm).

Cyclic voltammetry was used in order to estimate the HOMO and LUMO energies of each of the compounds. The details of the experimental setup are described in chapter 6. The electrochemical oxidation and reduction of compounds ND01-ND03 are shown below in figures 2.6-2.8. There is a common feature in the reduction of all the D-A-D compounds where the first reduction is irreversible. The potential at which this occurs in ND01 is more positive than that for the other two compounds but that can be explained by the electron-deficient nature of the compounds as a result of the –CN groups.

The irreversible wave shown in the reduction of ND01 is followed by two reversible waves, whilst there is one quasi-reversible wave upon oxidation. The electron-deficient nature of this compound contributes to calculated HOMO and LUMO energies of -5.84 and -3.42 eV respectively.

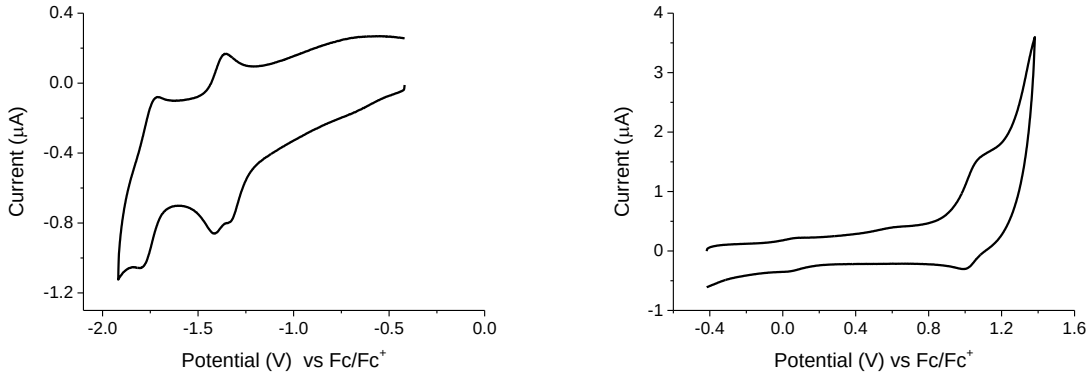

Figure 2.6. Reduction (left) and oxidation (right) of ND01 by cyclic voltammetry

There reduction of ND02 shows a reversible wave following on from the irreversible reduction that forms the radical anion. The oxidation of the compound results in a reversible wave and a quasi-reversible wave. The cathodic peak of the quasi-reversible wave seems to split.

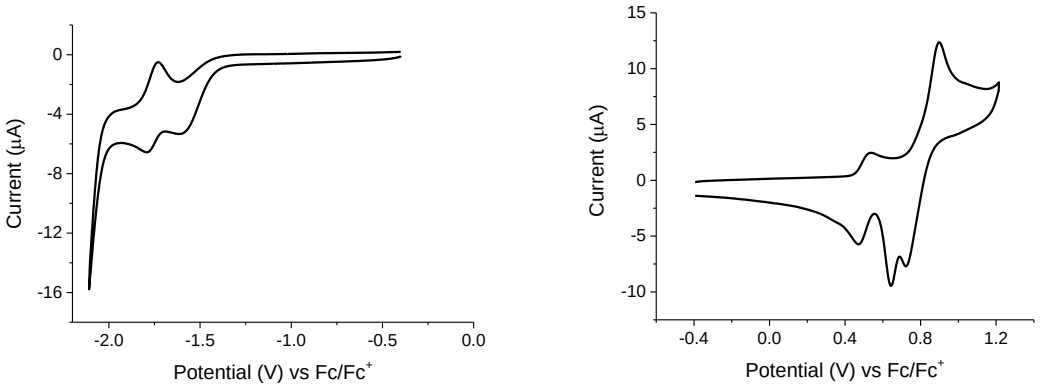

Figure 2.7. Reduction (left) and oxidation (right) of ND02 by cyclic voltammetry

In addition to the first irreversible reduction wave, there are two reversible waves shown in the reduction of ND03 whilst the oxidation shows two reversible oxidations. The optical HOMO-LUMO gap for ND02 and ND03 only differed by 0.02 eV and using the cyclic voltammetry results to calculated the HOMO and LUMO energies we see the same trend. The HOMO is the same for both compounds at -5.30 eV whereas the LUMO for ND02 is -3.14 eV which is 0.02 eV higher than the LUMO of ND03. Again this shows that the difference in heteroatom has little effect on the HOMO-LUMO gap.

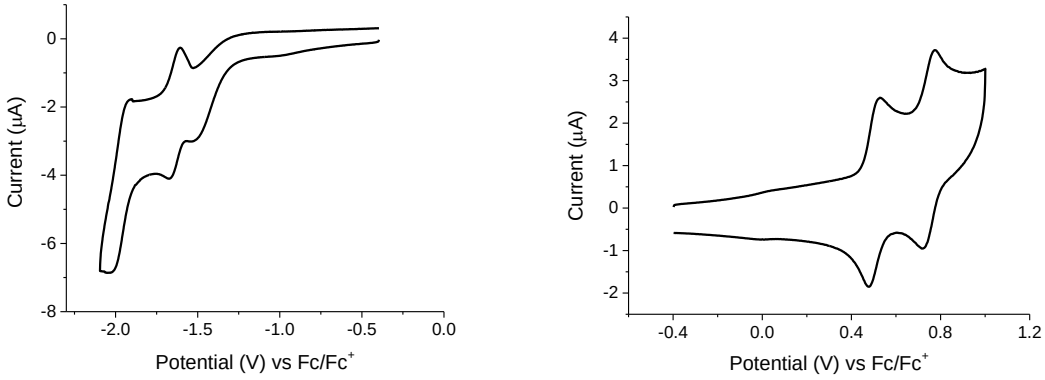

Figure 2.8. Reduction (left) and oxidation (right) of ND03 by cyclic voltammetry

The oxidations and reductions of the A-D-A compounds ND04-ND06 are shown in figures 2.9-2.11. First the electrochemical properties of isomers ND04 and ND05 were compared.

ND04 shows a reversible reduction wave and three quasi-reversible oxidation waves. There is a quasi-reversible wave shown in the reduction of ND05 although this occurs at a significantly lower (more negative) potential than the reduction of ND04. This corresponds to the LUMO calculated for ND05 being 0.54 eV higher than that of ND04. The reason for this will be discussed in the theoretical calculations section. There is a small difference in the HOMO energies, with the HOMO of ND05 being 0.05 eV higher than that of ND04.

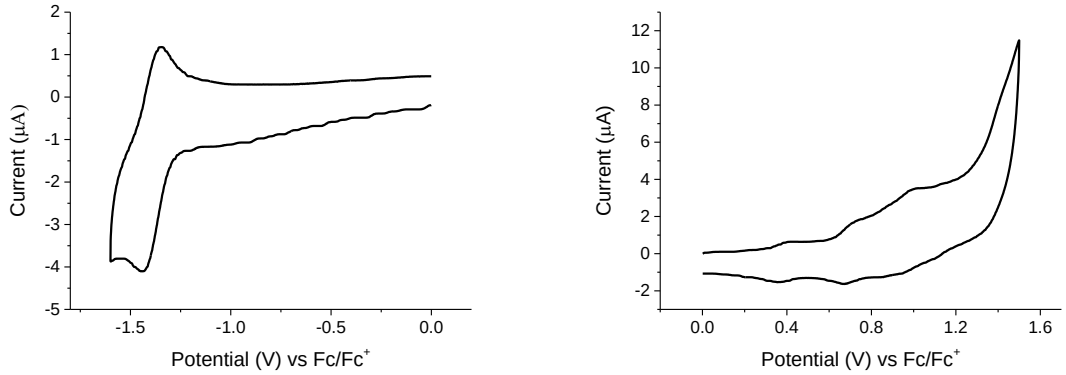

Figure 2.9. Reduction (left) and oxidation (right) of compound ND04

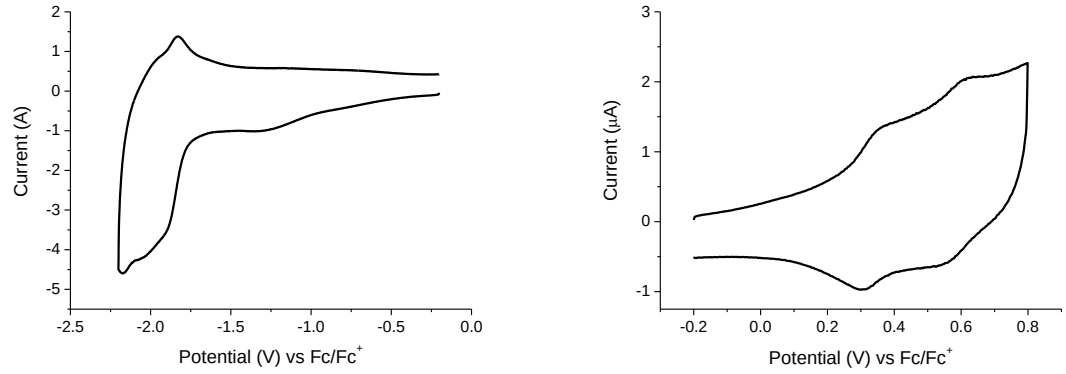

Figure 2.10. Reduction (left) and oxidation (right) of compound ND05

The reduction of ND06 shows an irreversible wave followed by a reversible wave whilst the oxidation shows a reversible wave followed by a quasi-reversible wave. Surprisingly, the

HOMO and LUMO levels calculated for ND06 (-5.47 and -3.50 eV respectively) are lower than those of compounds ND04 and ND05 despite the inclusion of more electron-rich thiophene units. This will be addressed in the theoretical calculations section.

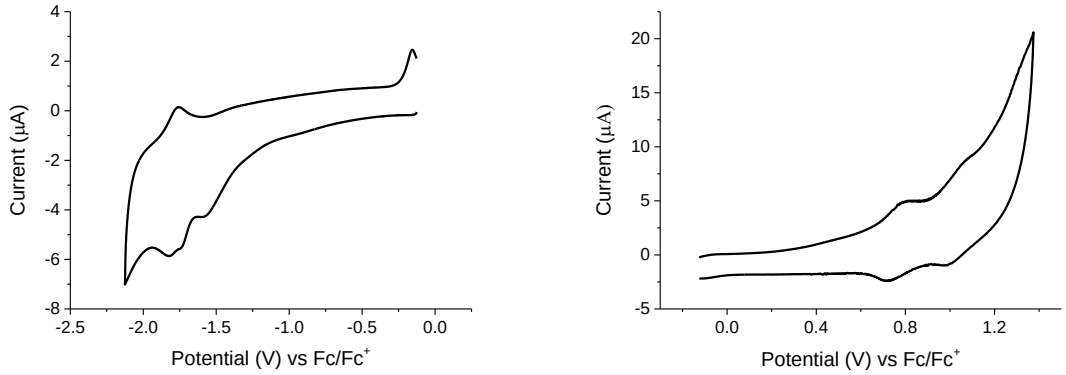

Figure 2.11. Reduction (left) and oxidation (right) of compound ND06

Table 2.1. Electrochemical and optical properties of novel ND-based compounds

Compound	λ_{max} (nm)	HOMO-LUMO (eV)[a]	HOMO (eV)[b]	LUMO (eV)[b]	E_{ox} (V)[c]	E_{red} (V)[c]
ND01	518	2.32 (2.42)	-5.84	-3.42	1.09/0.99,qr	-1.34, ir -1.42/-1.35 -1.80/-1.75
ND02	561	2.10 (2.16)	-5.30	-3.14	0.53/0.47 0.90/0.72, qr	-1.61, ir -1.79/-1.73
ND03	567	2.08 (2.14)	-5.30	-3.16	0.53/0.47, qr 0.78/0.72, qr	-1.51, ir -1.68/-1.61 -2.03/-1.92
ND04	542	1.99 (1.78)	-5.19	-3.41	0.42/0.36, qr 0.71/0.67, qr 1.01/0.95, qr	-1.44/-1.35
ND05	507	2.10 (2.28)	-5.14	-2.86	0.36/0.31, qr 0.62/0.55, qr	-2.09/-1.83, qr
ND06	559	1.92 (1.97)	-5.47	-3.50	0.80/0.72 1.07/0.99, qr	-1.57, ir -1.81/-1.76

[a]The optical HOMO–LUMO gap is calculated from the onset of absorption. The electrochemical HOMO–LUMO gap calculated from the difference in HOMO and LUMO energy level and is shown in parentheses. [b]HOMO(LUMO) calculated from $E_{HOMO(LUMO)} = (-4.80 - E_{onset}^{ox(red)})$. [c]The cathodic and anodic peaks are reported for reversible and quasi-reversible (qr) waves. The peak values on both forward and reverse scans are reported for reversible and quasi-reversible (qr) waves. The peak value on forward scan is shown for irreversible (ir) waves. The peak values are referenced to Fc/Fc+

2.3.4 Theoretical Calculations

In order to explain the optical and electrochemical properties further, particularly the differences between the two isomers ND04 and ND05, DFT and TDDFT calculations have been carried out. Inspection of the frontier orbitals calculated by TDDFT will provide information about the optical transitions and can also explain why the LUMO of compound ND05 is significantly higher than that of the other compounds synthesised. Each structure was optimised using CAM-B3LYP functional[112] with SVP[113] basis set and SMD solvent model[114] before TDDFT calculations using the same parameters mentioned for the optimisations. All calculations were performed using Gaussian 09[115] software. The TDDFT results and a comparison to the experimental absorption spectra is shown in table 2.2.

Table 2.2. TDDFT Calculation results

Compound	$\lambda_{max\text{-}exp}$ (nm)	$\lambda_{max\text{-}TDDFT}$ (nm)	TDDFT Transitions[a]	$\Delta_{exp\text{-}TDDFT}$ (nm)
ND04	542	518	HOMO-2 → LUMO+2 (12%) HOMO-1 → LUMO+1 (33%) HOMO → LUMO (54%)	24
ND05	507	491	HOMO-2 → LUMO+2 (15%) HOMO-1 → LUMO+1 (29%) HOMO → LUMO (47%) HOMO → LUMO+2 (9%)	16
ND06	559	530	HOMO-2 → LUMO+2 (15%) HOMO-1 → LUMO+1 (39%) HOMO → LUMO (46%)	29

[a]Molecular orbitals involved in transitions are described relative to the HOMO and LUMO. For example, the HOMO-1 describes the second highest occupied molecular orbital and LUMO+2 is the third lowest unoccupied molecular orbital

The TDDFT results listed in table 2.2 show the same general trend as the experimental results with only small deviations in the calculated λ_{max} with respect to the experimental values. The TDDFT transitions show that the HOMO-LUMO transition is the most dominant in each of the calculations, therefore the HOMO and LUMO diagrams for each compound are shown below in figures 2.12-2.14.

The cyclic voltammetry results show there to be a considerable difference in the LUMO energies of isomers ND04 an ND05. Considering the LUMO diagrams for each compound reveals an explanation for the LUMO ND05 being significantly higher than that of ND04. The

LUMO of ND04 shows delocalisation between the two ND units across the ter-thiophene bridge, but there is only a small contribution from the peripheral thiophenes. The terminal aromatic moieties in ND05 are the ND units, and the LUMO is shown to be delocalised between the ND units, across the 5T bridge. There is a greater proportion of the two ND units contributing to the LUMO of ND04 than that of ND05, explaining why the LUMO of ND04 is significantly lower. This is supported by the calculated LUMO of ND04 (-1.72 eV) being lower than that of ND05 (-1.56 eV).

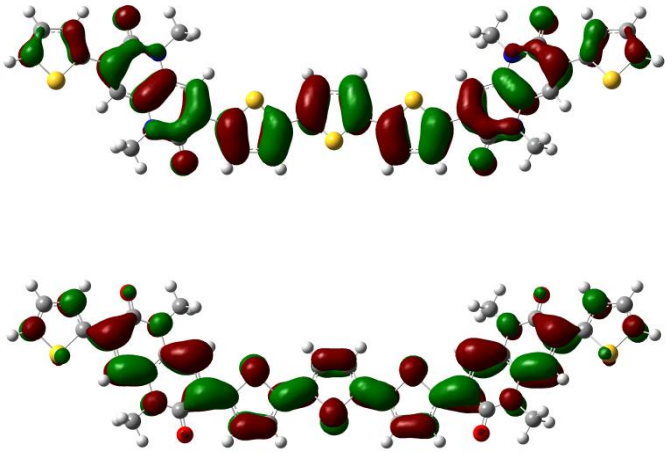

Figure 2.12. HOMO (top) and LUMO (bottom) of compound ND04. The positive and negative phases of the molecular orbital are shown in red and green respectively.

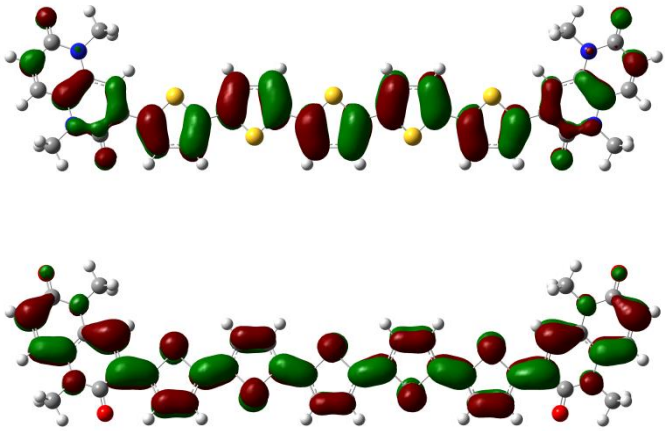

Figure 2.13. HOMO (top) and LUMO (bottom) of compound ND05. The positive and negative phases of the molecular orbital are shown in red and green respectively.

Both the HOMO and LUMO energies of ND06 determined by cyclic voltammetry are lower than those of ND04 and ND05. An explanation for the stabilisation of the HOMO energy could be due to the significant increase in conjugation length in ND06. However, the LUMO, which is dominated by acceptor moieties, is also lower. The LUMO diagram for ND06 shows a large area of the LUMO focussed on the electron-deficient acceptor units, explaining the reduction in the LUMO energy. The calculated LUMO of ND06 (-1.75 eV) is lower than those of ND04 and ND05, showing the same trend as the experimental results.

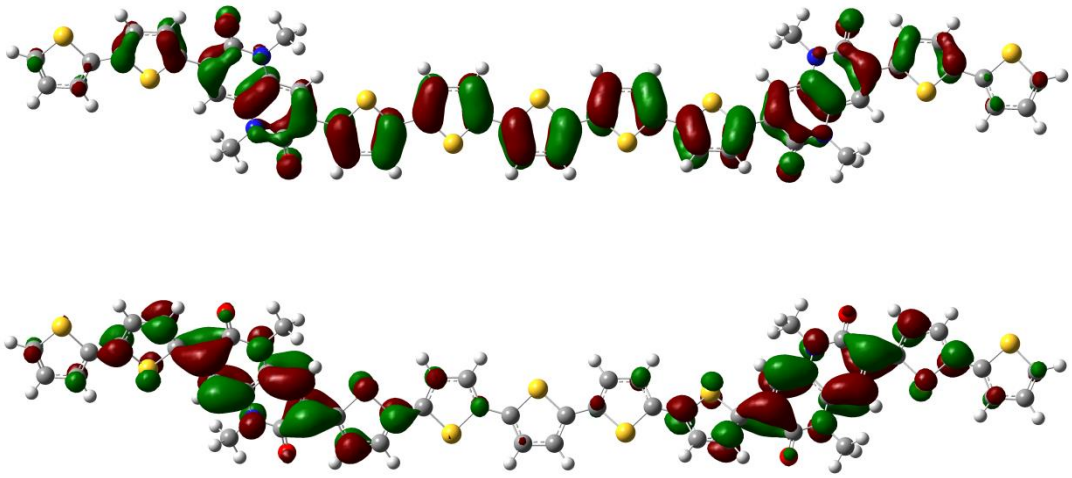

Figure 2.14. HOMO (top) and LUMO (bottom) of compound ND06

2.3.5 Organic Photovoltaic Devices

OPV devices were fabricated using compounds ND02-ND06. ND01 was not used due to its relatively high HOMO-LUMO gap, which would limit the performance of any devices. The general procedure for the preparation of the devices is described in chapter 6. Every device was prepared from a solution with 10 mg ml^{-1} donor concentration. The ratio of donor: PCBM is stated for each device fabricated, however it is worth noting that for each compound D:A ratios 1:1, 1:2, 1:3 and 1:4 were tested for each compound. The results presented here are the based on the optimum conditions. In general, the OPV results using non-optimum D: A ratios show poor efficiencies and so are not discussed.

The summarised OPV results from device fabricated using D-A-D compounds ND02 and ND03 are presented in table 2.3. Shown in figure 2.15 is the output for the OPV fabricated using 1:4 ratio of ND02:$PC_{61}BM$ in a 10 mg ml^{-1} (donor concentration) chloroform solution. An open-circuit voltage of 0.23 V, short-circuit current density of 1.40 mA cm^{-2} and fill factor of 0.31 lead to a PCE of 0.1%. The use of *o*-dichlorobenzene in this case decreases the efficiency. The poor performance of these devices can be explained by the poor solubility of ND02 (< 10 mg ml^{-1} at room temperature), suggesting this compound is not ideal for solution-processing.

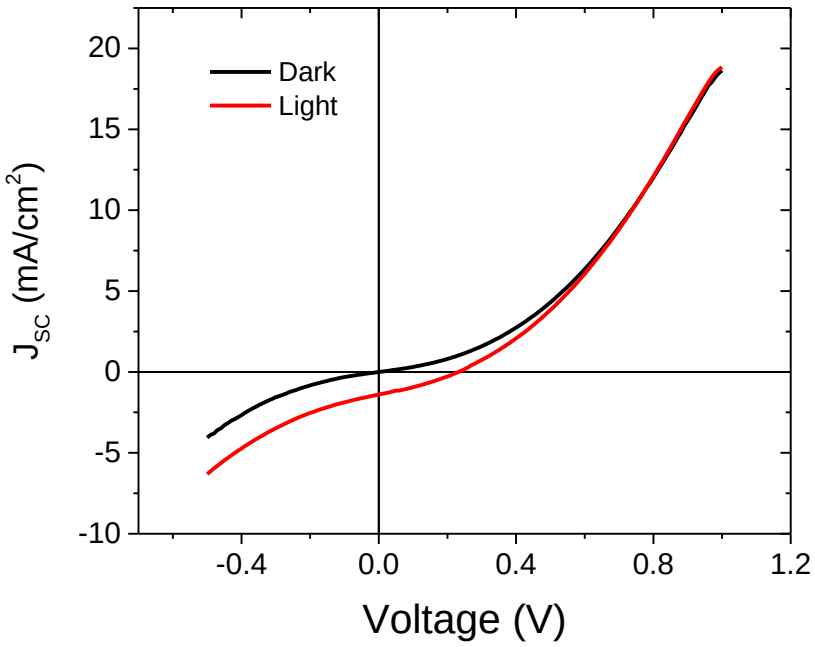

Figure 2.15. Best performing OPV fabricated using ND02

Substitution of an O atom in place of the S in the benzothiophene groups in ND02 leads to ND03 being more soluble than its analogue. As a result, the performance of OPV devices fabricated using ND03 is enhanced. Like devices containing ND02, a D: A ratio of 1:4 is optimum and in a chloroform solution the resulting PCE is 0.35%. However, the efficiency shows a greater than 2-fold increase as result of using o-dichlorobenzene as the solvent. The output for this device is shown in figure 2.16. The increase in the performance can be explained by slow drying of DCB leading to improved film morphology with respect to quick drying chloroform films.[116]

Donor compound ND03 shows a significantly better performance in the OPV device compared to ND02 which is also witnessed in performance between analogues in work by Nguyen et al.[111] In this case both the V_{OC} and J_{SC} are improved when using ND03 as a donor material in place of ND02 and this can be attributed to greater solubility and better charge transport.

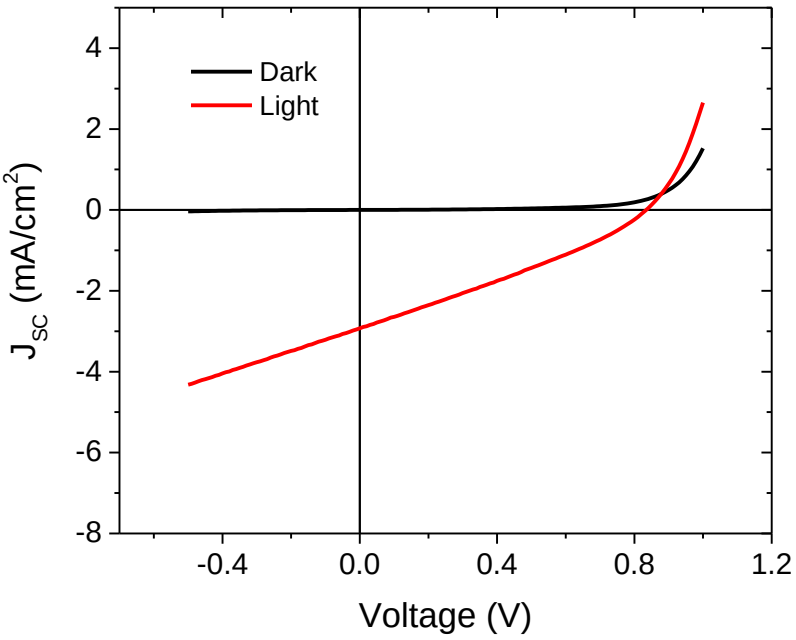

Figure 2.16. Best performing OPV fabricated using ND03

Table 2.3. Summary OPV results for D-A-D compounds

Donor Compound	**Solvent**	**V_{OC} (V)**	**J_{SC} (mA cm^{-2})**	**FF**	**PCE (%)**
ND02	$CHCl_3$	0.23	1.40	0.31	0.1
	DCB	0.03	1.16	0.22	0.01
ND03	$CHCl_3$	0.70	1.70	0.30	0.35
	DCB	0.83	2.92	0.30	0.72

The OPV results from the devices fabricated using A-D-A materials ND04-ND06 as donor materials. Any devices fabricated using ND05 failed to give a photovoltaic response. The devices which give the results shown below are fabricated using o-dichlorobenzene as the solvent and contain a 1:3 D: A ratio.

The best performing device prepared using ND04 has a VOC of 0.23 V but a very poor J_{SC} leading to a PCE of 0.01%.

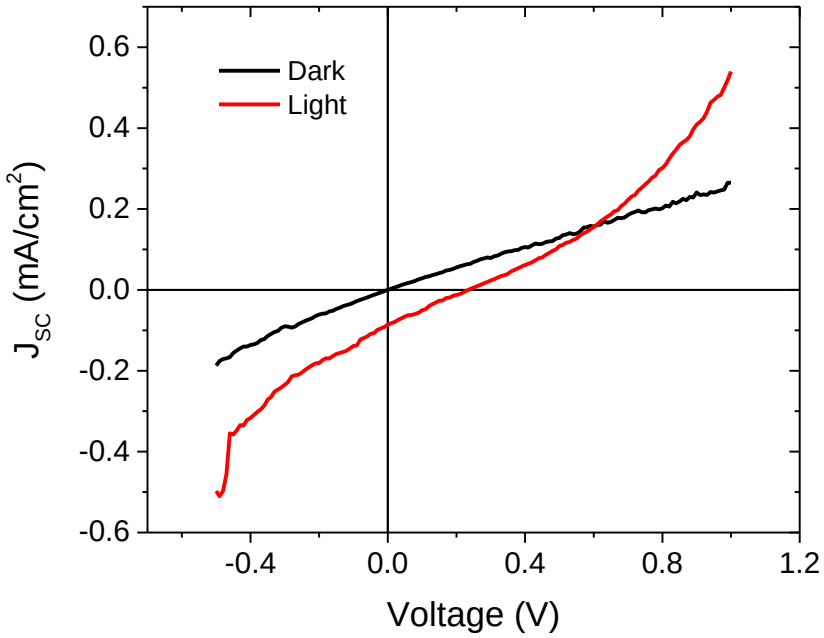

Figure 2.17. Best performing OPV fabricated using ND04

The output for the device fabricated using ND06 as the donor material is much improved with respect to that using ND04 with a good V_{OC} of 0.65 V although the J_{SC} and fill factor are poor at 2.32 mA cm^{-2} and 0.30 respectively. The resulting PCE is 0.46%, significantly higher than devices using ND02 and ND04 but not as high as ND03 containing devices.

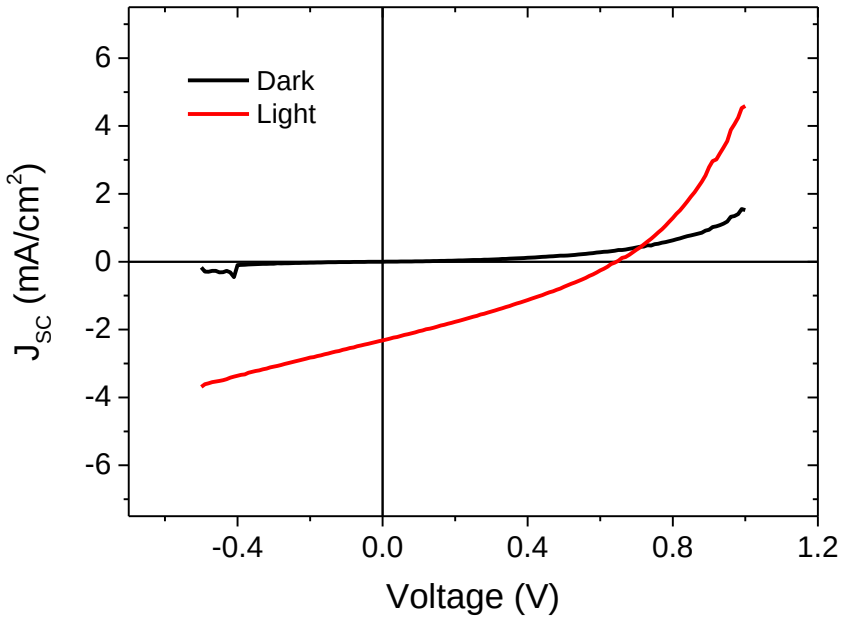

Figure 2.18. Best performing OPV fabricated using ND06

Table 2.4. Summary of OPV results using A-D-A compounds

Donor Compound	Solvent	V_{OC} (V)	J_{SC} (mA cm^{-2})	FF	PCE (%)
ND04	*o*-DCB	0.23	0.09	0.27	0.01
ND05	—	—	—	—	—
ND06	*o*-DCB	0.65	2.32	0.30	0.46

2.4 Conclusions/Future Work

In summary, six novel compounds containing the electron-deficient ND acceptor unit have been synthesised according to two general structures of compound: D-A-D and A-D-A. Using UV/Vis spectroscopy the optical HOMO-LUMO gap for each material was determined. It was

also shown that the spectra of the D-A-D compounds exhibited well-refined vibronic structure which was not present in the broad spectra of the A-D-A compounds, suggesting a greater degree of planarity in the former class of compounds. Cyclic voltammetry was also used to calculate the HOMO and LUMO energy values for each compound showing ND06 to have the lowest HOMO-LUMO gap, explained by its greater conjugation length. Using frontier orbitals determined from DFT calculations, it was possible to explain trends in the cyclic voltammetry results of the A-D-A compounds. Both UV/Vis spectroscopy and cyclic voltammetry showed the difference in optical and electrochemical properties between ND02 and ND03 to be minimal, showing the inclusion of O or S heteroatoms in the benzofuran(thiophene) group to have little impact on these properties.

Finally OPV devices were fabricated using compounds ND02-ND06, with devices fabricated using ND03 showing the highest PCE of 0.72%. ND06 was used in a device which showed the highest efficiency of the A-D-A compounds at 0.46% and if the solubility of this compound was improved, there could be potential for further improvement due to the good absorption properties of the compound.

Although the PCEs measured for the devices fabricated were low, the high V_{OC} for the devices suggested that there was effective charge separation in the bulk heterojunction, the J_{SC} was low, limiting performance for the OPV devices. The effect of different alkyl chain lengths on the morphology of the active layer was discussed in Chapter 1, and the fact that small changes to the chemical structure (i.e. shorten/lengthen solubilising alkyl groups) can have a large effect on device performance. Therefore, it may be possible to improve the J_{SC} by using different alkyl groups on the naphthyridine core. In chapter 1, the example of improving OPV swapping the position of alkyl groups onto different aromatic units in a compound, presented by McGehee *et al*,[78] was highlighted and the same principle could be applied to investigate whether this may improve OPV performance.

Chapter 3 – Synthesis of 1-Dodecyl-5-dodecoxynaphthyridine-2-one Based Materials and Their Application to OPV and OFET Devices

3.1 Abstract

In this chapter we discuss the synthesis, characterisation and application of novel compounds based on the asymmetric 1-dodecyl-5-dodecoxynaphthyridine-2-one unit. Only a mono-brominated product resulted from the bromination of this compound, therefore the target compounds to be synthesised were based on two different structures: asymmetric D-A compounds (NDO-2T-BF and NDO-3T-BF) and symmetric compounds $(NDO)_2$-3T and $(NDO\text{-}T)_2$-BT) containing two terminal 1-dodecyl-5-dodeoxynaphthyridine-2-one units. Cyclic voltammetry and UV/Vis spectroscopy were used in order to determine the electrochemical and optical properties of each compound.

OFETs were fabricated using each of the compounds with $(NDO\text{-}T)_2$-BT showing the highest hole mobility of 0.022 $cm^2\ V^{-1}\ s^{-1}$ after optimisation of the solvent, SAMs and annealing. NDO-2T-BF and NDO-3T-BF were also applied for the fabrication of OFETs although the performance of these devices was poor.

Finally, considering that the LUMO of $(NDO\text{-}T)_2$-BT was calculated to be similar to that of $PC_{61}BM$, OPVs were fabricated using P3HT as a donor and $(NDO\text{-}T)_2$-BT as the acceptor. The poor performance of these devices suggests that $(NDO\text{-}T)_2$-BT is not suitable as an n-type material. However, due to its broad absorption and high p-type mobility, it could be used as a donor material in OPVs with an acceptor with a LUMO level lower than $PC_{61}BM$.

3.2 Introduction

In the previous chapter, compounds based on the symmetric ND acceptor unit were studied. The naphthyridine-2,6-dione unit was solubilised by the substitution at the N atom with dodecyl chains. However, as well as this product, there were two isomeric by-products isolated. In this chapter we will focus on the properties of compounds containing one of these isomers: 1-dodecyl-6-dodecoxynaphthyridine-2-one. The electron donating dodecoxy group will lessen the electro-deficiency with respect to the ND unit. However, the electron deficient nature of naphthyridine and the presence of one electron withdrawing carbonyl group gave reason to study the use of this asymmetric unit as a donor moiety in organic semiconducting materials.

The majority of acceptor groups such as DPP, NDI, BODIPY and NDI are symmetric and are used as repeating units in polymers of moieties present in small molecules which can be compared with polymers. There are examples of asymmetric acceptor units being used in organic semiconductors such as rhodanine,[100, 117-119] indenedione[119, 120] or the dicyanovinyl group.[121-123] Normally, these electron-deficient units are used as terminal acceptor units in the conjugated molecule.

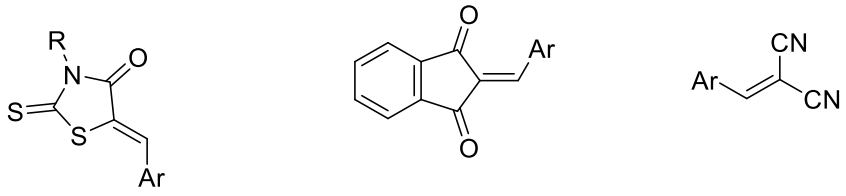

Figure 3.1. Chemical structures rhodanine (left) indenedione (centre) and the dicyanovinylene (right)

In this chapter compounds based on the novel 1-dodecyl-6-dodecoxy-naphthyridine-2-one have been synthesised and applied to OFET and OPV devices. Compounds $(NDO)_2$-3T and $(NDO\text{-}T)_2$-BT are based on two terminal acceptor units, whilst NDO-2T-BF and NDO-3T-BF and asymmetric structures based on one electron-deficient unit.

3.3 Results and Discussion

3.3.1 Synthesis

The reaction of 1-dodecyl-6-dodecoxynaphthyridine-2-one with bromine selectively yields the mono-brominated compound 28. Compound 28 was used in another Stille reaction with 2-tributylstannylthiophene in order to form compound 29 which was then brominated using NBS. The brominated product was then used in two separate Pd-catalysed cross coupling reactions: a Stille coupling with 2,5-bis(trimethylstannyl)thiophene to form **(NDO)$_2$-3T** and a Suzuki cross-coupling reaction with 2,1,3-benzothiadiazole-4,7-bis(boronic acid pinacol ester) in order to form **(NDO-T)$_2$-BT** (scheme 3.1).

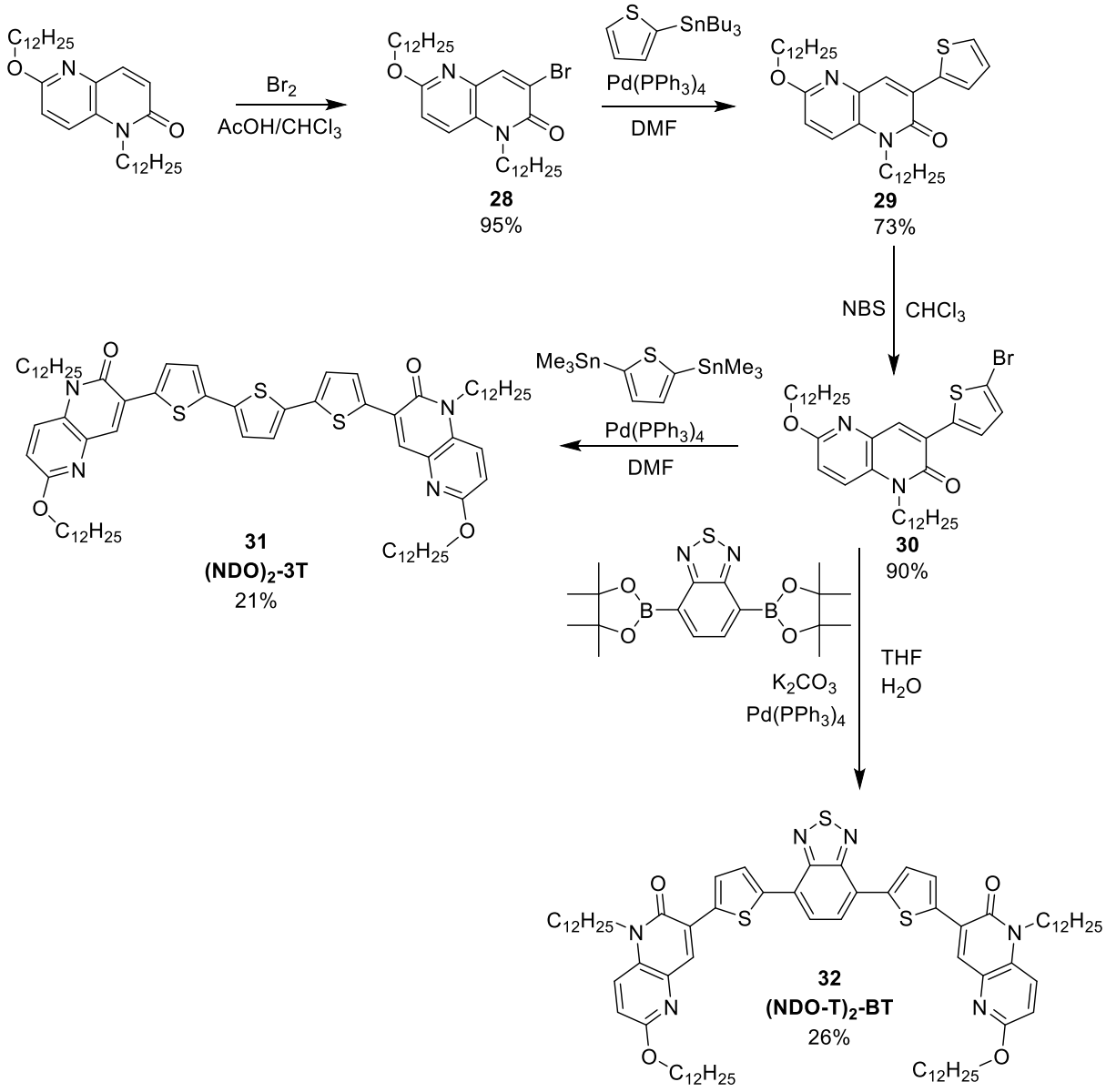

Scheme 3.1 Synthesis of **(NDO)$_2$-3T** and **(NDO)$_2$-T-BT**

Compound 30 was also used in a reaction with 5-tributylstannyl-2-(thiophen-2-yl)benzofuran in order to form the first of the asymmetric target materials, **NDO-2T-BF** , shown in scheme 3.2. This scheme also shows the synthesis of the more conjugated **NDO-3T-BF**, formed by Stille coupling of compound 29 with 2-tributylstannyl-2',5'-bithiophene, bromination of the product before another Stille reaction with 5-tributylstannyl-2-(thiophen-2-yl)benzofuran

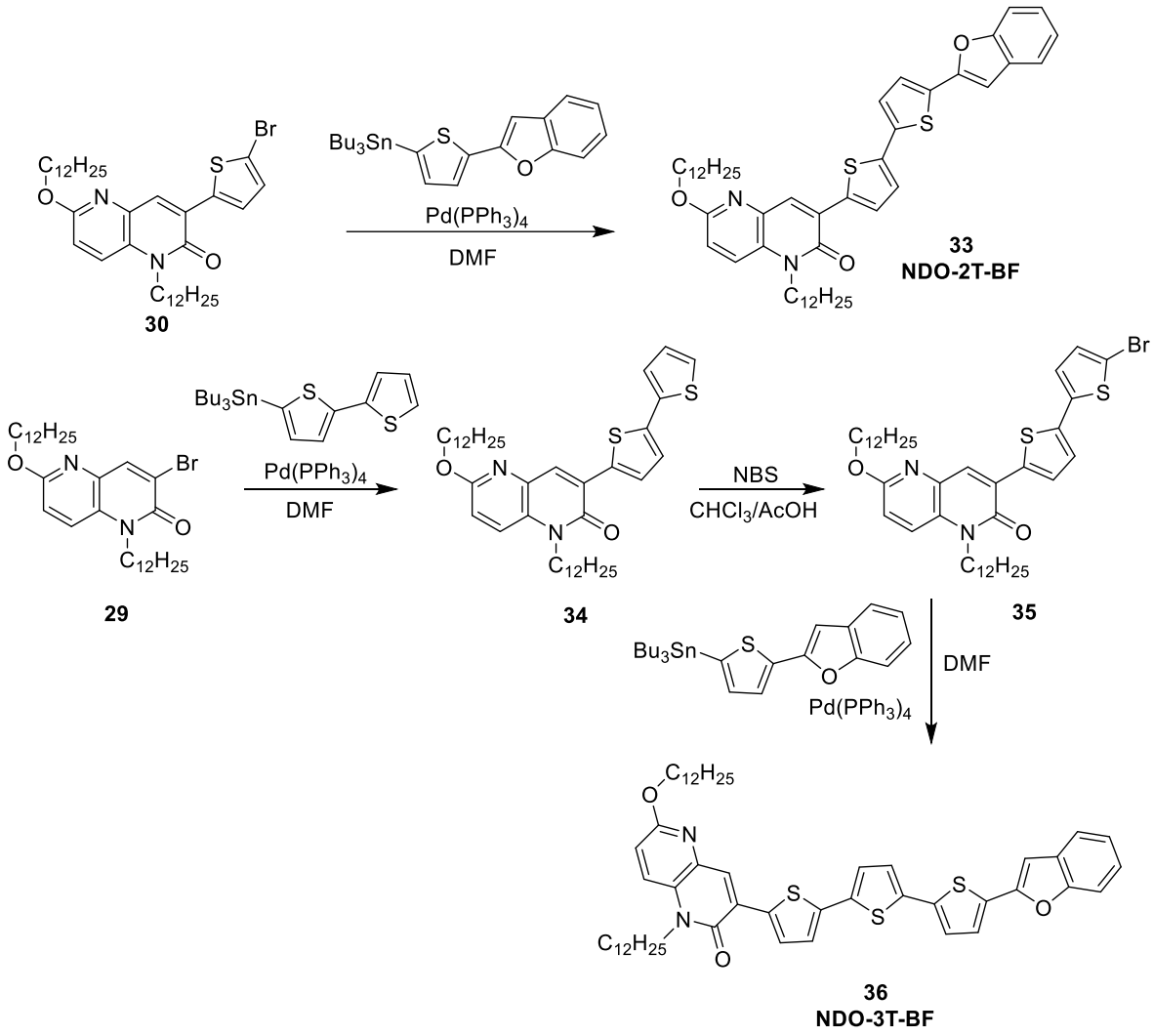

Scheme 3.2 Synthesis of **NDO-2T-BF** and **NDO-3T-BF**

3.3.2 X-Ray Crystallography

X-Ray crystallography measurements were performed and the structures solved by Dr Mateusz Pitak at UK National Crystallography Service.

Crystals of NDO-2T were formed by addition of methanol to a CH_2Cl_2 solution, whilst crystallisation of NDO-2T-BF was carried out by vapour diffusion of methanol into a CH_2Cl_2 solution of the compound.

The NDO-2T crystals were poor quality and the resulting R-factor for the structure solved was 9%. There is also distortion in the terminal thiophene with 81:19 ratio over the two sites. Interestingly there appears to be an S—O interaction which results in a dihedral angle of 6.83° between thiophene and the core. Interestingly this is present in the structure of NDO-2T-BF, suggesting that these structures are not influenced by the non-traditional hydrogen bonding suggested by Ratner *et al*.[23] The two compounds show similarities in the packing motif, where there is parallel displaced π-π stacking although, the displacement is greater in NDO-2T-BF.

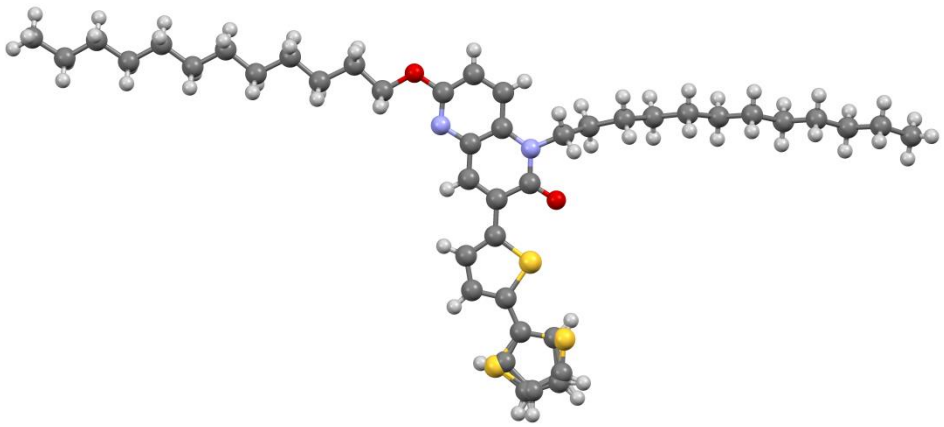

Figure 3.2 Structure of NDO-2T determined by X-Ray crystallography

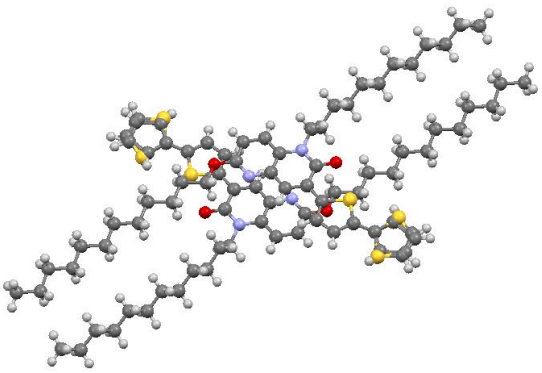

Figure 3.3 Packing of NDO-2T determined by X-Ray crystallography

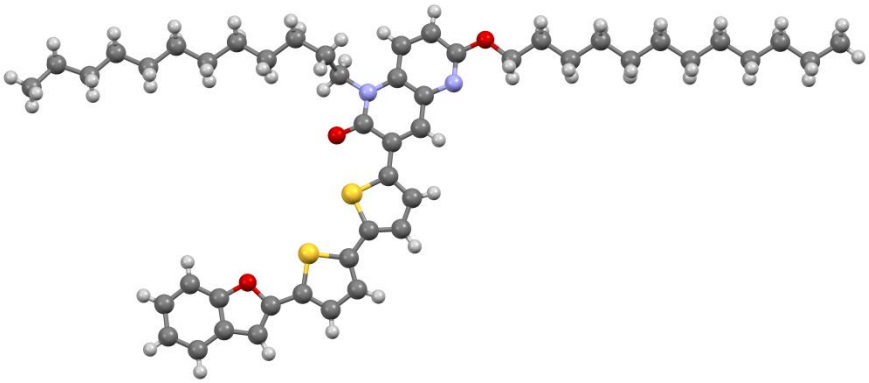

Figure 3.4 Structure of NDO-2T-BF determined by X-ray crystallography

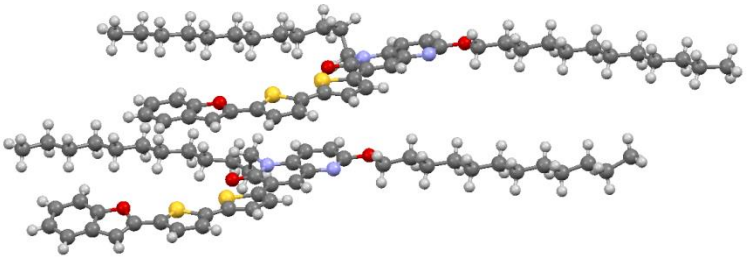

Figure 3.5 Packing of NDO-2T-BF determined by X-Ray crystallography

3.3.3 Optical and Electrochemical Properties

In order to understand the absorption properties of the different structures, UV/Vis spectroscopy was carried out for each compound. The solution-state absorption spectrum of $(NDO)_2$-3T shows one peak with a λ_{max} of 477 nm, whilst there is broadening in the solid-state spectrum, showing a wide range of absorption, which is favourable OPV applications. The HOMO-LUMO gap calculated from the onset of absorption in solution-state spectrum is 2.30 eV, whilst the optical HOMO-LUMO gap determined from the solid-state spectrum is 1.94 eV. This shows the effect of π-π stacking in the film.

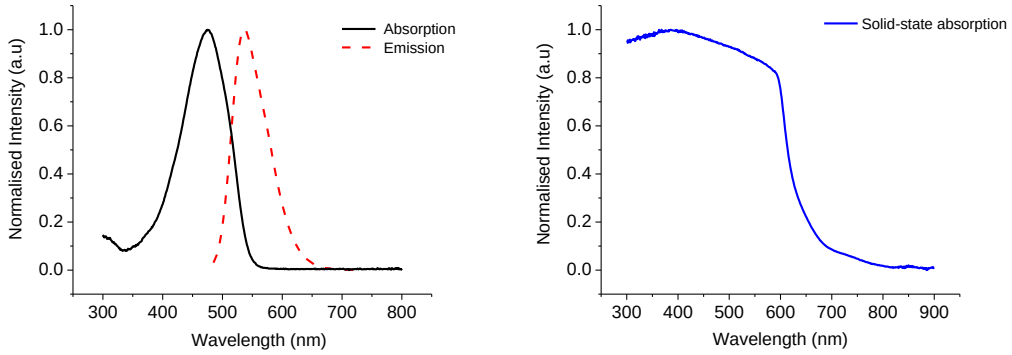

Figure 3.6 UV/Vis absorption spectrum of **$(NDO)_2$-3T** in solution (CH_2Cl_2) and solid-state. ε (at λmax in CH_2Cl_2 solution) = 63700 L mol^{-1} cm^{-1}.

The inclusion of the BT unit results in a 39 nm bathochromic shift in the λ_{max} of $(NDO\text{-}T)_2$-BT with respect to $(NDO)_2$-3T. The spectrum also shows a peak at lower wavelength, which is not present in the two previous spectra. Interestingly, there appears to be a solvatochromic effect. Non-polar solvents show very similar spectra, with a λ_{max} around 516 nm. However in different polar solvents, there is a noticeable change in the spectra, with a significantly higher λ_{max}. The solid-state spectrum is very broad, and the large shift of the lowest energy peak suggests good π-π stacking in the film. The calculated optical HOMO-LUMO gap in the film is 1.68eV. These properties suggest that the compounds can be a good candidate as an OPV material.

There are also considerable differences in the fluorescence spectra of both compounds. The $\lambda_{em\ max}$ for $(NDO)_2$-3T was 536 nm, giving a Stokes shift of 59 nm. However, the $\lambda_{em\ max}$ of $(NDO\text{-}T)_2$-BT at 609 nm results in a Stokes shift of 97 nm, a significant increase with respect to $(NDO)_2$-3T showing that including the BT unit in the conjugated backbone has a large effect on the physical properties of the molecule.

Interestingly, upon excitation at 597 nm, there is an emission peak at 693 nm in DMF solution, again highlighting how the physical properties of this compound change in solution with a polar solvent.

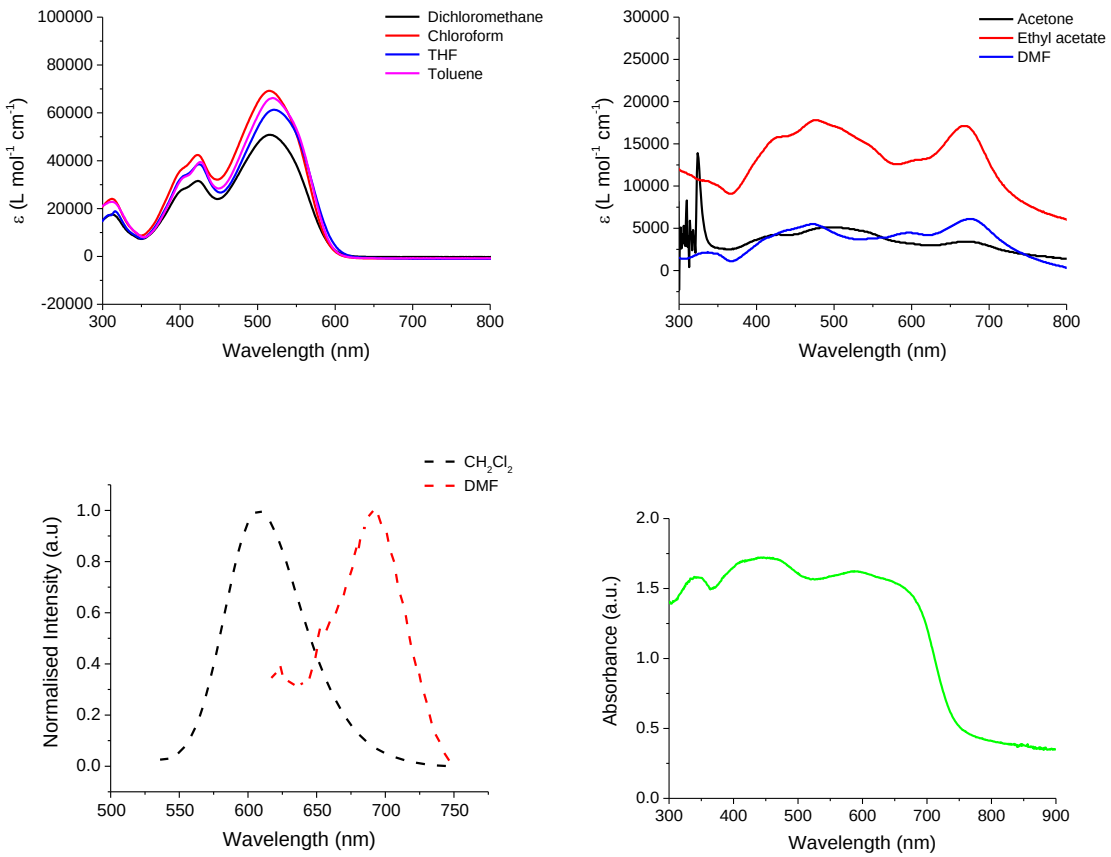

Figure 3.7 UV/Vis absorption spectra of **$(NDO\text{-}T)_2$-BT** in non-polar solvent (top, left), polar solvent (top, right) fluorescence spectra in CH_2Cl_2 and DMF (bottom, left), with excitation at 516 and 597 nm respectively and solid-state absorption spectrum (bottom, right).

The absorption spectra of the compounds containing a single naphthyridin-2-one unit are shown below in figure 3.8 and 3.9. These spectra show similar profiles but the increase in conjugation results in a 12 nm shift in the λ_{max} of NDO-3T-BF with respect to that of NDO-2T-BF. The solid-state spectrum for NDO-3T-BF is broader than that of NDO-2T-BF, resulting from scattering or reflection from the film. The calculated optical HOMO-LUMO gap is 1.93 eV, substantially lower than that for NDO-2T-BF, which is calculated at 2.29 eV. The difference in optical HOMO-LUMO gap in solution and film for NDO-3T-BF is 0.45 eV, a difference which is 0.27 eV larger than in NDO-2T-BF, suggesting more effective π-π stacking in NDO-3T-BF.

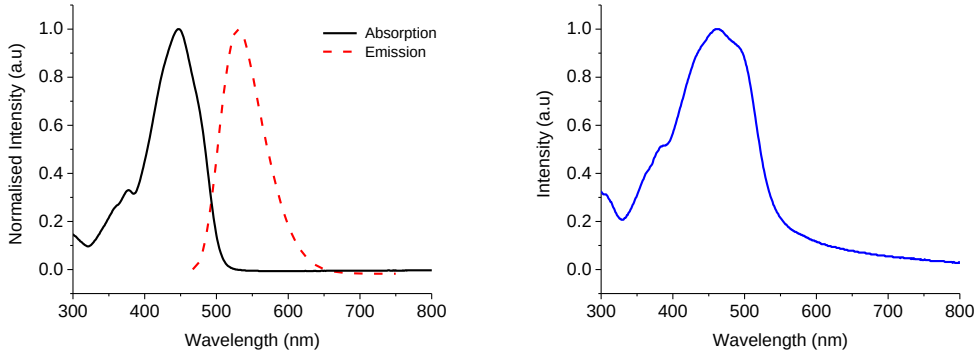

Figure 3.8 UV/Vis absorption spectra of **NDO-2T-BF** in solution (CH_2Cl_2) and solid-state. ε (at λmax in CH_2Cl_2 solution) = 61200 L mol^{-1} cm^{-1}.

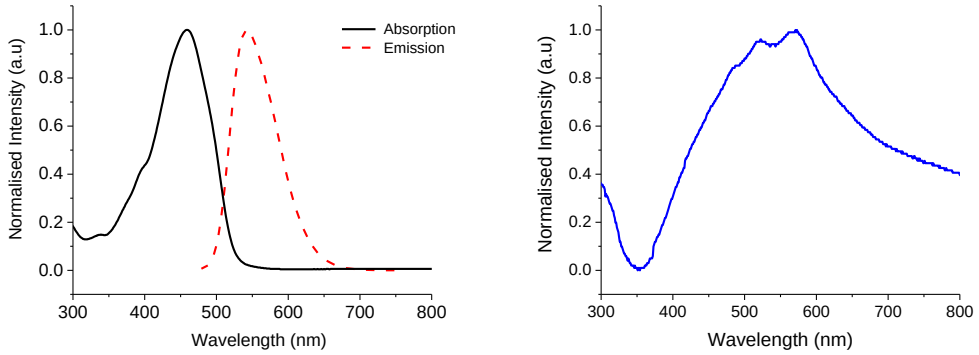

Figure 3.9 UV/Vis absorption spectrum of **NDO-3T-BF** in solution (CH_2Cl_2) and solid-state. ε (at λmax in CH_2Cl_2 solution) = 68500 L mol^{-1} cm^{-1}.

The electrochemical properties of the NDO compounds were examined by cyclic voltammetry and the oxidation and reduction potentials in addition to the calculated HOMO and LUMO energies are summarised in table 3.1. The voltammograms for $(NDO)_2$-3T show one irreversible oxidation peak and irreversible and quasi-reversible reduction waves respectively. The electron-deficient nature of this compound may explain why the oxidation is unstable and that there is a reversible nature to each of the reduction waves.

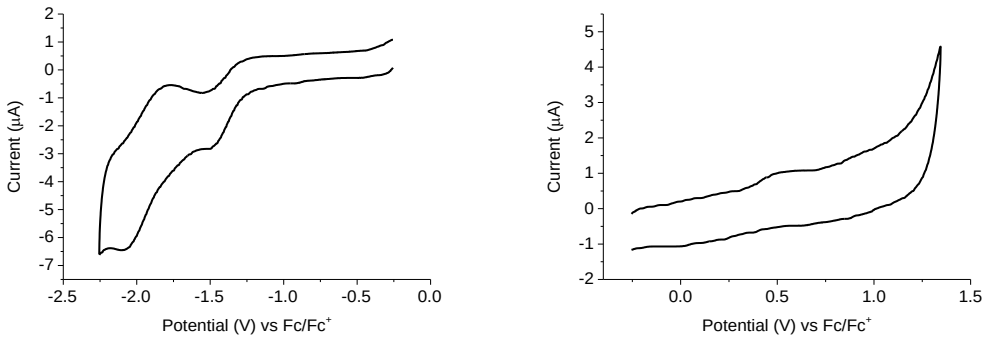

Figure 3.10 Reduction (left) and oxidation (right) of **$(NDO)_2$-3T**

The oxidation of $(NDO\text{-}T)_2$-BT shows two quasi-reversible waves. The first reduction occurs at a similar potential to that in $(NDO)_2$-3T, suggesting that the reduction occurs at the NDO unit. This explains the similarity in the calculated HOMO energies for each compound. It can

then be assumed that the second reduction of $(NDO\text{-}T)_2$-BT occurs at the benzothiadiazole portion of the molecule. In a comparison between $(NDO)_2$-3T and $(NDO\text{-}T)_2$-BT, we can see that the LUMO of $(NDO\text{-}T)_2$-BT is 0.55 eV lower than $(NDO)_2$-3T and this can be attributed to the inclusion of the electron deficient BT unit. This would suggest that the benzothiadiazole moiety is a more dominant acceptor that NDO.

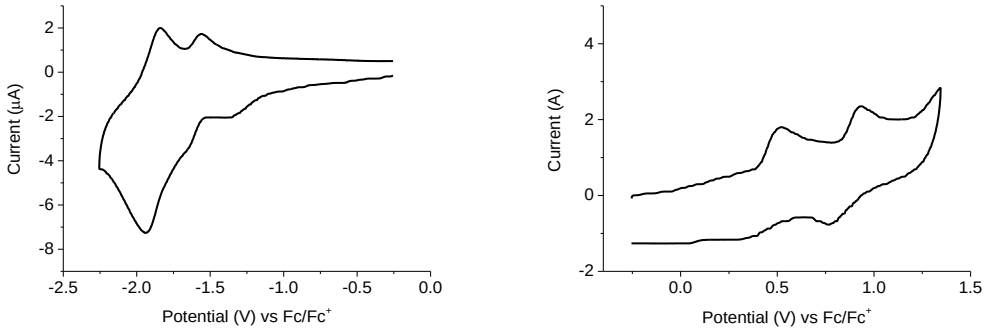

Figure 3.11 Reduction (left) and oxidation (right) of **$(NDO\text{-}T)_2$-BT**

Looking at the cyclic voltammetry of the D-A NDO-based compounds, there appears to be some similarities in the electrochemical properties. However, there is a noticeable difference in the oxidation voltammograms for the two compounds. The forward scan presents a complex picture, where there is an overlap between two peaks. In contrast, the oxidation of NDO-3T-BF shows two reversible peaks, which occur at similar potentials to the oxidations of NDO-2T-BF. However the oxidation waves for NDO-2T-BF are broad and both anodic and cathodic peaks overlap in the two waves. There are parallels in the reduction graphs of NDO-2T-BF and NDO-3T-BF, with both showing an irreversible peak followed by two successive quasi-reversible waves with only a slight variation in the reduction potentials. The potentials at which the first and second reductions occur in NDO-2T-BF are slightly lower than the corresponding voltages for NDO-3T-BF whilst this trend is reversed for the third reduction. The HOMO and LUMO energies calculated from these voltammograms are again very similar, resulting in the HOMO-LUMO gap of NDO-2T-BF being 0.05 eV lower than its analogue.

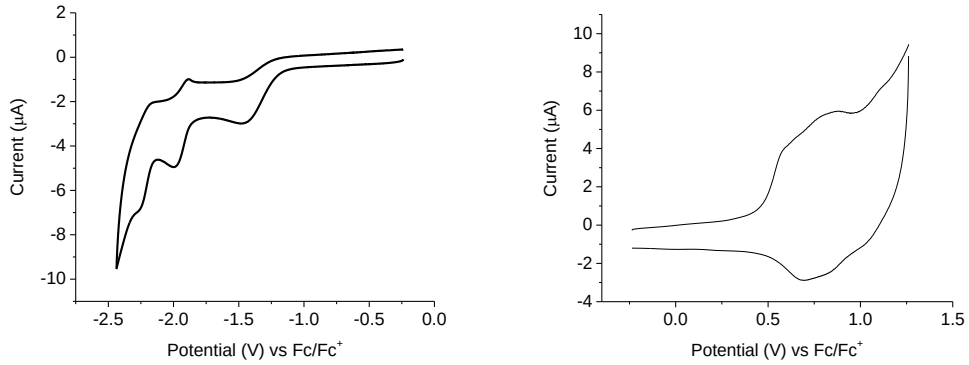

Figure 3.12 Reduction (left) and oxidation (right) of **NDO-2T-BF**

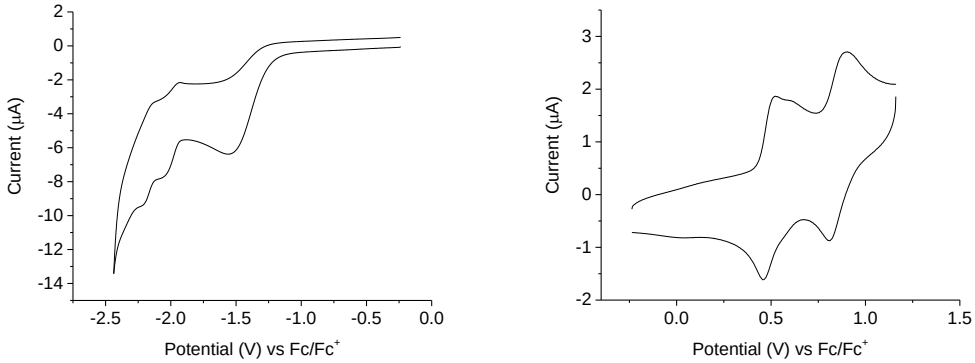

Figure 3.13 Reduction (left) and oxidation (right) of **NDO-3T-BF**

Table 3.1 UV/Vis absorption and cyclic voltammetry data

Compound	λ_{max} (nm)	$\lambda_{emission}$ (nm)	HOMO-LUMO (eV)[a]	HOMO (eV)[b]	LUMO (eV)[b]	E_{ox} (V)[c]	E_{red} (V)[c]
$(NDO)_2$-3T	477	536	2.30 (2.03)	-5.17	-3.14	0.51, ir	-1.50, ir -2.09/-1.78, qr
$(NDO-T)_2$-BT	516	609	2.09 (1.52)	-5.21	-3.69	0.51/0.35, qr 0.93/0.77, qr	-1.36, ir -1.65/-1.56, qr -1.94/-1.84
NDO-2T-BF	447	532	2.47 (1.65)	-5.25	-3.60	0.58 ir 0.84/0.68, qr	-1.46, ir -2.00/-1.89, qr -2.27/-2.17, qr
NDO-3T-BF	459	543	2.38 (1.69)	-5.24	-3.55	0.52/0.46 0.90/0.81	-1.55, ir -2.06/-1.94, qr -2.21/-2.13, qr

[a]The optical HOMO–LUMO gap is calculated from the onset of absorption. The electrochemical HOMO–LUMO gap calculated from the difference in HOMO and LUMO energy level and is shown in parentheses. [b]HOMO(LUMO) calculated from E HOMO(LUMO) = $(-4.80 - E_{onset}^{ox(red)})$. [c]The cathodic and anodic peaks are reported for reversible and quasi-reversible (qr) waves. The peak values on both forward and reverse scans are reported for reversible and quasi-reversible (qr) waves. The peak value on forward scan is shown for irreversible (ir) waves. The peak values are referenced to Fc/Fc+

3.3.4 OFETs

3.3.4.1 (NDO-T)2-BT

A study into the performance of OFET devices fabricated from $(NDO\text{-}T)_2$-BT was carried out. In order to maximise the performance, the effect of a number of parameters were investigated with respect to the device characteristics. These parameters were solvent, self-assembled monolayers and thermal annealing.

The prefabricated bottom gate, bottom contact devices with Au source and drain electrodes, n-doped Si gate electrode and SiO_2 dielectric were washed prior to deposition of SAMs. A 10 mg ml^{-1} solution of $(NDO\text{-}T)_2$ was prepared. The solution was spin-coated onto the surface at a spin-rate of 2000 rpm and left to dry at room temperature or anneal at 120°C. The output characteristics shows well-defined linear and saturation regions and the mobilities were calculated from the transfer curves in the saturation region. These values were calculated by fitting a straight line to V_{GS} vs $(I_{DS})^{1/2}$.

Firstly, the results for devices fabricated from *o*-dichlorobenzene solutions will be discussed. Pentafluorobenzenethiol (PFBT) was used as a SAM in each of the devices discussed, with OTS deposited on some of these. It is worth noting that devices spin-coated from o-dichlorobenzene solutions using OTS as the sole SAM were fabricated but gave a very poor response. The difference between devices that have and haven't been annealed will also be discussed in the results. A summary of the all device characteristics for OFETs fabricated with o-dichlorobenzene solution is shown in table 3.2.

Devices fabricated from **$(NDO\text{-}T)_2$-BT** solutions where chloroform is used as the solvent show overall higher hole mobilities than those spin-coated from *o*-dichlorobenzene solutions. The

results for these devices are generally improved and are shown in table 3.3 whilst results for devices fabricated using *o*-dichlorobenzene solutions are shown in table 3.2.

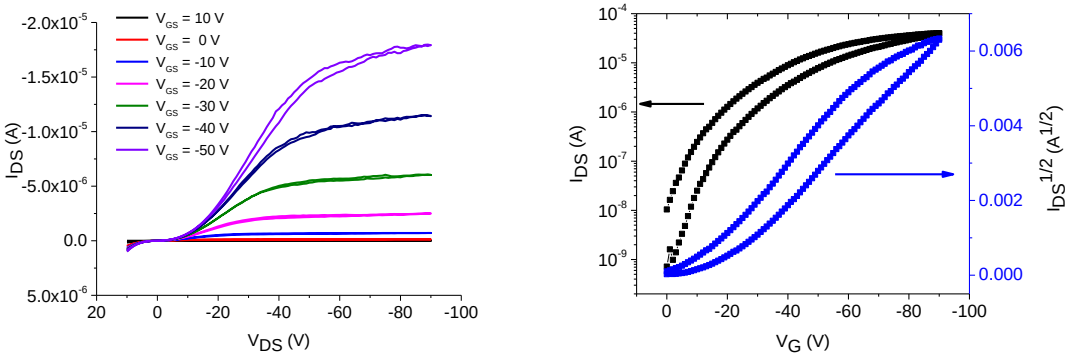

Figure 3.14. Output (left) and transfer (right) graphs. SAM = PFBT; solvent = *o*-dichlorobenzene; annealed at 120°C. Channel length = 5 µm; channel width = 1 cm.

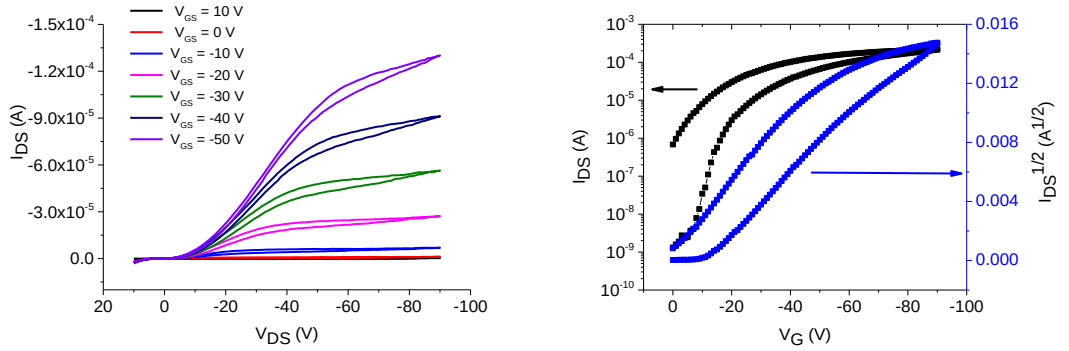

Figure 3.15. Output (left) and transfer (right) graphs. SAM = PFBT & OTS; solvent = *o*-dichlorobenzene; annealed at 120°C. Channel length = 5 µm; channel width = 1 cm.

A tapping-mode AFM image of the surface of OFET fabricated using PFBT and OTS SAMs with *o*-dichlorobenzene as the solvent used is shown below in figure 3.16. This image shows an uneven surface as a result of the use of *o*-dichlorobenzene as solvent, therefore there was no further optimization of the OFETs using this solvent.

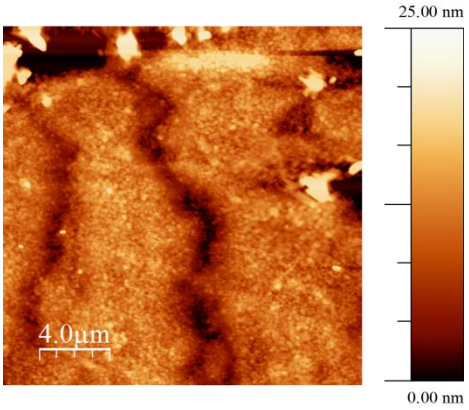

Figure 3.16. Atomic force microscopy image for surface of device fabricated using PFBT & OTS SAMs and *o*-dichlorobenzene solution.

Table 3.2. OFET characteristics of devices fabricated from *o*-dichlorobenzene

Solvent	**Self-assembled Monolayer**	**Annealing temperature (°C)**	**μ_h ($cm^2 V^{-1} s^{-1}$) average**	**ON/OFF ratio**	**V_T (V)**
o-DCB	PFBT	25	4.4×10^{-4}	10^4	-27
	PFBT/OTS	25	2.1×10^{-3}	10^4	-13
	PFBT	120	1.9×10^{-3}	10^4	-21
	PFBT/OTS	120	3.3×10^{-3}	10^4	-9

Chloroform was used instead of *o*-dichlorobenzene for the solution-processing and there was improvement in the OFET performance. The results of all devices fabricated from chloroform solutions are shown in table 3.3. If the optimum conditions for the OFET fabricated using *o*-dichlorobenzene are repeated using chloroform as the solvent instead then there is an increase in the hole mobility. Indeed, using PFBT (figure 3.17), PFBT/OTS (figure 3.18) and HMDS

(figure 3.19) SAMs in the fabrication of OFETs using chloroform as solvent for solution-processing, the resulting hole mobilities are similar in magnitude.

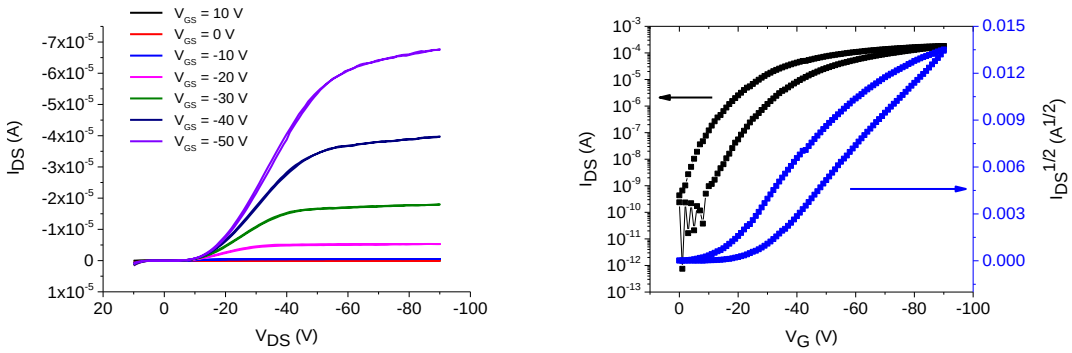

Figure 3.18. Output (left) and transfer (right) graphs. SAM = PFBT; solvent = $CHCl_3$; annealed at 120°C. Channel length = 10 µm; channel width = 1 cm.

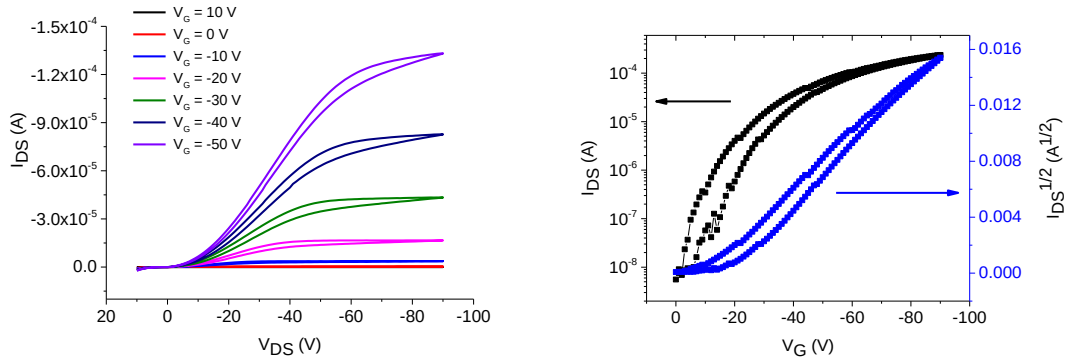

Figure 3.19. Output (left) and transfer (right) graphs. SAM = HMDS; solvent = $CHCl_3$; annealed at 120°C. Channel length = 10 µm; channel width = 1 cm.

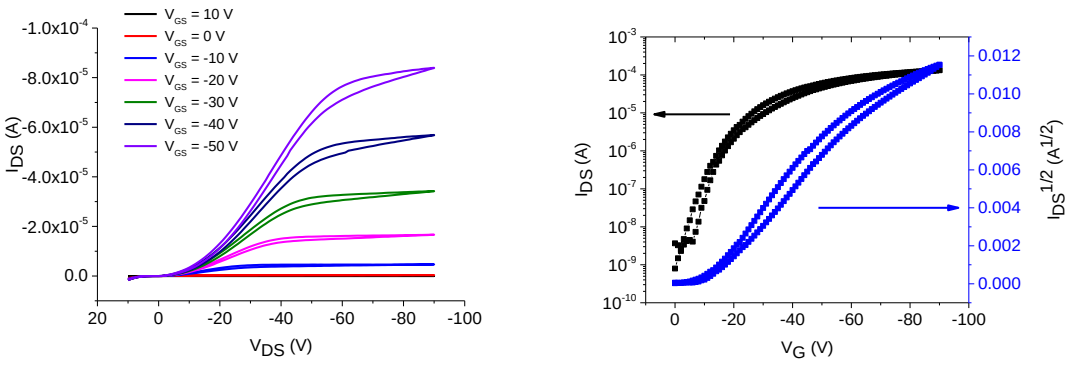

Figure 3.20. Output (left) and transfer (right) graphs. SAMs = PFBT & OTS; solvent = $CHCl_3$; annealed at 120°C. Channel length = 10 µm; channel length = 1 cm.

However the performance of $(NDO\text{-}T)_2$-BT based OFETs was further optimised by using OTS as the sole SAM. In fact, without annealing, the average hole mobility is calculated to be μ_h = 0.014 $cm^2\ V^{-1}\ s^{-1}$, significantly larger than any of the devices previously studied and If the device is annealed there is a further increase to μ_h = 0.022 $cm^2\ V^{-1}\ s^{-1}$. This suggests that the use of PFBT, which alters the work function of the gold electrodes, may increase the charge injection barrier for the OFET.

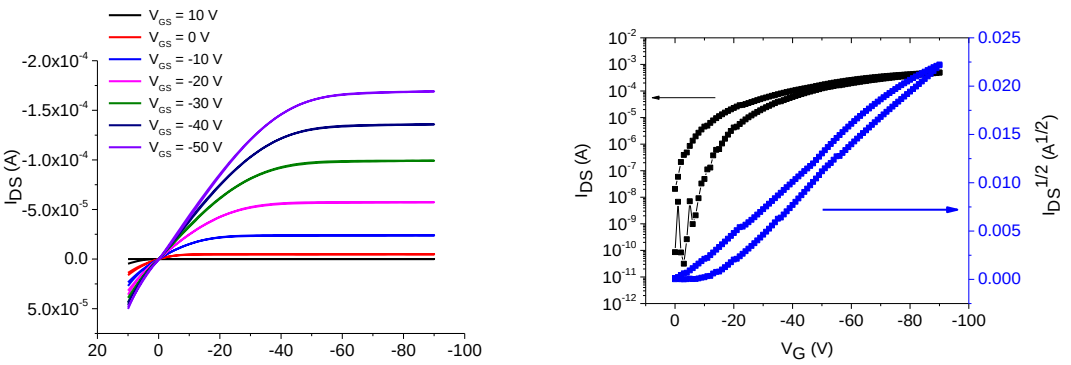

Figure 3.21. Output (left) and transfer (right) graphs. SAM = OTS; solvent = $CHCl_3$; unannealed. Channel length = 20 µm; channel width = 1 cm.

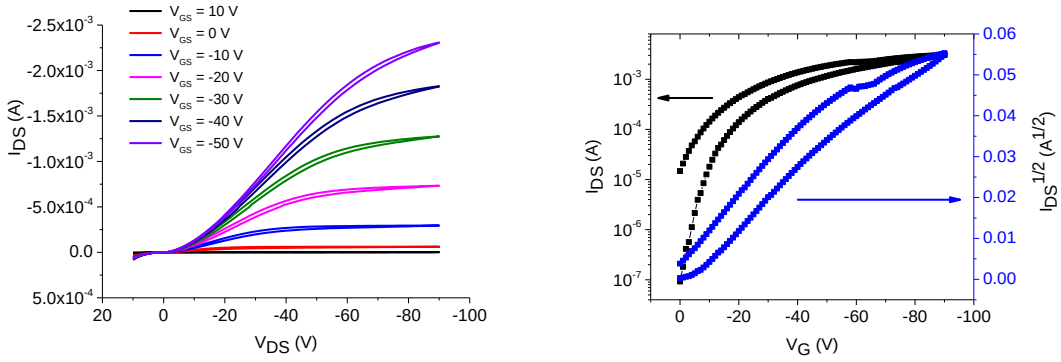

Figure 3.22. Output (left) and transfer (right) graphs. SAM = OTS; solvent = $CHCl_3$; annealed at 120°C. Channel length = 2.5 µm; channel width = 1 cm.

Table 3.3. OFET characteristics of devices fabricated from chloroform

Solvent	**Self-assembled Monolayer**	**Annealing temperature (°C)**	**μ_h ($cm^2\ V^{-1}\ s^{-1}$) average**	**ON/OFF ratio**	**V_T (V)**
$CHCl_3$	PFBT	25	3.6×10^{-3}	10^4	-22
	PFBT/OTS	25	2.3×10^{-3}	10^4	-21
	OTS	25	0.014	10^4	-28
	HMDS	25	5.5×10^{-3}	10^3	-34
	PFBT	120	4.6×10^{-3}	10^5	-20
	PFBT/OTS	120	4.7×10^{-3}	10^4	-12
	OTS	120	0.022	10^4	-16
	HMDS	120	3.9×10^{-3}	10^4	-28

Looking at AFM images, it is possible to explain the range of different performances resulting from different fabrication conditions. The surface of the device fabricated using both PFBT and OTS SAMs compared with that for the device fabricated using only OTS show similarities,

and although the RMS roughness of PFBT containing device is higher (6.7 vs 4.0 nm), it would seem that the reason for such deterioration in performance of the PFBT OFET can be explained by a charge injection barrier as a result of the modification of the work function of Au.

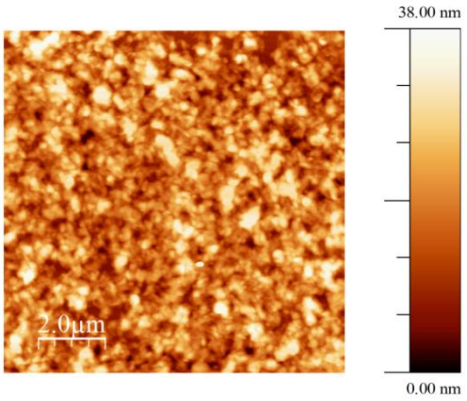

Figure 3.23. Atomic force microscopy image for surface of device fabricated using PFBT & OTS SAMs and $CHCl_3$ solution. RMS roughness = 6.3 nm

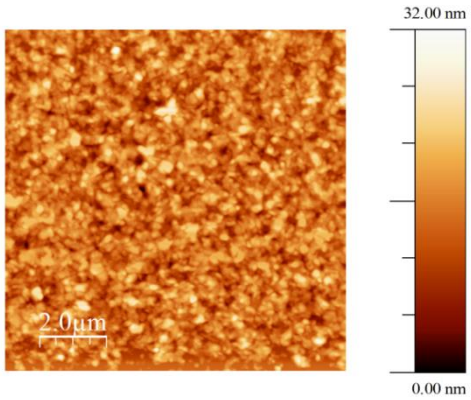

Figure 3.24. OFET fabricated using OTS SAM and film cast from $CHCl_3$ solution with annealing at 120°C. RMS roughness = 3.9 nm

AFM was also used in order to show the effect of annealing on the film morphology. The images of the annealed (figure 3.22) and unannealed (figure 3.23) devices show no obvious differences and the RMS roughness for each images is similar (4.0 and 3.8 nm respectively).

Although there is an increase in mobility as a result of annealing, the effect of this is not obvious from AFM image of the film. The additional thermal energy may improve interaction of (NDO-T)$_2$-BT with the electrodes or have an improvement in the orientation of the molecules.

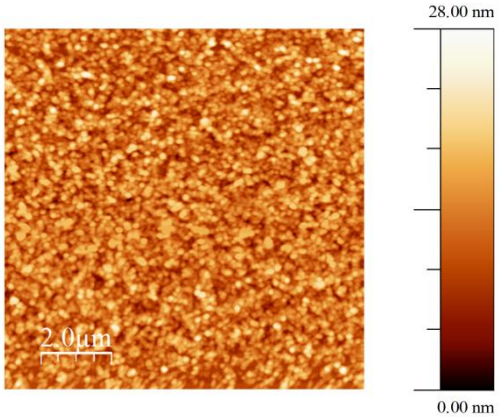

Figure 3.25. OFET fabricated using OTS SAMs and film cast from $CHCl_3$ solution without annealing. RMS roughness = 3.4 nm

3.3.4.1 NDO-2T-BF and NDO-3T-BF

OFETs were also fabricated using asymmetric compounds NDO-2T-BF and NDO-3T-BF. OTS was used as a SAM and the devices were not annealed on account of the low melting points for the two compounds. The performance of all OFETs tested was very poor with very few devices showing a field-effect. There was no mobility recorded for NDO-3T-BF. However NDO-2T-BF formed a working device and the output and transfer characteristics are shown below in figure 3.26.

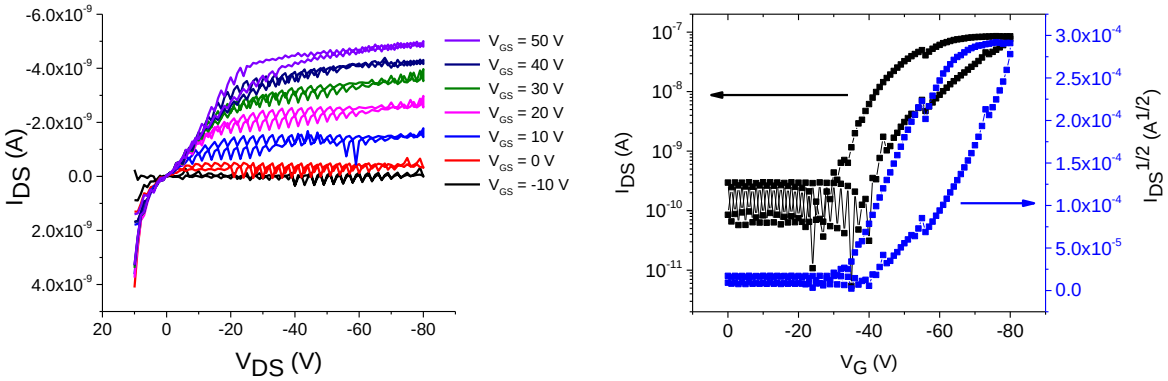

Figure 3.26. Output (left) and transfer (right) graphs for OFET fabricated using NDO-2T-BF. Channel length = 10 µm; channel width = 1cm.

The mobility calculated for this device was very low at 6.20×10^{-6} cm^2 V^{-1} s^{-1}, showing that NDO-2T-BF and NDO-3T-BF are poor materials for OFET devices.

3.3.5 OPV devices

Although $(NDO\text{-}T)_2$-BT shows good p-type mobility in OFET devices, the LUMO level of the material is similar to that of PCBM[124] suggesting that if this material is used as donor in a BHJ-OPV with a PCBM acceptor there will be poor charge separation. Therefore, given that the LUMO of $(NDO\text{-}T)_2$-BT is similar to that of PCBM, OPV devices were fabricated using $(NDO\text{-}T)_2$-BT as an acceptor material. The broad absorption of $(NDO\text{-}T)_2$-BT is also an advantage over PCBM. Although OFETs fabricated using the material showed no field-effect, this may be explained by the large injection barrier from gold to the LUMO of $(NDO\text{-}T)_2$-BT. By using this material as an acceptor in a BHJ-OPV, it is possible to determine whether it is effective as an n-type organic semiconductor.

OPV devices were fabricated according to the method described in chapter 6 with P3HT as a donor material and $(NDO\text{-}T)_2$-BT as an acceptor material at D: A ratios of 1:1, 1:2, 1:3 and 1:4 with a donor concentration of 10 mg ml^{-1} in *o*-dichlorobenzene. The results for each of the devices fabricated are summarised in table 3.4.

Overall, the use of $(NDO\text{-}T)_2$-BT as an acceptor material leads to OPV devices exhibiting poor PCEs. The highest performing device contains a 1:1 D: A ratio and results in a PCE of 0.02%. The output for this device is shown in figure 3.27. When the acceptor ratio is increased to twice that of the donor, the device shows a high V_{OC} of 0.87 V but there is a significant reduction in the J_{SC}. The high V_{OC} suggests there is effective charge transfer between donor and acceptor but the J_{SC} indicates poor charge transport. There is a further reduction in the PCE of the device fabricated using 1:3 ratio of D: A at 0.004% whilst a 1:4 ratio gives a slightly higher PCE at 0.006%. Despite the V_{OC} measured being particularly good in the device prepared with a 1:2 D:A ratio, with moderate values for devices formed with 1:3 and 1:4 ratios, the J_{SC} values determined in all the devices are very low and this indicates that $(NDO\text{-}T)_2$-BT is not a suitable n-type material.

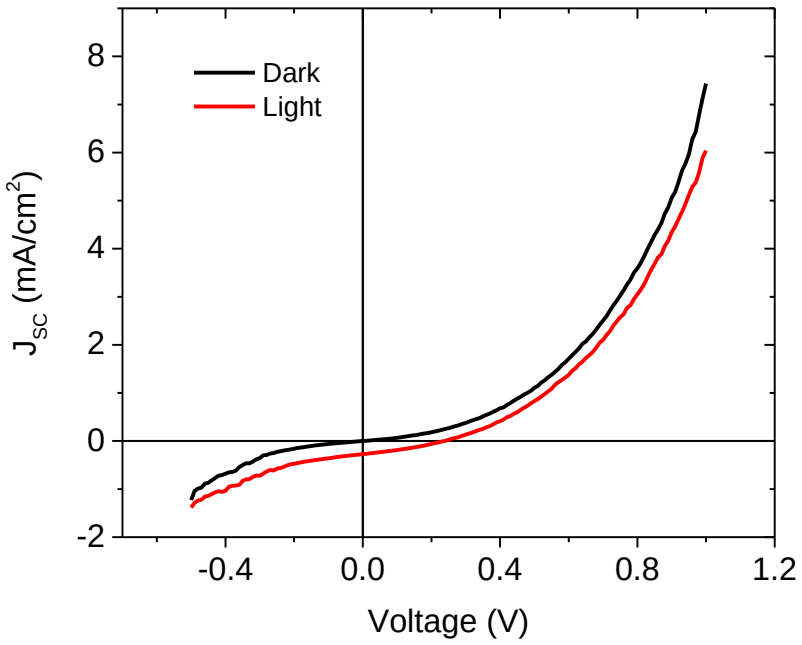

Figure 3.27. OPV results from P3HT/ $(NDO\text{-}T)_2$-BT (1:1 ratio) solution

Table 3.4. Summary of OPV results with $(NDO\text{-}T)_2$-BT as an acceptor material

Donor: Acceptor Ratio	V_{OC} (V)	J_{SC} (mA cm^{-2})	FF	PCE (%)
1:1	0.24	0.27	0.31	0.020
1:2	0.87	0.05	0.31	0.013
1:3	0.40	0.03	0.30	0.004
1:4	0.44	0.04	0.35	0.006

3.4 Conclusions/Future Work

In this chapter we have presented the synthesis of 4 novel compounds containing the novel 1-dodecyl-6-dodecoxynaphthyridine-2-one acceptor unit, an isomer of the ND unit used in chapter 2. These compounds were based on two general structures: symmetric compounds $(NDO\text{-}T)_2$-BT and $(NDO)_2$-3T and asymmetric compounds NDO-2T-BF and NDO-3T-BF.

During the testing of OFET devices fabricated from both $(NDO\text{-}T)_2$-BT and NDO-2T-BF, light emission was noticed in the higher performing devices made from these compounds and this is shown below in figure 3.28.

Figure 3.28. Images showing light emission (centre) from OFET fabricated from $(NDO\text{-}T)_2$-BT

It is possible that the hole mobility of $(NDO\text{-}T)_2$-BT could be further increased when applied to an OFET with a different architecture as there are examples of OFET mobility increasing as a result of using a top-gate bottom-contact OFET.[125] Although $(NDO\text{-}T)_2$-BT was not used successfully as an acceptor material in OPV devices, it is possible that it could act as an n-type material. The large difference between the work function of gold and the LUMO of $(NDO\text{-}T)_2$-BT (-5.1 and -3.69 eV respectively) suggests that the charge injection barrier would be too large for an effective n-type OFET. If a lower work function electrode was used, a lower injection barrier may contribute to a working device. An example of a more suitable electrode for this material could be a thiophenol modified silver electrode which has a reported work function of -4.14 eV.[126]

Chapter 4 – Investigation Into the Effect of Kesterite-based Nanoparticles in the Fabrication Solution-processable OFETs

4.1 Abstract

The addition of oleylamine coated Cu_2ZnSnS_4 (CZTS) nanoparticles to solutions of organic semiconductor prepared for Organic Field-effect Transistors (OFETs) *via* solution-processing has been studied. The nanoparticles were used without any further functionalisation or treatment to remove the capping ligand. OFETs were fabricated using the oligothiophene based small molecule 5T-TTF or the polymer poly(3-hexylthiophene) (P3HT) with various concentrations of CZTS to optimise charge carrier mobility. Atomic force microscopy (AFM) was used to characterise the surface morphology of the OFETs. The use of 5 and 10 wt% of the CZTS nanoparticles in 5T-TTF and P3HT solutions respectively appears to be a simple and effective way of improving OFET performance.

4.2 Introduction

In the efforts to enhance the performance of organic electronics, the use of additives to organic semiconductors has been studied. In chapter 1 the effect of additives such as DIO, chloronaphthalene and even polystyrene on improving the performance of OPV devices was discussed. The principle way that these additives improve the device performance of OPV devices is by optimising the bulk-heterojunction morphology.

Although heterojunctions can be applied to OFETs, such as a P3HT/PCBM blend typically used for solar cells,[127] most are fabricated using a single organic semiconductor material. However, additives have also been used with organic semiconductors materials in OFET devices in order to improve charge carrier mobility. For example, Heeney *et al*[128] used a blend of insulating poly(α-methyl styrene) with a DPP-based n-type material which increased vertical phase separation and induced favourable crystallisation of the DPP material, whilst Russel *et al*[129] showed that a blend of P3HT with quaterthiophene material D4HT improved field-effect mobility by an order of magnitude, again explained by crystallisation in the film. Attempts have also been made to further improve the charge carrier mobility of OFETs by providing more effective pathways for charge transport by using materials such as graphene[130, 131] or carbon nanotubes[132-134] in conjunction with the organic semiconductor material, whilst trying to maintain properties such of the I_{ON}/I_{OFF} ratio.

In this chapter we present a novel approach to enhancing the charge-carrier mobility in OFET devices by using kesterite nanoparticle additives. The nanoparticles

Cu_2ZnSnS_4 (CZTS), Cu_2FeSnS_4 (CFTS) and $Cu_2(ZnFe)SnS_4$ (CZFTS) were synthesised and characterised by Punarja Kevin from the Paul O'Brien group (University of Manchester) according to a previously reported procedure.[135] These nanoparticles were capped with oleylamine ligands. Often nanoparticles are processed in a ligand-exchange solution, with the long ligands of the nanoparticles exchanged for shorter ligands such as butylamine[136] ethanedithiol[137] or benzenedithiol,[138] in order to reduce the distance between particles. However, in this study we show that the kesterite nanoparticles capped with long ligands can be used in improving the performance of electronic devices. The simple addition of these nanoparticles to organic semiconductor solutions reduces the need for the complex processing techniques or toxic ligands normally required.

Kesterites such as CZTS have attracted considerable interest recently[139-141] because they are composed of elements of low toxicity that are largely abundant in the earth meaning these particles are relatively environmentally benign. In addition to their good absorption characteristics such as broad absorption spectra and tunable band gaps, kesterite nanoparticles exhibit good charge transport and have been used in devices such as field-effect transistors (FETs) with good performance.[141]

The organic materials selected for this study were 5T-TTF, first synthesised and characterised by Wright *et al*[142] and the much-studied polymer P3HT, both of which are solution-processable, exhibit good p-type mobility and provide a good benchmark. The 5T-TTF used in this study was synthesized by Rupert Taylor and Neil Findlay (University of Strathclyde, Prof Skabara group).

4.3 Results and Discussion

In order to understand the effect of the QD additive, the conditions for the fabrication of OFETs using 5T-TTF were consistent with those previously reported,[142] with the addition of differing amounts of kesterite nanoparticles the only variable. All OFETs fabricated using P3HT were made using PFBT and OTS SAMs and by spin-coating a 5 mg ml^{-1} solution of the polymer with varying amounts of nanoparticles onto the substrate and annealing at 150°C. Every OFET fabricated was spin-coated from a solution which had been subject to ultra-sonication for 20 minutes. It is worth noting that 10 mg ml^{-1} P3HT solutions were used but the resulting film was too thick to view the source and drain contacts and determine the channel length. Given that many QDs exhibit good electron mobility,[143, 144] the devices were tested for n-type mobility although this was not observed. For all OFETs studied an average of the results was based on 6 devices (the maximum number of devices for one solution tested was 12). This was taken as some devices short-circuited during testing or did not show saturation in the output and therefore were not suitable to be included. The standard deviation (σ) derived from the average results was also presented for each OFET. This was to demonstrate the consistency of the OFET properties as it was possible that any potential improvement could be limited to certain regions of the OFET given that such a small amount of quantum dots was used in the device fabrication.

The results for the OFETs fabricated using 5T-TTF are shown below in table 6.1. The average hole mobility measured for 5T-TTF was 9.5×10^{-3} cm^2 V^{-1} s^{-1}, which is

consistent with previously reported data (μ_h = 8.6 × 10^{-3} cm^2 V^{-1} s^{-1}).[142] The output and transfer characteristics for this device are shown below in figure 4.1.

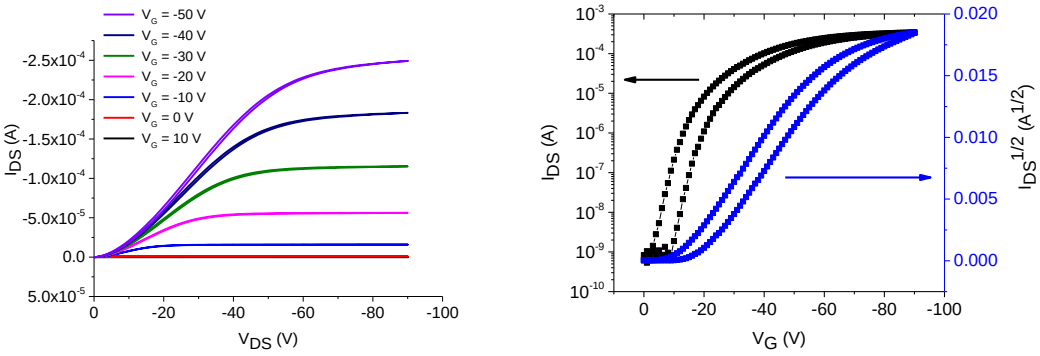

Figure 4.1 Output (left) and transfer (right) characteristics for OFET fabricated using 5T-TTF. Channel length = 10 µm; channel width = 1 cm.

The inclusion of both 5% CFTS or CZFTS is detrimental to the performance of the OFET with the hole mobility of devices containing of either QD decreasing with respect to that of the OFET fabricated using only 5T-TTF, although devices fabricated using 5% CFTS solution only show a small reduction in mobility. The standard deviation is larger than calculated average mobility, highlighting a large variation in results, possibly due to poor film uniformity. Only one device was fabricated with 5% CZFTS, devices tended to short-circuit at V_{DS} where the linear region would be expected to occur. The output and transfer characteristics for the OFETs fabricated using 5% CFTS and CZFTS are shown below in figure 4.2 and 4.3 respectively. As the concentration of these quantum dots is increased to 10%, there is a substantial decrease in performance – almost an order of magnitude for both quantum dots.

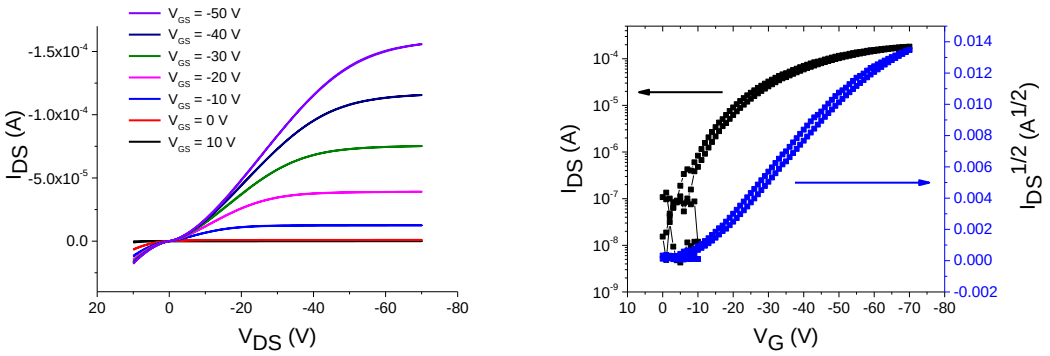

Figure 4.2 Output (left) and transfer (right) characteristics of OFET fabricated using 5T-TTF and 5% CFTS. Channel length = 10 µm; channel width = 1 cm.

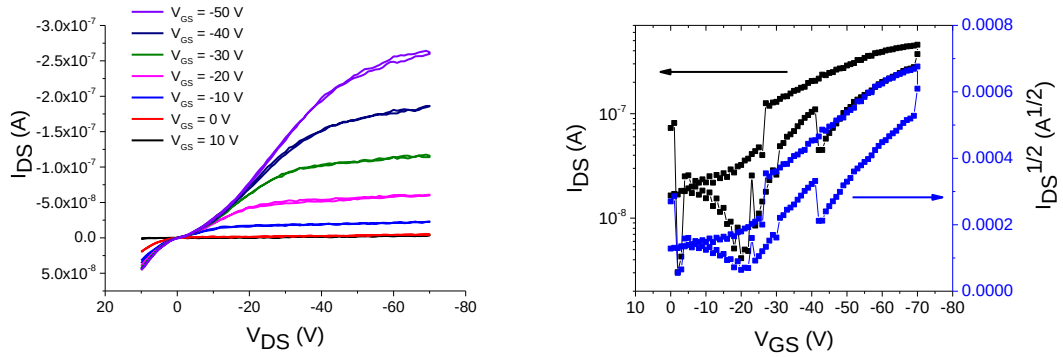

Figure 4.3 Output (left) and transfer (right) characteristics of OFET fabricated using 5T-TTF + 5% CZFTS. Channel width = 20 µm; channel width = 1 cm.

However, the use of 5T-TTF solution containing 5% CZTS results in a large increase in the average hole mobility of 89%. The output and transfer characteristics for this device are shown below in figure 4.4. The standard deviation for the mobility of the devices tested is lower than for the devices fabricated using only 5T-TTF, showing that the addition of 5% CZTS results in a smaller variation in results. The improved performance as result of the addition of 5% CZTS lead to further studies into the addition of this quantum dot at different concentrations. At concentrations of 1% and

2.5%, the average mobility is similar with respect to the two sets of devices fabricated and the performance of these is slightly reduced with respect to the pure 5T-TTF containing OFET. At a higher concentration of 10% CZTS, the devices were unstable and prone to short-circuiting. This will be addressed when discussing the AFM images.

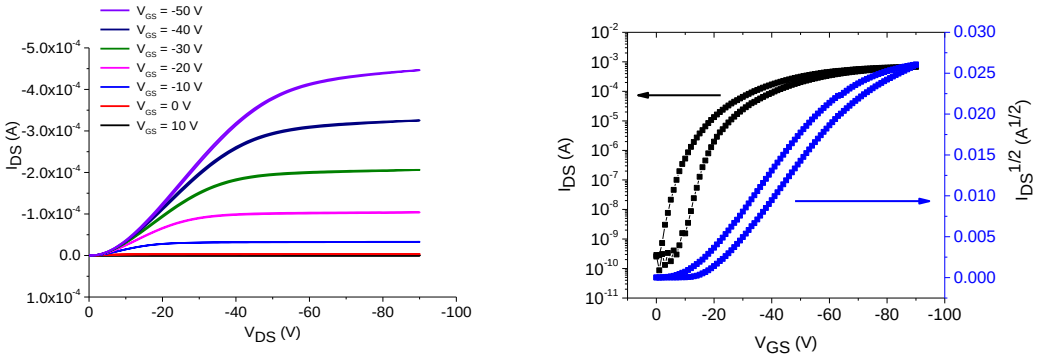

Figure 4.4. Output and transfer characteristics for OFET fabricated with 5T-TTF + 5% CZTS. Channel length = 5 μm; channel width = 1 cm.

The increase in QD concentration to 10% results in a significant drop in performance of the OFET, irrespective of the QD used, suggesting the increase in QD concentration inhibits charge transport through the organic semiconductor.

Table 4.1. Results for OFETs fabricated from 5T-TTF with CFTS and CZFTS

Compound	V_{Th} (V)	ON/OFF	μ_{hole} ($cm^2\ V^{-1}\ s^{-1}$)	$\sigma\ \mu_{hole}$
5T-TTF	-13	10^3	9.5×10^{-3}	5.8×10^{-3}
5T-TTF + 5% CFTS	-18	10^3	7.8×10^{-3}	8.4×10^{-3}
5T-TTF + 5% CZFTS	-10	10^1	1.2×10^{-5}	n/a
5T-TTF + 10% CFTS	-9	10^1	9.2×10^{-4}	5.9×10^{-4}
5T-TTF + 10% CZFTS	+10	10^1	4.4×10^{-6}	n/a

Table 4.2 Results for OFETs fabricated from 5T-TTF with CZTS

Compound	V_{Th} (V)	ON/OFF	μ_{hole} (cm^2 V^{-1} s^{-1})	σ μ_{hole}
5T-TTF	-13	10^3	9.5×10^{-3}	5.8×10^{-3}
5T-TTF + 1% CZTS	-17	10^3	8.5×10^{-3}	3.8×10^{-3}
5T-TTF + 2.5% CZTS	-17	10^3	8.3×10^{-3}	4.6×10^{-3}
5T-TTF + 5% CZTS	-15	10^3	0.018	4.6×10^{-3}
5T-TTF + 10% CZTS	–	–	–	–

In order to investigate the OFET performance further, atomic force microscopy (AFM) was used in tapping mode in order to characterise the surface morphology of the different devices. The surfaces of devices fabricated using solely 5T-TTF, 5%CZTS and 10% CZTS are shown in figure 4.5. The surface of the OFET fabricated using 5T-TTF solution is comparable to the image of the surface from the previously fabricated device.[142] Surprisingly, in spite of the surface of the device fabricated with 5 wt% CZTS being rougher, the hole mobility increases. This would suggest that although the surface may not be a smooth, there is improved charge transport with the addition of the nanoparticles. As the concentration of CZTS is increased to 10%, there is a significant change in morphology with the 5T-TTF domains being broken up. The emergence of a number of gaps in the film may explain the reason for the short-circuiting in these devices.

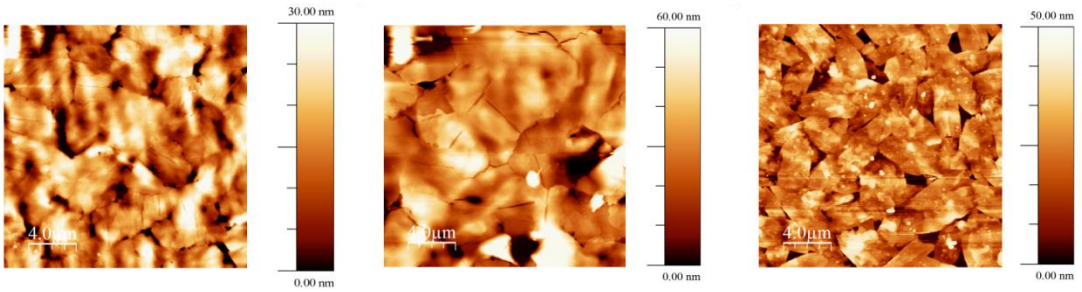

Figure 4.5. AFM images of OFETs fabricated from 5T-TTF (left), 5T-TTF + 5% CZTS (centre) and 5T-TTF + 10% CZTS (right)

The quantum dots were also applied to OFET devices fabricated using the polymer P3HT. Despite the fact that adding CFTS and CZFTS did not improve any OFET devices when used with 5T-TTF, these nanoparticles were studied at 5% concentration to see if this trend was also observed in OFETs fabricated using P3HT the results for these OFETs are presented in table 4.3. The average hole mobility for OFETs fabricated using P3HT is 0.041 $cm^2 V^{-1} s^{-1}$, which comparable to P3HT OFETs made previously.[145] When 5% CFTS is added to the solution, the resulting OFET has a mobility of 0.021 $cm^2 V^{-1} s^{-1}$ and if 5% CZFTS is used the mobility is 0.022 $cm^2 V^{-1} s^{-1}$. These mobilities show a deterioration in performance as a result of the use of these additives and because of this and the failure to improve the 5T-TTF OFETs, these quantum dots were not subject to further studies.

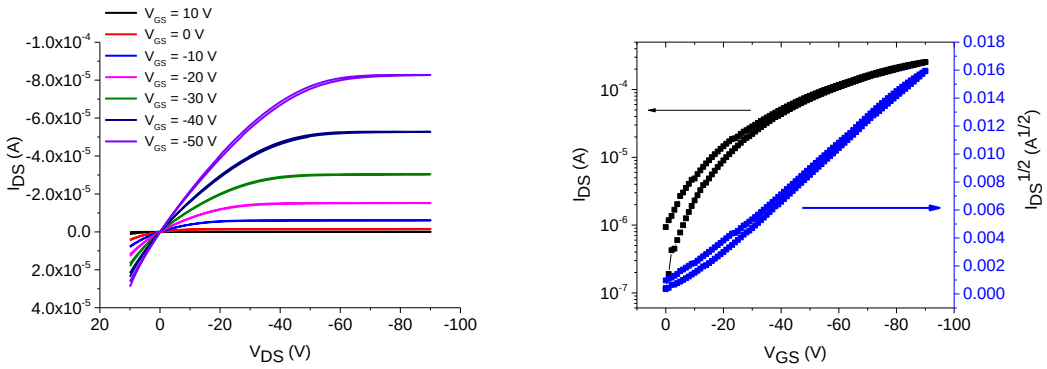

Figure 4.6 Output (left) and transfer (right) characteristics for OFET fabricated using P3HT. Channel length = 20 µm; channel width = 1 cm.

In contrast, the 5% CZTS solution, this time with P3HT as the OSC, again shows increased performance with respect to the OFET fabricated using the OSC alone. The average hole mobility was measured to be 0.053 cm^2 V^{-1} s^{-1}, which is a 29% increase with respect to the P3HT OFET. The consistency of the improved mobilities is also demonstrated by the reduction in standard deviation of mobility as a result of the addition of 5% CZTS. These results along with all those from devices containing CZTS are summarised in table 4.4. Although the percentage increase is smaller than that exhibited for the 5% CZTS 5T-TTF OFET, the magnitude of the increase is larger. The fact that the use of CZTS with two different OSC materials results in a significant increase in hole mobility, suggests that this QD has the potential to be applied as an additive for the improvement in performance of OFETs.

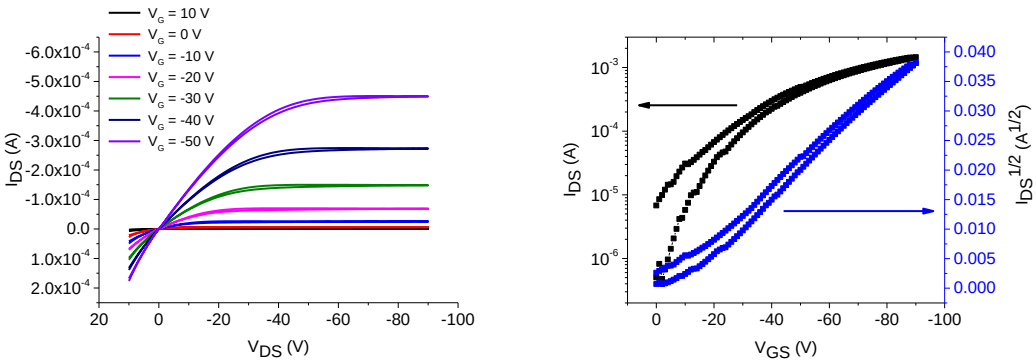

Figure 4.7 Output (left) and transfer (right) characteristics for OFET fabricated using P3HT + 5% CZTS. Channel length = 20 µm; channel width = 1 cm.

Moreover, unlike the oligomer based OFETs where 10% CZTS lead to a deterioration in performance, OFETs fabricated with P3HT and 10% CZTS show a further increase in charge carrier mobility, with the average mobility calculated as 0.088 $cm^2\ V^{-1}\ s^{-1}$, 114% increase compared to the device fabricated using only the polymer. Again the standard deviation for mobility is reduced with respect to that for devices containing only P3HT. A further increase in nanoparticle concentration to 15% and 20% shows charge carrier mobilities only slightly lower than the OFET fabricated with a neat P3HT film, showing that the polymer is substantially less sensitive the addition of nanoparticles with respect to the 5T-TTF oligomer.

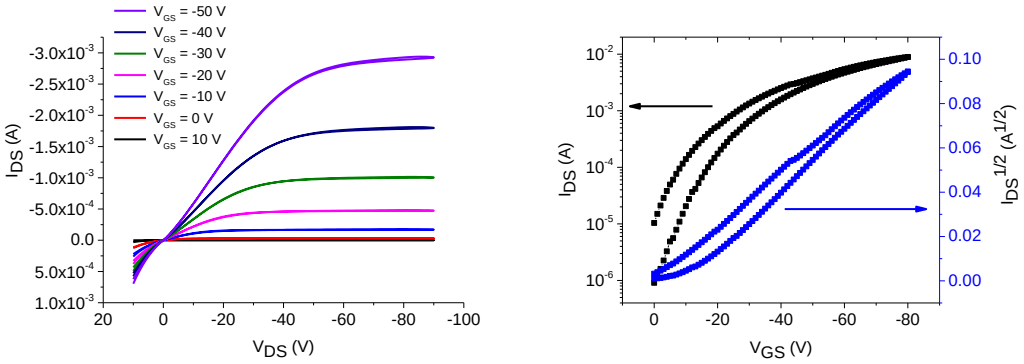

Figure 4.8 Output (left) and transfer (right) characteristics for OFET fabricated using P3HT + 10% CZTS. Channel length = 5 µm; channel width = 1cm.

Table 4.3 Results for OFETs fabricated from P3HT with CFTS and CZFTS

Compound	V_{Th} (V)	ON/OFF	μ_{hole} (cm^2 V^{-1} s^{-1})	σ μ_{hole}
P3HT	-8	10^2	0.041	0.015
P3HT +5% CFTS	-14	10^2	0.021	0.015
P3HT + 5% CZFTS	-24	10^1	0.022	0.010

Table 4.4 Results for OFETs fabricated from P3HT with CZTS

Compound	V_{Th} (V)	ON/OFF	μ_{hole} (cm^2 V^{-1} s^{-1})	σ μ_{hole}
P3HT	-8	10^2	0.041	0.015
P3HT + 5% CZTS	-9	10^2	0.053	0.012
P3HT + 10% CZTS	-10	10^2	0.083	0.013
P3HT + 15% CZTS	-10	10^2	0.037	9.6×10^{-3}
P3HT + 20% CZTS	-10	10^2	0.033	0.016

The AFM images for P3HT shown in figure 4.10 devices show a clearer trend. The device fabricated using P3HT shows a number of polymer aggregates on the surface. As 5 wt% CZTS is added to the solution, the resulting device still shows the P3HT aggregates although it appears that the number is reduced. There is also a smoothening of the surface as a consequence of the P3HT aggregates being broken up. There is a further reduction in the surface roughness as the CZTS concentration is increase to 10% and there appears to be a significant decrease in the size of any P3HT aggregates. The domain sizes are slightly larger when 15% CZTS is added and the surface is rougher than 10% nanoparticle concentration but the aggregates are smaller than those present in the neat polymer film. This suggests that, although the P3HT aggregates are being broken up in films formed from 15% and 20% CZTS solutions, charge transport is inhibited by the increased nanoparticle concentration and therefore leads to a charge carrier mobility that is slightly reduced with respect to OFETs fabricated using P3HT. It is interesting that the OFET performance does not tail off as significantly as when the CZTS concentration is increased for 5T-TTF containing OFETs.

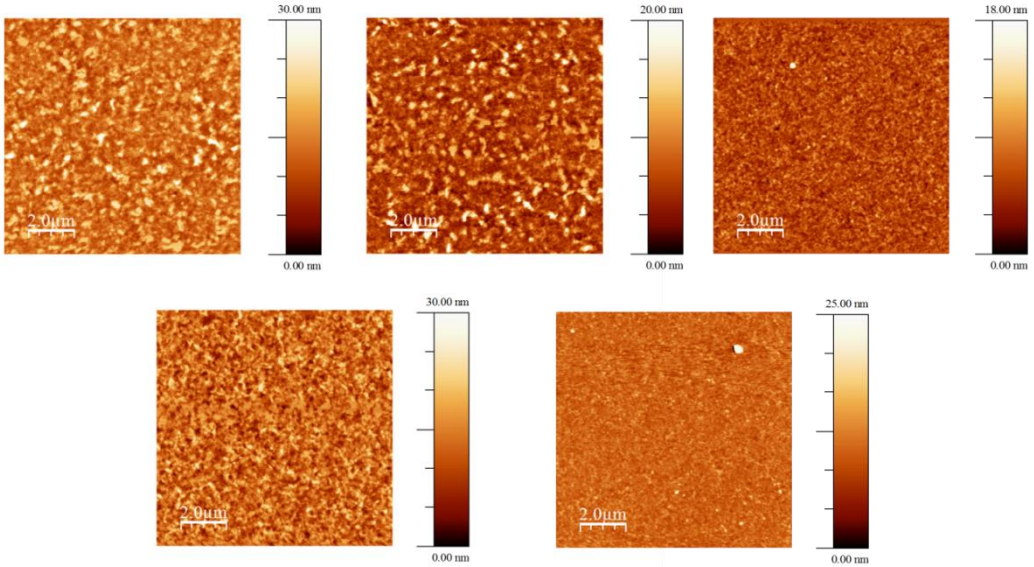

Figure 4.9 AFM images for OFETs fabricated using P3HT (top, left), P3HT + 5% CZTS (top, centre), P3HT + 10% CZTS (top, right), P3HT + 15% CZTS (bottom, left) and P3HT + 20% CZTS (bottom, right)

Finally, in an attempt to determine whether the nanoparticle is mainly responsible for the improved performance or whether this can be attributed to the long oleyl amine ligands, P3HT OFETs were fabricated using 5 v/v% and 10 v/v% oleyl amine and the output and transfer characteristics for each of these OFETs are shown in figure 4.10 and 4.11 respectively. The mobilites calculated for these devices are shown in table 4.5. The addition of 5% oleyl amine lead to a severely reduced mobility and although this is improved with 10% oleyl amine, the performance of these devices is considerably poorer than any of the devices fabricated using P3HT and CZTS. This would suggest that the quantum dot is responsible for improving the OFET performance rather than the long oleyl amine ligands.

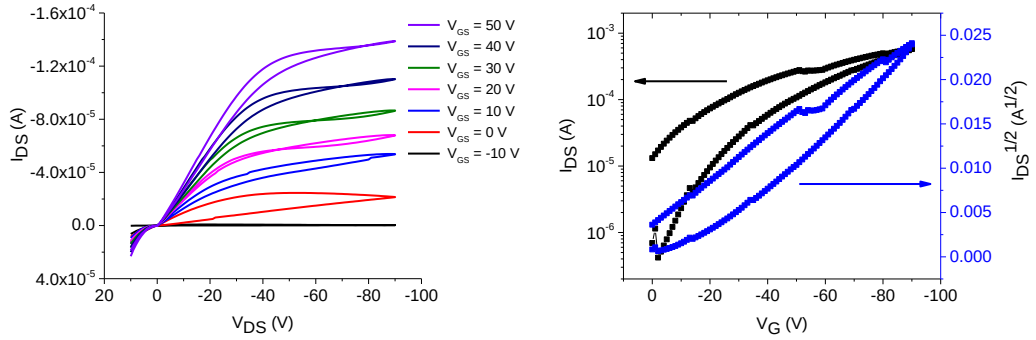

Figure 4.10 Output (left) and transfer (right) graphs for devices fabricated with P3HT and 5% oleyl amine. Channel length = 5 µm; channel width = 1 cm.

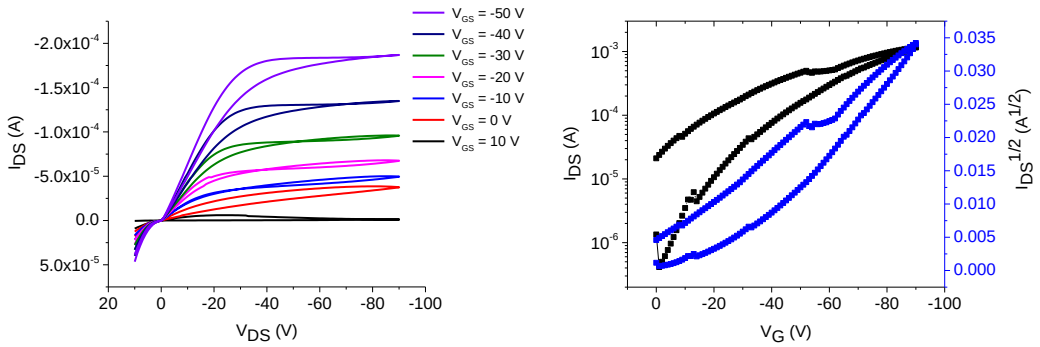

Figure 4.11 Output (left) and transfer (right) graphs for devices fabricated with P3HT and 10% oleyl amine. Channel length = 5 µm; channel width = 1 cm.

Table 4.5 Mobilities calculated for devices fabricated using P3HT and oleyl amine

Compound	μ_{hole} ($cm^2\ V^{-1}\ s^{-1}$)
P3HT + 5% Oleyl amine	2.83×10^{-3}
P3HT +10% Oleyl amine	6.07×10^{-3}

4.4 Conclusions

The synthesis and characterisation of oleylamine capped CZTS nanoparticles has been presented and these particles were used as additives in the solution-processed fabrication of OFETs. Using CZTS with 5T-TTF resulted in a hole mobility that was 68% higher than any devices previously fabricated using only the oligomer, whilst the addition of the nanoparticles to P3HT solutions was responsible for a 114% increase in the hole mobility compared to the OFET fabricated using neat P3HT. The simple, low-cost nature of the synthesis of the CZTS particles, without any ligand exchange, and the significant enhancement of charge carrier mobility achieved suggests that these nanoparticles have great potential in the improvement of OFETs and perhaps other organic electronic devices.

The use of inorganic nanoparticles in OFETs is not widely studied in the literature and has been mainly limited to their use as nanocomposites in gate dielectric layers.[146, 147] Zinc oxide nanoparticles have been used in polyfluorene composites for light-emitting field effect transistors,[148] whilst ZnO has been applied as a component in a hybrid OFET bilayer device fabricated with P3HT as the organic semiconductor.[149] Blends of P3HT and CdSe have been studied in OFETs[150] and also in organic photovoltaics devices.[151] However, the mechanism of charge transport in these composites is not well understood. It has been shown by low temperature light-induced electron spin resonance studies that there is a change in the morphology of P3HT in the presence of CdSe nanoparticles[150] and that charge transfer between the two components only takes place efficiently if the CdSe capping ligand is removed. The structure of the capping

ligand in P3HT/CdSe composites influences the value of the mobility.[151] This begs the question whether or not the inorganic nanoparticles in hybrid OFETs change the characteristics of the device as a function of morphology or if the role of the inorganic material is more complex. It is perhaps more intuitive to assume the former and the AFM images in figures 4.5 and 4.9 show that morphology changes under different loads of CZTS nanoparticles. However, a more in-depth study is required to determine what the exact role of CZTS in these composites is and it is necessary to observe if there is any electronic coherence between the organic-inorganic components that leads to truly hybrid charge transport.

One would expect that the inclusion of nanoparticles into pristine molecular (5T-TTF) and polymeric (P3HT) materials would disrupt long-range order and affect charge transport detrimentally, yet remarkably we see an increased hole mobility upon the application of CZTS nanoparticles. One possible explanation is that the inorganic material reduces the density of traps in the organic layer and this has been seen in the case of MEH-PPV/ZnO blends, where recombination of charge carriers is less likely to occur.[152]

4.5 Future Work

As mentioned in section 4.4, it is necessary to determine the exact function of the CZTS nanoparticles in the organic/inorganic blend. It is possible that preparing the nanoparticles in a ligand-exchange solution in order to reduce the length of ligands may give an insight into whether the morphological effect of the long ligands has the greatest influence on the performance of the organic/nanoparticle OFETs.

It is possible that organic semiconductors can be functionalised into a ligand to bind to the nanoparticles although a study from Skabara *et al*[153] showed that sexithiophene based compounds with alkyl end groups were able to quench luminescence from CdSe quantum dots as well as analogous compounds with Lewis base end groups. However, any binding of Lewis base functionalized organic semiconductors with inorganic nanoparticles may further improve the performance of OFETs by improving the order in the films. Through a bound organic/nanoparticle complex it may also be possible to use a larger amount of QDs without disrupting the charge transport and this could also be a means of improving the mobility of the OFET.

Chapter 5- Donor-Acceptor Compounds Thieno[3,2-b]thiophene-2,5-dione and Furo[3,2-b]furan-2,5-dione Accepting Units

5.1 Abstract

In this chapter, the synthesis of donor-acceptor compounds based on the analogous cores – thieno[3,2-b]thiophene-2,5-dione (TTD) and furo[3,2-b]furan-2,5-dione (FFD) is presented. The TTD core is coupled with the functionalised terthiophene donor arms and the optical and electrochemical properties of this compound are compared with previously synthesised TTD containing compounds. The stable electrochemical reductions of the compound in addition to the low LUMO level suggest that this compound could be applied as an effective n-type material; the broad absorption exhibited particularly desirable in a potential acceptor material for solar cells.

The synthesis of the novel 3,6-bis(thiophen-2yl)furo[3,2-b]furan-2,5-dione core is shown before this core was brominated in preparation for Pd-catalysed cross coupling reactions. The resulting compound formed was characterised by UV/Vis absorption and cyclic voltammetry and these results were compared with compounds based on the analogous TTD core.

5.2 Introduction

The success of DPP-based compounds in their application in organic semiconductor materials has led to the development of structural analogues. For example, Facchetti et al[154] have reported polymers synthesised containing the iso-DPP unit (figure 5.1). The change in position of the ketone groups actually leads to an increase in band gap in these polymers with respect to the DPP analogues and this is explained by a deeper HOMO level. DFT calculations show that there is little delocalisation of the HOMO across the nitrogen of iso-DPP, with the reduced delocalisation of iso-DPP contributing to its lower HOMO.[154] However, in this incidence, the deeper LUMO in the polymers contribute with to a higher V_{OC} and in fact substitution of DPP with iso-DPP results in an increased PCE in 1 out of the 2 analogues studied[154]. This highlights the how even small changes in chemical structure can make a large impact on performance of organic semiconductor materials.

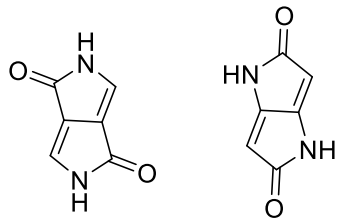

Figure 5.1. Structures of DPP (left) and iso-DPP (right)

The exploration of materials analogous to DPP however, has not only been limited to isomers. Attempts have been made to maintain the fused diketo-pentalene-type structure whilst including a different heteroatom to nitrogen. Indeed, a few years before the first OPV device had been published, the first thieno[3,2-b]thiophene-2,5-

dione compound was reported by Martelli *et al*[155], with further compounds based on the same unit described in a later paper[156]. However, it wasn't until Kobayashi *et al*[157] and Hünig *et al*[158] researched synthesis and electrochemical properties of thieno[3,2-b]thiophene-2,5-dione based compounds that these were described as acceptors, with cyclic voltammetry showing two reversible reductions. Despite this, the intensive research into donor-acceptor compounds has mostly eluded thieno[3,2-b]thiophene-2,5-dione. In 2011, the first example of such compounds being applied to organic semiconductor devices was reported[159] with OFETs fabricated showing 0.039 $cm^2 V^{-1} s^{-1}$ electron mobility. Interestingly, when the ketone groups are replaced with dicyanomethylene groups the electron mobility decreases by 3 orders of magnitude but the devices show improved air stability.[159] More recently Takimiya *et al*[160] reported the synthesis of two thieno[3,2-b]thiophene-2,5-dione based polymers which are used to fabricate OFETs which display good ambipolar mobilities, highlighting the potential this acceptor has in organic semiconductor devices.

Whilst it is evident that sulphur-containing iso-DPP analogues can be applied to high performing organic semiconductor devices in the future, it may be expected that furo[3,2-b]furan-2,5-dione based compounds can emulate the performance of the chalcogen containing analogue. Interestingly, diphenylfuro[3,2-b]furan-2,5-dione (pulvinic dilactone) has been found to be a component of some lichen species[161] though in an organic semiconductors context, there has been limited research. A study carried out by Hdina *et al*,[162] suggested that although the absorption furofuran-dione structure analogous to diphenyl-DPP is blue-shifted with respect to DPP, the absorption of structure analogous to iso-DPP is red-shifted with respect to diphenyl-iso-DPP. However the "iso" structures are blue shifted with respect to the DPP

structures as a result of reduced planarity.[162]

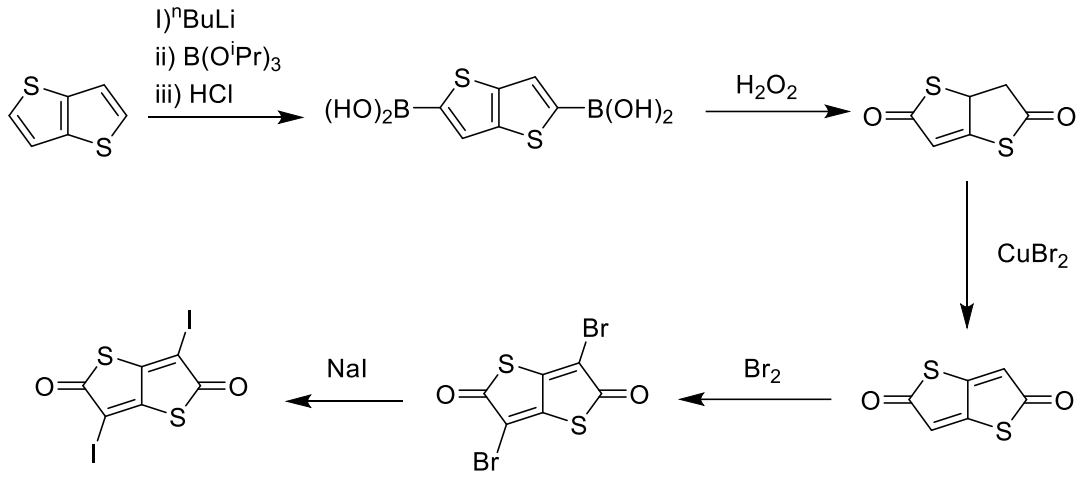

Scheme 5.1. Synthesis of 3,6-diiodothieno[3,2-b]thiophene-2,5-dione based on method reported by Günther and Hünig[158]

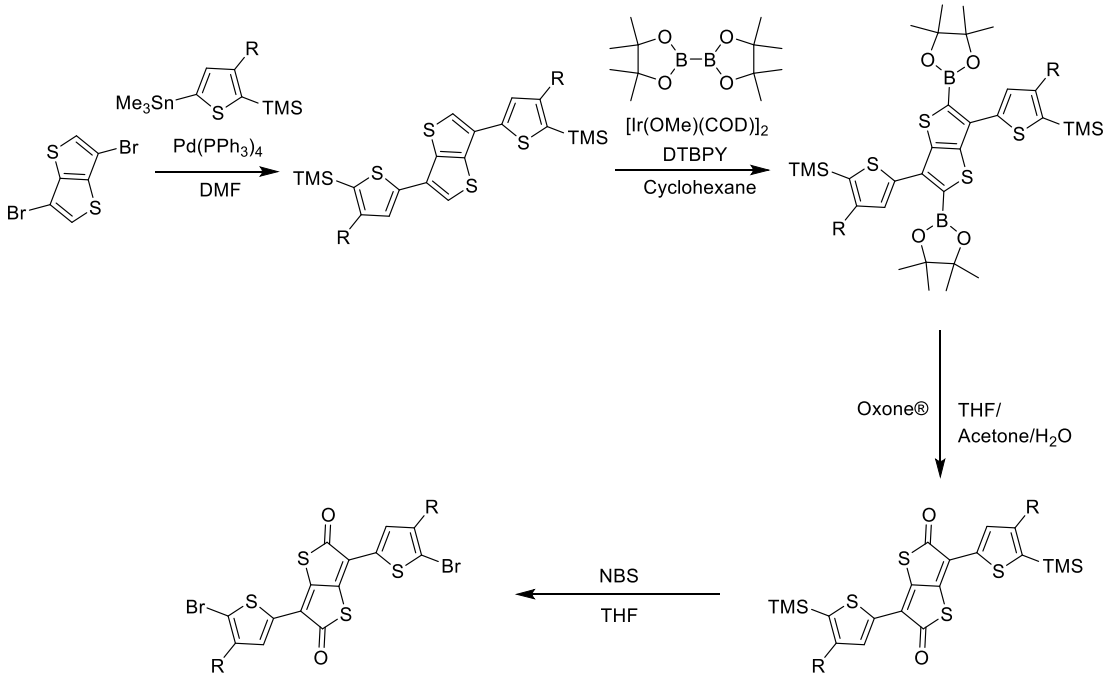

Scheme 5.2. Synthesis of thieno[3,2-b]thiophene-2,5-dione core reported by Takimiya et al[160]

In this chapter we present the synthesis of novel 3,6-dithienofuro[3,2-b]furan-2,5-dione core. From the core, novel compounds are synthesised organic semiconductor applications. The compounds were characterised using UV/Vis spectroscopy and cyclic voltammetry and the potential of using these compounds in organic semiconductor devices is discussed.

5.3 Results and Discussion

5.3.1 Synthesis

The first target material to be synthesised was 3,6-dithienofuro-[3,2-b]-furan-2,5-dione (compound 40) and the reaction scheme for the proposed synthetic route is shown below in scheme 5.3. Compounds 37 and 38 were formed in good yield by deprotonation and nucleophilic substitution of thiophene-2-acetonitrile. The next two steps were a Paal-Knorr type cyclisation to form the final product, compound 40. Intermediate compound 39 forms a by-product but the mixture was used to proceed with the next step for the formation of compound 40.

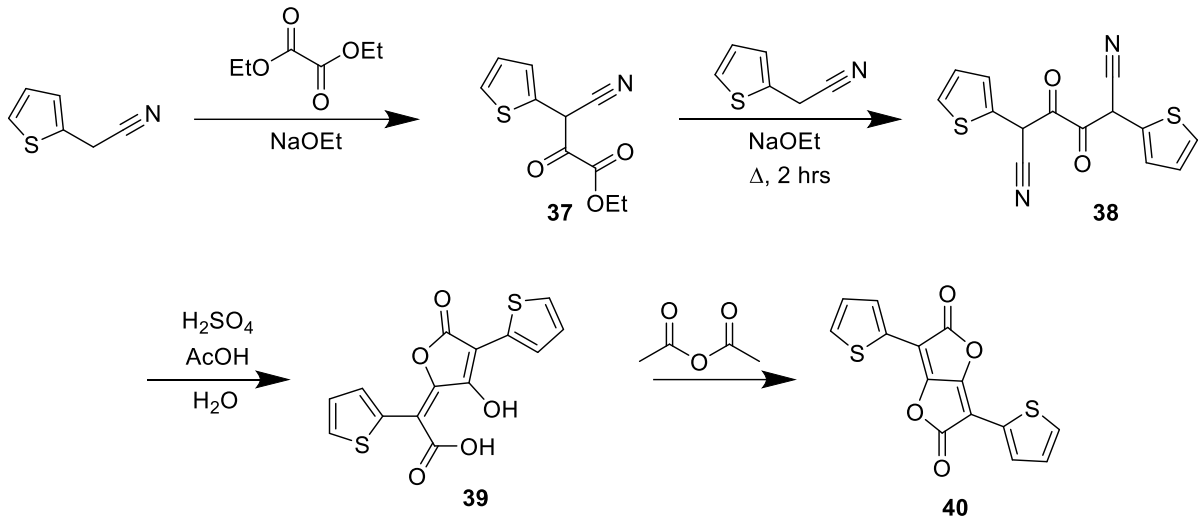

Scheme 5.3. Proposed synthesis of compound 40 (FFD-core)

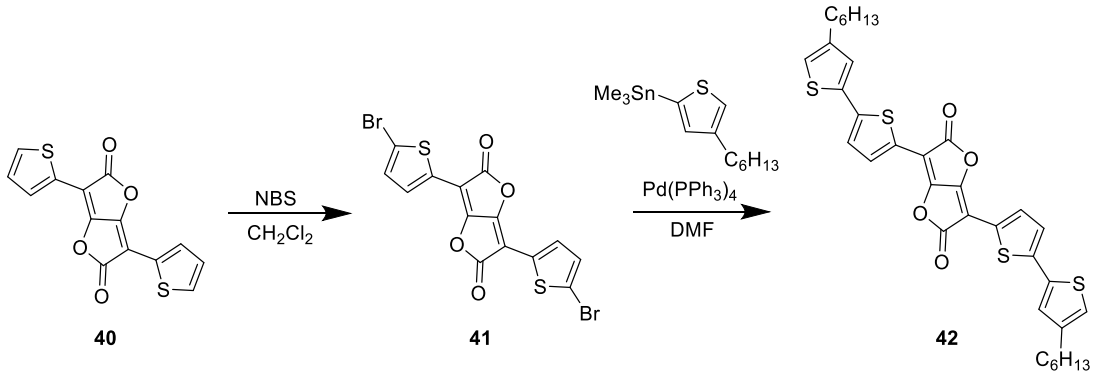

Scheme 5.4. Synthesis of **FF-1**

The core was brominated with NBS in order to be used in Pd-catalysed cross-coupling reactions. Shown in scheme 5.4 above is the synthesis of compound FFD-$(2T)_2$, which was formed by Stille cross-coupling.

The next target material was TTD-$(3T)_2$**,** the proposed synthesis of which is shown in scheme 5.5 below. 3-Hexylthiophene was stannylated to form compound 43 and a Stille coupling reaction was carried out in order to cross-couple this with the 3,6-

diiodothieno-[3,2-b]-thiophene-2,5-dione core, forming compound 44. A bromination was carried out using *N*-bromosuccinimide to form compound 45. Using compound 45, it would be possible to vary the donor substituent via cross-coupling of different stannanes. However, after many attempts of the Stille cross-coupling reaction of compound 45, with varying reaction conditions, TTD-$(3T)_2$ was not formed. Additionally, there was no starting material recovered, suggesting that there is decomposition of the starting material. Mass spectrometry and ^{1}H NMR spectroscopy were carried out on the isolated by-product but it was not possible to conclusively determine the structure.

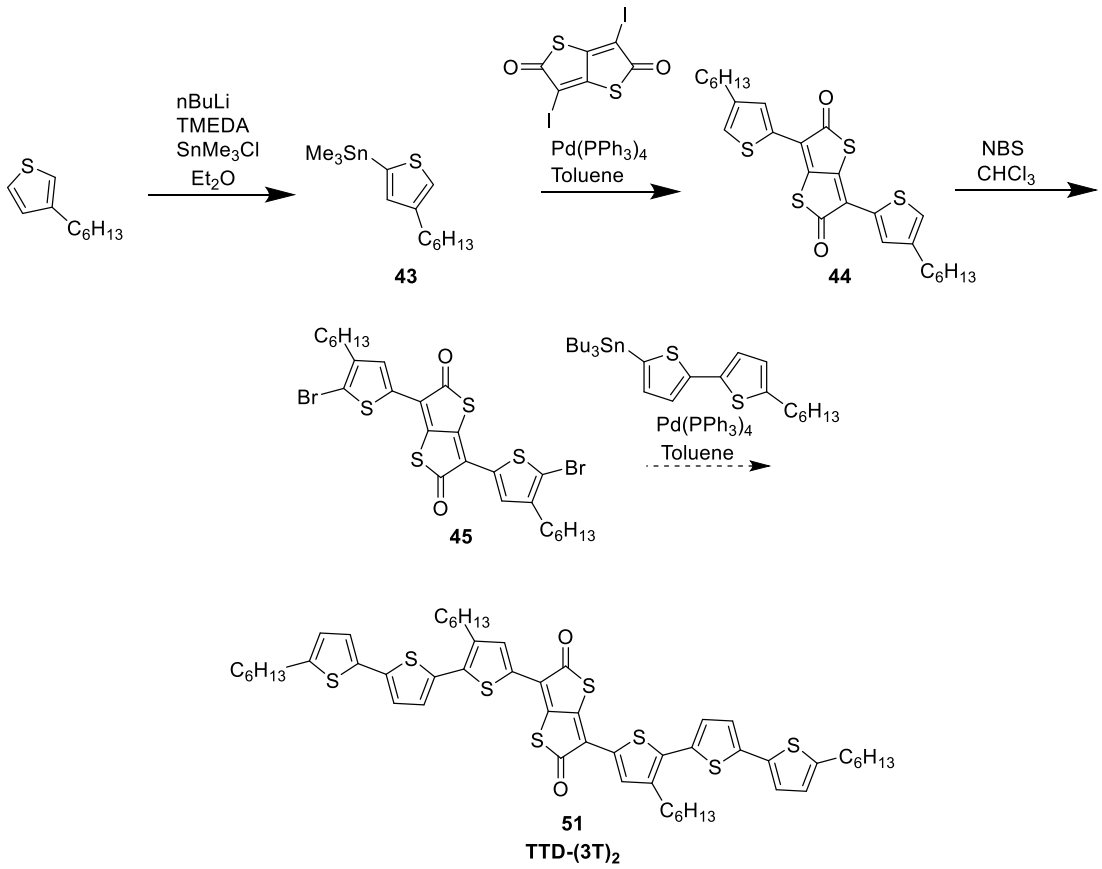

Scheme 5.5. Proposed synthesis of compound TTD-$(3T)_2$

It was therefore decided that an alternative synthetic strategy was required which is shown below in Scheme 5.6. 5'-Hexyl-2,2'-bithiophene was brominated using NBS and acetic acid to form compound 46, which was stannylated *via* a lithium-halogen exchange reaction to form compound 48. A bromination was also carried out on 3-hexylthiophene to form compound 47**,** which was subsequently used in a Stille coupling reaction with compound 48 to form the terthiophene arm, compound 49. This was functionalised with a tributylstannyl group to form compound 50 which was cross-coupled with the 3,6-diiodothieno-[3,2-b]-thiophene-2,5-dione core by Stille coupling, to give product TTD-$(3T)_2$ with a 35% yield.

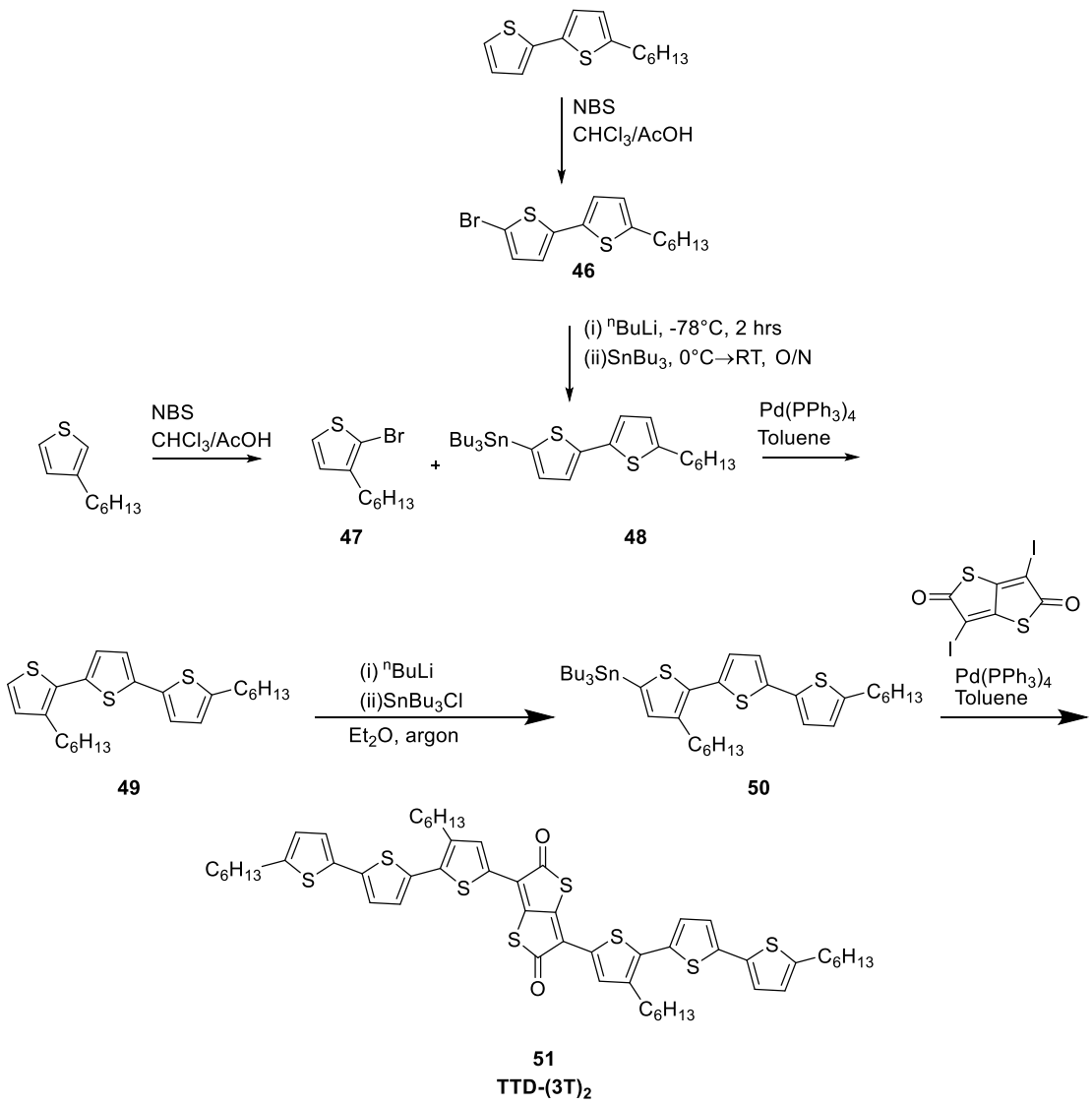

Scheme 5.6. Revised synthesis of TTD-$(3T)_2$

5.3.2 Optical and Electrochemical Properties

UV/Vis spectroscopy and cyclic voltammetry were used in order to study the physical properties of the FFD and TTD based compounds. These results are summarised in table 5.1.

Shown in figure 5.2 is the absorption spectrum for TTD-$(3T)_2$ in CH_2Cl_2 solution. The

absorption spectrum shows two bands, one at 371nm and another at 638nm. The first band can be assigned to a π-π* transition on the thieno-[3,2-b]-thiophene-2,5-dione core. This also seen in a similar compound reported in 2011 by Yamashita *et al,*[159] the structure of which is shown in figure 5.3.

The peak at 638 nm is a wide charge transfer band that can be assigned to excitation from the electron rich terthiophene arms to the electron-deficient core. This band is not present in Yamashita's compound,[159] which has electron-withdrawing trifluoromethylphenyl arms. This reflects on the optical HOMO-LUMO gap determined by the onset of absorption, which is 1.31eV lower in TTD-$(3T)_2$**.** The difference in structure and absorption properties of these two compounds illustrates the effect of having donor and acceptor moieties in a compound on the absorption profile and the HOMO-LUMO gap, and, specifically, the advantages of a donor-acceptor design for small molecules for OPV applications.

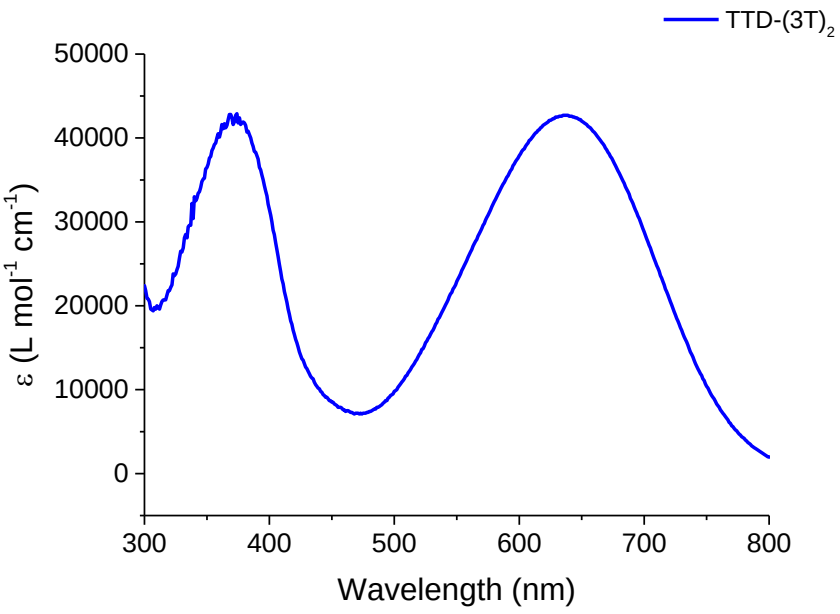

Figure 5.2. UV/Vis absorption spectrum of TTD-$(3T)_2$

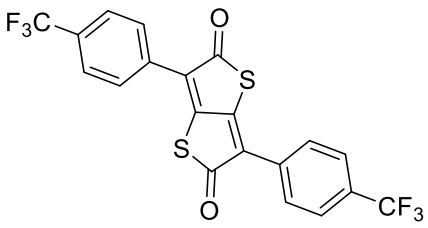

Figure 5.3. Thieno-[3,2-b]-thiophene-2,5-dione based compound synthesised by Yamashita *et al*[159]

The absorption spectrum of the FFD core and FFD-$(2T)_2$ is shown below in figure 1. The additional extended conjugation of FFD-$(2T)_2$ leads to a 75 nm red-shift, with FFD-$(2T)_2$ also showing broader absorption. An absorption spectra of a solid film of FFD-$(2T)_2$ was also recorded, showing it to be even broader than the solution-state spectrum, and the broad absorption is useful for the application to OPV devices. The optical HOMO-LUMO gap calculated from the solid-state spectrum is 0.27 eV lower than that calculated from the solution-state spectrum, owing to the presence of π-π stacking in the film.

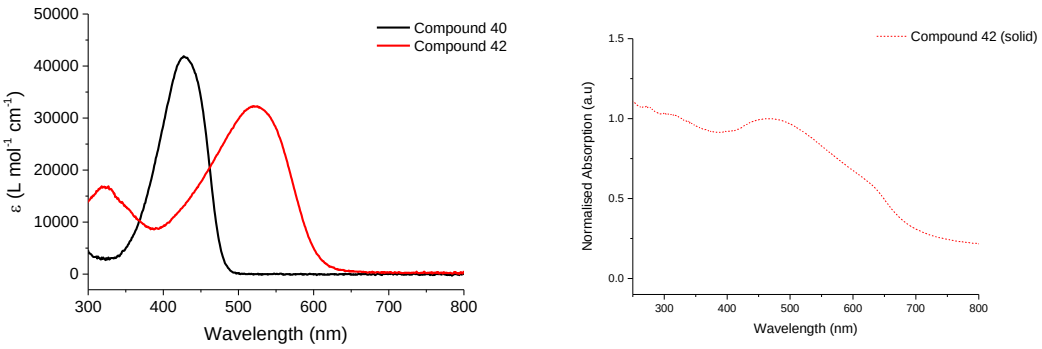

Figure 5.4. UV/Vis spectra of compounds 40 and 42 in CH_2Cl_2 (left) and the solid-state spectrum of compound 42 (right)

Cyclic voltammetry was also carried out in order to estimate the HOMO and LUMO energy values from the onset of oxidation and reduction potentials and this data is summarised in Table 5.1. The LUMO values for each compound are similar, suggesting that reduction takes place in the furo[3,2-b]furan core, whilst compound FFD-$(2T)_2$ has an increased HOMO level with respect to the FFD core, which is explained by the increased conjugation.

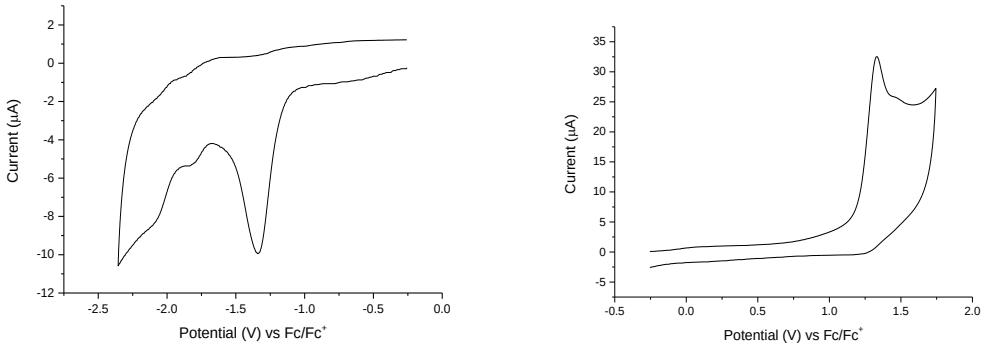

Figure 5.5. Reduction (left) and oxidation (right) of the FFD core by cyclic voltammetry

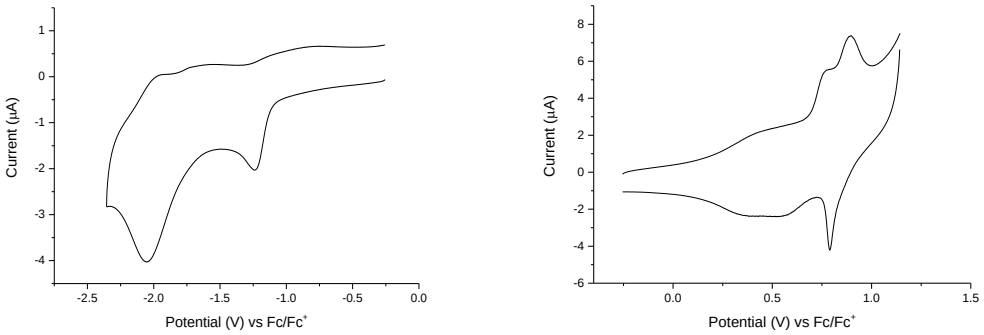

Figure 5.6. Reduction (left) and oxidation (right) of FFD-$(2T)_2$ by cyclic voltammetry

The electrochemical properties of TTD-$(3T)_2$ were studied by cyclic voltammetry, with particular interest in the determination of the HOMO and LUMO levels. The conditions are described in the experimental chapter.

The reduction and oxidation of TTD-$(3T)_2$ are shown below in Figure 5.7. The oxidation shows reversible and quasi-reversible peaks and the HOMO energy is determined to be -5.29 eV, significantly higher than Yamashita's compound (-6.75 eV). This difference can be ascribed to the increased donor ability of the terthiophene arm compared to the trifluoromethylphenyl arm.

The reduction is very similar to Yamashita's compound, showing two reversible peaks, a feature symptomatic of good electron transport[159], and the LUMO energy level determined is also very similar. This suggests that the reduction takes place on the thieno-[3,2-b]-thiophene-2,5-dione coreand that the core is an effective acceptor unit. Nguyen and coworkers[163] synthesised an analogous compound with the popular DPP core and ter-thiophene arms. Although the optical HOMO-LUMO gaps are similar, the HOMO-LUMO gap determined electrochemically for TTD-$(3T)_2$ is 0.39eV smaller than its DPP analogue, with the LUMO being 0.56eV lower. This demonstrates a high accepting ability of the thieno-[3,2-b]-thiophene-2,5-dione core, more suitable for this purpose than the well published DPP unit.

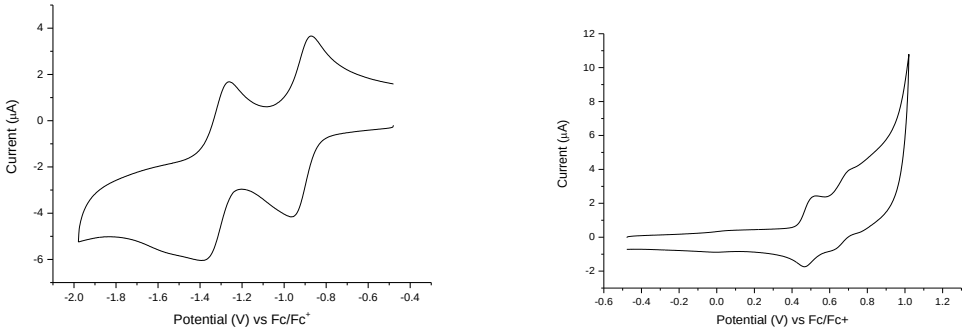

Figure 5.7. Reduction (left) and oxidation (right) of TTD-$(3T)_2$ by cyclic voltammetry

Table 5.1. Summary of optical and electrochemical properties of FFD and TTD-based compounds

Compound	λ_{max} (nm)	HOMO-LUMO (eV)[a]	HOMO (eV)[b]	LUMO (eV)[b]	E_{ox} (V)[c]	E_{red} (V)[c]
FFD-core	416	2.59 (2.36)	-6.00	-3.64	1.33, ir	-1.34,ir -1.97/-1.84, qr -2.10/-2.19, qr
FFD-(2T)$_2$	491	2.04 (1.81)	-5.50	-3.69	0.77/0.56.qr 0.89/0.79.qr	-1.24/-1.11, qr -2.05/-1.95, qr
TTD-(3T)$_2$	638	1.41 (1.60)	-5.29	-388	0.51/0.47 0.70/0.63	-0.97/-0.87 -1.39/-1.26, qr

[a]The optical HOMO–LUMO gap is calculated from the onset of absorption. The electrochemical HOMO–LUMO gap calculated from the difference in HOMO and LUMO energy level and is shown in parentheses. [b] HOMO (LUMO) calculated from E HOMO (LUMO) = ($-4.80 - E_{onset}^{ox(red)}$). [c] The cathodic and anodic peaks are reported for reversible and quasi-reversible (qr) waves. The peak values on both forward and reverse scans are reported for reversible and quasi-reversible (qr) waves. The peak value on forward scan is shown for irreversible (ir) waves. The peak values are referenced to Fc/Fc+

TTD-(3T)$_2$ has shown a significantly lower HOMO-LUMO gap than any other compounds synthesised containing a thieno-[3,2-b]-thiophene-2,5-dione core,[159] with its low HOMO-LUMO gap making it a suitable candidate for use as an OPV donor material. It also has been shown to have a lower LUMO than its DPP-analogue,[163] suggesting the use of this core can be used in the design of low HOMO-LUMO gap

small molecules for OPV applications. Nguyen's compound has an efficiency of 2.2%[164] in a BHJ-OPV and a hole mobility of 10^{-6} $cm^2/V.s$ in an OFET device (competitive with other donor compounds used for solar cells) and characterisation of TTD-$(3T)_2$ suggests that it could perform similarly. An increased accepting ability of the compound is characterised by the low LUMO level and this could even suggest that the compound may be able to be used in an ambipolar OFET. The LUMO however, is similar to that of $PC_{60}BM$ (-3.91eV),[165] which is commonly used as an acceptor in BHJ-OPV devices, and this may inhibit efficient exciton dissociation. However, the development of low LUMO acceptor compounds may mean that they could be used effectively with compound TTD-$(3T)_2$ in a BHJ-OPV, although will lead to a compromise on the V_{oc}.[64, 165]

5.3.3 DFT Calculations

In order to fully understand the effect of the furo[3,2-b]furan-2.5-dione core on the structure, DFT calculations were performed. In particular, analysis of the molecular orbitals was carried out to determine the effect of varying structure on the properties of the orbitals and both the HOMO and LUMO of each compound are shown below in figure 3.

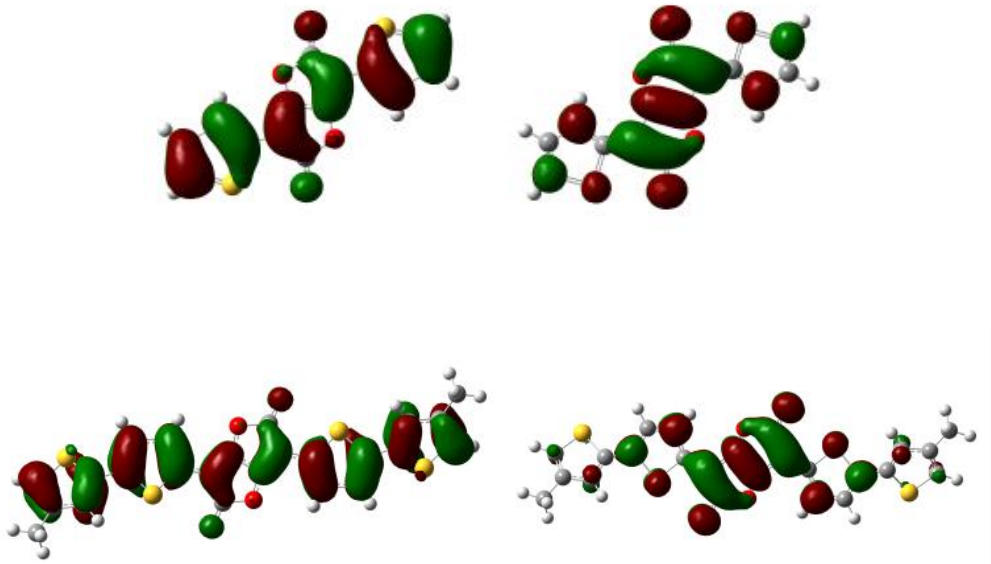

Figure 5.8. HOMO (left) and LUMO (right) of compounds 40 (top) and 42 (bottom)

The HOMOs of both compounds are similar as they are delocalised across the entire molecule, whilst each LUMOs of FFD core and FFD-$(2T)_2$ show variation. Despite the increased conjugation, there is very little of the LUMO localised on the peripheral thiophenes of FFD-$(2T)_2$, suggesting that the LUMO is dominated by the furo[3,2-b]furan-2,5-dione core. This is consistent with the cyclic voltammetry showing similar values for both compounds, which explained by the LUMO being localised on the furo[3,2-b]furan-2,5-dione core.

Table 5.2 TDDFT Results

	λ_{TDDFT} (nm)	λ max $_{EXP}$ (nm)
FFD core	432, 240	461, 250
FFD-$(2T)_2$	493, 300	491, 321

5.4 Conclusions/Future Work

In this chapter, the synthesis of materials based on analogous electron-deficient TTD and FFD cores has been discussed. The compounds TTD-$(3T)_2$ shows good redox properties and shows a charge transfer state in solution-state UV/Vis spectroscopy. Given that previously reported compounds containing the TTD core show ambipolar behaviour,[159, 160] it can be expected that this compound could be applied effectively in the fabrication of ambipolar OFET devices. The reversible reductions of the neutral and radical anion of the material suggest that this compound could be applied as an acceptor material with the LUMO slightly lower than that of $PC_{61}BM$.

The LUMO of FFD-$(2T)_2$ is slightly higher than the TTD containing compound although it is very similar to $PC_{61}BM$. However this compound does not show the reversible reductions that are present in the cyclic voltammetry of TTD-$(3T)_2$ and this may suggest that this material might not be as good as an organic semiconductor material.

The furo[3,2-b]furan-2,5-dione unit has not been used in the synthesis of polymers for organic electronic devices and given polymers have shown to out-perform small molecules in devices, particularly OPVs, it would be interesting to synthesise D-A polymers based on the novel acceptor unit. The bromide-functionalised compound 41 would be able to be used in polymerisation reactions with various monomers.

Chapter 6 – Conclusions and Future Work

6.1 Conclusions and Future Work

The main areas of discussion in this thesis have centred on two common themes. The first is the synthesis of novel small molecules and the explanation of the observed physical properties of these compounds with respect to the molecular structure of the target materials. The second key theme presented in this body of work is the fabrication of organic electronic devices and investigation into the optimization of these devices in order to maximise performance.

The synthesis of two different groups of compounds, donor-acceptor-donor (D-A-D) and acceptor-donor-acceptor (A-D-A) compounds, presented in chapter 2 produced compounds that had different properties on account of the number of ND acceptor units present in the conjugated backbone. The UV/Vis spectra of the D-A-D compounds showed well-defined splitting of peaks, typical in planar compounds, whilst the spectra produced using A-D-A compounds were single broad peaks. The indication that the D-A-D compounds are more planar, could then explain why the highest PCE from all OPV devices using ND compounds was obtained using ND03, a compound with a single acceptor unit.

In order to improve the PCE of OPV devices using donor materials based on the ND acceptor, the conjugation length can be increased or the conjugated backbone can be functionalised with electron-rich units in order to decrease the HOMO-LUMO gap, which is relatively high in the best performing compound ND03. A reduced HOMO-LUMO gap would lead to absorption of a larger area of the solar spectrum and this in

turn would lead to the generation of more charge carriers, which would be signified by an increased J_{SC}.

In chapter 3, the asymmetric acceptor unit NDO was used in the synthesis of compounds with two terminal acceptor units and linear D-A compounds. Unlike chapter 2, it was shown that the multiple acceptor containing compound $(NDO\text{-}T)_2$-BT, outperformed the single acceptor containing compounds when applied to OFET devices. Using $(NDO\text{-}T)_2$-BT, the effect of self-assembled monolayers on p-type mobility was studied, leading to a maximum mobility of 0.022 $cm^2\ V^{-1}\ s^{-1}$. The NDO based compounds were not suitable as donor materials for OPV applications due to as the LUMO energies for these compounds were similar to that of $PC_{61}BM$. However, the good p-type mobility exhibited by $(NDO\text{-}T)_2$-BT suggests that if an electron rich donor moiety was introduced into a NDO containing compound to increase the LUMO, compounds including NDO units could be used successfully as donors for OPV devices.

Having fabricated OFETs using single organic materials, inorganic nanoparticle additives were added to solutions of two organic p-type materials to determine how the nanoparticles would affect performance. The addition of Cu_2ZnSnS_4 (CZTS) nanoparticles at 5 and 10 wt% concentrations in 5T-TTF and P3HT OFETs respectively lead to an increase in the p-type mobility. There was a striking effect on the film morphology of the composite OFETs with increased loading appearing to break up large domains of the organic semiconductor. However, despite the fact there is an obvious morphological change, further studies are required to understand the exact mechanism of improved mobility in the composite OFETs.

Finally, the synthesis of novel compounds based on the analogous furo[3,2-b]fuan -2,5-dione (FFD) and thieno[3,2-b]thiophene-2,5-dione (TTD) acceptor moieties was presented in chapter 5 with the physical properties of these compounds discussed. The TTD based compounds showed reversible electrochemical reductions which were not present in the FFD based compounds, suggesting that molecules based on the former acceptor unit may be more suitable n-type materials. In order to test both compounds in n-type OFETs, it would be necessary to use source and drain electrodes with a work function of around 3.7 eV for effective charge injection.

Overall this body of work demonstrates the successful synthesis of target materials and the application of some of these small molecules into functioning organic electronic devices. The varying physical properties and device performances that were determined from similar compounds shows that even small differences in the molecular structure of molecules synthesised can have a large impact on the properties of a material. Through understanding these small differences, it is possible advance the design of organic semiconductors.

Chapter 7 - Experimental

7.1 General

For all reactions carried out in anhydrous conditions, glassware was dried in an oven at 120°C. Reagents were purchased from commercial sources without further purification unless otherwise stated. Dry solvents were obtained from a solvent purification system (SPS 400 by Innovative Technologies) with an alumina drying agent. *N*-butyllithium (2.50M in hexanes) was titrated with diphenyl acetic acid to determine its concentration. 3,6-Diiodothieno[3,2-b]thiophene-2,5-dione was provided by Merck Chemicals.

^{1}H and ^{13}C NMR spectra were recorded on DRX 500 or AV3 400 at 500 and 125 MHz or 400 and 100MHz. Chemical shifts are in ppm and *J* values are in Hz.

Melting points were determined using Stuart Scientific SMP1 Melting Point apparatus and are uncorrected.

Cyclic voltammetry measurements were carried out in order to characterise the HOMO and LUMO levels of each compound. This was performed using a CH Instruments 660A electrochemical workstation with *i*R compensation at a scan rate of 0.1 V s^{-1}. The concentration of analyte used was 1×10^{-4}M in CH_2Cl_2 with tetrabutylammonium hexafluorophosphate (0.1 M) used as an electrolyte. Glassy carbon, Ag wire and Pt wire were used as the working, counter and reference electrode respectively. Each value is corrected to the redox potential of ferrocene. The HOMO (LUMO) was calculated by subtracting the onset of oxidation (reduction) from -4.8 eV, the HOMO of ferrocene (i.e. 4.8 eV below vacuum).

The absorption profile of compounds using a Shimadzu UV-1800 spectrophotometer. Solution-state spectroscopy was carried out using 10^{-5} M solutions in CH_2Cl_2 unless otherwise stated, whilst solid-state spectroscopy was carried out by drop casting a 1 mg ml^{-1} solution onto a glass slide and allowing the solvent to evaporate. The onset of absorption was used in order to calculate the optical HOMO-LUMO gap for each compound.

Organic field-effect transistors were fabricated on SiO2 substrates with prefabricated interdigitated Au source-drain channels with lengths of 2.5, 5, 10 and 20 μm and width of 1 cm. N-doped Si and SiO2 are the gate electrode and gate dielectric respectively. The substrates were cleaned using water, acetone and ethanol before being treated with oxygen plasma cleaning (Diener Electronic, Zepto) for 30 seconds. The pentafluorobenzenethiol (PFBT) self-assembled monolayer (SAM) was prepared by drop casting a solution of PFBT (10 mM in ethanol) onto the substrate. After 1 min, the residual PFBT was then washed with ethanol and the substrate was dried over a stream of compressed air. Similarly, octadecyltrichlorosilane (OTS) SAM was prepared by drop casting an OTS solution (13 mM in toluene) onto the substrate which was washed with toluene and dried after 1 min. The organic semiconductor solution (10 mg ml^{-1} concentration for small molecules, 5 mg ml^{-1} for P3HT) was deposited *via* spin-coating (MB SC-200, Mbraun) at 2000 rpm before annealing at a stated temperature. Where inorganic nanoparticles had been used, the solutions had been placed in an ultrasonic bath at room temperature for 20 minutes prior to deposition. Current-voltage characteristics were recorded using a Keithley 4200 semiconductor parameter analyser at room temperature in a nitrogen atmosphere. The field-effect mobilities were determined from the saturation regime and calculated using the following equation:

$$\mu_{sat} = \frac{2L}{WC_i} \times \left(\frac{\partial\sqrt{I_{ds}}}{\partial V_g}\right)^2 \quad (11)$$

In OPV fabrication, an ITO glass slide was cleaned with acetone before the treatment with UV-ozone for 2 minutes. PEDOT: PSS was then spin-coated onto the ITO and the substrate was then annealed for 20 minutes at 120°C. After the substrates were taken into the glovebox with N_2 atmosphere, the active material was then spin-coated onto the substrate at 800 rpm before being annealed at stated temperature for 20 minutes. Calcium and Aluminium electrodes were then evaporated onto the active layer respectively with thickness of 40 nm for each metal. The

area of the electrodes deposited was 6 mm^2. The current-voltage characteristics were measured using a Keithley 4200 and the solar cells were illuminated by a Newton Solar Simulator with a calibrated solar cell.

The surface morphology was characterised using a Dimension 3100 atomic force microscopy (AFM) in tapping mode. The software WSxM 6.0[166] was used to analyse the roughness of the images.

7.2 Synthesis

1,5-Didodecyl-naphthyridine-2,6-dione (1)

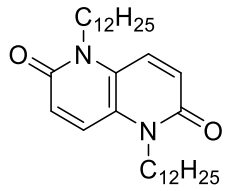

Naphthyridine-2,5-dione (5.0 g, 31 mmol) was added to a solution of 1-bromododecane (50 ml, 208 mmol), 40% tetrabutylammonium hydroxide in H_2O (247 ml, 370 mmol) and DMSO (60 ml). The reaction mixture was stirred at 65°C for 4 days before precipitation of the crude product by addition of saturated ammonium chloride solution (50 ml). The crude solid was then suspended in a 1:1 mixture of ethyl acetate: petroleum ether and the remaining yellow solid was collected. Yield = 1.86 g (12%): ^{1}H NMR (400 MHz, $CDCl_3$, ppm):δ = 7.55 (d, *J* = 10 Hz, 2H), 6.88 (d, *J* = 10 Hz, 2H), 4.23 (t, *J* = 7.76 Hz, 4H), 1.71 (m, 4H), 1.48-1.26 (m, 36H), 0.89 (t, *J* = 6.9 Hz, 6H): ^{13}C NMR (101 MHz, $CDCl_3$) δ 159.4, 127.9, 126.5, 124.8, 43.3, 32.0, 29.7, 29.69, 29.65, 29.5, 28.7, 27.0, 22.8, 14.2; m/z (MALDI): 499.4 $[M+H]^+$; Elemental Analysis: Found: C, 76.73, H, 10.93, N, 5.55, Expected: C, 77.06, H, 10.91, N, 5.62. Melting point: 144 - 146 °C.

1-Dodecyl-6-(dodecoxy)naphthyridine-2-one (2)

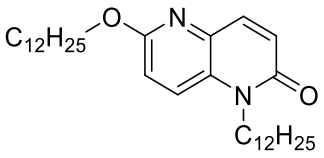

Compound 2 was isolated as a by-product in the formation of compound 1 by column chromatography (silica gel, eluent: 20% ethyl acetate: petroleum ether → 100% ethyl acetate) to give an off-white solid. Yield = 6.35 g (41%)^{1}H NMR (400 MHz, $CDCl_3$) δ 7.72 (d, *J* = 9.7 Hz, 1H), 7.59 (d, *J* = 9.2 Hz, 1H), 6.94 (d, *J* = 9.2 Hz, 1H), 6.85 (d, *J* = 9.7 Hz, 1H), 4.34 (t, *J* = 6.7 Hz, 2H), 4.27 – 4.15 (m, 2H), 1.87 – 1.64 (m, 4H), 1.51 – 1.16 (m, 36H), 0.88 (t, *J* = 6.8 Hz, 6H); ^{13}C NMR (101 MHz, $CDCl_3$) δ 161.2, 159.3, 139.6, 135.5, 131.3, 125.5, 125.2, 114.2, 66.5, 42.7, 32.1, 29.81, 29.75, 29.70, 29.68, 29.54, 29.52, 29.48, 29.1, 28.1, 27.1, 26.2, 22.8, 14.2.; m/z (MALDI): 499.59 $(M + H)^+$; Elemental Analysis: Found: C, 77.21; H, 11.19; N, 5.60; Expected: C, 77.06; H, 10.91; N, 5.62. Melting point: 72 – 74 °C.

2,6-Didodecoxynaphthyridine (3)

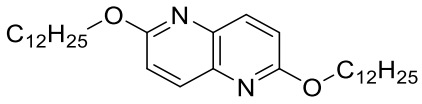

Compound 3 was isolated as a by-product in the formation of compound 1 by column chromatography (silica gel, eluent: 20% ethyl acetate: petroleum ether → 100% ethyl acetate) to give a white solid. Yield = 4.34 g (28%) ^{1}H NMR (400 MHz, $CDCl_3$) δ 7.95 (d, *J* = 8.8 Hz, 2H), 7.00 (d, *J* = 8.8 Hz, 2H), 4.40 (t, *J* = 6.7 Hz, 4H), 1.86 – 1.76 (m, 4H), 1.48 (m, 4H), 1.42 – 1.19 (m, 32H), 0.88 (t, *J* = 6.9 Hz, 6H); ^{13}C NMR (101 MHz, $CDCl_3$) δ 161.0, 139.2, 138.0, 115.7, 66.4, 32.1, 29.82, 29.75, 29.6, 29.5, 29.2, 26.3, 22.8, 14.2; m/z (MALDI): 499.49 $[M]^+$:

Elemental analysis: Found: C, 77.37, H, 11.07, N, 5.64; Expected: C, 77.06, H, 10.91, N, 5.64. Melting point: 76-78 °C.

3,7-Dibromo-1,5-didodecylnaphthyridine-2,6-dione (4)

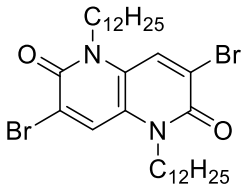

Bromine (0.258 ml, 5 mmol) in $CHCl_3$ (7 ml) was added slowly to a flask containing 1 (1 g, 2 mmol) in $CHCl_3$ (42 ml) at 0 °C. The reaction was then allowed to reflux overnight in the absence of light. Methanol was added (5 ml) at room temperature in order to quench the reaction and the resulting precipitate was collected by filtration. The solid was then washed with further methanol to yield the product as a yellow solid Yield = 0.89 g (68%) ^{1}H NMR (400 MHz, $CDCl_3$) δ 7.95 (s, 2H), 4.26 (m, 4H), 1.73 (m, 4H), 1.50 – 1.21 (m, 36H), 0.89 (t, *J* = 6.9 Hz, 6H); ^{13}C NMR (101 MHz, $CDCl_3$) δ 155.9, 129.8, 125.5, 122.3, 45.2, 32.1, 29.8, 29.71, 29.69, 29.6, 29.5, 29.3, 28.5, 26.9, 22.8, 14.3; m/z (MALDI): 655.26 ($[M+H]^+$, ^{79}Br × 2), 657.26 ($[M+H]^+$, ^{79}Br + ^{81}Br) 659.26 ($[M+H]^+$, ^{81}Br × 2);Elemental Analysis: Found: C, 58.60, H, 8.02, N, 4.07, Expected: C, 58.54, H, 7.98, N, 4.27. Melting point: 140 - 142 °C.

2-Bromo-5-cyanothiophene (5)

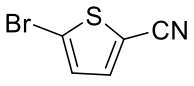

Iodine (2.93 g, 11.6 mmol) was slowly added to a mixture of 5-bromothiophene-2-carboxaldehyde (2.0 g, 10.5 mmol), THF (6 ml) and 35% aqueous ammonia (20 ml). The reaction mixture was stirred for 2 h at room temperature and then quenched with aqueous Na_2SO_3. The product was extracted with $CHCl_3$ before being washed with water (3 × 20 ml)

and dried over $MgSO_4$. The solvent was then evaporated to yield the crude product which was purified by column chromatography (silica gel, 2:1 $CHCl_3$: hexane mobile phase) to give the pure product as a colourless oil. NMR data is consistent with previously reported data.[167] Yield = 1.90 g (97%) ^{1}H NMR (400 MHz, $CDCl_3$, ppm):δ = 7.40 (d, *J* = 4 Hz, 1H), 7.11 (d, *J* = 4 Hz, 1H);^{13}C NMR (400 MHz, $CDCl_3$, ppm):δ = 138.1; 130.8; 120.3; 113.3; 111.6; m/z (GC-MS): 187.8 ($[M + H]^+$,^{79}Br), 189.8($[M+H]^+$, ^{81}Br) .

2-Tributylstannyl-5-cyanothiophene (6)

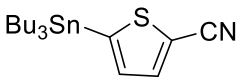

N-butyllithium (3.1 ml, 7.5 mmol, 2.42 M) was added a solution of 5-bromothiophene-2-carbonitrile (1 g, 5 mmol) in Et_2O (50 ml) under an inert atmosphere at -78°C. The solution was allowed to stir for 2 h at -78°C before the addition of tributyltinchloride (2.03 ml, 7.5 mmol) at 0°C. The mixture was left to stir for 16 hours before being washed with saturated $NaHCO_3$ solution (3 × 25ml). The solution was dried over $MgSO_4$ and the solvent was then evaporated to yield a yellow oil which was used without further purification. The ^{1}H NMR peaks correspond to the literature values.[110] Yield = 2.1 g (99%) ^{1}H NMR (400 MHz, $CDCl_3$) δ 7.71 (d, *J* = 3.5 Hz, 1H), 7.13 (d, *J* = 3.5 Hz, 1H), 1.71 – 0.84 (m, 27H).

3,7-Bis(5-cyanothiophen-2-yl)-1,5-didodecylnaphthyridine-2,6-dione (ND01) (7)

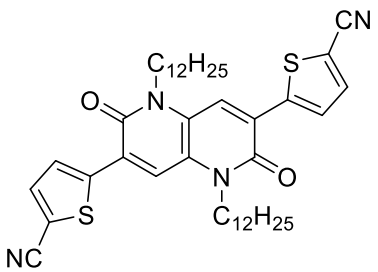

3,7-Dibromo-1,5-didodecylnaphthyridine-2,6-dione (0.4 g, 1.26 mmol), 5-tributylstannylthiophene-2-carbonitrile (0.55 g, 1.39 mmol) and toluene (20 ml) were added to

a flask under an inert atmosphere. The solution was degassed for 1 h by purging with N_2 before the addition of $Pd(PPh_3)_4$ (0.112 g, 0.097 mmol). The reaction was left to reflux for 16 hours. The solution was washed with saturated $NaHCO_3$ solution (3 × 10 ml) before being dried over $MgSO_4$ and the solvent was evaporated. The crude compound was purified using column chromatography (silica gel, 1:5 ethyl acetate/hexane mobile phase) to yield a red solid. Yield = 0.068 g (16%) ^{1}H NMR (400 MHz, $CDCl_3$, ppm):δ = 8.08 (s, 2H), 7.67 (m, 4H), 4.48 (m, 4H), 1.86 (m, 4H), 1.59-1.22 (m, 40H) 0.90 (t, *J* = 6.8 Hz, 6H); ^{13}C NMR (101 MHz, $CDCl_3$) δ 157.3, 136.3, 132.2, 128.7, 128.6, 126.3, 125.9, 124.9, 120.9, 44.4, 32.0, 29.84, 29.79, 29.75, 29.70, 29.65, 29.5, 28.6, 27.1, 22.8, 14.2; m/z (MALDI): 713.25 $[M]^+$; Elemental Analysis: Found: C, 70.31, H, 7.84, N, 7.92, Expected: C, 70.75, H, 7.92, N, 7.86. Melting point: 232 – 234°C.

2-Tributylstannylthianaphthene (8)

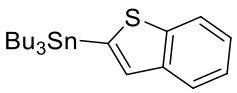

Thianaphthene (8.6 mmol, 1 ml) and THF (17 ml) were added to a flask under an inert atmosphere and the solution was cooled to -78°C before the slow addition of *n*-butyllithium (3.93 ml, 9.46 mmol, 2.41 M). The reaction was allowed to stir for 2 h at -78°C before the addition of tributyltin chloride (2.8 ml, 10.3 mmol) at 0°C. The reaction was left to stir overnight. The reaction mixture was then washed with brine (3 × 20 ml) before the organic phase was dried over $MgSO_4$ and the solvent was evaporated to yield a yellow oil. The product was used without further purification. ^{1}H NMR spectrum is consistent with previously reported data.[168] Yield = 3.46 g (96%); ^{1}H NMR (400 MHz, $CDCl_3$) δ 7.89 (m, 1H), 7.81 (d, *J* = 7.6 Hz, 1H), 7.39 (d, *J* = 0.7 Hz, 1H), 7.35 – 7.24 (m, 2H), 1.72 – 0.80 (m, 27H).

2-(Thiophen-2-yl)thianaphthene (9)

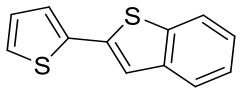

2-Bromothiophene (1 g, 6.13 mmol) and 2-tributylstannylthianaphthene (2.86 g, 6.75 mmol) were added to toluene (50 ml) under an inert atmosphere and the mixture was degassed with N_2 for 1 h. $Pd(PPh_3)_4$ (0.496 g, 0.429 mmol) was then added and the mixture was allowed to reflux for 16 h. The reaction mixture was washed with brine (3 × 50 ml) before being dried over $MgSO_4$. The solution was filtered and evaporated to yield a crude product. The crude solid was purified by column chromatography using ethyl acetate as mobile phase. A small impurity remained and the product was further purified by column chromatography using a hexane mobile phase to yield a white crystalline solid.^{1}H NMR spectrum is consistent with previously reported data.[169] Yield = 0.57 g (43%): ^{1}H NMR (400 MHz, $CDCl_3$, ppm):δ = 7.79 (d, *J* = 7.9 Hz, 1H), 7.74 (d, J = 7.5 Hz, 1H), 7.42 (s, 1H), 7.38-7.29 (m, 4H), 7.08 (dd, *J* = 5, 7.4 Hz, 1H); ^{13}C NMR (126 MHz, $CDCl_3$): δ = 140.5, 139.3, 137.6, 137.4, 128.1, 125.6, 125.2, 124.8, 124.6, 123.6, 122.3, 119.9; m/z (MALDI) = 215.88 $[M]^+$; Melting point: 129-131°C.

2-(5-Tributylstannylstannylthiophen-2-yl)thianaphthene (10)

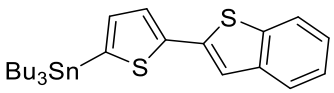

2-(Thiophen-2-yl)thianaphthene (0.42 g, 1.94 mmol was dissolved in anhydrous THF (20 ml) and cooled to -80°C before the slow addition of *n*-butyllithium under an Ar atmosphere. The solution was stirred for 1 h before the slow addition of tributyltinchloride (0.58 ml, 2.13 mmol) at -80°C. The reaction was then allowed to stir at room temperature for 16 hours. The reaction mixture was quenched with H_2O (100 ml) and extracted with CH_2Cl_2 (3 × 60 ml) before the combined organic layers were washed with brine (100 ml) and water (100 ml). The organic phase was then dried over $MgSO_4$ and the solvent was evaporated to reveal the crude product

as a brown oil. The product was used without further purification. Yield = 0.94 g (96%); ^{1}H NMR (400 MHz, $CDCl_3$) δ 7.83 – 7.78 (m, 1H), 7.75 (m, 1H), 7.44 (m, 1H), 7.39 – 7.28 (m, 3H), 7.14 (d, *J* = 3.4 Hz, 1H), 1.69 – 1.58 (m, 6H), 1.39 (m, 6H), 1.21 – 1.14 (m, 6H), 0.95 (m, 9H).

3,7-Bis(2-[thiophen-2-yl]-thianaphthene)-1,5-didodecylnaphthyridine-2,6-dione (ND02) (11)

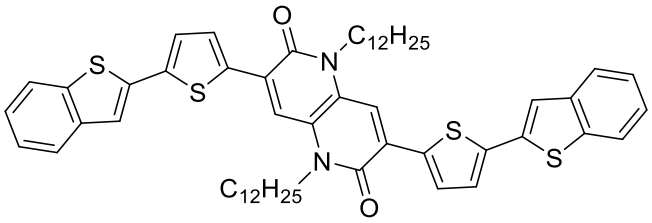

3,7-Dibromo-1,5-didodecylnaphthyridine-2,6-dione (0.3 g, 0.46 mmol) and 5-tributylstannyl-2-(thiophen-2-yl)benzothiophene (0.256 g, 0.506 mmol) and toluene (15 ml) were added to a flask under an inert atmosphere and the solution was purged with N_2 for 1 h. $Pd(PPh_3)_4$ (0.037g, 0.032 mmol) was then added to the solution which was stirred for 16 h. The crude mixture was washed with saturated $NaHCO_3$ solution (3 × 15 ml) before being dried over $MgSO_4$ and the solvent was evaporated. The crude compound was purified by column chromatography (mobile phase ethyl acetate followed by CH_2Cl_2) yielding the product as a sticky red solid. Yield = 0.242 g (57%): ^{1}H NMR (400 MHz, $CDCl_3$) δ 7.91 (s, 2H), 7.75 (dd, *J* = 18.0, 7.6 Hz, 4H), 7.64 (d, *J* = 3.9 Hz, 2H), 7.50 (s, 2H), 7.31 (m, 6H), 4.50 – 4.38 (m, 4H), 1.87 (m, 4H), 1.64 – 1.18 (m, 36H), 0.87 (t, *J* = 6.7 Hz, 6H).^{13}C NMR: m/z (MALDI): 927.70 $[M]^+$; Elemental Analysis: Found: C, 72.34, H, 7.18, N, 3.19, Expected: C, 72.53, H, 7.17, N, 3.02. Melting point: 165 – 167°C.

2-Tributylstannylbenzofuran (12)

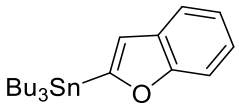

N-butyllithium (3.85 ml, 9.32 mmol, 2.42 M), was added to a solution of benzofuran (1 g, 8.47 mmol) and Et_2O (8 ml) under an inert atmosphere at -78°C. The reaction was stirred for 2 h before the addition of tributyltin chloride (2.76 ml, 10.16 mmol) at 0°C, after which, the reaction was allowed to stir for 16 h. The reaction was quenched with H_2O (2 ml) and the reaction mixture was washed with saturated $NaHCO_3$ solution (3 × 10 ml). The organic fraction was dried over $MgSO_4$ before evaporation of the solvent to yield a colourless oil which was used without further purification. ^{1}H NMR peaks are consistent with previously reported data.[170] Yield = 3.44 g (99%) ^{1}H NMR (400 MHz, $CDCl_3$, ppm): δ 7.57 – 7.47 (m, 2H), 7.21 – 7.15 (m, 2H), 6.90 (d, *J* = 1 Hz, 1 H), 1.64 – 1.54 (m, 6 H), 1.38 – 1.28 (m, 6 H), 1.25 – 1.13 (m, 6 H), 0.92 – 0.88 (m, 9 H).

2-(Thiophen-2-yl)benzofuran (13)

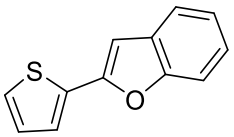

2-Bromothiophene (0.5 g, 3.06mmol), 2-tributylstannylbenzofuran (1.37 g, 3.36mmol) and toluene (30 ml) were added to a flask under an inert atmosphere and the solution was purged with N_2 for 1 h. $Pd(PPh_3)_4$ (0.247 g, 0.214mmol) was then added and the reaction was stirred at reflux for 16 h. The reaction mixture was washed with brine (3 × 30 ml) before the organic phase was dried over $MgSO_4$. The solvent was then evaporated to yield a crude solid which was purified by column chromatography (silica gel, hexane mobile phase). Some impurities

remained and the product was further purified by column chromatography using ethyl acetate as mobile phase giving the product as white crystalline solid. ^{1}H NMR spectrum consistent with previously reported data.[171] Yield = 0.375 g (61%);^{1}H NMR (400 MHz, $CDCl_3$) δ 7.59 – 7.53 (m, 1H), 7.53 – 7.47 (m, 2H), 7.38 – 7.33 (m, 1H), 7.32 – 7.26 (m, 1H), 7.26 – 7.20 (m, 1H), 7.14 – 7.09 (m, 1H), 6.88 (d, *J* = 0.8 Hz, 1H); ^{13}C NMR (101 MHz, $CDCl_3$) δ 154.8, 151.5, 133.5, 129.3, 128.1, 126.0, 124.8, 124.5, 123.3, 120.9, 111.3, 101.3; m/z (MALDI): 200.05 $[M]^+$; Melting point: 89 – 91 °C.

2-(5-Tributylstannylstannylthiophen-2-yl)benzofuran (14)

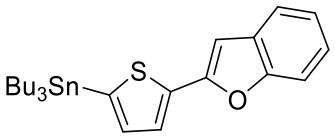

N-butyllithium (0.50ml, 1.20 mmol, 2.40 M) was added to a flask containing 2-(thiophene-2-yl)-benzofuran (0.20 g, 1.00 mmol) and Et_2O (10 ml) under an inert atmosphere at -78°C. The solution was allowed to stir for 2 h at -78°C before the addition of tributyltin chloride 0°C. The reaction mixture was stirred at room temperature for 16 h. The reaction was quenched with H_2O (2 ml) before the reaction mixture was washed with brine (3 × 10 ml). The organic phase was then dried over $MgSO_4$ and the solvent was evaporated to give a yellow/brown oil which was used without further purification. Yield = 0.49 g (99%) ^{1}H NMR (400 MHz, $CDCl_3$) δ 7.60 (d, *J* = 3.4 Hz, 1H), 7.55 – 7.51 (m, 1H), 7.51 – 7.46 (m, 1H), 7.23 (m, 2H), 7.15 (d, *J* = 3.4 Hz, 1H), 6.85 (d, *J* = 0.7 Hz, 1H), 1.66 – 1.55 (m, 6H), 1.42 – 1.30 (m, 6H), 1.19 – 1.09 (m, 6H), 0.91 (m, 9H).

3,7-Bis(2-[thiophen-2-yl]-benzofuran)-1,5-didodecylnaphthyridine-2,6-dione (ND03) (15)

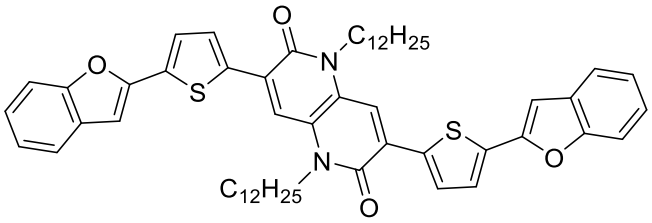

1,5-Didodecyl-3,7-dibromonaphthyridine-2,6-dione (0.4 g, 0.762 mmol), 5-tributylstannyl-2-(thiophene-2-yl)benzofuran (0.41 g, 0.838 mmol) and toluene (16 ml) were added to a flask under an inert atmosphere and the solution was purged with N_2 for 1 h. $Pd(PPh_3)_4$ (0.061 g, 0.053 mmol) was then added and the solution was stirred at reflux for 16 h. The reaction mixture was washed with brine (3 × 10 ml), dried over $MgSO_4$ and the solvent was then evaporated to yield the crude product. This was purified by column chromatography (silica gel). Ethyl acetate mobile phase was used to remove any impurities before the product was flushed through with CH_2Cl_2. The removal of solvent showed the product to be a sticky red solid. Yield = 0.229 g (42%) ^{1}H NMR (400 MHz, $CDCl_3$) δ 7.90 (s, 2H), 7.65 (d, *J* = 4.1 Hz, 2H), 7.54 (d, *J* = 7.2 Hz, 2H), 7.49 – 7.43 (m, 4H), 7.28 – 7.16 (m, 4H), 6.92 (s, 2H), 4.56 – 4.29 (m, 4H), 1.86 (m, 4H), 1.66 – 1.31 (d, *J* = 30.3 Hz, 36H), 0.87 (t, *J* = 6.8 Hz, 6H); ^{13}C NMR (101 MHz, $CDCl_3$) δ 157.5, 154.9, 151.2, 137.3, 137.1, 129.2, 126.4, 126.3, 125.4, 124.8, 124.3, 123.3, 121.1, 118.9, 111.2, 102.2, 44.2, 32.1, 29.81, 29.78, 29.52, 28.48, 27.2, 22.8, 14.3; m/z (MALDI): 894.63 $[M]^+$; Elemental Analysis: Found C, 75.34, H, 7.22, N, 3.10, Expected: C, 75.13, H, 7.43, N, 3.13. Melting point: 158 – 160°C.

3,7-Di(thiophene-2-yl)-1,5-didodecylnaphthyridine-2,6-dione (16)

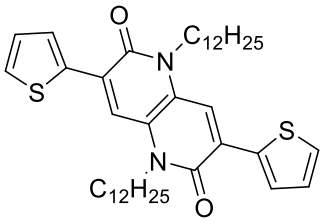

3,7-Dibromo-1,5-didodecylnaphthyridine-2,6-dione (0.25 g, 0.38 mmol) and 2-tributylstannylthiophene (0.351g, 0.94 mmol) were added to a flask under a N_2 atmosphere before the addition of anhydrous DMF (15 ml). The solution was purged with N_2 for 45 mins before the addition of $Pd(PPh_3)_4$ (0.061g, 0.053 mmol), after which the solution stirred at reflux for 16 h. The solution was diluted in CH_2Cl_2 (15 ml), washed with saturated $NaHCO_3$ solution (3 × 30 ml) and H_2O (3 × 30 ml) and dried over $MgSO_4$ evaporation of solvent. The crude product was then purified by column chromatography (silica gel, mobile phase 0% → 100% ethyl acetate: hexane) to give the product as an orange solid. Yield = 0.20 g (81%); ^{1}H NMR (400 MHz, $CDCl_3$) δ 7.97 (s, 2H), 7.78 (dd, *J* = 3.8, 1.1 Hz, 2H), 7.53 (dd, *J* = 5.1, 1.1 Hz, 2H), 7.18 (dd, *J* = 5.1, 3.8 Hz, 2H), 4.49 – 4.34 (m, 4H), 1.84 (m, 4H), 1.52 – 1.18 (m, 36H), 0.88 (t, *J* = 6.9 Hz, 6H); ^{13}C NMR (101 MHz, $CDCl_3$) δ 157.6, 137.5, 129.8, 127.1, 127.0, 126.2, 125.2, 120.0, 44.1, 32.1, 29.8, 29.7, 29.5, 28.5, 27.2, 22.8, 14.2; m/z (MALDI): 663.40 $[M]^+$; Elemental Analysis: Found: C, 72.33, H, 8.83, N, 4.32, Expected: C, 72.46, H, 8.82, N, 4.23; Melting point: 131 – 133 °C.

3-(5-Bromothiophen-2-yl)-1,5-didodecyl-7-(thiophen-2-yl)naphthyridine-2,6-dione (17)

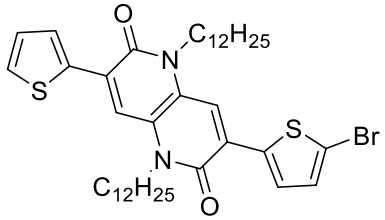

3,7-Dithiophen-2-yl-1,5-didodecylnaphthyridine-2,6-dione (0.14 g, 0.211 mmol), NBS (0.038g, 0.211 mmol) and $CHCl_3$ (5 ml) were added to a flask and the solution was allowed to

stir in the dark at room temperature for 2 h. The solution was diluted in 10 ml CH_2Cl_2 and washed with brine (3 × 20 ml) before being dried over $MgSO_4$. The solvent was evaporated to yield the crude product which was purified by column chromatography (silica gel, mobile phase 0% → 50% ethyl acetate: hexane) to give an orange solid. Yield = 0.14 g (90%) ^{1}H NMR (400 MHz, $CDCl_3$) δ 7.90 (s, 1H), 7.84 (s, 1H), 7.75 (dd, *J* = 3.8, 1.0 Hz, 1H), 7.50 (m, 1H), 7.40 (d, *J* = 4.1 Hz, 1H), 7.15 (dd, *J* = 5.1, 3.9 Hz, 1H), 7.08 (d, *J* = 4.1 Hz, 1H), 4.48 – 4.29 (m, 4H), 1.87 – 1.75 (m, 4H), 1.58 – 1.15 (m, 36H), 0.88 (t, *J* = 6.9 Hz, 6H); ^{13}C NMR (101 MHz, $CDCl_3$) δ 156.9, 156.7, 137.8, 136.7, 129.3, 128.8, 126.6, 126.5, 125.6, 125.3, 124.6, 124.5, 124.3, 119.1, 118.2, 117.7, 31.4, 31.1, 29.13, 29.06, 28.8, 27.8, 26.5, 22.2, 22.13, 22.10, 13.58, 13.55, 13.52; m/z (MALDI): 740.16 (M^+, ^{79}Br), 742.18 (M^+, ^{81}Br); Elemental Analysis: Found: C, 64.92, H, 7.91, N, 3.77, Expected: C, 64.76, H, 7.74, N, 3.78. Melting point: 146 – 148 °C.

7,7'-([2,2':5',2''-Terthiophene]-5,5''-diyl)bis(1,5-didodecyl-3-(thiophen-2-yl)naphthyridine-2,6-dione (ND04) (18)

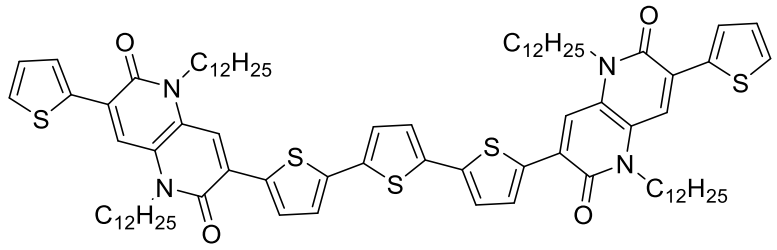

3-(5-Bromo-thiophen-2-yl)-1,5-didodecyl-7-(thiophen-2-yl)naphthyridine-2,6-dione (0.12 g, 0.162 mmol) and 2,5-bistributylstannylthiophene (0.049 g, 0.074 mmol) were added to a flask under a N_2 atmosphere before the addition of anhydrous DMF (8 ml). The solution was then degassed by purging with N_2 for 45 mins. $Pd(PPh_3)_4$ (0.012 g, 0.010 mmol) was added and the solution was stirred at reflux for 16 h. The resulting mixture was diluted with CH_2Cl_2 (25 ml) and was washed with saturated $NaHCO_3$ solution (3 × 50 ml) and H_2O (3 × 50 ml). The solution was dried over $MgSO_4$ and the solvent evaporated to yield the crude product which was purified

by column chromatography (silica gel, mobile phase 20% ethyl acetate: hexane), yielding a sticky red/purple solid. Yield = 0.14 g (33%) ^{1}H NMR (400 MHz, $CDCl_3$) δ 7.95 (s, 2H), 7.93 (s, 2H), 7.76 (d, *J* = 2.9 Hz, 2H), 7.64 (d, *J* = 4.1 Hz, 2H), 7.51 (d, *J* = 5.5 Hz, 2H), 7.23 (d, *J* = 4.0 Hz, 4H), 7.18 – 7.13 (m, 2H), 4.43 (m, 8H), 1.85 (m, 8H), 1.51 – 1.18 (m, 72H), 0.88 (m, 12H); m/z (MALDI): 1405.54 $[M]^{+}$; Elemental Analysis: Found: C, 71.33, H, 8.15, N, 4.06, Expected: C, 71.75, H, 8.32, N, 3.98.

3-Bromo-1,5-didodecylnaphthyridine-2,6-dione (19)

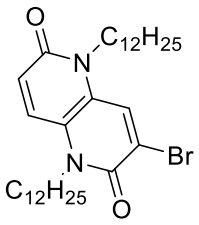

1,5-Didodecylnaphthyridine-2,6-dione (1 g, 2.00 mmol) and NBS (0.356g, 2.00 mmol) were added to a flask before the addition of $CHCl_3$ (50 ml). The reaction was allowed to stir in dark at RT for 2 h before the solution was washed with brine (3 × 50 ml) and dried over $MgSO_4$ before evaporation of the solvent. The crude product was then purified by column chromatography (silica gel, mobile phase: 20% ethyl acetate/hexane) to give a yellow solid. Yield = 0.53 g (46%); ^{1}H NMR (500 MHz, $CDCl_3$) δ 7.96 (s, 1H), 7.49 (d, *J* = 10.1 Hz, 1H), 6.85 (d, *J* = 10.1 Hz, 1H), 4.34 – 4.12 (m, 4H), 1.67 (m, 4H), 1.41 – 1.18 (m, 36H), 0.88 (m, 6H); ^{13}C NMR (101 MHz, $CDCl_3$) δ 159.2, 155.8, 129.8, 127.8, 126.0, 125.9, 125.0, 121.9, 45.1, 43.3, 32.0, 31.5, 29.7, 29.62, 29.56, 29.4, 29.3, 28.53, 28.47, 26.90, 26.86, 26.5, 22.8, 22.59, 22.57, 14.2, 14.1; m/z (MALDI): 577.50 ($[M+H]^{+}$, ^{79}Br), 579.54 ($[M+H]^{+}$, ^{81}Br). ; Elemental Analysis: Found: C, 66.70, H, 9.26, N, 4.90, Expected: C, 66.53, H, 9.26, N, 4.90. Melting point: 97 – 99°C.

5-Tributylstannyl-2,2'-bithiophene (20)

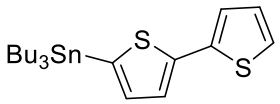

N-butyllithium (5.1 ml, 0.015 mol, 2.36 M) was added to a flask containing 2,2'-bithiophene (2 g, 0.015 mmol) and anhydrous THF (150 ml) at -78°C in a N_2 atmosphere. The solution was allowed to stir for 2 hours before the addition of tributyltin chloride (3.6 ml, 0.015 mol) at -78°C and the reaction mixture was allowed to stir for 16 h at room temperature. The reaction was then quenched with 10 ml H_2O before the organic phase was washed with $NaHCO_3$ (aq) solution (3 × 150 ml). The solution was then dried over $MgSO_4$ before evaporation of the solvent under reduced pressure to yield a yellow oil. Yield = 4.56 g (83%) The ^{1}H NMR is consistent with previously reported data.[172] ^{1}H NMR (400 MHz, CDCl3): δ 7.27 (d, 1H), 7.16 (dd, 2H), 7.04 (d, 1H), 6.97 (t, 1H), 1.54 (m, 6H), 1.31 (m, 6H), 1.10 (t, 6H), 0.89 (m, 9H).

3-(2,2'-Bithiophen]-5-yl)-1,5-didodecylnaphthyridine-2,6-dione (21)

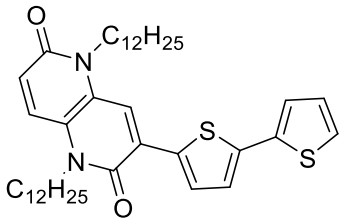

3-Bromo-1,5-didodecylnaphthyridine-2,6-dione (0.2 g, 0.35 mmol) and 5-tributylstannyl-2,2'-bithiophene (0.35 g, 0.77 mmol) were added to a flask containing DMF (15 ml) and the solution was degassed by bubbling N_2 for 45 mins. $Pd(PPh_3)_4$ (0.026 g, 0.022 mmol) was then added to the mixture which was stirred at reflux for 16 h. The solution was then diluted with Et_2O (20 ml) washed with saturated $NaHCO_3$ (aq) solution (3 × 50 ml) before the organic phase was dried over $MgSO_4$. The solvent was evaporated and the crude material purified by column chromatography (silica gel, mobile phase: 20% ethyl acetate/hexane) giving an orange solid . Yield = 0.13 g (42%); ^{1}H NMR (500 MHz, $CDCl_3$) δ 7.94 (s, 1H), 7.65 (d, *J* = 4.0 Hz, 1H),

7.54 (d, *J* = 10.1 Hz, 1H), 7.31 (dd, *J* = 3.6, 1.1 Hz, 1H), 7.25 (dd, *J* = 7.2, 2.6 Hz, 2H), 7.05 (dd, *J* = 5.1, 3.6 Hz, 1H), 6.83 (d, *J* = 10.0 Hz, 1H), 4.33 (m, 4H), 1.83 – 1.73 (m, 4H), 1.55 – 1.20 (m, 36H), 0.87 (t, *J* = 6.9 Hz, 6H). ^{13}C NMR (101 MHz, $CDCl_3$) δ 159.7, 157.2, 141.8, 137.5, 135.6, 128.2, 127.5, 127.4, 126.8, 126.7, 125.1, 124.9, 124.2, 123.8, 123.5, 119.4, 44.3, 43.1, 32.0, 29.8, 29.74, 29.69, 29.49, 29.47, 28.7, 28.5, 27.14, 27.05, 22.8, 14.2; m/z (MALDI): 662.96 $[M]^+$; Elemental Analysis: Found, C, 72.48, H, 8.75, N, 4.20, Expected: C, 72.46, H, 8.82, N, 4.23. Melting point: 160 – 162°C.

3-([5'-Bromo-2,2'-bithiophen]-5-yl)-1,5-didodecylnaphthyridine-2,6-dione (22)

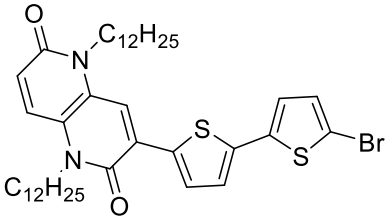

Compound 21 (0.08 g, 0.121 mmol) NBS (0.021 g, 0.121 mmol) and $CHCl_3$ (10 mL) were added to a flask and the contents were stirred at room temperature for 16 h in the absence of light. The reaction mixture was diluted in 10 mL $CHCl_3$ and washed with brine (3 × 20 mL). The organic phase was dried over $MgSO_4$ and the solvent evaporated to yield the crude product which was purified by column chromatography (silica gel, mobile phase: 15% ethyl acetate/hexane), yielding an orange solid. Yield = 0.077 g (87%); ^{1}H NMR (400 MHz, $CDCl_3$) δ 7.94 (s, 1H), 7.62 (d, *J* = 4.0 Hz, 1H), 7.54 (d, *J* = 10.0 Hz, 1H), 7.17 (d, *J* = 4.0 Hz, 1H), 7.02 (dd, *J* = 17.3, 3.8 Hz, 2H), 6.84 (d, *J* = 10.1 Hz, 1H), 4.44 – 4.20 (m, 4H), 1.87 – 1.69 (m, 4H), 1.54 – 1.15 (m, 36H), 0.88 (t, *J* = 6.3 Hz, 6H); ^{13}C NMR (101 MHz, $CDCl_3$) δ 159.7, 157.2, 140.7, 139.0, 136.0, 131.1, 127.5, 127.2, 126.8, 126.5, 125.0, 124.2, 124.1, 123.7, 119.6, 111.8, 44.4, 43.1, 32.1, 31.7, 29.83, 29.80, 29.75, 29.7, 29.50, 29.47, 28.7, 28.5, 27.13, 27.06, 22.8, 14.3; m/z (MALDI): 740.00 (M^+, ^{79}Br), 742.00 (M^+, ^{81}Br); Elemental Analysis: Found, C, 64.86, H, 7.79, N, 3.70, Expected: C, 64.76, H, 7.74 N, 3.78. Melting point: 170 – 172°C.

3,3'-([2,2':5',2'':5'',2''':5''',2''''-Quinquithiophene]-5,5''''-diyl)bis(1,5-didodecylnaphthyridine-2,6-dione) (ND05) (23)

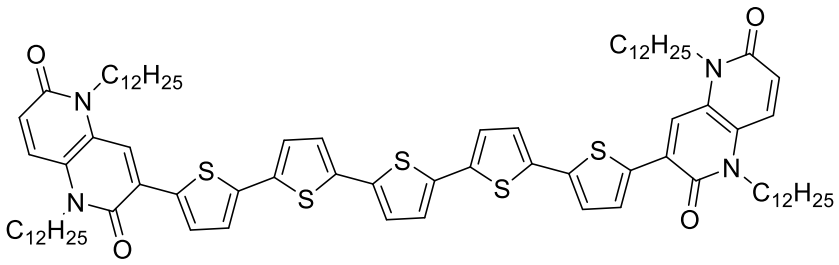

Compound 22 (0.075 g, 0.1 mmol) and 2,5-bis(tributylstannyl)thiophene (0.030 g, 0.046 mmol) were added to a microwave vial which was degassed and purged with N_2. DMF (7 ml) was then added and the solution was degassed by bubbling N_2 through for 45 mins. This was followed by the addition of $Pd(PPh_3)_4$ and the vial was closed with a cap and the reaction was heated at 160 °C for 2 h in the microwave reactor. The reaction mixture was then diluted with CH_2Cl_2 (20 ml) before being washed with saturated $NaHCO_3$ (aq) solution (2 × 25 ml) and brine (2 × 25 ml). The organic phase was then dried over $MgSO_4$ before the evaporation of the solvent under reduced pressure. The crude material was then purified by column chromatography (silica gel, mobile phase: CH_2Cl_2) giving the pure product as a sticky red/purple solid. Yield = 0.04 g (63%); ^{1}H NMR (500 MHz, $CDCl_3$) δ 7.94 (s, 2H), 7.65 (d, *J* = 4.1 Hz, 2H), 7.53 (d, *J* = 10.2 Hz, 2H), 7.25 – 7.20 (m, 4H), 7.15 – 7.08 (m, 4H), 6.83 (d, *J* = 10.0 Hz, 2H), 4.42 – 4.23 (m, 8H), 1.78 (dd, *J* = 14.9, 7.9 Hz, 8H), 1.53 – 1.18 (m, 72H), 0.88 (t, *J* = 7.0 Hz, 12H) ^{13}C NMR (101 MHz, $CDCl_3$) δ 157.4, 141.6, 137.5, 135.8, 128.2, 126.4, 126.2, 125.2, 125.0, 124.0, 123.4, 118.6, 44.1, 32.1, 29.80, 29.77, 29.5, 28.4, 27.2, 22.8, 14.2. m/z (MALDI): 1405.61 $[M]^+$; Elemental Analysis: Found, C, 71.29, H, 7.93, N, 4.13, Expected: C, 71.75, H, 8.32, N, 3.98. There was no observable melting point between 0 – 360°C.

3,7-Bis(5-bromothiophen-2-yl)-1,5-didodecylnaphthyridine-2,6-dione (24)

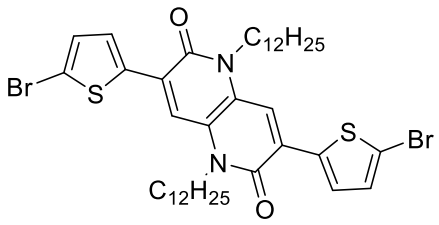

3,7-Dithiophen-2-yl-1,5-didodecylnaphthyridine-2,6-dione (0.6 g, 0.90 mmol), NBS (0.35 g, 1.98 mmol) and chloroform (20 ml) were added to a flask and the contents were stirred at room temperature in the absence of light for 16 h. The solution was washed with brine (3 × 30 ml) and was dried over $MgSO_4$ before the solvent was evaporated. The crude compound was then purified by column chromatography (silica gel, mobile phase: 40% ethyl acetate/hexane) to yield an orange solid. Yield = 0.53 g (71%). ^{1}H NMR (400 MHz, $CDCl_3$) δ 7.87 (s, 2H), 7.44 (d, *J* = 4.1 Hz, 2H), 7.12 (d, *J* = 4.1 Hz, 2H), 4.51 – 4.28 (m, 4H), 1.81 (m, 4H), 1.70 – 1.15 (m, 36H), 0.88 (t, *J* = 6.8 Hz, 6H); ^{13}C NMR (101 MHz, $CDCl_3$) δ 157.5, 138.3, 129.6, 126.4, 125.3, 118.8, 118.6, 44.1, 32.1, 29.8, 29.7, 29.47, 28.46, 27.1, 22.8, 14.2; m/z (MALDI): 818.00 (M^+, ^{79}Br × 2), 820.26 (M^+, ^{79}Br + ^{81}Br), 822.05 ($M^{+,}$ ^{81}Br × 2); Elemental Analysis: Found: C, 58.15, H, 6.84, N, 3.19; Expected: C, 58.53, H, 6.88, N, 3.41. Melting Point: 150 – 152 °C

3,7-Bis(5,5'-bithiophen-2-yl)-1,5-didodecylnaphthyridine-2,6-dione (25)

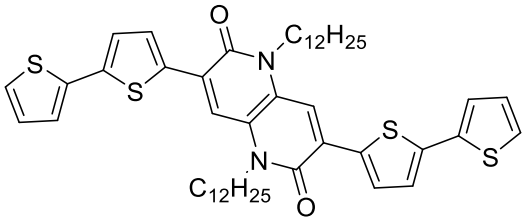

Compound 24 (0.5g, 0.609 mmol) and 2-tributylstannylthiophene (0.455 g, 1.22 mmol) were added to a flask under a N_2 atmosphere before DMF (30 ml) was added to the reaction vessel. The solution was degassed by purging with N_2 for 45 mins before $Pd(PPh_3)_4$ (0.098 g, 0.085

mmol) was added. The reaction mixture was stirred at reflux for 16 h. The solution was diluted with CH_2Cl_2 (30 ml) and washed with $NaHCO_3$ (3 × 60 ml) and H_2O (3 × 60 ml) before drying over $MgSO_4$ and evaporation of solvent. The crude product was then purified by column chromatography (silica gel, mobile phase: 50% ethyl acetate/hexane) giving a red solid. Yield = 0.42 g (82%).^{1}H NMR (400 MHz, $CDCl_3$) δ 7.84 (s, 2H), 7.57 (d, *J* = 2.8 Hz, 2H), 7.22 (m, 6H), 7.02 (m, 2H), 4.39 (m, 4H), 1.83 (m, 4H), 1.35 (m, 36H), 0.87 (m, 6H);^{13}C NMR (101 MHz, $CDCl_3$) δ 157.46, 141.69, 137.52, 135.82, 128.21, 126.41, 126.30, 125.22, 125.05, 124.09, 123.45, 118.67, 44.10, 32.06, 29.81, 29.77, 29.51, 28.42, 27.20, 22.83, 14.25; m/z (MALDI): 826.29 $[M]^+$; Elemental Analysis: Found: C, 69.34; H, 7.63; N, 3.45; Calculated: C, 69.69; H, 7.55; N, 3.67. Melting point: 184 – 186°C.

3-([2,2'-Bithiophen]-5-yl-7-(5'-bromo-[2,2'-bithiophen]-5-yl-1,5-didodecylnaphthyridine-2,6-dione (26)

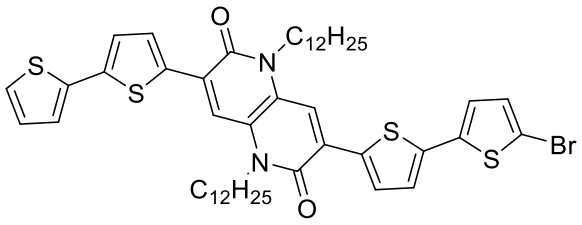

Compound 25 (0.35 g, 0.423 mmol) and NBS (0.075g, 0.423 mmol) were added to a flask before the addition of $CHCl_3$ (20 ml). The solution was allowed to stir in dark at RT for 2 h before being washed with brine (3 × 20 ml), dried over $MgSO_4$ and solvent was evaporated to yield the crude product which was purified by column chromatography (mobile phase: 50% ethyl acetate/hexane) to give the product as a red solid. Yield = 0.249 g (65%) ^{1}H NMR (400 MHz, $CDCl_3$) δ 7.91 (d, *J* = 2.6 Hz, 2H), 7.64 (d, *J* = 4.1 Hz, 1H), 7.60 (d, *J* = 4.1 Hz, 1H), 7.31 (dd, *J* = 3.6, 1.1 Hz, 1H), 7.26 – 7.20 (m, 2H), 7.16 (dd, *J* = 4.0, 0.8 Hz, 1H), 7.07 – 7.01 (m, 2H), 7.00 (s, 1H), 4.55 – 4.30 (m, 4H), 1.95 – 1.75 (m, 4H), 1.53 – 1.15 (m, 36H), 0.87 (dd, *J* = 7.3, 6.4 Hz, 6H); ^{13}C NMR (101 MHz, $CDCl_3$) δ 174.2, 172.3, 170.1, 168.9, 156.8,

143.3, 141.2, 140.0, 139.9, 138.8, 135.5, 135.1, 130.4, 127.6, 125.9, 125.8, 125.7, 125.6, 124.74, 124.66, 124.51, 124.45, 123.5, 123.0, 122.9, 118.0, 111.2, 43.5, 31.4, 29.2, 29.12, 29.10, 28.9, 27.8, 26.5, 22.2, 13.60; m/z (MALDI): 904.14 (M^+, ^{79}Br), 906.14 (M^+, ^{81}Br); Elemental Analysis: Found C, 63.74, H, 6.82, N, 3.05, Expected: C, 63.62, H, 6.79, N, 3.09. Melting point: 206 – 208 °C

7,7'-([2,2':5',2'':5'',2''':5''',2''''-Quinquithiophene]-5,5''''bis(3-([2,2'-bithiophen]-5-yl)-1,5-didodecylnaphthyridine-2,6-dione (ND06) (27)

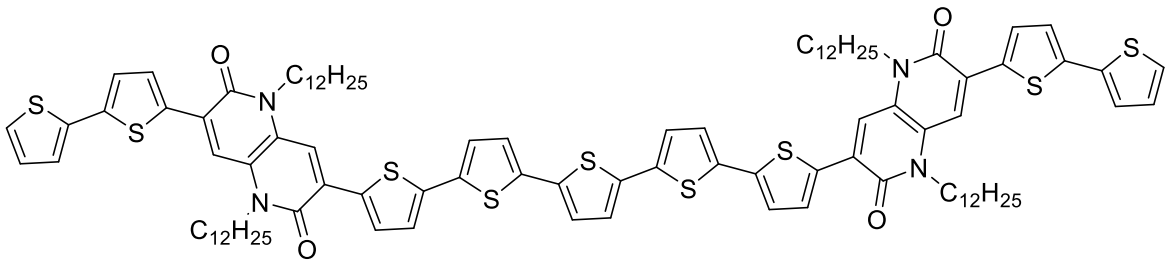

Compound 26 (0.22g, 0.243 mmol) and 2,5-bis(tributylstannyl)thiophene (0.073 g, 0.11 mmol) were added to a flask under N_2 before the addition of DMF (12 ml). The solution was then degassed by N_2 purging for 45 mins before the addition of anhydrous DMF (12 ml). The reaction mixture was stirred for 16 h at reflux. The solution was diluted with CH_2Cl_2 (10 ml) and washed with $NaHCO_3$ (3 × 30 ml) and H_2O (3 × 30 ml) before drying over $MgSO_4$ and evaporation of solvent. The crude product was then purified by column chromatography (silica gel, mobile phase: 0→100% CH_2Cl_2: Hexane) yielding a sticky, dark purple solid. It was not possible to obtain a ^{13}C NMR due to poor solubility of the compound. Yield = 0.088 g (46%); ^1H NMR (400 MHz, $CDCl_3$) δ 7.95 (m, 4H), 7.73 – 7.49 (m, 10H), 7.26 – 7.08 (m, 10H), 4.40 (m, 8H), 1.83 (m, 8H), 1.54 – 1.09 (m, 72H), 0.90 (t, *J* = 6.3 Hz, 12H); m/z (MALDI): 1734.49 $[M]^+$; Elemental Analysis: Found: C, 69.65, H, 7.02, N, 3.12, Expected: C, 69.24, H, 7.21, N, 3.23.

3-Bromo-1-dodecyl-6-dodecoxynaphthyridine-2one (28)

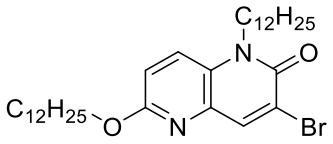

1-Dodecyl-6-decoxynaphthyridine-2-one (compound 2) (4 g, 8.02 mmol) was added to a flask before the addition of chloroform (33 ml) and acetic acid (14.5 ml). The flask was then cooled to 0^{o}C before the dropwise addition of bromine (1.24 ml, 24.06 mmol). The reaction was then refluxed for 16 h. The reaction mixture was diluted with CH_2Cl_2 (40 ml) before being washed with brine (3 × 100 ml). The crude product was then purified by column chromatography (silica gel, 1:5 CH_2Cl_2/hexane mobile phase) to yield the product as a yellow solid. Yield = 4.40 g (95%). ^{1}H NMR (500 MHz, $CDCl_3$) δ 8.22 (s, 1H), 7.59 (d, *J* = 9.2 Hz, 1H), 6.98 (d, *J* = 9.2 Hz, 1H), 4.34 (t, *J* = 6.7 Hz, 2H), 4.31 – 4.24 (m, 2H), 1.85 – 1.68 (m, 4H), 1.50 – 1.21 (m, 38H), 0.88 (t, *J* = 6.9 Hz, 6H) ^{13}C NMR (101 MHz, $CDCl_3$) δ 159.6, 157.4, 141.2, 134.7, 130.8, 125.7, 121.5, 114.7, 77.5, 77.2, 76.8, 66.7, 44.5, 32.0, 29.78, 29.75, 29.72, 29.66, 29.63, 29.60, 29.50, 29.45, 29.0, 28.0, 27.0, 26.2, 22.8, 14.21, 14.18, 14.15; m/z (MALDI): 576.37 (M^+, ^{79}Br), 578.37 (M^+, ^{81}Br); Elemental analysis: Found: C, 66.40; H, 9.36; N, 4.85; Expected: C, 66.53; H, 9.25; N, 4.85. Melting point: 61-63 °C.

3-(Thiophen-2-yl)-1-dodecyl-6-dodecoxynaphthyridine-2-one (29)

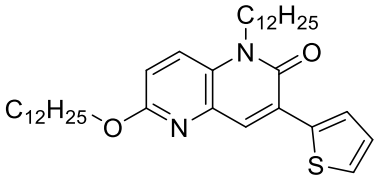

Compound 28 (2.5 g, 4.33 mmol) and 2-tributylstannylthiophene (1.51 ml, 4.76 mmol) were added to a round bottom flask which was subsequently evacuated and purged with N_2 before the addition of anhydrous DMF (155 ml). The mixture was then degassed by bubbling nitrogen

through the solution for 45 minutes before the addition of $Pd(PPh_3)_4$ (0.35 g, 0.303 mmol). The reaction was stirred at reflux for 16 h. The reaction mixture was allowed to cool, diluted in CH_2Cl_2 (100 ml) and washed with saturated aqueous $NaHCO_3$ solution (3 × 250 ml) and H_2O (2 × 250 ml). The solvent was removed by evaporation and the crude product was purified by column chromatography (silica gel, hexane mobile phase) to give a yellow solid. Yield = 1.85 g (73%). ^{1}H NMR (400 MHz, $CDCl_3$) δ 8.22 (s, 1H), 7.83 (dd, *J* = 3.8, 1.1 Hz, 1H), 7.60 (d, *J* = 9.2 Hz, 1H), 7.48 (dd, *J* = 5.1, 1.1 Hz, 1H), 7.14 (dd, *J* = 5.1, 3.8 Hz, 1H), 6.93 (d, *J* = 9.1 Hz, 1H), 4.39 (t, *J* = 6.7 Hz, 2H), 4.36 – 4.27 (m, 2H), 1.87 – 1.71 (m, 4H), 1.53 – 1.19 (m, 36H), 0.89 (t, *J* = 6.9 Hz, 6H); ^{13}C NMR (101 MHz, $CDCl_3$) δ 159.7, 159.2, 137.2, 135.3, 132.3, 130.0, 128.9, 128.2, 126.7, 126.0, 125.2, 113.9, 66.5, 43.6, 32.1, 29.81, 29.75, 29.69, 29.66, 29.63, 29.60, 29.56, 29.51, 29.47, 29.4, 29.2, 28.1, 28.0, 27.2, 27.0, 26.2, 22.8, 17.6, 14.2, 13.7; m/z (MALDI): 580.48 $[M]^+$ Elemental Analysis: Found: C, 74.20; H, 9.66; N, 4.72; Expected: C, 74.43; H, 9.72; N, 4.82. Melting point: 64-66 °C.

3-(5-Bromothiophen-2-yl)-1-dodecyl-6-dodecoxynaphthyridine-2-one (30)

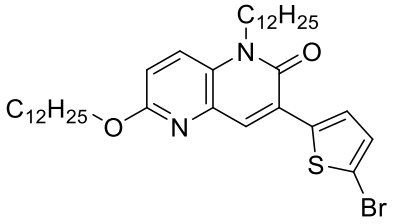

Compound 29 (1.75 g, 3.02 mmol), NBS (0.591 g, 3.32 mmol) and chloroform (125 ml) were added to a round bottom flask and the reaction mixture was allowed to stir at RT for 16 h in the absence of light. It was then washed with brine (3 × 150 ml) and the solvent was then evaporated before purification by column chromatography (silica gel, 1:5 CH_2Cl_2/Hexane mobile phase) to give a yellow solid. Yield = 1.79 g (90%). ^{1}H NMR (400 MHz, $CDCl_3$) δ 8.19 (s, 1H), 7.62 (d, *J* = 9.2 Hz, 1H), 7.53 (d, *J* = 4.1 Hz, 1H), 7.11 (d, *J* = 4.1 Hz, 1H), 6.96 (d, *J* = 9.1 Hz, 1H), 4.39 (t, *J* = 6.7 Hz, 2H), 4.36 – 4.27 (m, 2H), 1.87 – 1.71 (m, 4H), 1.53 – 1.17 (m, 36H), 0.89 (t, *J* = 6.9 Hz, 6H); ^{13}C NMR (101 MHz, $CDCl_3$) δ 159.9, 159.1, 138.2, 135.2,

131.4, 130.0, 129.3, 127.5, 125.3, 125.1, 117.2, 114.2, 66.6, 43.7, 32.1, 29.82, 29.75, 29.7, 29.6, 29.5, 29.2, 28.1, 27.2, 26.2, 22.8, 14.2; m/z (MALDI): 658.29 (M^+, ^{79}Br), 660.29 (M^+, ^{81}Br); Elemental Analysis: Found: C, 65.48; H, 8.35; N, 4.31; Expected: C, 65.53; H, 8.40; N, 4.31. Melting point: 59-61 °C.

3,3'-([2,2':5',2''-Terthiophene]-5,5''-diyl)bis(1-dodecyl-6-dodecoxynaphthyridine-2-one ($(NDO)_2$-3T) (31)

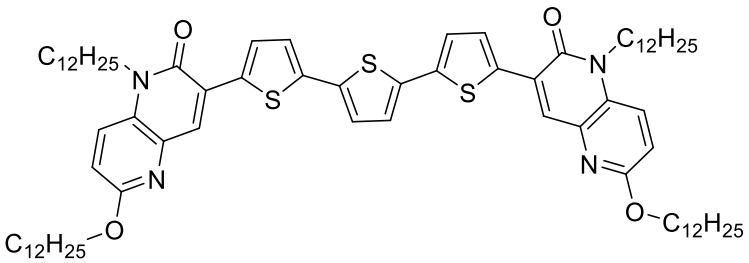

Compound 30 (0.747 g, 1.07 mmol) and 2,5-bis(trimethylstannyl)thiophene (0.2 g, 0.49 mmol) were added to a flask which was evacuated and purged before the addition of anhydrous DMF (13 ml). The solution was then degassed using N_2 for 45 minutes before the addition of $Pd(PPh_3)_4$ (0.079g, 0.068 mmol). The reaction was stirred at reflux for 16 h. Once cooled to room temperature, the solution was diluted with CH_2Cl_2 (15 ml) and washed with saturated $NaHCO_3$ (aq) solution (3 × 40 ml) and H_2O (2 × 40 ml). The solvent was then removed by evaporation and the compound was purified by column chromatography (silica gel, 1:2.5 ethyl acetate/hexane mobile phase), yielding a sticky red solid. Yield = 0.13 g (21%). ^1H NMR (400 MHz, $CDCl_3$) δ 8.21 (s, 2H), 7.72 (d, *J* = 4.0 Hz, 2H), 7.60 (d, *J* = 9.2 Hz, 2H), 7.21 (d, *J* = 4.3 Hz, 4H), 6.92 (d, *J* = 9.1 Hz, 2H), 4.39 (t, *J* = 6.7 Hz, 4H), 4.36 – 4.28 (m, 4H), 1.87 – 1.72 (m, 8H), 1.54 – 1.19 (m, 72H), 0.89 (t, *J* = 6.7 Hz, 12H); ^{13}C NMR (101 MHz, $CDCl_3$) δ 159.2, 158.5, 139.9, 136.2, 135.22, 134.7, 130.8, 129.3, 127.2, 125.9, 124.5, 124.1, 122.8, 113.2, 65.9, 43.1, 31.4, 29.2, 29.1, 29.1, 28.9, 28.9, 28.8, 28.5, 27.5, 26.6, 25.6, 22.2, 13.6; m/z (MALDI):

1241.99 $[M]^+$; Elemental Analysis: Found: C, 73.06, H, 8.98, N, 4.74, Expected: C, 73.50, H, 9.09, N, 4.51.

3,3'-(Benzo[1,2,5]thiadiazole-4,7-diylbis(thiophene,5,2-diyl))bis(1-dodecyl-6-dodecoxynaphthyridine-3-one) ((NDO-T)$_2$-BT) (32)

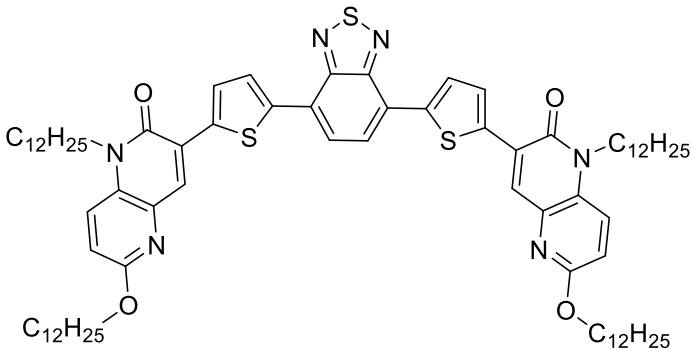

Compound 30 (1.8 g, 2.73 mmol) and 2,1,3-benzothiadiazole-4,7-bis(boronic acid pinacol ester) (0.33g, 0.85 mmol) and K_2CO_3 (0.352 g, 2.55 mmol) were added to a flask which was evacuated and purged with N_2 before the addition of anhydrous THF (20 ml) and degassed H_2O (0.7 ml). The solution was degassed for using N_2 for 45 minutes before the addition of $Pd(PPh_3)_4$ (0.196 g, 0.17 mmol). The reaction mixture was then stirred at reflux for 16 h. The mixture was allowed to cool to room temperature before being diluted with THF (20 ml) before being washed with brine (3 × 50 ml) before solvent was evaporated. The crude product was then purified by column chromatography (silica gel, 1:5 CH_2Cl_2/Hexane mobile phase) to give a sticky, dark green solid. Yield = 0.29 g (26 %). ^{1}H NMR (400 MHz, $CDCl_3$) δ 8.26 (s, 2H), 8.23 (d, *J* = 4.1 Hz, 2H), 7.97 (s, 2H), 7.87 (d, *J* = 4.1 Hz, 2H), 7.59 (d, *J* = 9.2 Hz, 2H), 6.91 (d, *J* = 9.1 Hz, 2H), 4.45 – 4.30 (m, 8H), 1.89 – 1.72 (m, 8H), 1.55 – 1.20 (m, 72H), 0.89 (t, *J* = 6.6 Hz, 12H); ^{13}C NMR (101 MHz, $CDCl_3$) δ 159.1, 158.5, 152.2, 141.9, 137.3, 134.6, 131.3, 129.5, 127.3, 127.1, 126.3, 125.5, 125.2, 124.5, 113.3, 65.9, 43.1, 31.4, 29.2, 29.1, 29.0, 28.9, 28.9, 28.6, 27.5, 26.6, 25.6, 22.2, 13.6; m/z (MALDI): 1293.96 $[M]^+$; Elemental Analysis: Found: C, 72.19; H, 8.72; N, 6.56; Calculated: C, 72.40; H, 8.72; N, 6.49. Melting point: 156 - 158 °C.

3-(5'-(Benzofuran-2-yl)-[2,2'-bithiophen]-5-yl)-1-dodecyl-6-dodceoxynaphthyridine-2-one (NDO-2T-BF) (33)

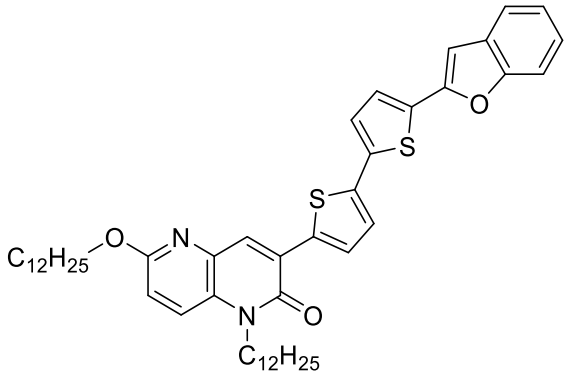

Compound 30 (0.35 g, 0.53 mmol) and compound 14 (0.313 g, 0.64 mmol) were added to a flask which was purged with N_2 and evacuated. Anhydrous DMF (15 ml) was then added to flask and the mixture was subsequently degassed by bubbling with N_2 for 45 mins. $Pd(PPh_3)_4$ (0.043 g, 0.037 mmol) was then added to the flask and the reaction mixture stirred at reflux for 16 h. Once cooled, the solution was diluted with diethyl ether (100 ml) and washed with saturated $NaHCO_3$ solution (2 × 60 ml) and brine (2 × 60 ml). The solvent was then evaporated to yield the crude product. This was purified by column chromatography (silica gel, 0%→50% CH_2Cl_2: hexane) to give a red crystalline solid. Yield = 0.280 g (68%). ^{1}H NMR (400 MHz, $CDCl_3$) δ 8.22 (s, 1H), 7.72 (d, *J* = 4.0 Hz, 1H), 7.59 (d, *J* = 9.2 Hz, 1H), 7.56 – 7.51 (m, 1H), 7.51 – 7.46 (m, 1H), 7.39 (d, *J* = 3.8 Hz, 1H), 7.30 – 7.20 (m, 4H), 6.92 (d, *J* = 9.1 Hz, 1H), 6.85 (d, *J* = 0.7 Hz, 1H), 4.36 (m, 4H), 1.87 – 1.71 (m, 4H), 1.53 – 1.19 (m, 36H), 0.88 (t, *J* = 6.9, 6H); ^{13}C NMR (101 MHz, $CDCl_3$) δ 159.9, 159.1, 154.8, 151.1, 140.2, 138.3, 136.3, 135.3, 132.0, 131.6, 130.1, 129.3, 127.7, 126.5, 125.6, 125.2, 124.5, 123.7, 123.3, 120.9, 114.0, 111.2, 101.4, 66.6, 43.8, 32.1, 29.8, 29.8, 29.7, 29.6, 29.53, 29.50, 29.2, 28.2, 27.2, 26.3, 22.8, 14.3; m/z (MALDI): 779.11 $[M]^+$; Elemental analysis: Found: C, 73.79; H, 7.72; N, 3.76; Calculated: C, 73.99; H, 8.02; N, 3.60. Melting point: 98 - 100 °C

3-([2,2'-Bithiophen]-5-yl)-1-dodecyl-6-dodecoxynaphthyridine-2-one (34)

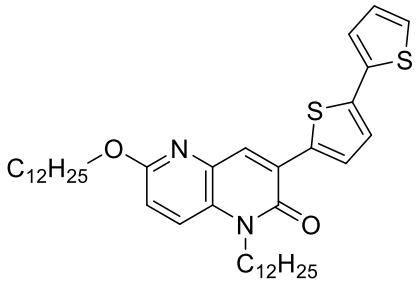

Compound 28 (0.5 g, 0.87 mmol) and 5-tributylstannyl-2,2'-bithiophene (0.433 g, 0.95 mmol) were added to a flask which was evacuated and purged with N_2. Anhydrous DMF (31 ml) was then added before the solution was degassed by bubbling through N_2 for 45 mins. $Pd(PPh_3)_4$ (0.07 g, 0.061 mmol) was then added and the reaction was stirred at reflux for 16 h. The solution was then diluted with diethyl ether (50 ml) before being washed with saturated $NaHCO_3$ (aq) solution (2 × 100 ml) and brine (2 × 100 ml). The organic phase was then dried over $MgSO_4$, the solvent evaporated under reduced pressure and the crude product purified by column chromatography (silica gel, 1:1 CH_2Cl_2: hexane mobile phase) giving the product as a yellow crystalline solid. Yield = 0.44 g (77 %). ^{1}H NMR (400 MHz, $CDCl_3$) δ 8.20 (s, 1H), 7.70 (d, *J* = 3.7 Hz, 1H), 7.59 (d, *J* = 9.1 Hz, 1H), 7.28 (d, *J* = 2.7 Hz, 1H), 7.22 (s, 2H), 7.09 – 6.97 (m, 1H), 6.92 (d, *J* = 9.0 Hz, 1H), 4.35 (m, 4H), 1.92 – 1.66 (m, 4H), 1.54 – 1.07 (m, 36H), 0.88 (t, *J* = 6.1 Hz, 6H); ^{13}C NMR (101 MHz, $CDCl_3$) δ 159.9, 159.2, 140.8, 137.9, 135.7, 135.4, 131.5, 123.0, 128.1, 128.0, 126.5, 125.2, 124.7, 123.9, 123.4, 113.9, 66.6, 43.7, 32.1, 29.8, 29.77, 29.7, 29.6, 29.54, 29.50, 29.2, 28.2, 26.3, 22.8, 14.3; m/z (MALDI): 663.03 $[M]^+$; Elemental Analysis: Found: C, 72.28; H, 8.78; N, 4.22; Expected: C, 72.46; H, 8.78; N, 4.22. Melting point: 84 – 86 °C.

3-([5-Bromo-2,2'-bithiophene-5'-yl)-1-dodecyl-6-dodecoxynaphthyridine-2-one (35)

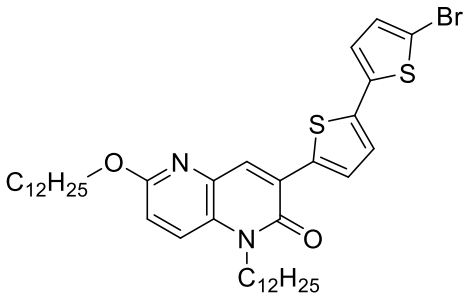

Chloroform (6 ml) and acetic acid (6 ml) were added to a flask containing compound 34 (0.255 g, 0.38 mmol) and NBS (0.075 g, 0.42 mmol) and the solution stirred for 16 h at room temperature in the absence of light. The reaction mixture was diluted with CH_2Cl_2 (20 ml) before being washed with 10% w/v KOH (aq) solution (3 × 30 ml). The organic phase was then dried over $MgSO_4$ before evaporation of the solvent to yield the crude product. This was then purified by column chromatography (silica gel, 3:2 CH_2Cl_2: hexane mobile phase) giving the product as a yellow solid. Yield = 0.23 g (81%); ^{1}H NMR (400 MHz, $CDCl_3$) δ 8.22 (s, 1H), 7.68 (d, *J* = 4.0 Hz, 1H), 7.61 (d, *J* = 9.2 Hz, 1H), 7.15 (d, *J* = 4.0 Hz, 1H), 7.02 (d, *J* = 3.9 Hz, 1H), 6.97 (d, *J* = 9.1 Hz, 1H), 6.96 – 6.91 (m, 1H), 4.35 (m, 4H), 1.86 – 1.71 (m, 4H), 1.52 – 1.15 (m, 36H), 0.88 (t, *J* = 6.8 Hz, 6H); ^{13}C NMR (101 MHz, $CDCl_3$) δ 159.9, 159.1, 145.1, 139.7, 139.5, 136.2, 135.3, 131.7, 131.0, 130.1, 127.7, 125.3, 123.9, 123.6, 114.1, 111.2, 66.6, 43.8, 32.1, 29.8, 29.8, 29.7, 29.6, 29.5, 29.19, 29.16, 28.1, 27.2, 26.3, 22.8, 14.3; m/z (MALDI): 740.81 (M^+, ^{79}Br), 742.80 (M^+, ^{81}Br); Elemental Analysis: Found: C, 64.42; H, 7.56; N, 3.61; Expected: C, 64.76; H, 7.74; N, 3.78. Melting point: 87 – 89 °C.

3-(5’’-Benzofuran-2-yl)-[2,2’:5’,2’’-terthiophen]-5-yl)-1-dodecyl-6-dodecoxynaphthyridine-2-one (NDO-3T-BF) (36)

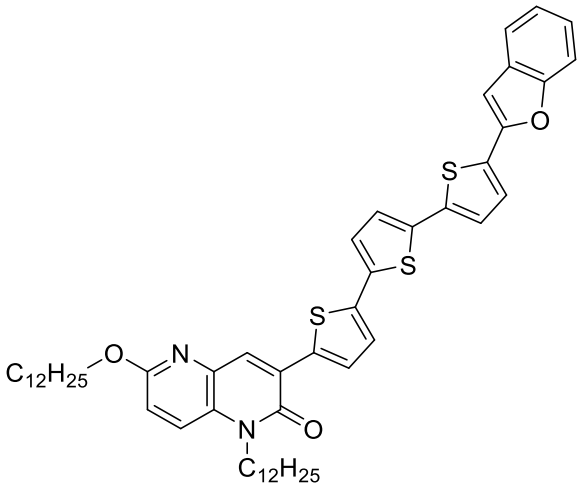

Compound 35 (0.18 g, 0.243 mmol) and compound 14 (0.143 g, 0.292 mmol) were added to a flask which was evacuated and purged with N_2. This was followed by the addition of anhydrous DMF (10 ml) and the solution was degassed by bubbling through N_2 gas for 45 mins. $Pd(PPh_3)_4$ (0.02 g, 0.017 mmol) was then added to solution and the reaction mixture was stirred at reflux for 16 h. The solution was diluted with diethyl ether (70 ml) and washed with sat. $NaHCO_3$ (aq) (2 × 50 ml) solution and brine (2 × 50 ml) before being dried over $MgSO_4$. The solvent was then evaporated to yield the crude product which was purified by column chromatography (silica gel, 2:3 CH_2Cl_2: hexane mobile phase) to give a red powder. Yield = 0.11 g (53%). ^{1}H NMR (400 MHz, $CDCl_3$) δ 8.23 (s, 1H), 7.73 (d, *J* = 4.0 Hz, 1H), 7.65 – 7.47 (m, 3H), 7.39 (d, *J* = 4.5 Hz, 1H), 7.32 – 7.22 (m, 4H), 7.16 (t, *J* = 3.5 Hz, 2H), 6.94 (d, *J* = 9.1 Hz, 1H), 6.87 (d, *J* = 0.7 Hz, 1H), 4.38 (m, 4H), 1.91 – 1.73 (m, 4H), 1.56 – 1.20 (m, 36H), 0.91 (t, *J* = 6.9 Hz, 6H) ^{13}C NMR (101 MHz, $CDCl_3$) δ 159.8, 159.1, 154.8, 150.9, 140.2, 137.7, 137.3, 136.0, 135.9, 135.3, 131.9, 131.5, 130.0, 129.3, 127.7, 126.5, 125.5, 125.2, 125.0, 124.6, 124.4, 123.5, 123.3, 120.9, 113.9, 111.2, 101.5, 66.6, 43.7, 32.1, 29.8, 29.8, 29.7, 29.6, 29.52, 29.49, 29.2,

28.1, 27.2, 26.3, 22.8, 14.3; m/z (MALDI): 861.04 $[M]^+$; Elemental Analysis: Found: C, 72.06, H, 7.33, N, 3.00; Expected: C, 72.52, H, 7.49, N, 3.25. Melting point: 82 - 84 °C.

Ethyl 3-cyano-2oxo-3-(thiophen-2-yl)propanoate (37)

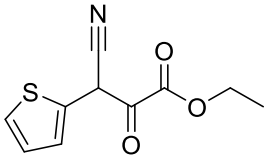

Anhydrous ethanol (18 ml, 308 mmol) was added to a flask under a nitrogen atmosphere. The flask was cooled to 0°C before the addition of sodium (0.386 g, 16.8 mmol) and the solution was stirred until all the metal had dissolved to form a saturated sodium ethoxide solution. Thiophene-2-acetonitrile (2.0 g, 16.2 mmol) and diethyl oxalate (5.7 g, 39.0 mmol) were added and the mixture was stirred at reflux for 2 h. The solution was diluted using water (40 ml) before extraction with diethyl ether (3 ×20 ml). The aqueous phase was then acidified using acetic acid which resulted in the formation of green needle crystals which were collected by filtration: Yield = 1.34 g (37%):^{1}H NMR (400 MHz, $CDCl_3$, ppm): 7.66 (dd, *J*= 4, 1.2 Hz, 1H), 7.55 (dd, *J*= 4, 1.2 Hz, 1H), 7.51 (s, 1H), 7.15 (dd, *J* = 4, 1.2 Hz, 1H), 4.54 (q, *J*=7.1Hz, 2H), 1.50 (t, *J*=7.1Hz, 3H); ^{13}C NMR (101 MHz, $CDCl_3$) δ 162.8, 145.3, 133.9, 130.2, 130.1, 127.0, 115.6, 93.8, 64.6, 14.0; m/z (GC-MS): 222.94 $[M]^+$; Elemental analysis: Found: C, 53.58; H, 3.91; N, 6.28; Calculated: C, 53.80; H, 4.06; N, 6.27. Melting point: 116 – 118°C.

3,4-Dioxo-2,5-di(thiophen-2-yl)hexanedinitrile (38)

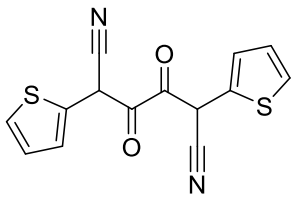

A saturated solution of sodium ethoxide was prepared by adding sodium (0.261 g, 11.3 mmol) to a flask containing ethanol (18 ml) at 0°C, before the addition of compound 37 (1.0 g, 4.5 mmol) and thiophene-2-acetonitrile (0.844 g, 6.9 mmol) and the mixture was refluxed for 16

h. The solution was cooled and diluted with water (20 ml) before acidification of the solution by dropwise addition of acetic acid until pH paper showed that the solution was acidic. The suspension was cooled in ice before filtration of the solid. The crude product was washed with water and dried, leaving a red solid which was collected by filtration: Yield = 0.87 g (64%): ^{1}H NMR (500 MHz, $(CD_3)_2CO$, ppm): 9.42 (s, br, 2H), 7.99 (dd, *J*= 5, 1 Hz, 1H), 7.71 (dd, *J* = 3.75, 1.5 Hz, 1H), 7.44 (dd, *J*= 5, 1 Hz, 1H), 7.31 (m, 2H), 7.11 (dd, *J*=5.5, 5.3 Hz, 1H); ^{13}C NMR (500 MHz, $(CD_3)_2CO$, ppm) 174.9, 169.9, 151.7, 133.2, 132.5, 131.7, 129.3, 127.3, 123.9, 122.0, 115.1; m/z (MALDI): 300.0 $[M]^+$; Elemental analysis: Found: C, 55.97; H, 2.63; N, 9.52; Calculated: C, 55.99; H, 2.68; N, 9.33. Melting point: 289 – 291°C.

(Z)-2-(3-hydroxy-5-oxo-4-(thiophen-2-yl)furan-2(5H)-ylidene-2-(thiophen-2-yl)acetic acid (39)

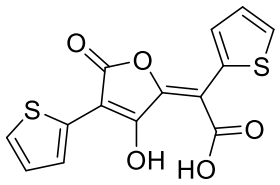

Compound 38 (1 g, 3.33 mmol) was added to flask containing water (8.3 ml), sulphuric acid (6.9 ml) and acetic acid (12.1 ml) before the solution was stirred at room temperature for 1 h. The suspension was cooled and poured into 30 ml of ice and water. The solid was then removed by filtering through a Buchner funnel and washed with water before being left to dry. The product was then washed with hot acetonitrile to yield an orange solid. The purified product was shown to contain some by-product which could not be removed by further purification. Yield = 0.59 g (55%) : ^{1}H NMR (500 MHz, $(CD_3)_2SO$, ppm): δ 8.81 (s, 1H), 8.10 (s, 1H), 7.82 (dd, *J* = 5.1, 1.2 Hz, 1H), 7.67 (dd, *J* = 3.7, 1.2 Hz, 1H), 7.62 (dd, *J* = 5.1, 1.1 Hz, 1H), 7.28 (dd, *J* = 3.6, 1.2 Hz, 1H), 7.19 (m, 2H); ^{13}C NMR (101 MHz, $(CD_3)_2SO$, ppm): δ 169.9, 165.6, 160.0, 149.8, 132.2, 131.0, 130.4, 129.9, 127.5, 127.4, 126.5, 125.5, 112.6, 99.5.; m/z (MALDI): 320.12 $[M]^+$. Melting point: 198 – 200 °C.

3,6-Bis(thiophen-2-yl)furo[3,2-b]furan-2,5-dione (40)

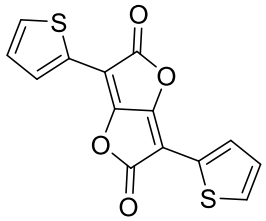

Acetic anhydride (174 ml) was added to a flask containing compound 39 (10 g, 31 mmol) and the solution was stirred at reflux for 16 h. The mixture was allowed to cool before being poured into a flask containing water and ice (630 ml). Ethanol (260 ml) was stirred into the mixture and the precipitate was removed by vacuum filtration and dried. Four precipitations of the crude compound using hot acetonitrile were required to give the product as an orange solid. Yield = 3.34 g (35%). ^{1}H NMR (400 MHz, $CDCl_3$) δ 7.80 (dd, *J* = 3.8, 1.1 Hz, 1H), 7.60 (dd, *J* = 5.1, 1.1 Hz, 1H), 7.21 (dd, *J* = 5.1, 3.8 Hz, 1H) ^{13}C NMR (101 MHz, DMSO) δ 167.7, 166.9, 166.2, 150.2, 135.5, 133.1, 130.5, 128.9, 126.6, 125.9, 122.9, 121.7, 111.6, 97.8; m/z (MALDI): 301.95 $[M]^+$; Elemental Analysis: Found: C, 55.91, H, 2.28, Expected: C, 55.62 H, 2.00. Melting point: 314 – 316°C.

3,6-Bis(5-bromothiophen-2-yl)furo[3,2-b]furan-2,5-dione (41)

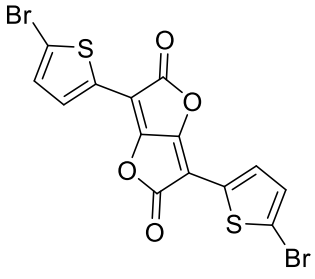

Compound 40 (1 g, 3.31 mmol) and NBS (1.18 g, 6.62 mmol) were added to a 50 ml round bottom flask before the addition of CH_2Cl_2 (16 ml). The solution was then allowed to stir overnight in the absence of light. The resulting mixture was diluted in CH_2Cl_2 (30 ml) and

washed with brine (3 × 50ml). The mixture was dried and solvent evaporated to yield the crude product. This was precipitated three times using acetonitrile to give the purified product as a brown solid. Yield = 0.78 g (51%): ^{1}H NMR (400 MHz, $CDCl_3$) δ 7.51 (d, *J* = 4.0 Hz, 1H), 7.17 (d, *J* = 4.0 Hz, 1H); ^{13}C NMR (101 MHz, DMSO) δ 168.6, 166.4, 166.1, 150.2, 137.3, 135.4, 131.6, 129.8, 129.2, 121.7, 116.2, 110.9, 108.5, 93.4; m/z (MALDI): 457.36 (M^+, ^{79}Br × 2), 459.35 (M^+, ^{79}Br + ^{81}Br), 461.35 (M^+, ^{81}Br × 2); Elemental Analysis: Found, C, 36.92 H, 1.07, Expected: C, 36.55 H, 0.88. Melting point: 282 – 284°C.

3,6-Bis(4'-hexyl-[2,2'-bithiophen]-5-yl)furo[3,2-b]furan-2,5-dione (42) (FFD-(2T)$_2$)

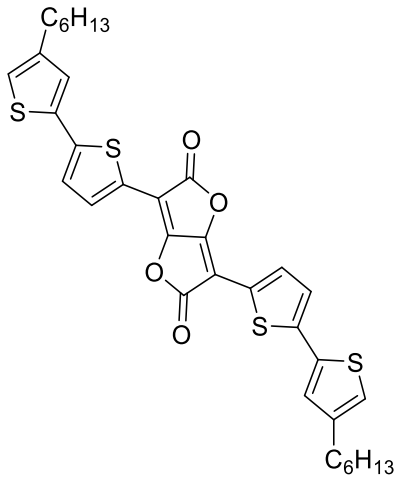

2-Trimethylstannyl-4-hexylthiophene (0.381 g, 1.15 mmol) and compound 41 (0.24 g, 0.522 mmol) were added to a 20 ml microwave vial which was evacuated and purged with N_2 before the addition of anhydrous DMF (10 ml). The solution was then purged with N_2 for 45 minutes before the addition of $Pd(PPh_3)_4$ (0.084 g, 0.073 mmol). The mixture was stirred in a microwave reactor at 160^{o}C for 2 hours. The reaction mixture was then diluted with dichloromethane (20 ml) and washed with brine (3 × 30 ml) before being dried over $MgSO_4$. Evaporation of the solvent followed to yield the crude product. This was purified by precipitation in DCM/Methanol to give a sticky, dark red solid. It was not possible to obtain a ^{13}C NMR due to poor solubility of the compound. Yield = 0.13 g (39%).^{1}H NMR (400 MHz, CD_2Cl_2) δ 7.66 (d, *J* = 4.0 Hz, 1H), 7.24 (d, *J* = 4.0 Hz, 1H), 7.19 (d, *J* = 1.3 Hz, 1H), 6.94 (d,

J = 1.1 Hz, 1H), 1.64 (m, 2H), 1.40 – 1.24 (m, 8H), 0.90 (m, 3H); m/z (MALDI): 634.62 $[M]^+$; Elemental Analysis: Found: C, 64.11, H, 5.35, Expected: C, 64.32, H, 5.40. Melting point: 194 – 196°C.

2-Trimethylstannyl-4-hexylthiophene (43)

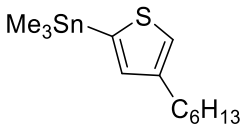

3-Hexylthiophene (3.21 ml, 17.83 mmol), diethyl ether (70 ml) and TMEDA (2.96 ml, 19.6 mmol) and *N*-butyllithium (8.45 ml, 19.6 mmol) were added to a flask under argon and the resulting mixture was stirred at reflux for 1 h before being cooled to 0ºC. Trimethyltin chloride in THF (19.6 ml, 19.6 mmol, 1.0 M) was then added and the reaction was stirred for 16 h at RT. The reaction was quenched using ammonium chloride solution (10 ml) before being washed with brine (3 x 40 ml). The solution was then dried over magnesium sulfate before the solvent was evaporated to yield the crude product as a yellow oil. The compound was used without further purification.^{1}H NMR is consistent with previously reported data:[173] Yield=5.43 g (92%):^{1}H NMR (500MHz, $CDCl_3$, ppm): 7.20 (m, 1H), 6.97 (s, 1H), 2.66 (t, *J*=7.5Hz, 2H), 1.64 (m, 2H), 1.34 (m, 6H), 0.91 (m, 12H).

3,6-Bis(4-hexylthiophen-2-yl)thieno[3,2-b]thieno[3.2-b]thiophene-2,5-dione (44)

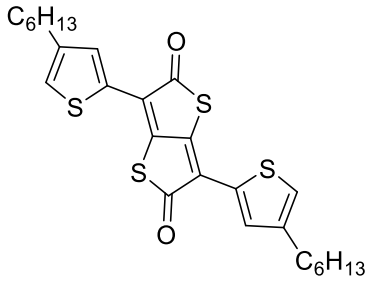

3,6-Diiodothieno[3,2-b]thiophene-2,5-dione (0.25 g, 0.59 mmol), 2-trimethylstannyl-4-hexylthiphene (0.43 g, 1.19 mmol) and toluene (15 ml) were added to a flask and the solution was degassed before the addition of $Pd(PPh_3)_4$ (0.014 g, 0.012 mmol). The reaction was left to

stir at reflux overnight. The reaction mixture was then washed with brine (3 x 10 ml) before being dried over magnesium sulphate. The solvent was then evaporated to yield a crude product which was subsequently purified by column chromatography (silica gel, toluene: CH_2Cl_2 100% toluene → 100% CH_2Cl_2 gradually) to elute the product as a red solid. Yield= 127mg (38%):^{1}H NMR (400 MHz, $CDCl_3$, ppm): 7.63 (d, *J*= 1.2 Hz, 2H), 7.21 (d, *J*= 1.0 Hz, 2H), 2.65 (t, *J*=7.6 Hz, 4H), 1.65 (m, 4H), 1.31 (m, 12H), 0.90 (m, 6H).

3,6-Bis(5-bromo-4-hexylthiophen-2-yl)thieno[3,2-b]thiophene-2,5-dione (45)

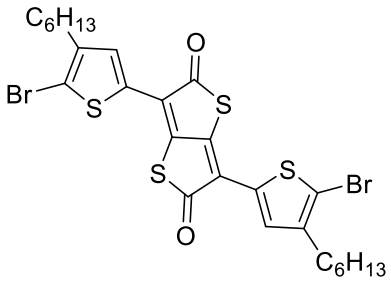

N-bromosuccinimide (0.078 g, 0.438 mmol) and compound **6** (0.1 g, 0.199 mmol) and chloroform (5 ml) were added to a flask and the reaction mixture was stirred in the dark overnight. The solution was washed with water (3 x 5 ml) before being dried over magnesium sulfate and the solvent was removed by evaporation to yield the crude product. This crude material was subsequently purified by column chromatography (silica gel, 1:1 CH_2Cl_2: hexane mobile phase) to yield a red solid. Yield= 70 mg (48%): ^{1}H NMR (400 MHz, $CDCl_3$, ppm): 7.40 (s, 2H), 2.61 (t, *J*=7.5 Hz, 4H), 1.63 (m, 4H), 1.32 (m, 12H), 0.91 (m, 6H):^{13}C NMR (400 MHz, $CDCl_3$, ppm): 187.7; 145.3; 132.0; 131.9; 126.5; 32.0; 30.7; 30.6; 29.2; 22.9; 14.4

5-Bromo-5'-hexyl-2,2'-bithiophene (46)

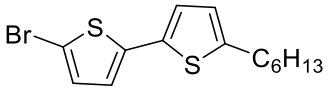

5-Hexyl-2,2'-bithiophene (1.5 g, 5.99 mmol) and *N*-bromosuccinimide (1.12 g, 6.31 mmol) were added to a flask containing acetic acid (10 ml) and chloroform (10 ml). The reaction was allowed to stir in the absence of light for 2 h before being washed with 10% potassium

hydroxide solution (3 x 10 ml) and water (2 x 10 ml). The organic phase was then dried over magnesium sulfate and the solvent was evaporated to yield the crude product. The product was then purified by column chromatography (silica gel, hexane mobile phase) giving a yellow/brown solid. ^{1}H NMR is consistent with reported data:[174] Yield=1.48 g (75%): ^{1}H NMR (400 MHz, $CDCl_3$, ppm): 6.94 (d, *J*=3.8 Hz, 1H), 6.92 (d, *J*=3.6 Hz, 1H), 6.84 (d, *J*=3.8 Hz, 1H), 6.67 (d, *J* = 3.8 Hz, 1H), 2.79 (t, *J*=7.5 Hz, 2H), 1.68 (m, 2H), 1.34 (m, 6H), 0.91 (m, 3H).

2-Bromo-3-hexyl-thiophene (47)

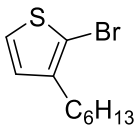

3-Hexylthiophene (0.53 ml, 2.97 mmol) and *N*-bromosuccinimide (0.53 g, 2.97 mmol) were added to a flask containing a 1:1 mixture of acetic acid (2.5 ml) and chloroform (2.5 ml). The reaction mixture was stirred for 1hr before being diluted with water (5 ml). The mixture was washed with 10% potassium hydroxide (3 x 5 ml) and water (2 x 5 ml) before being dried over magnesium sulfate. The solvent was then evaporated to give a crude product that was purified by distillation at 127^{o}C/7 mmHg, giving a colourless oil. The ^{1}H NMR is consistent with the reported data:[173] Yield=0.62g (84%): ^{1}H NMR (500MHz, $CDCl_3$, ppm): 7.19 (d, *J*=5.6 Hz, 1H), 6.80 (d, *J*=5.6 Hz, 1H), 2.57 (t, *J*= 7.6 Hz, 2H), 1.58 (m, 2H), 1.32 (m, 6H), 0.90 (m, 3H).

5-Tributylstannyl-5'-hexyl-2,2'-bithiophene (48)

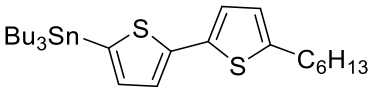

To a solution of 5-bromo-5'-hexyl-2,2'-bithiophene (1.2 g, 3.64 mmol) in THF (15 ml) was added *N*-Butyllithium (1.52 ml, 3.64 mmol) dropwise under an inert atmosphere at -80°C. The solution was allowed to stir for 1 h at 0^{o}C. The solution was then cooled to -80^{o}C for the addition of tributyltin chloride (1.02ml, 3.76 mmol) before the mixture was stirred for 16 h at

room temperature. The crude mixture was washed with brine (3 x 10 ml) before being dried over magnesium sulfate and the solvent was evaporated. The crude, yellow oil was used without further purification. ^{1}H NMR data is consistent with previously reported data:[175] Yield = 1.75g (89%): ^{1}H NMR (400MHz, $CDCl_3$, ppm): 7.22 (d, *J*= 3.6 Hz, 1H), 7.04 (d, *J*= 3.2 Hz, 1H), 6.98 (d, *J*= 3.6 Hz, 1H), 6.67 (d, *J*= 3.6Hz, 1H), 2.79 (t, *J*=7.6 Hz, 2H), 1.62 (m, 8H), 1.35 (m, 12H), 1.12 (m, 6H), 0.92 (m, 12H).

3,5''-Dihexyl-2,2':5',2''-terthiophene (49)

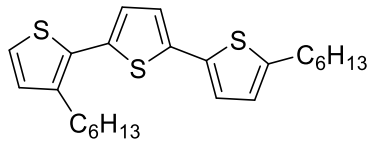

Compounds **10** (0.5 g, 2.02 mmol) and **11** (1.2g, 2.23 mmol) and DMF (30ml) were added to a flask and purged with argon for 1 h. $Pd(PPh_3)_4$ (0.23 g, 0.202 mmol) was then quickly added and the reaction was stirred at room temperature for 16 h. The mixture was then diluted with diethyl ether (20 ml) washed with water (5 x 40ml) before the solvent was evaporated. The crude material was purified by column chromatography, using hexane as the mobile phase, yielding a pale yellow oil: Yield= 0.269 g (32%): ^{1}H NMR (400 MHz, $CDCl_3$, ppm): 7.17 (d, *J* = 5.2 Hz, 1H), 7.04 (d, *J* = 3.8 Hz, 1H), 7.00 (m, 2H), 6.94 (d, *J* = 5.2 Hz, 1H), 6.69 (d, *J* = 3.6 Hz, 1H), 2.79 (m, 4H), 1.67 (m, 4H), 1.33 (m, 12H), 0.90 (m, 6H).

5-Tributylstannyl-3,5''-dihexyl-2,2':5',2''-terthiophene (50)

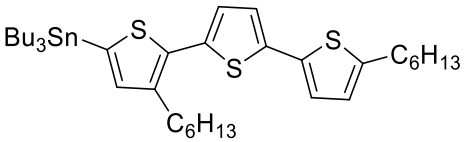

N-Butyllithium (0.22 ml, 0.53 mmol) was added dropwise to a flask containing compound **12** (0.2 g, 0.48 mmol) in diethyl ether (10 ml) and TMEDA (0.08 ml, 0.53 mmol) under argon at room temperature. The mixture was then stirred at reflux for 1 h and was cooled to 0^{o}C using an ice bath for the slow addition of tributyltin chloride (0.14 ml, 0.53 mmol). The reaction

mixture was allowed to stir overnight. It was then quenched using ammonium chloride (2 ml) before being washed with brine (3 x 10 ml) and dried using magnesium sulfate. The solvent was then evaporated, giving a crude product yellow/brown oil which was used without further purification: Yield= 336mg (98%): ^{1}H NMR (400 MHz, $CDCl_3$, ppm): 7.04 (d, *J* = 3.8 Hz, 1H), 6.99 (m, 2H), 6.96 (s, 1H), 6.69 (d, *J* = 3.5 Hz, 1H), 2.80 (m, 4H), 1.62 (m, 10H), 1.37 (m, 18H), 1.12 (m, 6H), 0.92 (m, 15H).

3,6-Bis(3,5''-dihexyl-[2,2:5',2''-terthiophen]-5-yl)thieno[3,2-b]thiophene-2,5-dione (51) (TTD-(3T)$_2$)

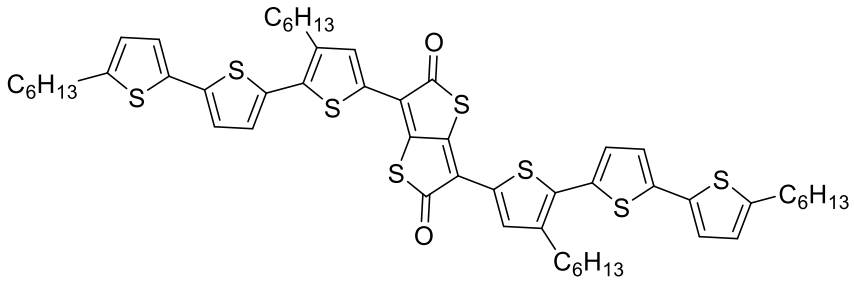

3-6-Diiodothieno[3,2-b]thiophene-2,5-dione (0.1g, 0.24 mmol) and compound **50** were added to a flask, to which toluene (10 ml) was added before the solution was degassed for 1 h using argon. $Pd(PPh_3)_4$ (0.06 g, 0.05 mmol) was then added and mixture was stirred in the microwave reactor at 120 ^{o}C for 2 h. The reaction mixture was then washed with saturated sodium bicarbonate solution (10 ml) before being dried over magnesium sulfate. The solvent was then evaporated to yield a crude solid. The crude material was purified by column chromatography, using CH_2Cl_2 as a mobile phase to elute the impurities, before gradually changing the mobile phase to ethyl acetate and the product was collected. Evaporation of the solvent showed the product to be a sticky, blue solid: Yield = 84mg (35%):^{1}H NMR (500 MHz, $CDCl_3$, ppm): 7.61 (s, 2H), 7.14 (d, *J*= 3.8 Hz, 2H), 7.07 (d, *J*= 3.8 Hz, 2H), 7.03 (d, *J*= 3.5 Hz, 2H), 6.71 (d, *J*= 3.5 Hz, 2H), 2.81 (m, 8H), 1.69 (m, 8H),1.37 (m, 24H), 0.92 (m, 12H); ^{13}C NMR (101 MHz, $CDCl_3$) δ 187.4, 146.3, 140.6, 139.1, 137.6, 136.0, 134.2, 133.5, 129.4, 127.2, 125.5, 125.0,

123.8, 123.4, 121.9, 31.8, 31.7, 31.6, 30.3, 30.23, 30.20, 29.8, 29.84, 29.79, 29.76, 29.5, 29.0, 22.8, 22.7, 14.3, 14.2; m/z (MALDI): 998.1 $[M]^+$.

Tetrakis(triphenylphosphine)palladium(0) (52)

$$Pd(PPh_3)_4$$

Palladium (II) chloride (0.5 g, 2.8 mmol) and triphenylphosphine (3.7 g, 14.1 mmol), suspended in dry DMSO (40 ml) under N_2, were heated at 140°C with stirring until the solid had completely dissolved. Hydrazine monohydrate (0.56 g, 11.3 mmol) was then added quickly *via* syringe to produce a dark solution. The solution was then allowed to cool to room temperature and was filtered under N_2. The precipitate was washed with CH_3OH (2 x 20 ml) and Et_2O (2 x 20 ml) to give the product as a bright yellow solid. Yield = 3.03 g (93%).

References

1. P. W. Atkins and J. De Paula, *Atkins' Physical chemistry*, Oxford University Press, Oxford ; New York, 9th edn., 2010.
2. C. J. Brabec, S. Gowrisanker, J. J. M. Halls, D. Laird, S. J. Jia and S. P. Williams, *Adv. Mater.*, 2010, **22**, 3839-3856.
3. X. Zhan and D. Zhu, *Polymer Chemistry*, 2010, **1**, 409-419.
4. Z. He, C. Zhong, S. Su, M. Xu, H. Wu and Y. Cao, *Nat Photon*, 2012, **6**, 591-595.
5. C.-F. Wang, W.-Y. Hung, M.-H. Cheng, J.-S. Hwang, M.-k. Leung and K.-T. Wong, *Org. Electron.*, 2013, **14**, 1958-1965.
6. N. J. Findlay, J. Bruckbauer, A. R. Inigo, B. Breig, S. Arumugam, D. J. Wallis, R. W. Martin and P. J. Skabara, *Adv. Mater.*, 2014, **26**, 7290-7294.
7. Y. Seino, H. Sasabe, Y.-J. Pu and J. Kido, *Adv. Mater.*, 2014, **26**, 1612-1616.
8. A. R. Murphy and J. M. J. Frechet, *Chem. Rev.*, 2007, **107**, 1066-1096.
9. D. Cortizo-Lacalle, S. Arumugam, S. E. T. Elmasly, A. L. Kanibolotsky, N. J. Findlay, A. R. Inigo and P. J. Skabara, *J. Mater. Chem.*, 2012, **22**, 11310-11315.
10. H. Sirringhaus, *Adv. Mater.*, 2014, **26**, 1319-1335.
11. I. A. Wright, A. L. Kanibolotsky, J. Cameron, T. Tuttle, P. J. Skabara, S. J. Coles, C. T. Howells, S. A. J. Thomson, S. Gambino and I. D. W. Samuel, *Angew. Chem. Int. Ed.*, 2012, **51**, 4562-4567.
12. J. Sakai, T. Taima and K. Saito, *Org. Electron.*, 2008, **9**, 582-590.
13. Y. Chen, X. Wan and G. Long, *Acc. Chem. Res.*, 2013, **46**, 2645-2655.
14. A. L. Kanibolotsky, F. Vilela, J. C. Forgie, S. E. T. Elmasly, P. J. Skabara, K. Zhang, B. Tieke, J. McGurk, C. R. Belton, P. N. Stavrinou and D. D. C. Bradley, *Adv. Mater.*, 2011, **23**, 2093-2097.
15. A. L. Kanibolotsky, R. Berridge, P. J. Skabara, I. F. Perepichka, D. D. C. Bradley and M. Koeberg, *J. Am. Chem. Soc.*, 2004, **126**, 13695-13702.

16. C. R. Belton, A. L. Kanibolotsky, J. Kirkpatrick, C. Orofino, S. E. T. Elmasly, P. N. Stavrinou, P. J. Skabara and D. D. C. Bradley, *Adv. Funct. Mater.*, 2013, **23**, 2792-2804.

17. M. J. Panzer, C. R. Newman and C. D. Frisbie, *Appl. Phys. Lett.*, 2005, **86**.

18. H. T. Yi, M. M. Payne, J. E. Anthony and V. Podzorov, *Nat Commun*, 2012, **3**, 1259.

19. J. Li, M. Wang, S. Ren, X. Gao, W. Hong, H. Li and D. Zhu, *J. Mater. Chem.*, 2012, **22**, 10496-10500.

20. J. Roncali, *Chem. Rev.*, 1997, **97**, 173-205.

21. M. Irimia-Vladu, E. D. Głowacki, P. A. Troshin, G. Schwabegger, L. Leonat, D. K. Susarova, O. Krystal, M. Ullah, Y. Kanbur, M. A. Bodea, V. F. Razumov, H. Sitter, S. Bauer and N. S. Sariciftci, *Adv. Mater.*, 2012, **24**, 375-380.

22. J. Roncali, P. Blanchard and P. Frere, *J. Mater. Chem.*, 2005, **15**, 1589-1610.

23. N. E. Jackson, B. M. Savoie, K. L. Kohlstedt, M. Olvera de la Cruz, G. C. Schatz, L. X. Chen and M. A. Ratner, *J. Am. Chem. Soc.*, 2013, **135**, 10475-10483.

24. Z. Fei, P. Pattanasattayavong, Y. Han, B. C. Schroeder, F. Yan, R. J. Kline, T. D. Anthopoulos and M. Heeney, *J. Am. Chem. Soc.*, 2014, **136**, 15154-15157.

25. H. T. Black, H. Lin, F. Belanger-Gariepy and D. F. Perepichka, *Faraday Discuss.*, 2014, **174**, 297-312.

26. D. Milstein and J. K. Stille, *J. Am. Chem. Soc.*, 1978, **100**, 3636-3638.

27. N. Miyaura, K. Yamada and A. Suzuki, *Tetrahedron Lett.*, 1979, **20**, 3437-3440.

28. A. O. King, N. Okukado and E.-i. Negishi, *J. Chem. Soc., Chem. Commun.*, 1977, 683-684.

29. K. Tamao, K. Sumitani and M. Kumada, *J. Am. Chem. Soc.*, 1972, **94**, 4374-4376.

30. A. S. Guram and S. L. Buchwald, *J. Am. Chem. Soc.*, 1994, **116**, 7901-7902.

31. F. Paul, J. Patt and J. F. Hartwig, *J. Am. Chem. Soc.*, 1994, **116**, 5969-5970.

32. R. F. Heck and J. P. Nolley, *J. Org. Chem.*, 1972, **37**, 2320-2322.

33. K. Sonogashira, Y. Tohda and N. Hagihara, *Tetrahedron Lett.*, 1975, **16**, 4467-4470.

34. X. Chen, K. M. Engle, D.-H. Wang and J.-Q. Yu, *Angew. Chem. Int. Ed.*, 2009, **48**, 5094-5115.

35. H. Bronstein, Z. Chen, R. S. Ashraf, W. Zhang, J. Du, J. R. Durrant, P. Shakya Tuladhar, K. Song, S. E. Watkins, Y. Geerts, M. M. Wienk, R. A. J. Janssen, T. Anthopoulos, H. Sirringhaus, M. Heeney and I. McCulloch, *J. Am. Chem. Soc.*, 2011, **133**, 3272-3275.

36. W. Wen, L. Ying, B. B. Y. Hsu, Y. Zhang, T.-Q. Nguyen and G. C. Bazan, *Chem. Commun.*, 2013, **49**, 7192-7194.

37. J. H. Bannock, M. Al-Hashimi, S. H. Krishnadasan, J. J. M. Halls, M. Heeney and J. C. de Mello, *Mater. Horiz.*, 2014, **1**, 214-218.

38. G. Gritzner and J. Kuta, *Pure Appl. Chem.*, 1984, **56**, 461-466.

39. H. M. Koepp, H. Wendt and H. Stkehlow, *Z. Elektrochemie*, 1960, **64**, 483-491.

40. C. M. Cardona, W. Li, A. E. Kaifer, D. Stockdale and G. C. Bazan, *Adv. Mater.*, 2011, **23**, 2367-2371.

41. B. W. D'Andrade, S. Datta, S. R. Forrest, P. Djurovich, E. Polikarpov and M. E. Thompson, *Org. Electron.*, 2005, **6**, 11-20.

42. J.-L. Bredas, *Mater. Horiz.*, 2014, **1**, 17-19.

43. http://www.sony.net/SonyInfo/News/Press/201005/10-070E/, 22 May 2016.

44. J. E. Lilienfeld, *US Pat.*, 1745175, 1930.

45. J. Wang, H. Wang, X. Yan, H. Huang, D. Jin, J. Shi, Y. Tang and D. Yan, *Adv. Funct. Mater.*, 2006, **16**, 824-830.

46. J. M. Mativetsky, M. Kastler, R. C. Savage, D. Gentilini, M. Palma, W. Pisula, K. Müllen and P. Samorì, *Adv. Funct. Mater.*, 2009, **19**, 2486-2494.

47. A. M. Zhong, Y. Z. Bian and Y. X. Zhang, *Journal of Physical Chemistry C*, 2010, **114**, 3248-3255.

48. J. L. Kan, Y. L. Chen, D. D. Qi, Y. Q. Liu and J. Z. Jiang, *Adv. Mater.*, 2012, **24**, 1755-1758.

49. H. Usta, C. Risko, Z. M. Wang, H. Huang, M. K. Deliomeroglu, A. Zhukhovitskiy, A. Facchetti and T. J. Marks, *J. Am. Chem. Soc.*, 2009, **131**, 5586-5608.

50. A. Casey, Y. Han, Z. Fei, A. J. P. White, T. D. Anthopoulos and M. Heeney, *J. Mater. Chem. C*, 2015, **3**, 265-275.

51. I. Kymissis, *Organic Field Effect Transistors: Theory, Fabrication and Characterization*, 2009.

52. L. H. Nguyen, H. Hoppe, T. Erb, S. Günes, G. Gobsch and N. S. Sariciftci, *Adv. Funct. Mater.*, 2007, **17**, 1071-1078.

53. A. C. Arias, J. D. MacKenzie, R. Stevenson, J. J. M. Halls, M. Inbasekaran, E. P. Woo, D. Richards and R. H. Friend, *Macromolecules*, 2001, **34**, 6005-6013.

54. S. Arumugam, I. A. Wright, A. R. Inigo, S. Gambino, C. T. Howells, A. L. Kanibolotsky, P. J. Skabara and I. D. W. Samuel, *J. Mater. Chem. C*, 2014, **2**, 34-39.

55. EREC, Mapping Renewable Energy Pathways Towards 2020, http://www.eufores.org/fileadmin/eufores/Projects/REPAP_2020/EREC-roadmap-V4.pdf).

56. A. E. Becquerel, *Comptes Rendus*, 1939, **9**, 561-567.

57. R. Williams, *J. Chem. Phys.*, 1960, **32**, 1505-1514.

58. F. C. Krebs, *Sol. Energy Mater. Sol. Cells*, 2007, **91**, 953-953.

59. C. W. Tang,*US Pat.*, 1979, US4164431 A

60. C. W. Tang, *Appl. Phys. Lett.*, 1986, **48**, 183-185.

61. C. J. Brabec, C. Winder, N. S. Sariciftci, J. C. Hummelen, A. Dhanabalan, P. A. van

Hal and R. A. J. Janssen, *Adv. Funct. Mater.*, 2002, **12**, 709-712.

62. G. Yu, J. Gao, J. C. Hummelen, F. Wudl and A. J. Heeger, *Science*, 1995, **270**, 1789-1791.

63. M. C. Scharber, D. Wuhlbacher, M. Koppe, P. Denk, C. Waldauf, A. J. Heeger and C. L. Brabec, *Adv. Mater.*, 2006, **18**, 789-794.

64. C. J. Brabec, A. Cravino, D. Meissner, N. S. Sariciftci, T. Fromherz, M. T. Rispens, L. Sanchez and J. C. Hummelen, *Adv. Funct. Mater.*, 2001, **11**, 374-380.

65. N. Blouin, A. Michaud, D. Gendron, S. Wakim, E. Blair, R. Neagu-Plesu, M. Belletete, G. Durocher, Y. Tao and M. Leclerc, *J. Am. Chem. Soc.*, 2008, **130**, 732-742.

66. W. Cai, X. Gong and Y. Cao, *Sol. Energy Mater. Sol. Cells*, 2010, **94**, 114-127.

67. A. Mishra and P. Bäuerle, *Angew. Chem. Int. Ed.*, 2012, **51**, 2020-2067.

68. Y.-T. Fu, C. Risko and J.-L. Brédas, *Adv. Mater.*, 2013, **25**, 878-882.

69. J. Peet, M. L. Senatore, A. J. Heeger and G. C. Bazan, *Adv. Mater.*, 2009, **21**, 1521-1527.

70. G. J. Hedley, A. J. Ward, A. Alekseev, C. T. Howells, E. R. Martins, L. A. Serrano, G. Cooke, A. Ruseckas and I. D. W. Samuel, *Nat Commun*, 2013, **4**.

71. F.-C. Chen, H.-C. Tseng and C.-J. Ko, *Appl. Phys. Lett.*, 2008, **92**, 103316.

72. B. R. Aïch, J. Lu, S. Beaupré, M. Leclerc and Y. Tao, *Org. Electron.*, 2012, **13**, 1736-1741.

73. Y. Huang, W. Wen, S. Mukherjee, H. Ade, E. J. Kramer and G. C. Bazan, *Adv. Mater.*, 2014, **26**, 4168-4172.

74. L. Yang, H. Zhou and W. You, *J Phys. Chem. C*, 2010, **114**, 16793-16800.

75. J. Li, K.-H. Ong, P. Sonar, S.-L. Lim, G.-M. Ng, H.-K. Wong, H.-S. Tan and Z.-K. Chen, *Polymer Chemistry*, 2013, **4**, 804-811.

76. C. Piliego, T. W. Holcombe, J. D. Douglas, C. H. Woo, P. M. Beaujuge and J. M. J.

Fréchet, *J. Am. Chem. Soc.*, 2010, **132**, 7595-7597.

77. I. Kang, H.-J. Yun, D. S. Chung, S.-K. Kwon and Y.-H. Kim, *J. Am. Chem. Soc.*, 2013, **135**, 14896-14899.

78. K. R. Graham, C. Cabanetos, J. P. Jahnke, M. N. Idso, A. El Labban, G. O. Ngongang Ndjawa, T. Heumueller, K. Vandewal, A. Salleo, B. F. Chmelka, A. Amassian, P. M. Beaujuge and M. D. McGehee, *J. Am. Chem. Soc.*, 2014, **136**, 9608-9618.

79. Z. C. He, C. M. Zhong, S. J. Su, M. Xu, H. B. Wu and Y. Cao, *Nature Photonics*, 2012, **6**, 591-595.

80. M. Sommer, *J. Mater. Chem. C*, 2014, **2**, 3088-3098.

81. Y. Sun, G. C. Welch, W. L. Leong, C. J. Takacs, G. C. Bazan and A. J. Heeger, *Nat. Mater*, 2012, **11**, 44-48.

82. C. J. Takacs, Y. Sun, G. C. Welch, L. A. Perez, X. Liu, W. Wen, G. C. Bazan and A. J. Heeger, *J. Am. Chem. Soc.*, 2012, **134**, 16597-16606.

83. J. J. Jasieniak, B. B. Y. Hsu, C. J. Takacs, G. C. Welch, G. C. Bazan, D. Moses and A. J. Heeger, *ACS Nano*, 2012, **6**, 8735-8745.

84. T. S. van der Poll, J. A. Love, T.-Q. Nguyen and G. C. Bazan, *Adv. Mater.*, 2012, **24**, 3646-3649.

85. A. K. K. Kyaw, D. H. Wang, C. Luo, Y. Cao, T.-Q. Nguyen, G. C. Bazan and A. J. Heeger, *Adv. Energy Mater.*, 2014, **4**, n/a-n/a.

86. D. H. Wang, A. K. K. Kyaw, V. Gupta, G. C. Bazan and A. J. Heeger, *Adv. Energy Mater.*, 2013, **3**, 1161-1165.

87. V. Gupta, A. K. K. Kyaw, D. H. Wang, S. Chand, G. C. Bazan and A. J. Heeger, *Sci. Rep.*, 2013, **3**, 1965.

88. A. K. K. Kyaw, D. H. Wang, D. Wynands, J. Zhang, T.-Q. Nguyen, G. C. Bazan and A. J. Heeger, *Nano Lett.*, 2013, **13**, 3796-3801.

89. P. Gautam, R. Misra, S. A. Siddiqui and G. D. Sharma, *ACS Appl. Mater. Interfaces*, 2015, **7**, 10283-10292.

90. L.-Y. Lin, Y.-H. Chen, Z.-Y. Huang, H.-W. Lin, S.-H. Chou, F. Lin, C.-W. Chen, Y.-H. Liu and K.-T. Wong, *J. Am. Chem. Soc.*, 2011, **133**, 15822-15825.

91. W. Kylberg, P. Sonar, J. Heier, J.-N. Tisserant, C. Muller, F. Nuesch, Z.-K. Chen, A. Dodabalapur, S. Yoon and R. Hany, *Energy Environ. Sci.*, 2011, **4**, 3617-3624.

92. J.-W. Mun, I. Cho, D. Lee, W. S. Yoon, O. K. Kwon, C. Lee and S. Y. Park, *Org. Electron.*, 2013, **14**, 2341-2347.

93. O. P. Lee, A. T. Yiu, P. M. Beaujuge, C. H. Woo, T. W. Holcombe, J. E. Millstone, J. D. Douglas, M. S. Chen and J. M. J. Fréchet, *Adv. Mater.*, 2011, **23**, 5359-5363.

94. S. Wang, L. Hall, V. V. Diev, R. Haiges, G. Wei, X. Xiao, P. I. Djurovich, S. R. Forrest and M. E. Thompson, *Chem. Mater.*, 2011, **23**, 4789-4798.

95. H. Sasabe, T. Igrashi, Y. Sasaki, G. Chen, Z. Hong and J. Kido, *RSC Advances*, 2014, **4**, 42804-42807.

96. L. Beverina, M. Drees, A. Facchetti, M. Salamone, R. Ruffo and G. A. Pagani, *Eur. J. Org. Chem.*, 2011, **2011**, 5555-5563.

97. Y. Lin and X. Zhan, *Mater. Horiz.*, 2014, **1**, 470-488.

98. X. Zhang, Z. Lu, L. Ye, C. Zhan, J. Hou, S. Zhang, B. Jiang, Y. Zhao, J. Huang, S. Zhang, Y. Liu, Q. Shi, Y. Liu and J. Yao, *Adv. Mater.*, 2013, **25**, 5791-5797.

99. Q. Yan, Y. Zhou, Y.-Q. Zheng, J. Pei and D. Zhao, *Chem. Sci.*, 2013, **4**, 4389-4394.

100. S. Holliday, R. S. Ashraf, C. B. Nielsen, M. Kirkus, J. A. Röhr, C.-H. Tan, E. Collado-Fregoso, A.-C. Knall, J. R. Durrant, J. Nelson and I. McCulloch, *J. Am. Chem. Soc.*, 2015, **137**, 898-904.

101. H. U. Kim, J.-H. Kim, H. Suh, J. Kwak, D. Kim, A. C. Grimsdale, S. C. Yoon and D.-H. Hwang, *Chem. Commun.*, 2013, **49**, 10950-10952.

102. S.-Y. Liu, C.-H. Wu, C.-Z. Li, S.-Q. Liu, K.-H. Wei, H.-Z. Chen and A. K. Y. Jen, *Adv. Sci.*, 2015, **2**, 1500014.

103. T. Earmme, Y.-J. Hwang, N. M. Murari, S. Subramaniyan and S. A. Jenekhe, *J. Am. Chem. Soc.*, 2013, **135**, 14960-14963.

104. H. Rapoport and A. D. Batcho, *J. Org. Chem*, 1963, **28**, 1753-1759.

105. L. Nanson, N. Blouin, W. Mitchell, S. Tierney, T. Cull, PCT Int. Appl. (2013), WO 2013182262 A1 20131212.

106. J. Liu, Y. Sun, P. Moonsin, M. Kuik, C. M. Proctor, J. Lin, B. B. Hsu, V. Promarak, A. J. Heeger and T.-Q. Nguyen, *Adv. Mater.*, 2013, **25**, 5898-5903.

107. D. Cortizo-Lacalle, C. T. Howells, U. K. Pandey, J. Cameron, N. J. Findlay, A. R. Inigo, T. Tuttle, P. J. Skabara and I. D. W. Samuel, *Beilstein. J. Org. Chem.*, 2014, **10**, 2683-2695.

108. R. Kroon, A. Diaz de Zerio Mendaza, S. Himmelberger, J. Bergqvist, O. Bäcke, G. C. Faria, F. Gao, A. Obaid, W. Zhuang, D. Gedefaw, E. Olsson, O. Inganäs, A. Salleo, C. Müller and M. R. Andersson, *J. Am. Chem. Soc.*, 2015, **137**, 550-550.

109. B. He, A. B. Pun, L. M. Klivansky, A. M. McGough, Y. Ye, J. Zhu, J. Guo, S. J. Teat and Y. Liu, *Chem. Mater.*, 2014, **26**, 3920-3927.

110. 2003.

111. J. Liu, B. Walker, A. Tamayo, Y. Zhang and T.-Q. Nguyen, *Adv. Funct. Mater.*, 2013, **23**, 47-56.

112. T. Yanai, D. P. Tew and N. C. Handy, *Chem. Phys. Lett.*, 2004, **393**, 51-57.

113. A. Schäfer, H. Horn and R. Ahlrichs, *J. Chem. Phys*, 1992, **97**, 2571-2577.

114. A. V. Marenich, C. J. Cramer and D. G. Truhlar, *J. Phys. Chem. B*, 2009, **113**, 6378-6396.

115. M. J. Frisch, G. W. Trucks, H. B. Schlegel, G. E. Scuseria, M. A. Robb, J. R.

Cheeseman, G. Scalmani, V. Barone, B. Mennucci, G. A. Petersson, H. Nakatsuji, M. Caricato, X. Li, H. P. Hratchian, A. F. Izmaylov, J. Bloino, G. Zheng, J. L. Sonnenberg, M. Hada, M. Ehara, K. Toyota, R. Fukuda, J. Hasegawa, M. Ishida, T. Nakajima, Y. Honda, O. Kitao, H. Nakai, T. Vreven, J. A. Montgomery Jr., J. E. Peralta, F. Ogliaro, M. J. Bearpark, J. Heyd, E. N. Brothers, K. N. Kudin, V. N. Staroverov, R. Kobayashi, J. Normand, K. Raghavachari, A. P. Rendell, J. C. Burant, S. S. Iyengar, J. Tomasi, M. Cossi, N. Rega, N. J. Millam, M. Klene, J. E. Knox, J. B. Cross, V. Bakken, C. Adamo, J. Jaramillo, R. Gomperts, R. E. Stratmann, O. Yazyev, A. J. Austin, R. Cammi, C. Pomelli, J. W. Ochterski, R. L. Martin, K. Morokuma, V. G. Zakrzewski, G. A. Voth, P. Salvador, J. J. Dannenberg, S. Dapprich, A. D. Daniels, Ö. Farkas, J. B. Foresman, J. V. Ortiz, J. Cioslowski and D. J. Fox, *Gaussian*, 2009, A.02

116. J. Huang, C. Zhan, X. Zhang, Y. Zhao, Z. Lu, H. Jia, B. Jiang, J. Ye, S. Zhang, A. Tang, Y. Liu, Q. Pei and J. Yao, *ACS Appl. Mater. Interfaces*, 2013, **5**, 2033-2039.

117. K. Sun, Z. Xiao, S. Lu, W. Zajaczkowski, W. Pisula, E. Hanssen, J. M. White, R. M. Williamson, J. Subbiah, J. Ouyang, A. B. Holmes, W. W. H. Wong and D. J. Jones, *Nat Commun*, 2015, **6**.

118. J. Zhou, Y. Zuo, X. Wan, G. Long, Q. Zhang, W. Ni, Y. Liu, Z. Li, G. He, C. Li, B. Kan, M. Li and Y. Chen, *J. Am. Chem. Soc.*, 2013, **135**, 8484-8487.

119. G. Long, X. Wan, B. Kan, Y. Liu, G. He, Z. Li, Y. Zhang, Y. Zhang, Q. Zhang, M. Zhang and Y. Chen, *Adv. Energy Mater.*, 2013, **3**, 639-646.

120. S. Shen, P. Jiang, C. He, J. Zhang, P. Shen, Y. Zhang, Y. Yi, Z. Zhang, Z. Li and Y. Li, *Chem. Mater.*, 2013, **25**, 2274-2281.

121. A. Riano, P. Mayorga Burrezo, M. J. Mancheno, A. Timalsina, J. Smith, A. Facchetti, T. J. Marks, J. T. Lopez Navarrete, J. L. Segura, J. Casado and R. Ponce Ortiz, *J. Mater. Chem. C*, 2014, **2**, 6376-6386.

122. R. Fitzner, E. Reinold, A. Mishra, E. Mena-Osteritz, H. Ziehlke, C. Körner, K. Leo, M. Riede, M. Weil, O. Tsaryova, A. Weiß, C. Uhrich, M. Pfeiffer and P. Bäuerle, *Adv. Funct. Mater.*, 2011, **21**, 897-910.

123. S. Mohamed, D. Demeter, J.-A. Laffitte, P. Blanchard and J. Roncali, *Sci. Rep.*, 2015, **5**.

124. E. J. Meijer, D. M. de Leeuw, S. Setayesh, E. van Veenendaal, B. H. Huisman, P. W. M. Blom, J. C. Hummelen, U. Scherf and T. M. Klapwijk, *Nat Mater*, 2003, **2**, 678-682.

125. D. K. Hwang, C. Fuentes-Hernandez, J. Kim, W. J. Potscavage, S.-J. Kim and B. Kippelen, *Adv. Mater.*, 2011, **23**, 1293-1298.

126. J.-P. Hong, A.-Y. Park, S. Lee, J. Kang, N. Shin and D. Y. Yoon, *Appl. Phys. Lett.*, 2008, **92**, 143311.

127. S. Cho, J. Yuen, J. Y. Kim, K. Lee and A. J. Heeger, *Appl. Phys. Lett.*, 2006, **89**, 153505.

128. H. Zhong, J. Smith, S. Rossbauer, A. J. P. White, T. D. Anthopoulos and M. Heeney, *Adv. Mater.*, 2012, **24**, 3205-3211.

129. D. M. Russell, C. J. Newsome, S. P. Li, T. Kugler, M. Ishida and T. Shimoda, *Appl. Phys. Lett.*, 2005, **87**, 222109.

130. J. Huang, D. R. Hines, B. J. Jung, M. S. Bronsgeest, A. Tunnell, V. Ballarotto, H. E. Katz, M. S. Fuhrer, E. D. Williams and J. Cumings, *Org. Electron.*, 2011, **12**, 1471-1476.

131. M. El Gemayel, A. Narita, L. F. Dossel, R. S. Sundaram, A. Kiersnowski, W. Pisula, M. R. Hansen, A. C. Ferrari, E. Orgiu, X. Feng, K. Mullen and P. Samori, *Nanoscale*, 2014, **6**, 6301-6314.

132. S. Park, S. Jin, G. Jun, S. Jeon and S. Hong, *Nano Res.*, 2011, **4**, 1129-1135.

133. Y. D. Park, J. A. Lim, Y. Jang, M. Hwang, H. S. Lee, D. H. Lee, H.-J. Lee, J.-B. Baek

and K. Cho, *Org. Electron.*, 2008, **9**, 317-322.

134. X.-Z. Bo, C. Y. Lee, M. S. Strano, M. Goldfinger, C. Nuckolls and G. B. Blanchet, *Appl. Phys. Lett.*, 2005, **86**, 182102.

135. K. Ramasamy, M. A. Malik and P. O'Brien, *Chem. Commun.*, 2012, **48**, 5703-5714.

136. G. Konstantatos, I. Howard, A. Fischer, S. Hoogland, J. Clifford, E. Klem, L. Levina and E. H. Sargent, *Nature*, 2006, **442**, 180-183.

137. J. M. Luther, M. Law, Q. Song, C. L. Perkins, M. C. Beard and A. J. Nozik, *ACS Nano*, 2008, **2**, 271-280.

138. G. I. Koleilat, L. Levina, H. Shukla, S. H. Myrskog, S. Hinds, A. G. Pattantyus-Abraham and E. H. Sargent, *ACS Nano*, 2008, **2**, 833-840.

139. W. Wang, M. T. Winkler, O. Gunawan, T. Gokmen, T. K. Todorov, Y. Zhu and D. B. Mitzi, *Adv. Energy Mater.*, 2014, **4**, 1301465.

140. P. Jackson, D. Hariskos, E. Lotter, S. Paetel, R. Wuerz, R. Menner, W. Wischmann and M. Powalla, *Progress in Photovoltaics: Research and Applications*, 2011, **19**, 894-897.

141. W. Yang, H.-S. Duan, K. C. Cha, C.-J. Hsu, W.-C. Hsu, H. Zhou, B. Bob and Y. Yang, *J. Am. Chem. Soc.*, 2013, **135**, 6915-6920.

142. I. A. Wright, N. J. Findlay, S. Arumugam, A. R. Inigo, A. L. Kanibolotsky, P. Zassowski, W. Domagala and P. J. Skabara, *J. Mater. Chem. C*, 2014, **2**, 2674-2683.

143. Z. Ning, O. Voznyy, J. Pan, S. Hoogland, V. Adinolfi, J. Xu, M. Li, A. R. Kirmani, J.-P. Sun, J. Minor, K. W. Kemp, H. Dong, L. Rollny, A. Labelle, G. Carey, B. Sutherland, I. Hill, A. Amassian, H. Liu, J. Tang, O. M. Bakr and E. H. Sargent, *Nat Mater*, 2014, **13**, 822-828.

144. A. T. Fafarman, W.-k. Koh, B. T. Diroll, D. K. Kim, D.-K. Ko, S. J. Oh, X. Ye, V. Doan-Nguyen, M. R. Crump, D. C. Reifsnyder, C. B. Murray and C. R. Kagan, *J. Am. Chem. Soc.*, 2011, **133**, 15753-15761.

145. K. A. Singh, G. Sauvé, R. Zhang, T. Kowalewski, R. D. McCullough and L. M. Porter, *Appl. Phys. Lett.*, 2008, **92**, 263303.

146. M. R. Beaulieu, J. K. Baral, N. R. Hendricks, Y. Tang, A. L. Briseño and J. J. Watkins, *ACS Appl. Mater. Interfaces*, 2013, **5**, 13096-13103.

147. L. Huang, Z. Jia, I. Kymissis and S. O'Brien, *Adv. Funct. Mater.*, 2010, **20**, 554-560.

148. N. A. Andrey and P. S. Igor, *J. Phys. D: Appl. Phys.*, 2010, **43**, 315104.

149. R. A. Picca, M. C. Sportelli, D. Hötger, K. Manoli, C. Kranz, B. Mizaikoff, L. Torsi and N. Cioffi, *Electrochim. Acta*, 2015, **178**, 45-54.

150. U. Bielecka, P. Lutsyk, M. Nyk, K. Janus, M. Samoc, W. Bartkowiak and S. Nespurek, *Mater Sci-Pol*, 2013, **31**, 288-297.

151. M. D. Heinemann, K. von Maydell, F. Zutz, J. Kolny-Olesiak, H. Borchert, I. Riedel and J. Parisi, *Adv. Funct. Mater.*, 2009, **19**, 3788-3795.

152. Z.-X. Xu, V. A. L. Roy, P. Stallinga, M. Muccini, S. Toffanin, H.-F. Xiang and C.-M. Che, *Appl. Phys. Lett.*, 2007, **90**, 223509.

153. C. R. Mason, Y. Li, P. O'Brien, N. J. Findlay and P. J. Skabara, *Beilstein. J. Org. Chem.*, 2011, **7**, 1722-1731.

154. S. Lu, M. Drees, Y. Yao, D. Boudinet, H. Yan, H. Pan, J. Wang, Y. Li, H. Usta and A. Facchetti, *Macromolecules*, 2013, **46**, 3895-3906.

155. G. Martelli, L. Testaferri, M. Tiecco and P. Zanirato, *J. Org. Chem*, 1975, **40**, 3384-3391.

156. L. Testaferri, M. Tiecco, P. Zanirato and G. Martelli, *J. Org. Chem*, 1978, **43**, 2197-2200.

157. Y. Mazaki, N. Takiguchi and K. Kobayashi, *Chem. Lett.*, 1991, **20**, 1117-1120.

158. E. Günther and S. Hünig, *Chem. Ber.*, 1992, **125**, 1235-1241.

159. S. Y. Chen, A. Bolag, J. Nishida and Y. Yamashita, *Chemistry Letters*, 2011, **40**, 998-

1000.

160. I. Osaka, T. Abe, H. Mori, M. Saito, N. Takemura, T. Koganezawa and K. Takimiya, *J. Mater. Chem. C*, 2014, **2**, 2307-2312.

161. S. E. J. Villar, H. G. M. Edwards and M. R. D. Seaward, *Analyst*, 2005, **130**, 730-737.

162. S. Luňák Jr, J. Vyňuchal and R. Hrdina, *J. Mol. Struct.*, 2009, **919**, 239-245.

163. A. B. Tamayo, M. Tantiwiwat, B. Walker and T.-Q. Nguyen, *J. Phys. Chem. C*, 2008, **112**, 15543-15552.

164. A. B. Tamayo, B. Walker and T.-Q. Nguyen, *J. Phys. Chem. C*, 2008, **112**, 11545-11551.

165. Y. He and Y. Li, *Phys. Chem. Chem. Phys.*, 2011, **13**, 1970-1983.

166. I. Horcas, R. Fernández, J. M. Gómez-Rodríguez, J. Colchero, J. Gómez-Herrero and A. M. Baro, *Rev. Sci. Instrum.*, 2007, **78**, 013705.

167. T. Yasuda, T. Shimizu, F. Liu, G. Ungar and T. Kato, *J. Am. Chem. Soc.*, 2011, **133**, 13437-13444.

168. V. Fargeas, F. Favresse, D. Mathieu, I. Beaudet, P. Charrue, B. Lebret, M. Piteau and J.-P. Quintard, *Eur. J. Org. Chem.*, 2003, **2003**, 1711-1721.

169. H. K. Tian, J. W. Shi, B. He, N. H. Hu, S. Q. Dong, D. H. Yan, J. P. Zhang, Y. H. Geng and F. S. Wang, *Adv. Funct. Mater.*, 2007, **17**, 1940-1951.

170. L. Torun, B. K. Madras and P. C. Meltzer, *Biorg. Med. Chem.*, 2012, **20**, 2762-2772.

171. G. W. Kabalka, L. Wang and R. M. Pagni, *Tetrahedron*, 2001, **57**, 8017-8028.

172. S. S. Zhu and T. M. Swager, *J. Am. Chem. Soc.*, 1997, **119**, 12568-12577.

173. G. Barbarella, A. Bongini and M. Zambianchi, *Macromolecules*, 1994, **27**, 3039-3045.

174. Y. Nicolas, P. Blanchard, E. Levillain, M. Allain, N. Mercier and J. Roncali, *Org. Lett.*, 2003, **6**, 273-276.

175. I. Barlow, S. Sun, G. J. Leggett and M. Turner, *Langmuir*, 2010, **26**, 4449-4458.

Appendix – Crystal Data

NDO-2T

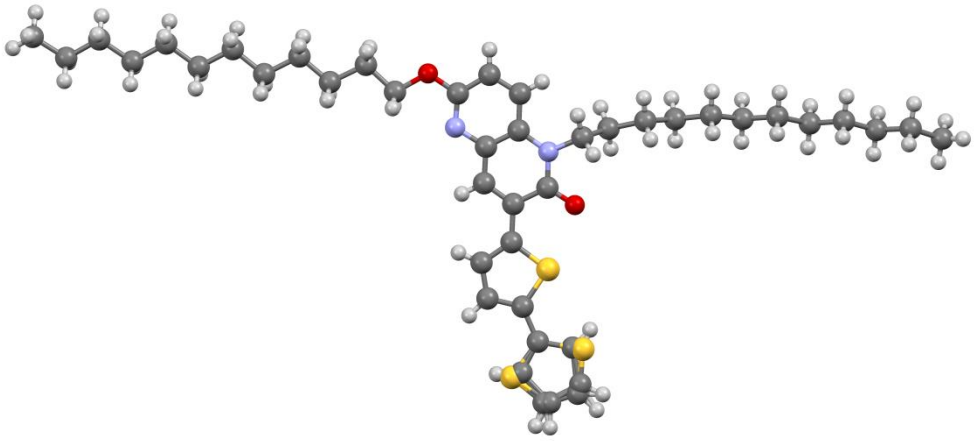

Table 1. Crystal data and structure refinement details.

Identification code	**2015ncs0074 (JC NDO-2T)**	
Empirical formula	$C_{40}H_{58}N_2O_2S_2$	
Formula weight	663.00	
Temperature	100.0 K	
Wavelength	0.71075 Å	
Crystal system	Triclinic	
Space group	*P*–1	
Unit cell dimensions	*a* = 9.7426(8) Å	α = 87.440(6)°
	b = 11.2041(7) Å	β = 85.817(7)°
	c = 17.2231(15) Å	γ = 77.814(6)°
Volume	1831.9(2) Å^3	
Z	2	
Density (calculated)	1.202 Mg / m^3	
Absorption coefficient	0.182 mm^{-1}	
F(000)	720	
Crystal	Fragment; yellow	
Crystal size	0.077 × 0.03 × 0.01 mm^3	
θ range for data collection	2.971 – 25.026°	
Index ranges	$-10 \le h \le 11$, $-13 \le k \le 13$, $-20 \le l \le 20$	
Reflections collected	19460	
Independent reflections	6467 [R_{int} = 0.0752]	
Completeness to θ = 26.000°	89.8 %	
Absorption correction	Semi–empirical from equivalents	
Max. and min. transmission	1.00000 and 0.92035	
Refinement method	Full-matrix least-squares on F^2	
Data / restraints / parameters	6467 / 839 / 448	
Goodness-of-fit on F^2	1.098	
Final *R* indices [$F^2 > 2\sigma(F^2)$]	*R1* = 0.0911, *wR2* = 0.2409	
R indices (all data)	*R1* = 0.1465, *wR2* = 0.2693	

Extinction coefficient	n/a
Largest diff. peak and hole	0.755 and −0.327 e Å^{-3}

Table 2. Atomic coordinates [$\times 10^4$], equivalent isotropic displacement parameters [Å$^2 \times 10^3$] and site occupancy factors. U_{eq} is defined as one third of the trace of the orthogonalized U^{ij} tensor.

Atom	*x*	*y*	*z*	U_{eq}	*S.o.f.*
C1	7717(5)	4765(4)	5505(3)	26(1)	1
C2	8407(6)	4089(4)	4872(3)	27(1)	1
C3	7766(6)	3255(5)	4580(3)	29(1)	1
C4	6464(5)	3106(4)	4919(3)	24(1)	1
C5	5829(5)	3860(4)	5527(3)	25(1)	1
C6	4506(5)	3759(4)	5857(3)	23(1)	1
C7	3800(6)	2945(5)	5604(3)	25(1)	1
C8	4447(6)	2153(5)	4972(3)	27(1)	1
C9	2443(6)	2805(5)	5958(3)	26(1)	1
C10	1738(6)	3376(5)	6608(3)	37(2)	1
C11	474(6)	3060(6)	6827(4)	40(2)	1
C12	158(6)	2239(5)	6343(3)	28(1)	1
C13	−1094(6)	1728(5)	6404(3)	28(1)	1
C14	−2253(14)	2035(12)	6888(8)	32(2)	0.814(7)
C15	−3335(15)	1396(12)	6799(9)	29(2)	0.814(7)
C16	−2954(9)	575(10)	6230(7)	32(2)	0.814(7)
S2A	−2425(16)	2246(15)	7074(8)	32(3)	0.186(7)
C14A	−1320(40)	910(40)	5910(30)	32(2)	0.186(7)
C15A	−2580(40)	510(50)	6130(30)	30(6)	0.186(7)
C16A	−3290(70)	1200(70)	6720(40)	31(7)	0.186(7)
C17	6477(6)	1281(5)	4135(3)	31(1)	1
C18	6145(7)	1496(6)	3311(4)	42(2)	1
C19	6723(7)	311(6)	2844(4)	45(2)	1
C20	6220(7)	324(6)	2060(4)	43(2)	1
C21	6685(7)	−892(6)	1653(4)	45(2)	1
C22	6028(7)	−1000(6)	909(4)	46(2)	1
C23	6470(7)	−2237(6)	552(4)	48(2)	1
C24	5718(7)	−2402(6)	−163(4)	47(2)	1
C25	6175(7)	−3635(6)	−508(4)	47(2)	1
C26	5395(7)	−3859(6)	−1182(4)	45(2)	1
C27	5834(7)	−5117(6)	−1514(4)	52(2)	1
C28	4998(7)	−5318(7)	−2168(4)	56(2)	1
C29	7803(6)	6194(5)	6474(3)	29(1)	1
C30	8764(6)	6996(5)	6690(3)	30(1)	1
C31	8139(6)	7756(5)	7389(3)	32(1)	1
C32	9095(6)	8535(5)	7660(3)	33(1)	1
C33	8383(6)	9369(5)	8312(4)	36(1)	1
C34	9305(6)	10177(5)	8596(3)	36(1)	1
C35	8519(7)	11069(5)	9193(4)	39(2)	1
C36	9451(6)	11811(5)	9543(3)	36(1)	1
C37	8644(7)	12712(5)	10129(4)	41(2)	1
C38	9575(6)	13409(5)	10528(3)	35(1)	1

C39	8721(7)	14326(6)	11090(4)	42(2)	1
C40	9613(7)	15030(6)	11503(4)	42(2)	1
N1	6485(5)	4692(4)	5826(3)	26(1)	1
N2	5764(4)	2245(4)	4674(2)	26(1)	1
O1	3850(4)	1405(3)	4713(2)	33(1)	1
O2	8424(4)	5554(3)	5792(2)	29(1)	1
S1	1451(1)	1863(1)	5617(1)	28(1)	1
S2	−1290(2)	570(2)	5813(1)	31(1)	0.814(7)

Table 3. Bond lengths [Å] and angles [°].

C1–C2	1.401(7)
C1–N1	1.301(6)
C1–O2	1.359(6)
C2–H2	0.9500
C2–C3	1.361(7)
C3–H3	0.9500
C3–C4	1.396(7)
C4–C5	1.400(7)
C4–N2	1.388(6)
C5–C6	1.394(7)
C5–N1	1.373(6)
C6–H6	0.9500
C6–C7	1.357(7)
C7–C8	1.455(7)
C7–C9	1.452(7)
C8–N2	1.370(7)
C8–O1	1.231(6)
C9–C10	1.378(7)
C9–S1	1.721(5)
C10–H10	0.9500
C10–C11	1.375(8)
C11–H11	0.9500
C11–C12	1.365(7)
C12–C13	1.448(7)
C12–S1	1.709(5)
C13–C14	1.347(13)
C13–S2A	1.695(12)
C13–C14A	1.34(4)
C13–S2	1.734(5)
C14–H14	0.9500
C14–C15	1.414(18)
C15–H15	0.9500
C15–C16	1.353(9)
C16–H16	0.9500
C16–S2	1.723(7)
S2A–C16A	1.74(7)
C14A–H14A	0.9500
C14A–C15A	1.41(3)
C15A–H15A	0.9500
C15A–C16A	1.352(19)
C16A–H16A	0.9500
C17–H17A	0.9900
C17–H17B	0.9900
C17–C18	1.476(8)
C17–N2	1.480(6)
C18–H18A	0.9900

C18–H18B	0.9900
C18–C19	1.562(8)
C19–H19A	0.9900
C19–H19B	0.9900
C19–C20	1.468(9)
C20–H20A	0.9900
C20–H20B	0.9900
C20–C21	1.527(8)
C21–H21A	0.9900
C21–H21B	0.9900
C21–C22	1.493(9)
C22–H22A	0.9900
C22–H22B	0.9900
C22–C23	1.507(8)
C23–H23A	0.9900
C23–H23B	0.9900
C23–C24	1.516(9)
C24–H24A	0.9900
C24–H24B	0.9900
C24–C25	1.495(8)
C25–H25A	0.9900
C25–H25B	0.9900
C25–C26	1.490(9)
C26–H26A	0.9900
C26–H26B	0.9900
C26–C27	1.510(8)
C27–H27A	0.9900
C27–H27B	0.9900
C27–C28	1.489(9)
C28–H28A	0.9800
C28–H28B	0.9800
C28–H28C	0.9800
C29–H29A	0.9900
C29–H29B	0.9900
C29–C30	1.502(7)
C29–O2	1.432(6)
C30–H30A	0.9900
C30–H30B	0.9900
C30–C31	1.519(7)
C31–H31A	0.9900
C31–H31B	0.9900
C31–C32	1.514(7)
C32–H32A	0.9900
C32–H32B	0.9900
C32–C33	1.523(7)
C33–H33A	0.9900
C33–H33B	0.9900
C33–C34	1.521(7)
C34–H34A	0.9900

C34–H34B	0.9900
C34–C35	1.515(7)
C35–H35A	0.9900
C35–H35B	0.9900
C35–C36	1.524(8)
C36–H36A	0.9900
C36–H36B	0.9900
C36–C37	1.516(7)
C37–H37A	0.9900
C37–H37B	0.9900
C37–C38	1.530(8)
C38–H38A	0.9900
C38–H38B	0.9900
C38–C39	1.514(7)
C39–H39A	0.9900
C39–H39B	0.9900
C39–C40	1.522(8)
C40–H40A	0.9800
C40–H40B	0.9800
C40–H40C	0.9800

N1–C1–C2	125.6(5)
N1–C1–O2	119.0(4)
O2–C1–C2	115.5(4)
C1–C2–H2	121.1
C3–C2–C1	117.8(5)
C3–C2–H2	121.1
C2–C3–H3	120.4
C2–C3–C4	119.2(5)
C4–C3–H3	120.4
C3–C4–C5	118.8(4)
N2–C4–C3	122.8(4)
N2–C4–C5	118.4(4)
C6–C5–C4	119.9(4)
N1–C5–C4	121.8(5)
N1–C5–C6	118.3(4)
C5–C6–H6	119.1
C7–C6–C5	121.9(5)
C7–C6–H6	119.1
C6–C7–C8	118.9(5)
C6–C7–C9	122.3(4)
C9–C7–C8	118.7(4)
N2–C8–C7	118.1(4)
O1–C8–C7	121.8(5)
O1–C8–N2	120.1(4)
C7–C9–S1	124.1(4)
C10–C9–C7	127.1(5)
C10–C9–S1	108.9(4)
C9–C10–H10	122.5

C11–C10–C9	115.0(5)
C11–C10–H10	122.5
C10–C11–H11	123.8
C12–C11–C10	112.4(5)
C12–C11–H11	123.8
C11–C12–C13	126.6(5)
C11–C12–S1	111.2(4)
C13–C12–S1	122.2(4)
C12–C13–S2A	120.3(6)
C12–C13–S2	122.1(4)
C14–C13–C12	128.5(6)
C14–C13–S2	109.4(6)
C14A–C13–C12	123.3(17)
C14A–C13–S2A	116.2(17)
C13–C14–H14	122.1
C13–C14–C15	115.8(9)
C15–C14–H14	122.1
C14–C15–H15	124.6
C16–C15–C14	110.7(10)
C16–C15–H15	124.6
C15–C16–H16	123.8
C15–C16–S2	112.4(8)
S2–C16–H16	123.8
C13–S2A–C16A	86.8(15)
C13–C14A–H14A	124.3
C13–C14A–C15A	111(3)
C15A–C14A–H14A	124.3
C14A–C15A–H15A	125.2
C16A–C15A–C14A	110(3)
C16A–C15A–H15A	125.2
S2A–C16A–H16A	122.4
C15A–C16A–S2A	115(4)
C15A–C16A–H16A	122.4
H17A–C17–H17B	107.4
C18–C17–H17A	108.3
C18–C17–H17B	108.3
C18–C17–N2	115.7(5)
N2–C17–H17A	108.3
N2–C17–H17B	108.3
C17–C18–H18A	109.6
C17–C18–H18B	109.6
C17–C18–C19	110.2(5)
H18A–C18–H18B	108.1
C19–C18–H18A	109.6
C19–C18–H18B	109.6
C18–C19–H19A	108.4
C18–C19–H19B	108.4
H19A–C19–H19B	107.5
C20–C19–C18	115.4(6)

C20–C19–H19A	108.4
C20–C19–H19B	108.4
C19–C20–H20A	108.8
C19–C20–H20B	108.8
C19–C20–C21	114.0(6)
H20A–C20–H20B	107.7
C21–C20–H20A	108.8
C21–C20–H20B	108.8
C20–C21–H21A	108.2
C20–C21–H21B	108.2
H21A–C21–H21B	107.3
C22–C21–C20	116.5(6)
C22–C21–H21A	108.2
C22–C21–H21B	108.2
C21–C22–H22A	108.7
C21–C22–H22B	108.7
C21–C22–C23	114.3(6)
H22A–C22–H22B	107.6
C23–C22–H22A	108.7
C23–C22–H22B	108.7
C22–C23–H23A	108.5
C22–C23–H23B	108.5
C22–C23–C24	115.2(6)
H23A–C23–H23B	107.5
C24–C23–H23A	108.5
C24–C23–H23B	108.5
C23–C24–H24A	108.7
C23–C24–H24B	108.7
H24A–C24–H24B	107.6
C25–C24–C23	114.2(6)
C25–C24–H24A	108.7
C25–C24–H24B	108.7
C24–C25–H25A	108.3
C24–C25–H25B	108.3
H25A–C25–H25B	107.4
C26–C25–C24	115.8(6)
C26–C25–H25A	108.3
C26–C25–H25B	108.3
C25–C26–H26A	108.4
C25–C26–H26B	108.4
C25–C26–C27	115.6(6)
H26A–C26–H26B	107.5
C27–C26–H26A	108.4
C27–C26–H26B	108.4
C26–C27–H27A	108.8
C26–C27–H27B	108.8
H27A–C27–H27B	107.7
C28–C27–C26	113.9(6)
C28–C27–H27A	108.8

C28–C27–H27B	108.8
C27–C28–H28A	109.5
C27–C28–H28B	109.5
C27–C28–H28C	109.5
H28A–C28–H28B	109.5
H28A–C28–H28C	109.5
H28B–C28–H28C	109.5
H29A–C29–H29B	108.4
C30–C29–H29A	110.1
C30–C29–H29B	110.1
O2–C29–H29A	110.1
O2–C29–H29B	110.1
O2–C29–C30	108.0(4)
C29–C30–H30A	109.4
C29–C30–H30B	109.4
C29–C30–C31	111.1(4)
H30A–C30–H30B	108.0
C31–C30–H30A	109.4
C31–C30–H30B	109.4
C30–C31–H31A	108.9
C30–C31–H31B	108.9
H31A–C31–H31B	107.7
C32–C31–C30	113.6(5)
C32–C31–H31A	108.9
C32–C31–H31B	108.9
C31–C32–H32A	109.2
C31–C32–H32B	109.2
C31–C32–C33	112.0(5)
H32A–C32–H32B	107.9
C33–C32–H32A	109.2
C33–C32–H32B	109.2
C32–C33–H33A	108.8
C32–C33–H33B	108.8
H33A–C33–H33B	107.7
C34–C33–C32	113.7(5)
C34–C33–H33A	108.8
C34–C33–H33B	108.8
C33–C34–H34A	109.2
C33–C34–H34B	109.2
H34A–C34–H34B	107.9
C35–C34–C33	112.1(5)
C35–C34–H34A	109.2
C35–C34–H34B	109.2
C34–C35–H35A	108.9
C34–C35–H35B	108.9
C34–C35–C36	113.3(5)
H35A–C35–H35B	107.7
C36–C35–H35A	108.9
C36–C35–H35B	108.9

C35–C36–H36A	109.1
C35–C36–H36B	109.1
H36A–C36–H36B	107.8
C37–C36–C35	112.6(5)
C37–C36–H36A	109.1
C37–C36–H36B	109.1
C36–C37–H37A	108.9
C36–C37–H37B	108.9
C36–C37–C38	113.5(5)
H37A–C37–H37B	107.7
C38–C37–H37A	108.9
C38–C37–H37B	108.9
C37–C38–H38A	109.3
C37–C38–H38B	109.3
H38A–C38–H38B	107.9
C39–C38–C37	111.8(5)
C39–C38–H38A	109.3
C39–C38–H38B	109.3
C38–C39–H39A	108.9
C38–C39–H39B	108.9
C38–C39–C40	113.3(5)
H39A–C39–H39B	107.7
C40–C39–H39A	108.9
C40–C39–H39B	108.9
C39–C40–H40A	109.5
C39–C40–H40B	109.5
C39–C40–H40C	109.5
H40A–C40–H40B	109.5
H40A–C40–H40C	109.5
H40B–C40–H40C	109.5
C1–N1–C5	116.7(4)
C4–N2–C17	121.0(4)
C8–N2–C4	122.7(4)
C8–N2–C17	115.9(4)
C1–O2–C29	117.2(4)
C12–S1–C9	92.5(2)
C16–S2–C13	91.6(4)

Symmetry transformations used to generate equivalent atoms:

Table 4. Anisotropic displacement parameters [Å$^2\times$ 10^3]. The anisotropic displacement factor exponent takes the form: $-2\pi^2[h^2a^{*2}U^{11} + \cdots + 2\ h\ k\ a^*\ b^*\ U^{12}\ ]$.

Atom	U^{11}	U^{22}	U^{33}	U^{23}	U^{13}	U^{12}
C1	26(2)	18(2)	36(3)	−7(2)	2(2)	−9(2)
C2	28(3)	18(2)	36(3)	−6(2)	3(2)	−8(2)
C3	28(3)	24(3)	36(3)	−10(2)	4(2)	−7(2)
C4	24(2)	18(2)	30(3)	−10(2)	3(2)	−7(2)
C5	27(2)	18(2)	32(3)	−9(2)	2(2)	−8(2)
C6	25(2)	19(2)	26(3)	−8(2)	4(2)	−6(2)
C7	28(2)	20(2)	29(3)	−9(2)	2(2)	−7(2)
C8	28(2)	22(2)	33(3)	−13(2)	4(2)	−10(2)
C9	28(2)	21(3)	34(3)	−11(2)	1(2)	−10(2)
C10	37(3)	37(3)	43(3)	−25(3)	8(2)	−20(3)
C11	40(3)	44(3)	42(3)	−25(3)	10(3)	−24(3)
C12	31(3)	21(3)	33(3)	−11(2)	5(2)	−10(2)
C13	33(2)	20(2)	33(3)	−7(2)	0(2)	−12(2)
C14	35(4)	24(4)	41(5)	−12(4)	1(3)	−13(3)
C15	33(3)	21(5)	35(5)	−7(3)	1(3)	−12(3)
C16	29(4)	26(4)	44(5)	−14(3)	7(4)	−13(4)
S2A	31(5)	35(6)	33(6)	−8(4)	7(4)	−14(4)
C14A	35(4)	24(4)	41(5)	−12(4)	1(3)	−13(3)
C15A	32(8)	24(10)	37(11)	−1(8)	−6(7)	−9(7)
C16A	31(7)	27(12)	39(12)	−2(10)	−3(7)	−11(8)
C17	27(3)	28(3)	39(3)	−21(2)	6(2)	−9(2)
C18	36(3)	49(4)	40(3)	−18(3)	2(3)	−2(3)
C19	43(4)	42(3)	49(3)	−20(3)	7(3)	−7(3)
C20	42(4)	38(3)	49(3)	−15(3)	8(3)	−12(3)
C21	45(4)	48(4)	38(3)	−17(3)	6(3)	0(3)
C22	45(4)	47(4)	50(4)	−17(3)	7(3)	−19(3)
C23	45(4)	56(4)	44(3)	−19(3)	1(3)	−7(3)
C24	43(4)	46(3)	55(4)	−17(3)	0(3)	−17(3)
C25	46(4)	57(4)	38(3)	−17(3)	2(3)	−9(3)
C26	41(4)	48(4)	50(4)	−17(3)	0(3)	−15(3)
C27	54(4)	57(4)	45(4)	−20(3)	6(3)	−10(3)
C28	55(4)	58(4)	56(4)	−29(3)	5(3)	−14(3)
C29	28(3)	24(3)	36(3)	−13(2)	10(2)	−14(2)
C30	35(3)	24(3)	34(3)	−10(2)	2(2)	−17(2)
C31	41(3)	23(3)	37(3)	−11(2)	3(2)	−15(2)
C32	39(3)	25(3)	37(3)	−11(2)	1(3)	−13(2)
C33	44(3)	22(3)	44(3)	−16(2)	0(3)	−12(2)
C34	46(3)	27(3)	39(3)	−14(2)	−3(3)	−15(3)
C35	51(4)	28(3)	40(3)	−15(3)	−5(3)	−12(3)
C36	45(3)	28(3)	37(3)	−15(2)	0(3)	−9(3)
C37	51(4)	31(3)	44(4)	−20(3)	0(3)	−12(3)
C38	47(3)	27(3)	33(3)	−12(2)	−3(3)	−7(3)
C39	45(4)	34(3)	46(4)	−22(3)	−1(3)	−7(3)
C40	56(4)	37(3)	37(4)	−21(3)	−1(3)	−12(3)

N1	28(2)	19(2)	33(2)	−12(2)	4(2)	−11(2)
N2	28(2)	20(2)	31(2)	−15(2)	5(2)	−8(2)
O1	32(2)	30(2)	41(2)	−21(2)	7(2)	−16(2)
O2	29(2)	24(2)	39(2)	−16(2)	7(2)	−15(2)
S1	27(1)	25(1)	36(1)	−15(1)	6(1)	−14(1)
S2	36(1)	25(1)	38(1)	−14(1)	3(1)	−18(1)

NDO-2T-BF

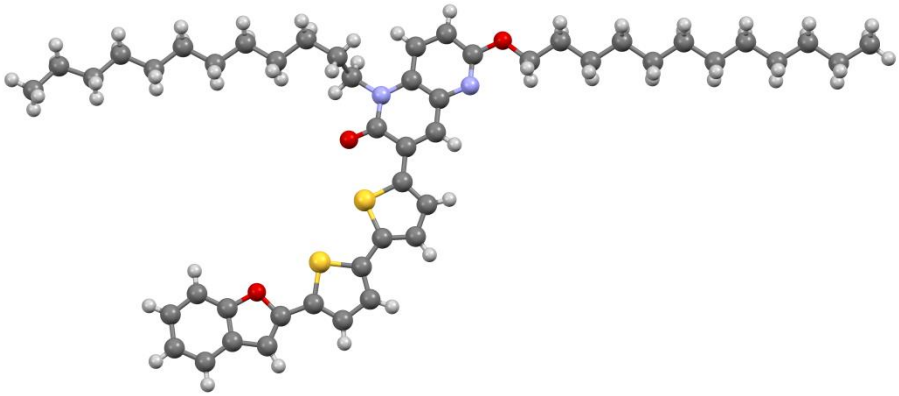

Table 1. Crystal data and structure refinement details.

Identification code	**2015ncs0248 (JC NDO-2T-BF)**	
Empirical formula	$C_{48}H_{62}N_2O_3S_2$	
Formula weight	779.11	
Temperature	100.15 K	
Wavelength	0.71075 Å	
Crystal system	Triclinic	
Space group	*P*–1	
Unit cell dimensions	*a* = 15.981(5) Å	α = 101.469(3)°
	b = 16.606(4) Å	β = 110.961(3)°
	c = 18.414(5) Å	γ = 103.406(3)°
Volume	4220(2) Å^3	
Z	4	
Density (calculated)	1.226 Mg / m^3	
Absorption coefficient	0.170 mm^{-1}	
F(000)	1680	
Crystal	Column; orange	
Crystal size	0.23 × 0.02 × 0.02 mm^3	
θ range for data collection	2.153 – 27.506°	
Index ranges	$-20 \le h \le 20$, $-21 \le k \le 20$, $-23 \le l \le 23$	
Reflections collected	56199	
Independent reflections	19270 [R_{int} = 0.0523]	
Completeness to θ = 25.242°	99.8 %	
Absorption correction	Semi–empirical from equivalents	
Max. and min. transmission	1.000 and 0.686	
Refinement method	Full-matrix least-squares on F^2	
Data / restraints / parameters	19270 / 0 / 995	
Goodness-of-fit on F^2	1.115	
Final *R* indices [$F^2 > 2\sigma(F^2)$]	*R1* = 0.0640, *wR2* = 0.1529	
R indices (all data)	*R1* = 0.0796, *wR2* = 0.1619	
Extinction coefficient	n/a	

Largest diff. peak and hole	0.319 and −0.334 e Å^{-3}

Table 2. Atomic coordinates [$\times 10^4$], equivalent isotropic displacement parameters [Å$^2 \times 10^3$] and site occupancy factors. U_{eq} is defined as one third of the trace of the orthogonalized U^{ij} tensor.

Atom	*x*	*y*	*z*	U_{eq}	*S.o.f.*
S1	6317(1)	3017(1)	2891(1)	27(1)	1
S2	7696(1)	2176(1)	3959(1)	25(1)	1
O1	6031(1)	4271(1)	2040(1)	30(1)	1
O2	11045(1)	−436(1)	6917(1)	27(1)	1
O3	9584(1)	2606(1)	4567(1)	30(1)	1
N1	10046(1)	161(1)	6117(1)	23(1)	1
N2	10573(1)	1989(1)	5320(1)	25(1)	1
C1	5827(2)	4873(1)	1639(1)	29(1)	1
C2	6492(2)	5596(2)	1674(1)	34(1)	1
C3	6131(2)	6129(2)	1240(2)	35(1)	1
C4	5155(2)	5931(2)	796(2)	36(1)	1
C5	4509(2)	5192(2)	761(2)	36(1)	1
C6	4852(2)	4647(2)	1199(1)	29(1)	1
C7	4435(2)	3855(2)	1332(1)	31(1)	1
C8	5156(2)	3660(1)	1839(1)	27(1)	1
C9	5219(2)	2975(1)	2212(1)	26(1)	1
C10	4519(2)	2247(2)	2113(1)	30(1)	1
C11	4874(2)	1716(2)	2580(1)	30(1)	1
C12	5845(2)	2046(1)	3030(1)	26(1)	1
C13	6478(2)	1675(1)	3544(1)	26(1)	1
C14	6253(2)	909(1)	3724(1)	29(1)	1
C15	7062(2)	739(1)	4203(1)	29(1)	1
C16	7909(1)	1363(1)	4390(1)	24(1)	1
C17	8869(1)	1378(1)	4881(1)	24(1)	1
C18	9024(1)	791(1)	5289(1)	24(1)	1
C19	9952(1)	782(1)	5729(1)	23(1)	1
C20	10911(2)	167(1)	6525(1)	24(1)	1
C21	11742(2)	763(1)	6591(1)	27(1)	1
C22	11650(2)	1376(1)	6195(1)	27(1)	1
C23	10730(1)	1393(1)	5745(1)	24(1)	1
C24	9677(2)	2038(1)	4906(1)	25(1)	1
C25	10208(2)	−1021(1)	6895(1)	26(1)	1
C26	10511(2)	−1651(1)	7340(1)	26(1)	1
C27	9662(2)	−2350(1)	7280(1)	28(1)	1
C28	9949(2)	−2951(1)	7777(1)	26(1)	1
C29	9111(2)	−3721(1)	7648(1)	26(1)	1
C30	9417(2)	−4353(1)	8094(1)	27(1)	1
C31	8597(2)	−5119(1)	7983(1)	27(1)	1
C32	8909(2)	−5779(1)	8388(1)	28(1)	1

C33	8085(2)	−6527(1)	8303(1)	28(1)	1
C34	8386(2)	−7216(1)	8669(1)	31(1)	1
C35	7549(2)	−7962(1)	8571(2)	33(1)	1
C36	7846(2)	−8661(2)	8921(2)	47(1)	1
C37	11379(2)	2604(1)	5277(1)	27(1)	1
C38	11903(2)	3408(1)	6016(1)	30(1)	1
C39	12716(2)	4039(1)	5935(1)	31(1)	1
C40	12378(2)	4554(1)	5356(1)	29(1)	1
C41	13193(2)	5184(1)	5279(1)	29(1)	1
C42	12859(2)	5808(1)	4827(1)	29(1)	1
C43	13644(2)	6513(1)	4798(1)	31(1)	1
C44	13241(2)	7128(1)	4374(1)	31(1)	1
C45	13962(2)	7874(2)	4330(2)	36(1)	1
C46	13499(2)	8481(2)	3944(2)	40(1)	1
C47	14148(2)	9224(2)	3835(2)	53(1)	1
C48	13647(3)	9831(2)	3495(2)	60(1)	1
S101	1373(1)	2611(1)	−1943(1)	30(1)	1
S102	2729(1)	1707(1)	−946(1)	28(1)	1
O101	1048(1)	4052(1)	−2518(1)	30(1)	1
O102	6061(1)	−801(1)	2167(1)	26(1)	1
O103	4617(1)	2242(1)	−188(1)	29(1)	1
N101	5064(1)	−259(1)	1289(1)	22(1)	1
N102	5600(1)	1731(1)	704(1)	22(1)	1
C101	883(2)	4647(1)	−2939(1)	27(1)	1
C102	1525(2)	5449(2)	−2768(1)	33(1)	1
C103	1220(2)	5940(2)	−3276(2)	34(1)	1
C104	318(2)	5622(2)	−3924(2)	36(1)	1
C105	−306(2)	4803(2)	−4091(2)	35(1)	1
C106	−20(2)	4308(1)	−3578(1)	28(1)	1
C107	−438(2)	3451(2)	−3546(1)	30(1)	1
C108	222(2)	3330(1)	−2909(1)	27(1)	1
C109	273(2)	2620(1)	−2566(1)	27(1)	1
C110	−435(2)	1896(2)	−2671(1)	30(1)	1
C111	−87(2)	1335(2)	−2244(1)	30(1)	1
C112	885(2)	1632(1)	−1824(1)	27(1)	1
C113	1511(2)	1244(1)	−1324(1)	26(1)	1
C114	1280(2)	522(1)	−1080(1)	28(1)	1
C115	2087(2)	355(1)	−591(1)	27(1)	1
C116	2937(2)	942(1)	−451(1)	24(1)	1
C117	3895(1)	960(1)	47(1)	22(1)	1
C118	4046(1)	337(1)	415(1)	23(1)	1
C119	4976(1)	390(1)	936(1)	21(1)	1
C120	5927(1)	−191(1)	1782(1)	23(1)	1
C121	6755(1)	490(1)	1959(1)	24(1)	1
C122	6666(1)	1136(1)	1610(1)	24(1)	1
C123	5756(1)	1097(1)	1081(1)	22(1)	1
C124	4709(1)	1686(1)	167(1)	23(1)	1
C125	5229(1)	−1506(1)	2000(1)	25(1)	1
C126	5549(2)	−2068(1)	2524(1)	26(1)	1
C127	4718(2)	−2830(1)	2406(1)	27(1)	1

C128	5023(2)	−3445(1)	2878(1)	26(1)	1
C129	4202(2)	−4209(1)	2774(1)	28(1)	1
C130	4529(2)	−4813(1)	3256(1)	26(1)	1
C131	3717(2)	−5587(1)	3157(1)	30(1)	1
C132	4048(2)	−6157(1)	3677(1)	28(1)	1
C133	3244(2)	−6927(1)	3592(1)	30(1)	1
C134	3570(2)	−7423(1)	4194(1)	32(1)	1
C135	2774(2)	−8207(2)	4104(1)	34(1)	1
C136	3069(2)	−8564(2)	4827(2)	42(1)	1
C137	6404(2)	2507(1)	884(1)	24(1)	1
C138	6979(2)	2342(1)	397(1)	26(1)	1
C139	7821(2)	3152(1)	609(1)	26(1)	1
C140	7538(2)	3896(1)	329(1)	28(1)	1
C141	8382(2)	4655(1)	449(1)	27(1)	1
C142	8063(2)	5344(1)	98(1)	27(1)	1
C143	8836(2)	6108(1)	130(1)	26(1)	1
C144	8387(2)	6697(1)	−305(1)	27(1)	1
C145	9074(2)	7501(1)	−311(1)	28(1)	1
C146	8542(2)	8006(1)	−808(1)	31(1)	1
C147	9176(2)	8834(1)	−820(2)	35(1)	1
C148	8610(2)	9311(2)	−1323(2)	45(1)	1

Table 3. Bond lengths [Å] and angles [°].

S1–C9	1.729(2)
S1–C12	1.724(2)
S2–C13	1.731(2)
S2–C16	1.737(2)
O1–C1	1.387(2)
O1–C8	1.393(3)
O2–C20	1.358(2)
O2–C25	1.441(2)
O3–C24	1.239(2)
N1–C19	1.373(2)
N1–C20	1.313(3)
N2–C23	1.393(2)
N2–C24	1.391(3)
N2–C37	1.484(3)
C1–C2	1.381(3)
C1–C6	1.389(3)
C2–H2	0.9500
C2–C3	1.394(3)
C3–H3	0.9500
C3–C4	1.397(3)
C4–H4	0.9500
C4–C5	1.382(3)
C5–H5	0.9500
C5–C6	1.404(3)
C6–C7	1.440(3)
C7–H7	0.9500
C7–C8	1.353(3)
C8–C9	1.445(3)
C9–C10	1.374(3)
C10–H10	0.9500
C10–C11	1.421(3)
C11–H11	0.9500
C11–C12	1.379(3)
C12–C13	1.461(3)
C13–C14	1.378(3)
C14–H14	0.9500
C14–C15	1.408(3)
C15–H15	0.9500
C15–C16	1.378(3)
C16–C17	1.466(3)
C17–C18	1.358(3)
C17–C24	1.467(3)
C18–H18	0.9500
C18–C19	1.419(3)
C19–C23	1.398(3)
C20–C21	1.409(3)

C21–H21	0.9500
C21–C22	1.370(3)
C22–H22	0.9500
C22–C23	1.416(3)
C25–H25A	0.9900
C25–H25B	0.9900
C25–C26	1.514(3)
C26–H26A	0.9900
C26–H26B	0.9900
C26–C27	1.520(3)
C27–H27A	0.9900
C27–H27B	0.9900
C27–C28	1.523(3)
C28–H28A	0.9900
C28–H28B	0.9900
C28–C29	1.530(3)
C29–H29A	0.9900
C29–H29B	0.9900
C29–C30	1.519(3)
C30–H30A	0.9900
C30–H30B	0.9900
C30–C31	1.519(3)
C31–H31A	0.9900
C31–H31B	0.9900
C31–C32	1.523(3)
C32–H32A	0.9900
C32–H32B	0.9900
C32–C33	1.521(3)
C33–H33A	0.9900
C33–H33B	0.9900
C33–C34	1.525(3)
C34–H34A	0.9900
C34–H34B	0.9900
C34–C35	1.525(3)
C35–H35A	0.9900
C35–H35B	0.9900
C35–C36	1.525(3)
C36–H36A	0.9800
C36–H36B	0.9800
C36–H36C	0.9800
C37–H37A	0.9900
C37–H37B	0.9900
C37–C38	1.510(3)
C38–H38A	0.9900
C38–H38B	0.9900
C38–C39	1.542(3)
C39–H39A	0.9900
C39–H39B	0.9900
C39–C40	1.526(3)

C40–H40A	0.9900
C40–H40B	0.9900
C40–C41	1.538(3)
C41–H41A	0.9900
C41–H41B	0.9900
C41–C42	1.527(3)
C42–H42A	0.9900
C42–H42B	0.9900
C42–C43	1.530(3)
C43–H43A	0.9900
C43–H43B	0.9900
C43–C44	1.527(3)
C44–H44A	0.9900
C44–H44B	0.9900
C44–C45	1.522(3)
C45–H45A	0.9900
C45–H45B	0.9900
C45–C46	1.525(3)
C46–H46A	0.9900
C46–H46B	0.9900
C46–C47	1.514(3)
C47–H47A	0.9900
C47–H47B	0.9900
C47–C48	1.522(4)
C48–H48A	0.9800
C48–H48B	0.9800
C48–H48C	0.9800
S101–C109	1.728(2)
S101–C112	1.725(2)
S102–C113	1.728(2)
S102–C116	1.731(2)
O101–C101	1.388(2)
O101–C108	1.392(3)
O102–C120	1.361(2)
O102–C125	1.442(2)
O103–C124	1.240(2)
N101–C119	1.373(2)
N101–C120	1.315(3)
N102–C123	1.393(2)
N102–C124	1.387(3)
N102–C137	1.476(2)
C101–C102	1.377(3)
C101–C106	1.389(3)
C102–H102	0.9500
C102–C103	1.392(3)
C103–H103	0.9500
C103–C104	1.395(3)
C104–H104	0.9500
C104–C105	1.386(3)

C105–H105	0.9500
C105–C106	1.397(3)
C106–C107	1.449(3)
C107–H107	0.9500
C107–C108	1.355(3)
C108–C109	1.448(3)
C109–C110	1.372(3)
C110–H110	0.9500
C110–C111	1.419(3)
C111–H111	0.9500
C111–C112	1.375(3)
C112–C113	1.463(3)
C113–C114	1.379(3)
C114–H114	0.9500
C114–C115	1.409(3)
C115–H115	0.9500
C115–C116	1.378(3)
C116–C117	1.465(3)
C117–C118	1.366(3)
C117–C124	1.468(3)
C118–H118	0.9500
C118–C119	1.423(3)
C119–C123	1.402(3)
C120–C121	1.410(3)
C121–H121	0.9500
C121–C122	1.365(3)
C122–H122	0.9500
C122–C123	1.410(3)
C125–H12A	0.9900
C125–H12B	0.9900
C125–C126	1.514(3)
C126–H12C	0.9900
C126–H12D	0.9900
C126–C127	1.522(3)
C127–H12E	0.9900
C127–H12F	0.9900
C127–C128	1.523(3)
C128–H12G	0.9900
C128–H12H	0.9900
C128–C129	1.523(3)
C129–H12I	0.9900
C129–H12J	0.9900
C129–C130	1.527(3)
C130–H13A	0.9900
C130–H13B	0.9900
C130–C131	1.527(3)
C131–H13C	0.9900
C131–H13D	0.9900
C131–C132	1.523(3)

C132–H13E	0.9900
C132–H13F	0.9900
C132–C133	1.525(3)
C133–H13G	0.9900
C133–H13H	0.9900
C133–C134	1.527(3)
C134–H13I	0.9900
C134–H13J	0.9900
C134–C135	1.527(3)
C135–H13K	0.9900
C135–H13L	0.9900
C135–C136	1.530(3)
C136–H13M	0.9800
C136–H13N	0.9800
C136–H13O	0.9800
C137–H13P	0.9900
C137–H13Q	0.9900
C137–C138	1.526(3)
C138–H13R	0.9900
C138–H13S	0.9900
C138–C139	1.533(3)
C139–H13T	0.9900
C139–H13U	0.9900
C139–C140	1.530(3)
C140–H14A	0.9900
C140–H14B	0.9900
C140–C141	1.531(3)
C141–H14C	0.9900
C141–H14D	0.9900
C141–C142	1.522(3)
C142–H14E	0.9900
C142–H14F	0.9900
C142–C143	1.526(3)
C143–H14G	0.9900
C143–H14H	0.9900
C143–C144	1.530(3)
C144–H14I	0.9900
C144–H14J	0.9900
C144–C145	1.524(3)
C145–H14K	0.9900
C145–H14L	0.9900
C145–C146	1.530(3)
C146–H14M	0.9900
C146–H14N	0.9900
C146–C147	1.517(3)
C147–H14O	0.9900
C147–H14P	0.9900
C147–C148	1.525(3)
C148–H14Q	0.9800

C148–H14R	0.9800
C148–H14S	0.9800
C12–S1–C9	92.43(10)
C13–S2–C16	92.27(10)
C1–O1–C8	105.75(16)
C20–O2–C25	116.53(15)
C20–N1–C19	117.14(17)
C23–N2–C37	120.19(17)
C24–N2–C23	123.29(17)
C24–N2–C37	116.51(16)
O1–C1–C6	110.22(19)
C2–C1–O1	125.2(2)
C2–C1–C6	124.6(2)
C1–C2–H2	122.1
C1–C2–C3	115.8(2)
C3–C2–H2	122.1
C2–C3–H3	119.3
C2–C3–C4	121.4(2)
C4–C3–H3	119.3
C3–C4–H4	119.4
C5–C4–C3	121.3(2)
C5–C4–H4	119.4
C4–C5–H5	120.7
C4–C5–C6	118.5(2)
C6–C5–H5	120.7
C1–C6–C5	118.4(2)
C1–C6–C7	105.89(18)
C5–C6–C7	135.7(2)
C6–C7–H7	126.5
C8–C7–C6	107.0(2)
C8–C7–H7	126.5
O1–C8–C9	114.22(17)
C7–C8–O1	111.15(19)
C7–C8–C9	134.6(2)
C8–C9–S1	119.05(16)
C10–C9–S1	110.80(16)
C10–C9–C8	130.1(2)
C9–C10–H10	123.5
C9–C10–C11	113.1(2)
C11–C10–H10	123.5
C10–C11–H11	123.6
C12–C11–C10	112.8(2)
C12–C11–H11	123.6
C11–C12–S1	110.89(15)
C11–C12–C13	129.6(2)
C13–C12–S1	119.47(16)
C12–C13–S2	120.01(16)
C14–C13–S2	110.98(15)

C14–C13–C12	128.9(2)
C13–C14–H14	123.7
C13–C14–C15	112.69(19)
C15–C14–H14	123.7
C14–C15–H15	123.0
C16–C15–C14	114.00(19)
C16–C15–H15	123.0
C15–C16–S2	110.06(15)
C15–C16–C17	127.22(18)
C17–C16–S2	122.72(15)
C16–C17–C24	118.12(17)
C18–C17–C16	122.07(18)
C18–C17–C24	119.79(18)
C17–C18–H18	119.1
C17–C18–C19	121.83(18)
C19–C18–H18	119.1
N1–C19–C18	118.12(17)
N1–C19–C23	122.65(18)
C23–C19–C18	119.23(17)
O2–C20–C21	115.72(18)
N1–C20–O2	119.62(18)
N1–C20–C21	124.66(18)
C20–C21–H21	120.9
C22–C21–C20	118.28(19)
C22–C21–H21	120.9
C21–C22–H22	120.5
C21–C22–C23	119.09(19)
C23–C22–H22	120.5
N2–C23–C19	119.07(18)
N2–C23–C22	122.77(18)
C19–C23–C22	118.17(18)
O3–C24–N2	120.47(18)
O3–C24–C17	122.85(19)
N2–C24–C17	116.67(17)
O2–C25–H25A	110.1
O2–C25–H25B	110.1
O2–C25–C26	107.79(16)
H25A–C25–H25B	108.5
C26–C25–H25A	110.1
C26–C25–H25B	110.1
C25–C26–H26A	109.3
C25–C26–H26B	109.3
C25–C26–C27	111.67(17)
H26A–C26–H26B	107.9
C27–C26–H26A	109.3
C27–C26–H26B	109.3
C26–C27–H27A	109.0
C26–C27–H27B	109.0
C26–C27–C28	112.79(17)

H27A–C27–H27B	107.8
C28–C27–H27A	109.0
C28–C27–H27B	109.0
C27–C28–H28A	108.8
C27–C28–H28B	108.8
C27–C28–C29	113.61(17)
H28A–C28–H28B	107.7
C29–C28–H28A	108.8
C29–C28–H28B	108.8
C28–C29–H29A	109.0
C28–C29–H29B	109.0
H29A–C29–H29B	107.8
C30–C29–C28	112.94(17)
C30–C29–H29A	109.0
C30–C29–H29B	109.0
C29–C30–H30A	108.7
C29–C30–H30B	108.7
H30A–C30–H30B	107.6
C31–C30–C29	114.03(17)
C31–C30–H30A	108.7
C31–C30–H30B	108.7
C30–C31–H31A	108.8
C30–C31–H31B	108.8
C30–C31–C32	113.83(18)
H31A–C31–H31B	107.7
C32–C31–H31A	108.8
C32–C31–H31B	108.8
C31–C32–H32A	108.8
C31–C32–H32B	108.8
H32A–C32–H32B	107.7
C33–C32–C31	113.60(18)
C33–C32–H32A	108.8
C33–C32–H32B	108.8
C32–C33–H33A	108.7
C32–C33–H33B	108.7
C32–C33–C34	114.12(18)
H33A–C33–H33B	107.6
C34–C33–H33A	108.7
C34–C33–H33B	108.7
C33–C34–H34A	109.0
C33–C34–H34B	109.0
H34A–C34–H34B	107.8
C35–C34–C33	113.13(19)
C35–C34–H34A	109.0
C35–C34–H34B	109.0
C34–C35–H35A	108.9
C34–C35–H35B	108.9
C34–C35–C36	113.2(2)
H35A–C35–H35B	107.7

C36–C35–H35A	108.9
C36–C35–H35B	108.9
C35–C36–H36A	109.5
C35–C36–H36B	109.5
C35–C36–H36C	109.5
H36A–C36–H36B	109.5
H36A–C36–H36C	109.5
H36B–C36–H36C	109.5
N2–C37–H37A	109.0
N2–C37–H37B	109.0
N2–C37–C38	113.07(17)
H37A–C37–H37B	107.8
C38–C37–H37A	109.0
C38–C37–H37B	109.0
C37–C38–H38A	109.4
C37–C38–H38B	109.4
C37–C38–C39	111.30(17)
H38A–C38–H38B	108.0
C39–C38–H38A	109.4
C39–C38–H38B	109.4
C38–C39–H39A	108.8
C38–C39–H39B	108.8
H39A–C39–H39B	107.7
C40–C39–C38	113.64(18)
C40–C39–H39A	108.8
C40–C39–H39B	108.8
C39–C40–H40A	108.9
C39–C40–H40B	108.9
C39–C40–C41	113.36(18)
H40A–C40–H40B	107.7
C41–C40–H40A	108.9
C41–C40–H40B	108.9
C40–C41–H41A	109.2
C40–C41–H41B	109.2
H41A–C41–H41B	107.9
C42–C41–C40	112.14(18)
C42–C41–H41A	109.2
C42–C41–H41B	109.2
C41–C42–H42A	108.4
C41–C42–H42B	108.4
C41–C42–C43	115.33(18)
H42A–C42–H42B	107.5
C43–C42–H42A	108.4
C43–C42–H42B	108.4
C42–C43–H43A	109.4
C42–C43–H43B	109.4
H43A–C43–H43B	108.0
C44–C43–C42	111.03(18)
C44–C43–H43A	109.4

C44–C43–H43B	109.4
C43–C44–H44A	108.3
C43–C44–H44B	108.3
H44A–C44–H44B	107.4
C45–C44–C43	115.76(19)
C45–C44–H44A	108.3
C45–C44–H44B	108.3
C44–C45–H45A	109.3
C44–C45–H45B	109.3
C44–C45–C46	111.7(2)
H45A–C45–H45B	107.9
C46–C45–H45A	109.3
C46–C45–H45B	109.3
C45–C46–H46A	108.3
C45–C46–H46B	108.3
H46A–C46–H46B	107.4
C47–C46–C45	116.0(2)
C47–C46–H46A	108.3
C47–C46–H46B	108.3
C46–C47–H47A	109.0
C46–C47–H47B	109.0
C46–C47–C48	112.8(3)
H47A–C47–H47B	107.8
C48–C47–H47A	109.0
C48–C47–H47B	109.0
C47–C48–H48A	109.5
C47–C48–H48B	109.5
C47–C48–H48C	109.5
H48A–C48–H48B	109.5
H48A–C48–H48C	109.5
H48B–C48–H48C	109.5
C112–S101–C109	92.31(10)
C113–S102–C116	92.62(10)
C101–O101–C108	105.85(16)
C120–O102–C125	117.07(15)
C120–N101–C119	116.86(17)
C123–N102–C137	119.86(16)
C124–N102–C123	123.26(16)
C124–N102–C137	116.87(16)
O101–C101–C106	110.18(19)
C102–C101–O101	125.4(2)
C102–C101–C106	124.4(2)
C101–C102–H102	122.0
C101–C102–C103	116.1(2)
C103–C102–H102	122.0
C102–C103–H103	119.4
C102–C103–C104	121.1(2)
C104–C103–H103	119.4
C103–C104–H104	119.3

C105–C104–C103	121.4(2)
C105–C104–H104	119.3
C104–C105–H105	120.9
C104–C105–C106	118.2(2)
C106–C105–H105	120.9
C101–C106–C105	118.7(2)
C101–C106–C107	106.05(18)
C105–C106–C107	135.2(2)
C106–C107–H107	126.7
C108–C107–C106	106.5(2)
C108–C107–H107	126.7
O101–C108–C109	113.81(18)
C107–C108–O101	111.39(19)
C107–C108–C109	134.8(2)
C108–C109–S101	118.83(17)
C110–C109–S101	110.93(16)
C110–C109–C108	130.2(2)
C109–C110–H110	123.6
C109–C110–C111	112.9(2)
C111–C110–H110	123.6
C110–C111–H111	123.5
C112–C111–C110	113.0(2)
C112–C111–H111	123.5
C111–C112–S101	110.86(15)
C111–C112–C113	129.9(2)
C113–C112–S101	119.28(16)
C112–C113–S102	119.95(16)
C114–C113–S102	110.81(15)
C114–C113–C112	129.2(2)
C113–C114–H114	123.7
C113–C114–C115	112.56(19)
C115–C114–H114	123.7
C114–C115–H115	122.9
C116–C115–C114	114.14(18)
C116–C115–H115	122.9
C115–C116–S102	109.87(15)
C115–C116–C117	127.35(18)
C117–C116–S102	122.77(15)
C116–C117–C124	118.47(17)
C118–C117–C116	121.94(18)
C118–C117–C124	119.57(18)
C117–C118–H118	119.3
C117–C118–C119	121.44(18)
C119–C118–H118	119.3
N101–C119–C118	117.70(17)
N101–C119–C123	122.80(17)
C123–C119–C118	119.49(17)
O102–C120–C121	115.61(17)
N101–C120–O102	119.84(17)

N101–C120–C121	124.55(18)
C120–C121–H121	120.8
C122–C121–C120	118.49(18)
C122–C121–H121	120.8
C121–C122–H122	120.4
C121–C122–C123	119.25(18)
C123–C122–H122	120.4
N102–C123–C119	118.96(17)
N102–C123–C122	123.00(18)
C119–C123–C122	118.04(17)
O103–C124–N102	120.58(18)
O103–C124–C117	122.28(18)
N102–C124–C117	117.14(16)
O102–C125–H12A	110.3
O102–C125–H12B	110.3
O102–C125–C126	107.31(16)
H12A–C125–H12B	108.5
C126–C125–H12A	110.3
C126–C125–H12B	110.3
C125–C126–H12C	109.3
C125–C126–H12D	109.3
C125–C126–C127	111.70(17)
H12C–C126–H12D	107.9
C127–C126–H12C	109.3
C127–C126–H12D	109.3
C126–C127–H12E	109.0
C126–C127–H12F	109.0
C126–C127–C128	113.07(17)
H12E–C127–H12F	107.8
C128–C127–H12E	109.0
C128–C127–H12F	109.0
C127–C128–H12G	108.7
C127–C128–H12H	108.7
H12G–C128–H12H	107.6
C129–C128–C127	114.02(17)
C129–C128–H12G	108.7
C129–C128–H12H	108.7
C128–C129–H12I	109.0
C128–C129–H12J	109.0
C128–C129–C130	112.85(17)
H12I–C129–H12J	107.8
C130–C129–H12I	109.0
C130–C129–H12J	109.0
C129–C130–H13A	108.8
C129–C130–H13B	108.8
C129–C130–C131	113.82(17)
H13A–C130–H13B	107.7
C131–C130–H13A	108.8
C131–C130–H13B	108.8

C130–C131–H13C	108.9
C130–C131–H13D	108.9
H13C–C131–H13D	107.7
C132–C131–C130	113.26(18)
C132–C131–H13C	108.9
C132–C131–H13D	108.9
C131–C132–H13E	108.8
C131–C132–H13F	108.8
C131–C132–C133	113.81(18)
H13E–C132–H13F	107.7
C133–C132–H13E	108.8
C133–C132–H13F	108.8
C132–C133–H13G	108.9
C132–C133–H13H	108.9
C132–C133–C134	113.15(18)
H13G–C133–H13H	107.8
C134–C133–H13G	108.9
C134–C133–H13H	108.9
C133–C134–H13I	108.8
C133–C134–H13J	108.8
C133–C134–C135	113.65(19)
H13I–C134–H13J	107.7
C135–C134–H13I	108.8
C135–C134–H13J	108.8
C134–C135–H13K	109.2
C134–C135–H13L	109.2
C134–C135–C136	112.0(2)
H13K–C135–H13L	107.9
C136–C135–H13K	109.2
C136–C135–H13L	109.2
C135–C136–H13M	109.5
C135–C136–H13N	109.5
C135–C136–H13O	109.5
H13M–C136–H13N	109.5
H13M–C136–H13O	109.5
H13N–C136–H13O	109.5
N102–C137–H13P	108.9
N102–C137–H13Q	108.9
N102–C137–C138	113.24(16)
H13P–C137–H13Q	107.7
C138–C137–H13P	108.9
C138–C137–H13Q	108.9
C137–C138–H13R	109.2
C137–C138–H13S	109.2
C137–C138–C139	112.15(17)
H13R–C138–H13S	107.9
C139–C138–H13R	109.2
C139–C138–H13S	109.2
C138–C139–H13T	108.7

C138–C139–H13U	108.7
H13T–C139–H13U	107.6
C140–C139–C138	114.21(17)
C140–C139–H13T	108.7
C140–C139–H13U	108.7
C139–C140–H14A	108.8
C139–C140–H14B	108.8
C139–C140–C141	113.61(17)
H14A–C140–H14B	107.7
C141–C140–H14A	108.8
C141–C140–H14B	108.8
C140–C141–H14C	109.3
C140–C141–H14D	109.3
H14C–C141–H14D	107.9
C142–C141–C140	111.80(17)
C142–C141–H14C	109.3
C142–C141–H14D	109.3
C141–C142–H14E	108.1
C141–C142–H14F	108.1
C141–C142–C143	116.90(17)
H14E–C142–H14F	107.3
C143–C142–H14E	108.1
C143–C142–H14F	108.1
C142–C143–H14G	109.7
C142–C143–H14H	109.7
C142–C143–C144	110.02(17)
H14G–C143–H14H	108.2
C144–C143–H14G	109.7
C144–C143–H14H	109.7
C143–C144–H14I	108.2
C143–C144–H14J	108.2
H14I–C144–H14J	107.4
C145–C144–C143	116.21(17)
C145–C144–H14I	108.2
C145–C144–H14J	108.2
C144–C145–H14K	109.4
C144–C145–H14L	109.4
C144–C145–C146	111.32(18)
H14K–C145–H14L	108.0
C146–C145–H14K	109.4
C146–C145–H14L	109.4
C145–C146–H14M	108.6
C145–C146–H14N	108.6
H14M–C146–H14N	107.6
C147–C146–C145	114.57(19)
C147–C146–H14M	108.6
C147–C146–H14N	108.6
C146–C147–H14O	109.1
C146–C147–H14P	109.1

C146–C147–C148	112.4(2)
H14O–C147–H14P	107.9
C148–C147–H14O	109.1
C148–C147–H14P	109.1
C147–C148–H14Q	109.5
C147–C148–H14R	109.5
C147–C148–H14S	109.5
H14Q–C148–H14R	109.5
H14Q–C148–H14S	109.5
H14R–C148–H14S	109.5

Symmetry transformations used to generate equivalent atoms:

Table 4. Anisotropic displacement parameters [Å$^2\times$ 10^3]. The anisotropic displacement factor exponent takes the form: $-2\pi^2[h^2a^{*2}U^{11} + \cdots + 2\ h\ k\ a^*\ b^*\ U^{12}\ ]$.

Atom	U^{11}	U^{22}	U^{33}	U^{23}	U^{13}	U^{12}
S1	24(1)	29(1)	28(1)	13(1)	8(1)	12(1)
S2	24(1)	25(1)	28(1)	13(1)	10(1)	11(1)
O1	26(1)	31(1)	34(1)	15(1)	9(1)	14(1)
O2	24(1)	27(1)	32(1)	19(1)	10(1)	10(1)
O3	29(1)	27(1)	38(1)	20(1)	12(1)	11(1)
N1	25(1)	22(1)	25(1)	12(1)	9(1)	9(1)
N2	24(1)	23(1)	32(1)	15(1)	12(1)	8(1)
C1	31(1)	33(1)	29(1)	14(1)	10(1)	19(1)
C2	29(1)	36(1)	39(1)	16(1)	12(1)	14(1)
C3	34(1)	36(1)	41(1)	20(1)	16(1)	15(1)
C4	36(1)	41(1)	41(1)	22(1)	17(1)	22(1)
C5	32(1)	44(1)	39(1)	22(1)	13(1)	21(1)
C6	25(1)	37(1)	30(1)	14(1)	11(1)	16(1)
C7	24(1)	39(1)	35(1)	16(1)	11(1)	14(1)
C8	25(1)	31(1)	26(1)	7(1)	10(1)	11(1)
C9	26(1)	32(1)	24(1)	10(1)	11(1)	15(1)
C10	23(1)	37(1)	32(1)	14(1)	9(1)	13(1)
C11	28(1)	31(1)	35(1)	14(1)	14(1)	12(1)
C12	28(1)	30(1)	24(1)	11(1)	11(1)	14(1)
C13	27(1)	29(1)	22(1)	9(1)	9(1)	12(1)
C14	24(1)	29(1)	32(1)	13(1)	9(1)	8(1)
C15	27(1)	26(1)	35(1)	16(1)	12(1)	9(1)
C16	25(1)	24(1)	26(1)	12(1)	12(1)	10(1)
C17	24(1)	24(1)	26(1)	11(1)	10(1)	10(1)
C18	24(1)	24(1)	26(1)	12(1)	12(1)	7(1)
C19	24(1)	21(1)	23(1)	10(1)	8(1)	8(1)
C20	27(1)	22(1)	25(1)	13(1)	10(1)	10(1)
C21	25(1)	26(1)	32(1)	14(1)	11(1)	11(1)
C22	26(1)	24(1)	34(1)	14(1)	13(1)	8(1)
C23	25(1)	22(1)	25(1)	11(1)	10(1)	9(1)
C24	27(1)	24(1)	26(1)	12(1)	11(1)	10(1)
C25	25(1)	27(1)	31(1)	16(1)	12(1)	8(1)
C26	27(1)	26(1)	28(1)	16(1)	11(1)	10(1)
C27	28(1)	27(1)	32(1)	16(1)	11(1)	10(1)
C28	27(1)	27(1)	29(1)	16(1)	13(1)	10(1)
C29	29(1)	23(1)	32(1)	14(1)	14(1)	10(1)
C30	28(1)	26(1)	33(1)	16(1)	15(1)	12(1)
C31	30(1)	26(1)	30(1)	15(1)	14(1)	10(1)
C32	30(1)	27(1)	37(1)	16(1)	18(1)	13(1)
C33	31(1)	26(1)	32(1)	15(1)	14(1)	9(1)
C34	35(1)	27(1)	41(1)	19(1)	22(1)	14(1)
C35	42(1)	27(1)	39(1)	17(1)	21(1)	13(1)
C36	62(2)	34(1)	65(2)	30(1)	37(2)	22(1)
C37	29(1)	24(1)	31(1)	14(1)	14(1)	11(1)
C38	32(1)	28(1)	29(1)	10(1)	12(1)	9(1)
C39	29(1)	29(1)	34(1)	13(1)	10(1)	8(1)

C40	26(1)	26(1)	36(1)	14(1)	11(1)	6(1)
C41	29(1)	26(1)	36(1)	14(1)	16(1)	10(1)
C42	30(1)	27(1)	30(1)	12(1)	14(1)	7(1)
C43	32(1)	28(1)	36(1)	14(1)	18(1)	8(1)
C44	34(1)	28(1)	31(1)	13(1)	15(1)	9(1)
C45	46(1)	31(1)	41(1)	16(1)	26(1)	13(1)
C46	56(2)	33(1)	39(1)	17(1)	26(1)	15(1)
C47	66(2)	36(1)	64(2)	25(1)	34(2)	13(1)
C48	91(2)	37(2)	73(2)	28(2)	48(2)	27(2)
S101	27(1)	34(1)	34(1)	17(1)	11(1)	16(1)
S102	25(1)	31(1)	35(1)	20(1)	14(1)	15(1)
O101	29(1)	32(1)	30(1)	14(1)	9(1)	16(1)
O102	22(1)	24(1)	31(1)	17(1)	7(1)	7(1)
O103	29(1)	27(1)	38(1)	20(1)	15(1)	12(1)
N101	22(1)	21(1)	25(1)	12(1)	10(1)	8(1)
N102	22(1)	19(1)	27(1)	12(1)	11(1)	6(1)
C101	28(1)	31(1)	30(1)	14(1)	14(1)	17(1)
C102	28(1)	35(1)	35(1)	11(1)	11(1)	15(1)
C103	33(1)	33(1)	45(1)	17(1)	20(1)	16(1)
C104	36(1)	40(1)	43(1)	24(1)	19(1)	21(1)
C105	29(1)	42(1)	38(1)	20(1)	12(1)	16(1)
C106	26(1)	32(1)	32(1)	14(1)	13(1)	15(1)
C107	25(1)	34(1)	32(1)	14(1)	10(1)	13(1)
C108	25(1)	30(1)	27(1)	9(1)	12(1)	12(1)
C109	30(1)	34(1)	27(1)	14(1)	13(1)	20(1)
C110	26(1)	38(1)	31(1)	15(1)	11(1)	17(1)
C111	27(1)	33(1)	33(1)	15(1)	13(1)	14(1)
C112	28(1)	32(1)	28(1)	13(1)	13(1)	16(1)
C113	26(1)	31(1)	25(1)	11(1)	10(1)	15(1)
C114	24(1)	29(1)	32(1)	11(1)	10(1)	10(1)
C115	28(1)	26(1)	31(1)	15(1)	12(1)	12(1)
C116	27(1)	26(1)	25(1)	13(1)	12(1)	13(1)
C117	24(1)	24(1)	25(1)	12(1)	13(1)	11(1)
C118	22(1)	22(1)	26(1)	11(1)	10(1)	7(1)
C119	21(1)	21(1)	22(1)	10(1)	9(1)	8(1)
C120	23(1)	23(1)	24(1)	12(1)	9(1)	8(1)
C121	21(1)	25(1)	25(1)	11(1)	7(1)	7(1)
C122	21(1)	23(1)	27(1)	11(1)	9(1)	5(1)
C123	24(1)	21(1)	23(1)	10(1)	11(1)	9(1)
C124	26(1)	23(1)	27(1)	14(1)	14(1)	12(1)
C125	23(1)	24(1)	30(1)	16(1)	10(1)	7(1)
C126	25(1)	26(1)	30(1)	15(1)	10(1)	9(1)
C127	24(1)	26(1)	34(1)	17(1)	10(1)	10(1)
C128	25(1)	24(1)	33(1)	17(1)	11(1)	9(1)
C129	26(1)	28(1)	35(1)	18(1)	13(1)	10(1)
C130	25(1)	24(1)	32(1)	14(1)	12(1)	7(1)
C131	28(1)	27(1)	36(1)	18(1)	13(1)	8(1)
C132	29(1)	28(1)	33(1)	16(1)	14(1)	10(1)
C133	27(1)	27(1)	36(1)	17(1)	12(1)	7(1)
C134	31(1)	30(1)	38(1)	19(1)	14(1)	10(1)
C135	37(1)	30(1)	39(1)	17(1)	18(1)	7(1)

C136	45(2)	41(1)	50(2)	27(1)	24(1)	14(1)
C137	27(1)	20(1)	28(1)	10(1)	13(1)	6(1)
C138	28(1)	24(1)	29(1)	11(1)	14(1)	9(1)
C139	26(1)	27(1)	30(1)	14(1)	13(1)	9(1)
C140	26(1)	26(1)	32(1)	14(1)	12(1)	7(1)
C141	26(1)	25(1)	33(1)	13(1)	13(1)	7(1)
C142	26(1)	25(1)	31(1)	12(1)	12(1)	7(1)
C143	26(1)	24(1)	32(1)	14(1)	13(1)	9(1)
C144	28(1)	24(1)	33(1)	14(1)	11(1)	11(1)
C145	31(1)	22(1)	33(1)	13(1)	14(1)	10(1)
C146	36(1)	25(1)	33(1)	13(1)	13(1)	11(1)
C147	42(1)	26(1)	42(1)	18(1)	19(1)	13(1)
C148	55(2)	38(1)	59(2)	31(1)	27(1)	25(1)